Exploring friction at the smallest scale *pp. 1089 & 1115*

Overseas ozone complicates regional regulation *p. 1096*

Human meiosis revealed in living color *p. 1143*

Science

$10
5 JUNE 2015
sciencemag.org
AAAS

Out of the forest

Isolated tribes emerge into a perilous future

pp. 1061 & 1072

CONTENTS

5 JUNE 2015 • VOLUME 348 • ISSUE 6239

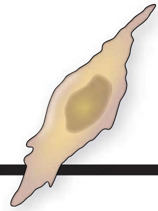

NEWS

INSIGHTS

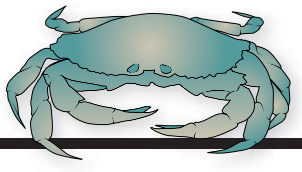

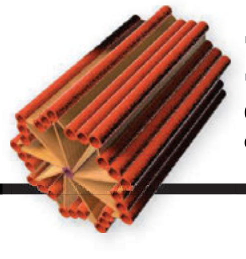

LETTERS

DEPARTMENTS

RESEARCH

IN BRIEF

RESEARCH ARTICLES

REPORTS

ON THE COVER

The Awá people of the Brazilian Amazon. Some of the Awá have recently contacted the outside world, and such contacts with isolated tribes are on the rise. Anthropologists say that these emerging tribes are threatened by common Western diseases and exploitative outsiders and may face a dangerous future without protection. See pages 1061, 1072, and 1080. *Photo: Domenico Pugliese/Survival International*

SCIENCE (ISSN 0036-8075) is published weekly on Friday, except the last week in December, by the American Association for the Advancement of Science, 1200 New York Avenue, NW, Washington, DC 20005. Periodicals mail postage (publication No. 484460) paid at Washington, DC, and additional mailing offices.

Domestic individual membership and subscription (51 issues): \$153 (\$74 allocated to subscription). Domestic institutional subscription (51 issues): \$1282; Foreign postage extra: Mexico, Caribbean (surface mail) \$55; other countries (air assist delivery) \$85. First class, airmail, student, and emeritus rates on request. Canadian rates with GST available upon request, GST #1254 88122. Publications Mail Agreement Number 1069624. **Printed in the U.S.A.**
Change of address: Allow 4 weeks, giving old and new addresses and 8-digit account number. **Postmaster:** Send change of address to AAAS, P.O. Box 96178, Washington, DC 20090–6178. **Single-copy sales:** \$10.00 current issue, \$15.00 back issue prepaid includes surface postage; bulk rates on request. **Authorization to photocopy** material for internal or personal use under circumstances not falling within the fair use provisions of the Copyright Act is granted by AAAS to libraries and other users registered with the Copyright Clearance Center (CCC) Transactional Reporting Service, provided that \$30.00 per article is paid directly to CCC, 222 Rosewood Drive, Danvers, MA 01923. The identification code for *Science* is 0036-8075. *Science* is indexed in the *Reader's Guide to Periodical Literature* and in several specialized indexes.

Protecting isolated tribes

There are about 50 isolated indigenous societies across lowland South America, with limited to no contact with the outside world. Despite displacements, epidemics, and hostile interactions with outsiders, such tribes still manage to survive. How can we ensure the well-being of humanity's last known isolated peoples under such enormous and mounting pressure from external threats?

Generally, the current policy of governments, primarily those of Brazil and Peru, and supported by the United Nations, is a "leave them alone" strategy. There are two implicit assumptions in a no-contact approach, however: that isolated populations are viable in the long term, and that they would choose isolation if they had full information (i.e., if they were aware that contact would not lead to massacre and enslavement). The first assumption is unlikely. Ethnohistorical accounts reveal the real risk of severe depopulation or extinction during intermittent hostile and sporadic interaction with the outside world. Miners, loggers, and hunters penetrate into the homelands of isolated tribes despite government "protection." Unless protection efforts against external threats and accidental encounters are drastically increased, the chances that these tribes will survive are slim. Disease epidemics, compounded by demographic variability and inbreeding effects, makes the disappearance of small, isolated groups very probable in the near future. The second assumption is also unlikely. Interviews indicate that contacted groups had mainly chosen isolation out of fear of being killed or enslaved, but they also wanted outside goods and innovations and positive social interactions with neighbors.

"Controlled contact with isolated peoples is a better option than a no-contact policy."

Controlled contact with isolated peoples is a better option than a no-contact policy. This means that governments should initiate contact only after conceiving a well-organized plan. In the past, there have been many poorly planned contacts with isolated Amazonian tribes by both missionaries and government agencies. The absence of health care professionals and health monitoring led to many deaths of these vulnerable peoples. One of us (K.R.H.) was on site within weeks of the first peaceful contacts with Aché, Yora, Mascho-Piro, and Matsiguenga communities in Paraguay and Peru when they were extremely isolated and suffering from new contact-related epidemics (from the late 1970s to mid-1980s), even though intermittent contact (mostly accidental) had occurred for 25 years. The most important lesson learned from these experiences is that mortality can be reduced to near zero if the contact team is prepared to provide sustained, around-the-clock medical treatment, as well as food. A well-designed contact can be quite safe, compared to the disastrous outcomes from accidental contacts. But safe contact requires a qualified team of cultural translators and health care professionals that is committed to staying on site for more than a year. For example, foreign missionaries provided great care for the Yora for up to 6 months, but when they decided to take a furlough, dozens of Yora died within a few weeks. Similarly, in 1975, missionaries provided care to an Aché community for a year, but when they took a vacation, many Aché died. Fortunately, there have been some success stories such as a 1978 contact with a band of Northern Aché. Missionaries and anthropologists treated them with antibiotics when primary respiratory infections progressed to pneumonia. They also provided food to the sick.

Given that isolated populations are not viable in the long term, well-organized contacts are today both humane and ethical. We know that soon after peaceful contact with the outside world, surviving indigenous populations rebound quickly from population crashes, ,with growth rates over 3% per year. Once a sustained peaceful contact occurs, it becomes much easier to protect native rights than it otherwise would be for isolated populations. Leaving groups isolated, yet still exposed to dangerous and uncontrolled interactions with the outside world, is a violation of governmental responsibility. By refusing authorized, well-planned contacts, governments are simply guaranteeing that accidental and disastrous contacts will take place instead.

–**Robert S. Walker and Kim R. Hill**

Robert S. Walker is an assistant professor in the Department of Anthropology at the University of Missouri, Columbia, MO. E-mail: walkerro@missouri.edu

Kim R. Hill is a professor in the School of Human Evolution and Social Change at Arizona State University, Tempe, AZ. E-mail: kim.hill@asu.edu

PHOTOS: (TOP RIGHT) UNIVERSITY OF MISSOURI; (BOTTOM RIGHT) ARIZONA STATE UNIVERSITY; (INSET) © SPLASH NEWS/CORBIS

10.1126/science.aac6540

NEWS

"It's going to end brain research in this country. It will be disastrous."

David Nutt, a former chief drug adviser to the U.K. government, complaining that a new bill to ban the sale of all psychoactive substances in the country will stifle scientists' access to compounds.

IN BRIEF

Mystery malady kills saiga antelopes

Burial pit for saiga antelopes that have died in central Kazakhstan.

A mysterious illness is sweeping through the critically endangered saiga antelopes of Central Asia. Since 10 May, some 120,000—about half of the world's saiga (*Saiga tatarica*) population—have died of the unidentified ailment, which causes severe diarrhea and respiratory problems. Saiga (pictured above) are known for these strange die-offs, particularly during calving season when herds of females give birth within 1 week, creating perfect conditions for disease to spread because of their close proximity. But the current crisis is more alarming—and puzzling—as entire herds of mothers and calves are falling ill at the same time, even when hundreds of kilometers apart. Using tissue samples collected from the Betpak-Dala region of Kazakhstan, where the die-off is centered, scientists at the Royal Veterinary College in Hatfield, U.K., have narrowed the possible diseases to two types of bacterial infections or to a viral ailment transmitted by mosquitoes. They hope lab tests will provide a definitive diagnosis.

AROUND THE WORLD

Asia battles MERS outbreak

SEOUL | Authorities in South Korea and China are scrambling to contain an outbreak of the deadly Middle East respiratory syndrome (MERS), a viral disease discovered in 2012 that has sickened at least 1000 people and killed more than 500, most of them in the Arabian Peninsula. The Asian cluster of cases, already the largest ever outside the Middle East, started when a South Korean business traveler returned to Seoul from the Middle East in early May. He fell ill a week later and was diagnosed with MERS on 20 May after being treated at three different clinics. As *Science* went to press, 24 others had been diagnosed with MERS as well, and two had died. Korea has already quarantined 700 people, but one contact broke his quarantine and, after a 26 May stop in Hong Kong, traveled to China's Guangdong province, where he was diagnosed with MERS. So far, no further cases have been reported from China or Hong Kong. http://scim.ag/MERSkorea

ERC shielded from cuts

BRUSSELS | The European Commission will cut €2.2 billion from its research program Horizon 2020 to fodder a controversial new investment fund aimed at boosting Europe's sluggish economy. But the European Research Council (ERC), a popular basic science fund that's part of Horizon 2020, will escape the budget knife thanks to intense pressure from E.U. parliamentarians and scientists. In January, the commission had proposed trimming €2.7 billion from Horizon 2020's budget—which totals €74 billion through 2020—including €221.2 million from ERC's envelope. After a series of talks, the commission announced on 28 May that it would find €500 million elsewhere. Also safe from cuts are the Marie Skłodowska-Curie actions, which provide funding for Ph.D. and postdoc fellowships, and a program called Spreading Excellence and Widening Participation, which aims at helping member states with poor research performance. http://scim.ag/ERCcut

PHOTO: SERGEI KHOMENKO/FAO

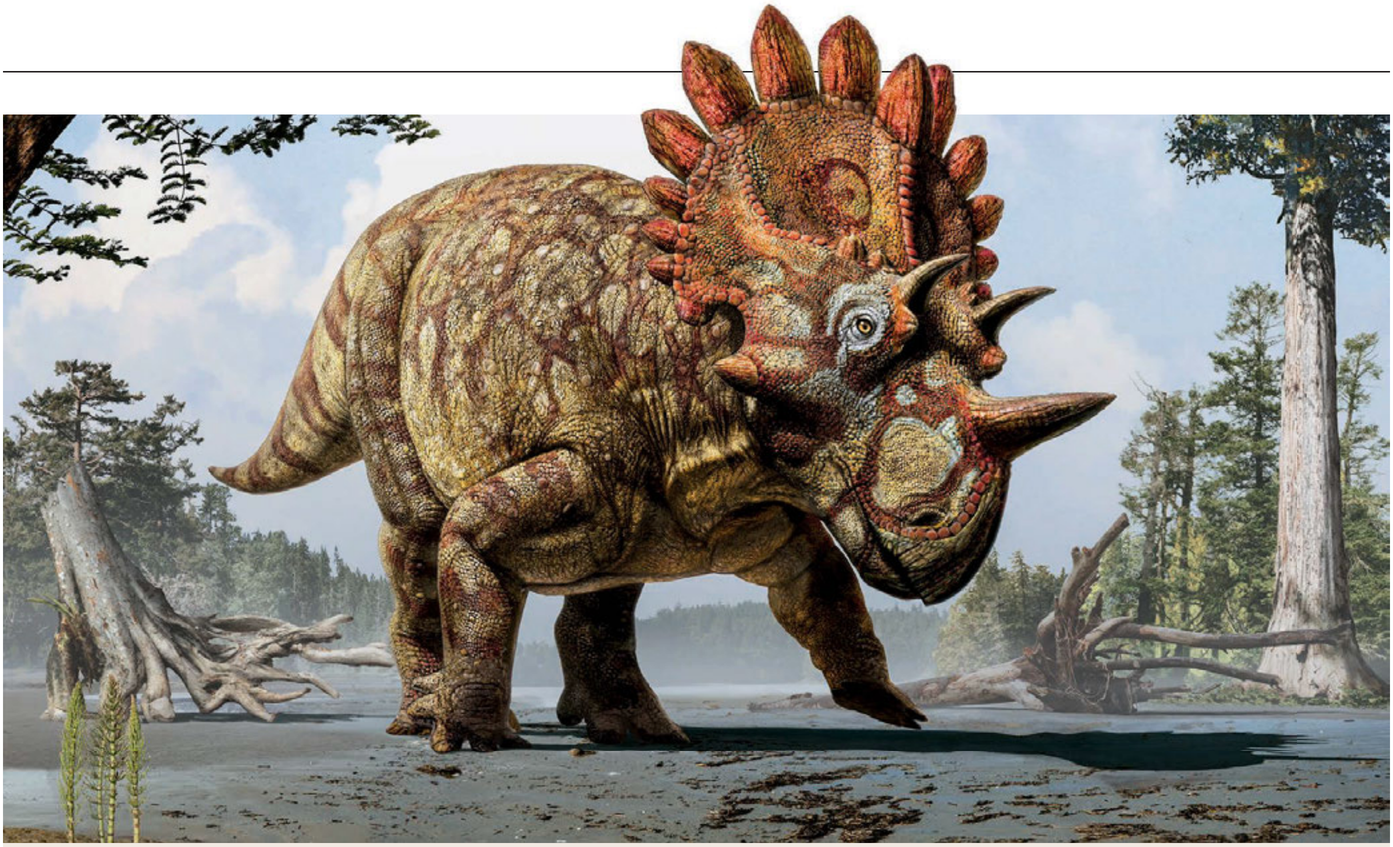

'Hellboy' dino was a close relative of *Triceratops*

They call him "Hellboy," and it's easy to see why. In addition to the sharp horns on his nose and over his eyes, which were probably used for defense against predators like *Tyrannosaurus rex*, the newly dubbed *Regaliceratops peterhewsi* dinosaur had a particularly ornate frill behind its head, most likely for sexual display. Although he is definitely a cousin of the famed *Triceratops*, Hellboy's horns and frill more closely resemble those of another group of horned dinos that includes *Centrosaurus*. Those dinos were already extinct by the time the new dino roamed what is now Alberta province in Canada, 68 million years ago, the researchers report online this week in *Current Biology*. That means his ornamentation is a case of independent evolutionary invention, the authors say. The paper includes another example of what might be called sexual display: At its very end, the lead author asks a fellow researcher at the museum to marry him. (After seeing a preprint, she said yes.) **http://scim.ag/dinohellboy**

Treat HIV immediately

WASHINGTON, D.C. | Last week, a study of 4685 HIV-infected people across 35 countries was halted early, because results showed that immediate treatment with antiviral drugs cut the risk of disease and death in half; the study's placebo arm will now be offered the drugs. The finding brings to a close a divisive issue. The United States and many other countries already recommended treating everyone diagnosed with an HIV infection, but guidelines in the United Kingdom and elsewhere called for starting treatment only after immune system damage occurs, in part because of worries about long-term toxicities of the drugs. The Strategic Timing of Antiretroviral Treatment trial, which began in April 2009 and was supposed to run through 2016, was the first randomized, controlled clinical trial to evaluate the benefits of early treatment. Its data also validate the push to use treatment as a prevention tool, as HIV-infected people on antiretrovirals are far less likely to transmit the virus to others.

Chimp care in Liberia assailed

MONROVIA | A dispute over who should fund the care and feeding of 66 chimpanzees living on island sanctuaries in Liberia has sparked a campaign for the animals. Researchers with the New York Blood Center (NYBC) in New York City had tested hepatitis vaccines in the chimps before moving them in 2006 to mangrove islands, where they roam freely. NYBC was contributing to the estimated $30,000 per month required for the chimps' care. But the center recently cut off funding and is in arbitration with the Liberian government over sharing the financial burden for the animals' well-being. Concerned that the sanctuaries are not supplying the chimps with food and water, Brian Hare, a great ape researcher at Duke University in Durham, North Carolina, has launched a petition (http://bit.ly/chimppetition) urging NYBC to restore funding.

Chimps at the Liberian rehabilitation center for apes.

IMAGES: (TOP TO BOTTOM) JULIUS T. CSOTONYI/COURTESY OF ROYAL TYRRELL MUSEUM, DRUMHELLER, ALBERTA; © ALBRECHT G. SCHAEFER/CORBIS

Great Barrier Reef still a World Heritage Site—for now

Australia's Great Barrier Reef (GBR) has narrowly avoided earning an embarrassing "in danger" listing by the United Nations Organization for Education, Science and Culture's World Heritage Committee. In a draft decision announced on 29 May, the World Heritage Committee working group noted "with concern" that the overall outlook for the reef is "poor," and that climate change, poor water quality, and coastal development are major threats to its health. The decision—which will be approved or amended by the full committee later this month—allows the GBR (shown) to keep its current World Heritage Area status, but requires Australia to report on progress to safeguard the reef from further decline by 1 December 2016. If "anticipated progress" is not demonstrated by that time, an "in danger" listing will be reconsidered in 2017. Australia will also have to report in 2020 on whether the nation's Reef 2050 Long-Term Sustainability Plan is meeting its targets. **http://scim.ag/GBRWHC**

IS group to spare Palmyra

PALMYRA, SYRIA | An Islamic State military commander said last week that the archaeological sites at the central Syrian city of Palmyra will not be destroyed. Palmyra is one of six World Heritage Sites in Syria, and archaeologists feared that the city's beautifully preserved ruins dating back to roughly 2000 years ago would be looted and torn down. The Islamic State group has bulldozed the ruins of another World Heritage Site—the city of Hatra in northern Iraq—and licensed the sale of archaeological artifacts. Although the group has said that Palmyra will not be targeted, it does plan to destroy religious buildings and artifacts such as statues, which it believes violate the Islamic law against idolatry. Satellite images confirm that Palmyra's archaeological sites are intact for now. Many, but not all, of the city's statues and artifacts were evacuated by President Bashar al-Assad's forces before the Islamic State group took the city.

U.S. revises wetlands rule

WASHINGTON, D.C. | Seasonal streams and small wetlands in the United States will get greater protection from development under a controversial federal rule issued on 27 May. The rule, written by the U.S. Army Corps of Engineers and the Environmental Protection Agency, is designed to clarify which water bodies are covered by the Clean Water Act. Builders and others will now be required to receive a permit before disturbing smaller water bodies that have a hydrological connection to a larger river or lake. Many conservation scientists welcomed the rule, which they say will help protect vulnerable ecosystems. Industry and farm groups, however, have vowed to block its implementation in court or through action by Congress.

BY THE NUMBERS

47

Number of colleges that graduated half of all 918 MacArthur Foundation "genius" award winners, according to a report intended to highlight the diversity of recipients. Eleven percent of fellows attended either Harvard University or Princeton University.

40

Number of robotics engineers that Uber Technologies Inc. has hired away from Carnegie Mellon University, to develop autonomous vehicles that can replace human drivers.

$4 million

Funds raised so far for the Big Bang Theory Scholarship Endowment by the cast and crew of the popular TV show to help support University of California, Los Angeles, students in STEM fields.

NEWSMAKERS

Explaining sleep to 11-year-olds

"Danger! If you don't sleep, you'll die!" That's the prizewinning message from materials scientist **Brandon Aldinger** in the latest version of the Flame Challenge—an annual competition to encourage scientists to share their research in clear and accessible terms. Some 20,000 11-year-old judges from around the world decided Aldinger, who designs transparent armor for soldiers at a small company in Saxonburg, Pennsylvania, should receive the $1000 prize for best written answer. Health physics master's student **Eric Galicia** of the Illinois Institute of Technology won $1000 for the best video. The contest, created by actor and science communicator Alan Alda and sponsored in part by AAAS, which publishes *Science*, has previously challenged scientists to explain flame, time, and color.

IN DEPTH

CLIMATE SCIENCE

Lost and found: Earth's missing heat

A reanalysis of surface temperatures suggests there never was a global warming hiatus

By **Carolyn Gramling**

What if the missing heat has been there all along? In 2013, the Intergovernmental Panel on Climate Change (IPCC) flagged an odd phenomenon: Atmospheric temperature data collected over the past few decades suggested that global warming had slowed down beginning around 1998. Global warming skeptics crowed, and scientists delved into the global climate system to find out where the missing heat had gone. But a new analysis suggests that the real culprits are the data themselves. When better corrections for various sources of bias are applied to the data, the authors say, the so-called global warming hiatus vanishes—and in fact, they argue, global warming may have sped up.

That won't startle some scientists, who say the "hiatus" was always a misnomer. "There is no hiatus or pause," says climate scientist Michael Mann of Pennsylvania State University, University Park, who prefers the term "temporary slowdown." But he and others do think something has changed since the late 1990s: Perhaps the deep waters of the Pacific and Atlantic oceans are storing more heat, or volcanic eruptions and pollution have been shading the planet and offsetting the warming. What's more, they note, 1998 was a particularly strong (and hot) El Niño year—not an ideal starting point for determining a subsequent trend.

But the temperature data themselves—collected by a variety of techniques from land and sea—have also been a source of concern, says Thomas Karl, director of the National Oceanic and Atmospheric Administration's National Climatic Data Center in Asheville, North Carolina, and the lead author on the new paper published online this week in *Science* (http://scim.ag/TKarl). Climate scientists have worked for years to improve corrections for bias in the data. "It's an ongoing activity," Karl says.

Creating a single, self-consistent, long-term record of sea surface temperature (SST) has proven especially tricky. For much of the past 2 centuries, ocean temperatures were measured from ships, by means of a bucket thrown over the side. Different fleets used different measurement techniques and, over time, various types of buckets—first wooden ones, then specially designed canvas ones. Eventually, buckets gave way to ship engine intake measurements, taken when water was brought in to cool the machinery. And by the end of the 20th century, far more accurate buoy measurements took over. Each technique required different corrections.

Another challenge was incorporating land-based readings from thousands of new measurement stations in regions that have long had scant coverage, particularly Asia, South America, and Africa. New data from these regions have been amassed over the past 5 years as part of the International Surface Temperature Initiative, which released its first report just last year.

In their paper, Karl's team sums up the combined effect of additional land temperature stations, corrected commercial ship temperature data, and corrected ship-to-buoy calibrations. The group estimates that the world warmed at a rate of 0.086°C per decade between 1998 and 2012—more than twice the IPCC's estimate of about 0.039°C per decade. The new estimate, the researchers note, is much closer to the rate of 0.113°C per decade estimated for 1950 to 1999. And for the period from 2000 to 2014,

Vanishing hiatus

New data and corrections for bias suggest global warming rates (squares) are higher than scientists thought (circles).

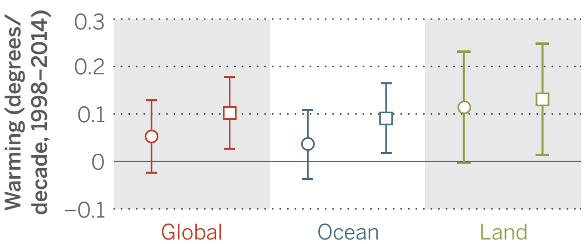

CREDITS: (PHOTO) CLAUDIA KÜNKEL; (DATA) KARL *ET AL.* (ADVANCED ONLINE PUBLICATION, 4 JUNE)

Published by AAAS

Buoys, such as this 3-meter discus buoy beached in California, provide temperature data worldwide.

the new analysis suggests a warming rate of 0.116°C per decade—slightly higher than the 20th century rate. "What you see is that the slowdown just goes away," Karl says.

And that's without including the elephant in the room: Arctic warming. A 2014 paper in the *Quarterly Journal of the Royal Meteorological Society* highlighted how the scarcity of temperature data from the Arctic, which is warming twice as fast as the rest of the planet, has produced a significant "cool" bias in the global trends, especially since 1997.

"The post-1998 period is really difficult, partially because of Arctic warming and partly because of the change in SST measurements," says Kevin Cowtan, a computational scientist at the University of York in the United Kingdom, who co-authored the 2014 paper. "The fact that it's caused problems is completely understandable, if unfortunate."

To estimate how Arctic warming might alter global trends, Karl's team used a nonlinear technique to fill in the data gaps for the polar region. Including the Arctic, they found, would add between 0.02°C and 0.03°C of warming per decade. Karl notes that this is just an estimate, however, and wasn't included in the paper's final reanalysis of recent warming.

Not everyone agrees that the 21st century slowdown is entirely a data artifact. Mann notes that there is "very clear" evidence of a slowdown in large-scale warming in the tropical Pacific; in a previous paper, he and others linked it to a natural decades-long climate pattern that brought about La Niña–like cooler conditions in the past decade (*Science*, 27 February, p. 988). "The tropical Pacific definitely warmed less over that time period than climate models had predicted," Mann says.

Cowtan agrees, adding that there are a lot of lingering uncertainties in the data, particularly in the Arctic, as well as in some of the shipboard corrections during the last century. "My feeling is, they've got the right answer—but not for quite the right reasons," Cowtan says. "My guess is there's a little bit too much ocean warming [in their calculations], and not enough from the Arctic."

Karl says his team is planning ways to address the Arctic temperature issue next. He also says research into the slowdown has spurred important insights that help clarify the global climate system. "Global temperatures might have been even warmer than we're reporting had some of these other factors not come into play," Karl says. "And once these things play out, we may find we're warming at an even more rapid rate than we saw at the end of the last century." ■

SCIENCE POLICY

Russian foundation tarred with 'foreign' label

Founder may pull plug on private research funder

By **Vladimir Pokrovsky**, *in Moscow*

Wrapping up a postdoc in Italy in 2003, Sergei Popov faced a dilemma. The astrophysicist wanted to return to his native Russia but received "quite a good offer" to stay abroad. He was about to accept it, he says, when Russia's only private research funder, the Dynasty Foundation, offered him a ticket home: a grant for young Ph.D.s. "It's owing to Dynasty that I still work in Russia," says Popov, a specialist on neutron stars here at the Sternberg Astronomical Institute.

But Dynasty's days are numbered. Last week, Russia's Justice Ministry branded the foundation a "foreign agent." The move threatens to strangle the foundation in red tape, and, Popov says, future Dynasty grantees would effectively be ostracized.

The designation infuriates Dynasty's founder, telecom tycoon Dmitry Zimin. Reached by phone, he told *Science* that he would simply "stop financing the foundation." That prospect is sending shock waves through the scientific community. "The main thing that we have lost is hope," says Valery Rubakov, a physicist here at the Russian Academy of Sciences' (RAS's) Institute for Nuclear Research. One of Russia's top biologists—Mikhail Gelfand of RAS's Institute for Information Transmission Problems—and other prominent researchers have vowed to stage a rally here on 6 June to protest the government's "disrespect to science and education" and "consistent elimination of the seedlings of civil society."

Zimin, a co-founder of the national cellular network VimpelCom, set up Dynasty in 2002. Each year since then, he says, he has transferred about $10 million of his fortune to Dynasty. The Moscow-based foundation last year spent that sum on 20 projects supporting young researchers (mainly mathematicians and physicists), competitions for science teachers, science festivals, and public lectures by world-class researchers.

As part of a campaign to crack down on nongovernmental organizations focused on human rights and free elections, the Russian government in July 2012 adopted the foreign agent law, which piles reporting requirements on designated organizations and compels them to label anything they produce, from conferences to reports, as foreign agent activities. Since then, 67 organizations have been caught in the dragnet. Some have shuttered operations in Russia, and others are fighting the designation.

In labeling Dynasty a foreign agent, officials cited its funding from offshore accounts owned by Zimin. At a press conference called last week after Dynasty's designation drew widespread condemnation, Justice Minister Alexander Konovalov stood firm. "We do not exclude that there were positive motives for the foundation's activities," he said, "but that does not exclude the necessity to implement the law." Nor is it likely that Russian President Vladimir Putin will overrule him. Putin's spokesman, Dmitry Peskov, declared last week that if Dynasty "gets money from abroad, then it *is* a foreign agent." The government is not forcing Dynasty to close, Peskov added: That's Zimin's decision, he said.

Dmitry Zimin is livid over foreign agent label.

Dynasty officials plan to meet on 8 June to decide the foundation's fate. In a letter last week to Russian scientists, Zimin wrote, "I or my heirs will renew and maybe even broaden these activities as soon as our existence in our country will become more civilized."

Dynasty had an outsized impact on Russian science, researchers say. "My personal feeling is that Dynasty made a bigger contribution than the whole state," says Boris Shtern of the RAS Institute for Nuclear Research. "Many rich people invest their money in sports clubs, in yachts, and only one of them invests in his own country's science and education," he continues. "The country has never known this kind of absurdity." ■

PHOTO: © ITAR-TASS PHOTO AGENCY/ALAMY

Published by AAAS

GENETICS

Did good genes help people outlast brutal Leningrad siege?

Study hints at more efficient metabolism in survivors

By **Yulia Smirnova** *and* **Angelina Davydova**, *in St. Petersburg, Russia*

In September 1941, German troops and Finnish allies encircled Leningrad, trapping 3 million residents in the Baltic city famed for its canals that is now called St. Petersburg. Food shortages grew acute; some inhabitants resorted to cannibalism. By the time the siege ended 872 days later, as many as 1.1 million people had starved to death.

But hundreds of thousands survived—and researchers think they've identified what gave some people an edge. Six years ago, Oleg Glotov, a geneticist here at the Ott Research Institute of Obstetrics and Gynecology, and colleagues set out to probe the genetics of survivors. After tracking down 206 of them, they found that the survivors included in the study are more likely than controls to have three gene variations, or alleles, associated with more economical energy metabolism in humans starved for calories.

The study, published in *Advances in Gerontology*, a Russian journal, is "fascinating" and "provocative," says geneticist Stephen O'Brien, chief scientific officer here at the Theodosius Dobzhansky Center for Genome Bioinformatics. L. H. Lumey, a medical epidemiologist at Columbia University who has examined survivors of a similar famine, the Dutch Hunger Winter in the German-occupied Netherlands of 1944 to 1945, agrees that the work "is extremely interesting." But he cautions that Glotov's conclusions may be premature. The small pool of survivors, Lumey says, makes the results "very difficult to interpret."

Glotov says the study is still in its infancy. His team is enrolling more survivors and developing new ways to probe their genetics. The research will continue long after the last survivor succumbs to old age: Their blood and saliva will be among the first samples stored in a national biobank that Glotov, his twin brother Andrey, and others are set to launch later this month.

More than 70 years later, the siege remains a touchy subject here. Questioning whether Leningrad should have surrendered to save lives is off-limits; the official line, Glotov says, is that the siege should be remembered for suffering and heroism. Because that memory "is sacred," he says, the siege "is not really open to further analysis or alternative interpretations."

Glotov's colleagues sought to dissuade him from a "taboo" topic. He was undeterred, partly because of family history. His grandmother was one of about 840,000 people who escaped Leningrad during the siege. Most fled in truck convoys in wintertime, across a frozen Lake Ladoga east of the city.

The first winter was the harshest. For about a month at the end 1941, the trapped residents were consuming, on average, a paltry 125 grams of starch a day—amounting to less than 200 calories—including roughage like linseed cake, pine bark, and birch buds. Leningrad health records show that 90% of the registered population lost weight—in some cases, as much as half of their body mass—that first winter. Surviving such a trauma did not guarantee good health later. After the war, about 29% of survivors developed diabetes, compared with 3% to 4% of the general population, says Lydia Khoroshinina, a biomedical scientist here at the I. I. Mechnikov North-Western State Medical University. That 2002 finding jibes with elevated rates of diabetes and other chronic diseases seen in survivors of the Hunger Winter and other prolonged famines.

Ill health after the war could be a downside of the same factors that helped people survive it, Glotov's work suggests. His group used PCR to latch onto five target genes, all of which help regulate the metabolism of lipids and glucose, in the white blood cells of survivors and in 139 people of similar age who reside here but did not experience the siege. The survivors, they found, are about 30% more likely than controls to have variants linked to thriftier metabolism in three of the five genes: one coding for an uncoupling protein (*UCP3*), which affects the efficiency of cells' power plants, and two coding for so-called peroxisome proliferator-activated receptors (*PPARA* and *PPARD*).

Weakened by hunger and cold, workers labor to clear snow in Leningrad during the winter of 1941 to 1942, when the city was encircled by German troops. New data suggest that gene variants involved in a more efficient metabolism helped some survive the siege.

The differences in allele frequencies "are not really overwhelming," O'Brien says. "They are more suggestive than anything else." And the study is rife with other uncertainties. For starters, Glotov acknowledges that it's impossible to be sure how much food the survivors ate during the siege, or whether they benefited from social connections that upped their rations.

Another caveat is that postwar lifestyle habits or environmental factors may have skewed the genetics of the survivors by preferentially killing off those with particular genes. And as survivors wink out, the diminishing pool of subjects raises another question, Lumey says: "Is this a type of study that could ever be reproduced?"

By building a survivor biobank, Glotov hopes to ensure that it can be reproduced. And he intends to boost the study's statistical power by expanding it. His wife's 90-year-old grandmother is a siege survivor—and she plans to enroll as a subject. ■

PHOTO: AP-PHOTO/RW/MW/STR

Thirteen telescopes now dot Mauna Kea on Hawaii's Big Island, the oldest dating back to 1970.

ASTRONOMY

Hawaii's governor proposes telescope swap

Thirty Meter Telescope can move forward, but existing instruments must be culled

By **Adrian Cho** *and* **Ilima Loomis**

A proposed solution to the impasse over construction of the mammoth new Thirty Meter Telescope (TMT) on Hawaii's Mauna Kea volcano is less bold than it seems—and potentially more difficult. The proposal, to dismantle one-quarter of Mauna Kea's 13 existing telescopes in return for allowing construction to proceed, would only accelerate vague existing plans to shutter some of the telescopes. Yet it promises no end of political pain, forcing researchers from different institutions and countries to compete over which telescopes to keep alive. And it may not defuse the protests that have blocked the TMT project.

"It's going to be complicated," predicts Sunil Golwala, a physicist at the California Institute of Technology (Caltech) in Pasadena, who uses one of the existing telescopes. "There are legal issues and leases that can't necessarily be broken right away." The shutdowns could also cost millions of dollars per telescope. "In many cases it is actually cheaper to keep [telescopes] running than to pay for the deconstruction and site restoration," says Lynne Hillenbrand, an optical astronomer at Caltech.

The proposed culling is one of 10 new conditions on the mountain's use that Hawaii Governor David Ige (D) announced during a 26 May press conference. The measures aim to address the concerns of Native Hawaiian protesters who claim the mountain as sacred ground and have blocked access to the TMT construction site (*Science*, 8 May, p. 614). "We have not done right by a very special place and we must act immediately to change that," Ige said.

Ige affirmed that the TMT team has a right to proceed with construction. But he called for removal of 25% of Mauna Kea's existing telescopes by the time the TMT is finished, perhaps by 2022. He also asked the University of Hawaii (UH), which leases the summit from the state, to agree that the TMT will be the last new observatory site on Mauna Kea, to return 4000 hectares of unused land, and to shorten a proposed 65-year renewal of its lease, which expires in 2033.

Protesters weren't swayed and vow to continue blocking access to the construction site. "It's contradictory to say, 'We're going to do a better job, but we're going to start after the TMT,' " says Kahookahi Kanuha, a protest organizer.

Astronomers have already thought about closing some of Mauna Kea's existing telescopes. In 2010, a UH contractor wrote a decommissioning report as part of a broader management plan, ordered in 2006 by a state judge who blocked a NASA-funded project to add four to six small "outrigger" telescopes around the twin 10-meter Keck I and Keck II telescopes. Although the report mostly describes the process for decommissioning an observatory, it also estimates that by 2033 there should be just 10 telescopes on Mauna Kea—including TMT—and even provides a rough list of facilities that might come down.

That list shouldn't be taken as definite, cautions Günther Hasinger, director of the Institute for Astronomy at UH Manoa. Still, it points to a trend that's likely to sway deliberations, others say.

Mauna Kea's telescopes come in two types. Nine are optical and infrared (IR) telescopes housed in swiveling domes, with mirrors ranging from 0.9 to 10 meters in diameter. Four are dishes or arrays of dishes that collect radio waves and microwaves. The decommissioning report suggests that only one of the four radio and microwave facilities would remain by 2033, whereas eight of the nine optical and IR telescopes would stay.

The move away from the radio facilities reflects the fact that they have been surpassed by the 66-dish Atacama Large Millimeter/submillimeter Array (ALMA) in Chile, astronomers say. "It's clear that Atacama is a better submillimeter site than Mauna Kea," says Dariusz Lis, an astronomer at the Paris Observatory. Still, researchers say that at least one of instruments—the James Clerk Maxwell Telescope, a 15-meter dish built in

PHOTO: © RICHARD WAINSCOAT/ALAMY

1987—is a better survey instrument than ALMA, as it has a wider field of view.

Among the optical and infrared telescopes, the four newest and biggest—Keck I and Keck II, Japan's 8.3-meter Subaru Telescope, and the international 8.1-meter Gemini North Telescope—are vital, says Paul Schechter, an astronomer at the Massachusetts Institute of Technology in Cambridge. He served on a recent National Research Council panel that examined how to optimize the U.S. optical and infrared science program and says that the four instruments "are things that the people on our committee would be horrified to see shut down."

In principle, some of the smaller optical telescopes could go without damaging scientific capabilities, says Robert Lupton, an astronomer at Princeton University. "They could get down to below 10 [telescopes] with no loss to U.S. astronomy," he says. But shuttering the smaller observatories may prove difficult for political reasons.

Canadian researchers, for example, hope to replace the 3.6-meter Canada-France-Hawaii Telescope, built in 1979, with a 10-meter telescope in the same dome. UH is already upgrading its 2.2-meter telescope, built in 1970, with state-of-the-art robotic optics. Even the 3.8-meter United Kingdom Infrared Telescope, which the decommissioning report suggested closing, has advocates. It's a better survey telescope than some of the bigger instruments, Caltech's Hillenbrand says.

How researchers will decide which telescopes to kill remains to be determined—as does how those decisions will be enforced on various funding agencies and foreign partners. But removing the instruments will be expensive. Currently only the Caltech Submillimeter Observatory, a 10.4-meter dish built in 1987, is slated for decommissioning—at a cost that's not yet known. "You can guess that it's bigger than a million dollars and smaller than 10 million," Caltech's Golwala says. Decommissioning costs fall to a telescope's owner. ■

Ilima Loomis is a freelance journalist in Maui, Hawaii.

A crowded summit

A 2010 report suggests that one of the nine optical and infrared telescopes and some combination of three of the four radio telescopes on Mauna Kea could be removed (*) by 2033.

TELESCOPE	MIRROR DIAMETER (METERS)	OWNER	BUILT
OPTICAL/INFRARED			
UH Hilo Educational Telescope	0.9	University of Hawaii	2008
UH 2.2-meter Telescope	2.2	University of Hawaii	1970
NASA Infrared Telescope Facility	3.0	NASA	1979
Canada-France-Hawaii Telescope	3.6	France, Canada, University of Hawaii	1979
United Kingdom Infrared Telescope *	3.8	University of Hawaii	1979
Keck I	10	California Institute of Technology and University of California	1993
Keck II	10	California Institute of Technology and University of California	1996
Subaru Telescope	8.3	Japan	1999
Gemini North Telescope	8.1	International	1999
RADIO/MICROWAVE			
Caltech Submillimeter Observatory *	10.4	California Institute of Technology	1987
James Clerk Maxwell Telescope *	15	East Asian Observatory	1987
Submillimeter Array *	8 x 6	Smithsonian Astrophysical Observatory, Taiwan	2002
Very Long Baseline Array *	25	U.S. National Science Foundation	1992

DATA: OFFICE OF MAUNA KEA MANAGEMENT, UNIVERSITY OF HAWAII, HILO

GEOPHYSICS

Polar scientists to peer beneath largest ice shelf

Seafloor map would offer clues to the fate of Antarctica's Ross Ice Shelf

By **Eric Hand**

The Ross Ice Shelf, a thick, floating tongue of solid ice the size of Spain, is the biggest of the many such barriers that ring Antarctica and keep its ice sheets from sliding into the sea. Yet the shape of the sea floor beneath—a critical factor in how fast the shelf might melt—is virtually unknown. The ice keeps sonar-carrying ships out, and the water beneath it blocks radar. "It's the least known piece of ocean floor on our planet," says Robin Bell, a geophysicist at Columbia University's Lamont-Doherty Earth Observatory in Palisades, New York.

Now, Bell and colleagues plan to fill in the giant blank spot. They have recently received a grant to survey the shelf with an ultrasensitive airborne gravity detector. The sensor detects tiny changes in gravity: the boosts caused by the extra mass of seafloor hills and the decreases from troughs. After a test flight over the mountains of Vermont next month, her team plans to crisscross the Ross shelf in 36 flights over two 3-week-long campaigns, one in November and a second in 2016. They hope to map features as small as 50 meters tall—dramatically better than the present map, which scientists pieced together in the 1970s by setting off small explosions on the ice every 50 kilometers and recording the echoes.

Knowing the shape of the sea floor could give climate scientists important clues about how warm ocean water could melt the ice from below—a process with repercussions that could extend far beyond Antarctica. Floating ice does not affect global sea levels when it melts. But a thinned—or worse, collapsed—ice shelf could clear the way for more of Antarctica's continent-covering ice sheets to enter the ocean and push up sea levels. "Remove that plug, and the ice starts to flow faster," says Helen Fricker, a co-principal investigator for the survey and a glaciologist at the Scripps Institution of Oceanography in San Diego, California.

Gravity sensor being loaded into a C-130 cargo plane for a November 2014 test on the Ross Ice Shelf.

The Ross shelf, roughly 600 meters thick and sitting over about 200 meters of water, has been relatively stable in recent decades. But ice shelves can be capricious: On the Antarctic Peninsula, an area of the Larsen B shelf the size of Rhode Island collapsed in a matter of months in 2002. Fricker wants to gather baseline parameters before Ross suddenly changes. “We don’t know for sure that the Ross shelf won’t change in the next 15 years,” she says.

Antarctica is ringed by the circumpolar current, which carries a deep slug of warm water clockwise around the continent, generally at a safe distance from ice shelves. According to a study published in *Science* last December (*Science*, 5 December 2014, p. 1227), the current has been warming since the 1970s and rising closer to the shelves, especially along the western peninsula of Antarctica. A new map could reveal whether that water has ready access to the underside of the Ross shelf. “Is there a deep pathway, a canyon, a valley that the water can run up like a road?” Bell asks.

At a finer scale, knowing how rough or smooth the sea floor is will help ocean modelers gauge the threat from turbulent eddies that could bring that warm water up to the ice’s underbelly. The rougher the bottom, the more vigorous the eddies. The 1970s-era map suggests that the sea floor is relatively smooth. But Bell says that a test flight with an older gravity sensor last November already revealed surprising roughness, suggesting that mixing is underestimated.

In May, Bell’s team received a $2.2 million commitment from the Gordon and Betty Moore Foundation to fly the new gravity sensor aboard four-engine C-130 cargo planes, which fly longer distances in more types of weather than the Twin Otter, a workhorse of polar research. The gravity meter will be sensitive to changes as small as a milligal, which is the difference in gravity between the bottom and the top of a 3-meter stepladder. Bell is now waiting on an additional $3.4 million from the National Science Foundation that she needs to embark on the campaign.

After demonstrating her instrument’s capabilities at the Ross shelf, Bell hopes it will be used to probe the underpinnings of other shelves in Antarctica and Greenland. “The Ross is where I get people to go ‘Wow,’ ” she says.

To wow her colleagues, however, she will have to navigate some pitfalls. The team has to compensate for any bumps during the flight, using GPS, an internal motion sensor, and a laser altimeter trained on the ice below. Even then, the variable density of seafloor rocks can make the gravity data hard to interpret. Keith Nicholls, a polar scientist at the British Antarctic Survey in Cambridge, U.K., says the soft sediments that cover the seafloor bedrock can change thickness drastically. “If you don’t know your geology, you’re stuffed,” he says. Nicholls and his colleagues have used autonomous submersibles to map the seafloor geology beneath a few small ice shelves. But he says even their latest submersible, which could last for several months beneath the ice, would be hard-pressed to canvas the sea floor covered by a shelf as big as the Ross.

Douglas MacAyeal, a polar scientist at the University of Chicago in Illinois, is glad to see scientists returning to the Ross shelf. As a graduate student, he helped create the first map from 1972 to 1978. After hand-augering holes the width of a beer can and a few meters deep, he tamped down the explosive charges. He still recalls the whump of the ice-muffled detonations. In later decades, scientists concentrated on the land-based ice streams and ice sheets, he says, but now they’re realizing that the fate of the land-based ice depends in large part on those floating fringes. “We have to go back,” he says. “The limiting knowledge gap is no longer in the ice streams but is back again in the ice shelves.” ■

Beneath the ice

By mapping the sea floor under ice shelves, scientists can identify terrain that lets warm ocean water enter and mix.

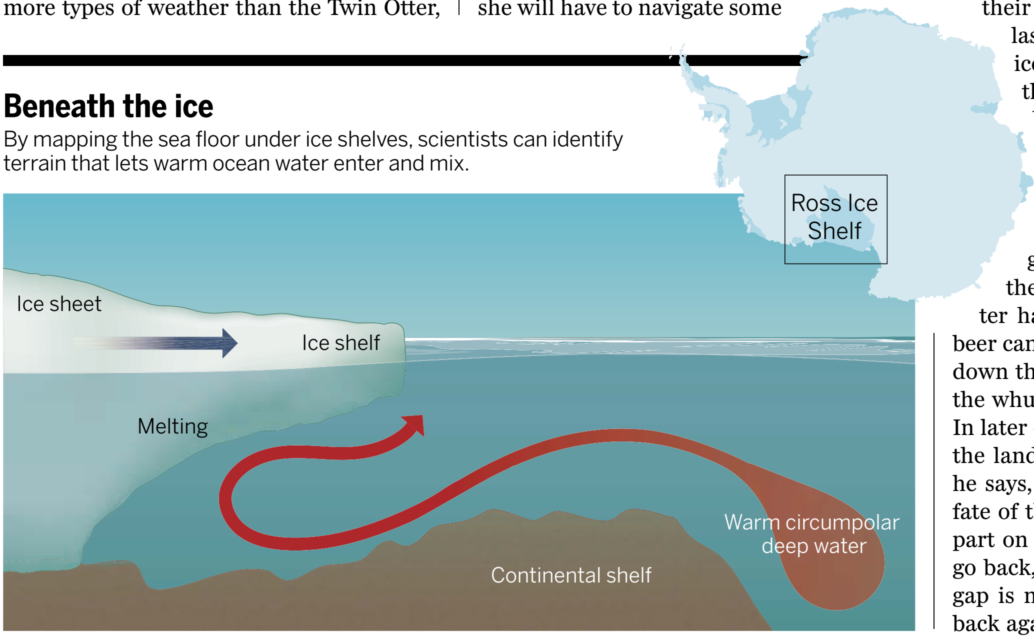

IMAGES: (TOP TO BOTTOM) ROBIN BELL; P. HUEY/*SCIENCE*

Isolated tribes' territory lies far up the Curanja River in the remote Peruvian Amazon.

MAKING CONTACT

Some of the last isolated tribes are emerging from Peru's rainforests

By **Andrew Lawler***; photography by* **Jason Houston***, along the Curanja River, Peru*

At first the signs were subtle. A banana tree was stripped of ripe fruit. Papaya and watermelon vanished. A machete went missing. Clothes hanging off a scarecrow disappeared.

The indigenous villagers who hunt and farm manioc in small clearings here already knew they were not alone. The oldest among them remember growing up naked and on the move, living off the bounty of the Amazon rainforest. But their cousins who remained in the jungle typically avoided all contact with outsiders.

Now, the villagers along the muddy banks of the Curanja River, which snakes for 200 kilometers through the rainforest of eastern Peru, are reporting not just signs of the mysterious forest people, but frequent sightings and even raids. “Since 2011, there have been regular incidents with the naked ones,” says Delicia Roque Samuel, 42, speaking in her native Huni Kuin language through an interpreter. Last year, women watched strangers take bananas from their gardens, and a girl picking lemons saw a naked man across the river, motioning her to come with him. When villagers all along the river canoed downstream to vote in regional elections last October, people in three villages returned to find their houses ransacked by isolated people who had previously avoided contact.

Samuel, who lives in the small settlement of Nueva Vida, points to one side of her thatched hut. “They broke this wall, entered, and took pots, pans, clothes, mosquito nets, and hammocks. … We are scared now to go very far, and I’ve planted a garden closer to my house.”

The villagers empathize with their forest-dwelling cousins and say the isolated people “harvest” rather than “steal” goods. But their patience is wearing thin. “The next time,” warns Nolso Torres Prado, head of a village that was abandoned entirely after the October raids, “I will kill them.”

The tension extends beyond this remote corner of eastern Peru. A surge in sightings and raids in both Peru and Brazil may be a sign that some of the world’s last peoples living outside the global economy are emerging. “No one knows what is happening” within these groups, says Francisco Estremadoyro, director of the Lima-based nonprofit ProPurús, which promotes sustainable development in the region. “But there is no question that this is a historic moment.”

Centuries of history show how contact can go wrong. The events along the Curanja are the last, lingering echoes of the collision of cultures that began in 1492, in which an estimated 50 million to 100 million native people perished and entire cultures vanished. Now, anthropologists and officials wonder if they can minimize the human toll of this final act. Lacking immunity to common pathogens and requiring large tracts of intact forest for food, medicines, and materials, the isolated tribes “are some of the world’s most vulnerable people,” says Beatriz Huertas, an anthropologist based in Lima who has extensively studied the groups.

Epa straddles life between the rainforest and the village.

The primary danger is disease transmitted by outsiders such as loggers, miners, missionaries, drug traffickers, and even television crews. These groups threaten tribes and the rainforest on which they depend in other ways, too. In some instances,

outsiders have violently attacked isolated peoples. Even well-intentioned gifts like a flashlight—which requires toxic batteries and transforms the night—may disrupt traditional ways of life.

On paper, the solutions seem straightforward: vaccinations for both forest tribes who emerge and those who contact them, medical care in remote locations, limits on the transfer of modern technologies, and reserves that prevent outsiders from exploiting isolated peoples. But if recent incidents along the Curanja are any guide, the Peruvian government is unprepared to cope with forest people's emergence in remote corners of the Amazon. "There is a time bomb in the Curanja," says Chris Fagan, executive director of the Upper Amazon Conservancy (UAC), a U.S.-based nonprofit that works closely with ProPurús to preserve ecological and cultural diversity. Adds Estremadoyro: "We are on the threshold of large extinctions of cultures."

ONE THOUSAND KILOMETERS WEST of the Curanja, across the Andes mountains in Peru's capital of Lima, cultures hidden deep in the jungle seem like a distant dream or even a fantasy. More than 95% of the country's population lives in the mountains or along the coast, and until recently government officials dismissed isolated forest peoples as fanciful—a stark contrast with policies in neighboring Brazil (see companion story, p. 1080).

"The figure of the uncontacted native jungle dweller" is a fiction created by environmentalists eager to halt oil and gas development in the Amazon, Peru's then-President Alan García said in 2007. That same year, Daniel Saba, who headed the state-owned oil company Perupetro, called it "absurd to say that there are uncontacted peoples when no one has seen them." Carlos Mora Bernasconi, an anthropologist at Peru's powerful Ministry of Energy and Mines in Lima, insists that other anthropologists and indigenous groups intentionally skew results to stop development.

As reports of contacts proliferate, however, the reality of at least some isolated tribes has become impossible to ignore. In August 2013, some 100 armed members of the Mashco Piro, an isolated tribe that lives primarily in national parks in eastern Peru, appeared near the community of Monte Salvado and made threatening gestures. Then, last fall, some 100 Mashco Piro warriors raided the village while most inhabitants were away, killing dogs and chickens, smashing windows, and destroying clothes. The four remaining community members fled. On 1 May, south of the Curanja and just outside Manu National Park, Mashco Piro men shot an arrow that

The poisoned necklace

By **Andrew Lawler**, *in Columbiana, Peru*

One day in the early 1950s, when he was a young child living with his family in the Amazon rainforest, Marcelino Pinedo Cecilio encountered his first outsiders. At the sight of light-skinned people who wore clothes, "my mother grabbed me and we ran into the forest," recalls the 69-year-old.

Not long after, a man whom Cecilio remembers as a German anthropologist visited their isolated village on the upper Curanja River in this remote corner of the Amazon. (Anthropologists say the visitor may have been ethnographer and photographer Harald Schultz, who worked for what later became FUNAI, the Brazilian governmental agency that protects indigenous people.) "We were naked," Cecilio says. "He came with machetes, mosquito nets, axes, and clothes."

The visitor stayed 1 night before heading upriver, then returned a couple of weeks later, leaving behind a necklace of fish bones as a gift. Soon after, villagers developed a sore throat and burning fever. Cecilio estimates that 200 people died and the tribe scattered. "We were so weak, and some vanished into the forest." The tribe blamed the necklace, thinking it was poisoned.

Marcelino Pinedo Cecilio can still remember life as a child living in the rainforest.

Cecilio remembers growing up in a huge long house with dozens of families. They grew manioc, yucca, peanuts, corn, and jungle potato, sometimes using a root with spines to clear fields. They made arrows using bamboo, sharpening points with the teeth of a large rodent. "We kept good relations with other tribe members who lived in the area, celebrating together and holding competitive games as well," he says. The brief visit from the outside spelled an end to that life.

Like so many indigenous peoples since the arrival of the Portuguese and Spanish here in the 16th century, Cecilio's group was likely struck down by a common Western disease—maybe influenza or whooping cough—inadvertently carried by the visitor. It is an old story: Within a year of the arrival of Spanish conquistador Hernán Cortés and his smallpox-carrying troops in 1519, for example, half the population of the Aztec capital of Tenochtitlán perished, historians estimate. Today's isolated tribes are in the same position as those New World peoples 5 centuries ago, with immune systems naive to such pathogens, says Lima-based anthropologist Beatriz Huertas. "They are particularly susceptible to respiratory and eye diseases," she says.

In the past century, American missionaries, anthropologists, and loggers brought the pathogens. Now, drug traffickers and television crews play that role. In Manu National Park, just south of where Cecilio lives, at least four people of the Matsiguenka forest community died in an epidemic in 2007. A 2008 report by Peruvian anthropologist Daniel Rodriguez links the illness to a visit by a film crew who wanted to include the Matsiguenka in the popular British series *World's Lost Tribes: New Adventures of Mark and Ollie*. Rodriguez concluded that the crew strayed beyond the area included in their permits, which were designed to avoid such transmissions. The company denied both charges.

As increasing numbers of isolated people emerge from the forest, their risk of disease is growing. Finding ways to protect them is an urgent concern (see main story, p. 1072), anthropologists say.

Today, Cecilio again lives along the Curanja, where he makes feathered headbands and cultivates a garden. This spring, he shared his knowledge of traditional plant medicines with a visiting German biologist.

Despite the bitter memories, Cecilio's gentle smile radiates kindness. Asked whether he misses his youthful days in the forest, he doesn't hesitate. "No!" he says firmly. He would like to find a way to talk with the peoples still in isolation. "I want them to know there is another way of life." ■

killed a 20-year-old indigenous villager.

Other regions, such as the mountains of New Guinea and the Andaman Islands in the Indian Ocean, are also home to isolated peoples. But by far the largest numbers are found across the Amazon. And it is in Peru that the situation appears most dire, with large numbers of isolated people—Huertas estimates as many as 8000, scattered in small bands—and a history of neglect.

These are not the uncontacted people of romantic imagination. Most of these groups had traumatic interactions with industrial society about a century ago, when the upper Amazon filled with tens of thousands of outsiders eager to make a fortune from rubber. The difficult and dirty work of tapping the white sap from rubber trees was assigned to indigenous people, who long ago had learned to use the sap to make waterproof shoes or balls. In return, the tribes often received only basic supplies like hammocks, machetes, and clothes; they lived in what amounted to slavery. Scholars estimate that as many as 250,000 natives in Peru and Brazil, or one in 10, died.

Some tribes escaped into the forest, relying on deep knowledge of the ecosystem for all of their needs. They fashioned bows and arrows from local materials to kill game, made poisons to fish, and used diverse plants for medicine and ceremonies. Some groups abandoned traditional skills such as farming and canoe construction in order to avoid detection, Huertas says.

She ticks off the forces that may now be forcing isolated people from their hideouts: food shortages, intertribal conflicts, illegal loggers, and oil and gas exploration. Peru is the world's top producer of illegal cocaine and exports much of it to Brazil, with the remote Amazon jungle serving as a smuggling route. Isolated peoples "are being pushed to the last remnants of intact forest in the headwaters, the most secluded areas," says ProPurús Director Estremadoyro during an interview in Lima. "They are already in the deepest jungle they can find."

Peru is at last acknowledging the crisis. "Until a few years ago, the government denied their existence, but now it is finally instituting policies to protect them," Huertas says. In recent years, the Peruvian government has set aside 3 million hectares in five reserves as safe havens and has forbidden efforts to contact isolated peoples. In a small office she shares with a half-dozen co-workers within Lima's modernist concrete Ministry of Culture, Lorena Prieto leads the effort to add another five reserves. Teams are in the field now to gather evidence on the location and numbers of isolated peoples—and to understand their emergence. Prieto acknowledges the role of mining and logging, but says "there is something else at play here, though there's not enough research yet to know what."

"MALOCA!" SAYS UAC'S FAGAN, his index finger jabbing at the window. "There!" For the previous hour, passengers on a 10-seater charter prop plane have seen only unbroken green jungle and sinuous brown rivers. Now, two clearings, tawny against the emerald foliage, swim into view. Communal thatched huts—malocas—line up in one clearing, while the other appears to be a farm field. Fagan has spotted the settlement of an isolated tribe, far from any known villages—an extremely rare sighting.

After flying over unbroken jungle and rivers for another hour, the plane bumps to a halt in Puerto Esperanza, the capital of Peru's remote Purús province, which is wedged up against the Brazilian border. A straggling town of fewer than 2000 people unconnected by roads and served only by occasional flights (see sidebar, p. 1078), it is the gateway to the Purús Communal Reserve and the Alto Purús National Park, which border other protected areas. Together, these lands form a Virginia-sized region of tropical rainforest that is home to isolated people as well as threatened and endangered species like pink-hued dolphins, harpy eagles, and black caimans.

Villagers along the Curanja paint traditional designs using local plant dyes.

Aboard the plane is a team organized by UAC and ProPurús to investigate the recent raids and gauge the villagers' preparedness for future encounters. The nine-person team includes interpreters for native languages and Rafael Pino Solano, chief of the Purús Communal Reserve. Along with gear and food, the group crams into a motorized canoe christened *Lobo del Rio*—river wolf—after a giant endangered Amazonian otter.

The Curanja River lies a day's journey from Puerto Esperanza, up the milk chocolate–colored Purús River amid swarms of biting gnats, frequent rain showers, and calls of birds and monkeys in the thick rainforest lining the banks. Distance here is measured not by kilometers but by turns of the wide river.

At Curanjillo, a hamlet of seven families upstream from where the Curanja joins the Purús, villagers worry that isolated people will continue

Up the Curanja

Settlements are strung like beads along rivers in Peru's Purús province, where a canoe is the best means of transport. From Puerto Esperanza to Santa Rey is a 2-day journey.

son. The chief chose to treat the boy with traditional plant medicines rather than send him a day's journey downstream to Puerto Esperanza. But when the team offers antivenom, the father relents. The boy ultimately recovers.

Silva also lacks the tools to protect emerging tribes from their biggest danger: infections that can lurk in something as innocent as a cast-off T-shirt. "Most authorities don't take this problem seriously," Huertas says. "A cold for us is an inconvenience; for them it can be a tragedy," she says. Influenza can abruptly wipe out whole tribes (see sidebar, p. 1075). In the 1980s, half of one isolated tribe—some 300 to 400 people—perished after workers for the Dutch oil company Shell passed on pathogens, she says.

A HALF-DAY'S CANOE RIDE upstream in Santa Rey, the last village before the wilderness, Abilio Roque came back from voting in October to find his entire house burned to the ground, including the hunting and fishing gear he uses to survive.

The culprit was Epa, a man from an isolated tribe who was enticed out of the forest a dozen years ago by missionaries. Roque had allowed Epa to stay in his house during the elections, and the tribesman later admitted that he had burned it down by accident, according to Roque's grandson. Known along the Curanja as a man who inhabits a netherworld between isolated and settled people, Epa embodies the tensions brought by this new wave of contact, and some villagers have grown to distrust him.

The expedition pushes off from Santa Rey and sets off into Epa's territory, just inside the communal reserve. Accompanied now by a small flotilla of forest rangers and local villagers, the *Lobo del Rio* ties up along the north side of the riverbank, near where Epa is known to live with his two wives and a mother-in-law. An older woman appears. "Help! My leg hurts—give me a shot," she wails in the Mastanahua language, falling to the ground in distress. She explains that her name is Maria and that Epa, her son-in-law, has gone to visit his family in the forest. Visitors follow her limping figure about a hundred meters to a makeshift compound hidden in the jungle. Two dozen dogs bark wildly within a palm-fronded shelter strung with small hammocks, one per dog. Dozens of empty turtle shells litter the slope below.

Although Maria's leg appears slightly swollen, the interpreter says that her distress centers on the recent death of a pet dog and monkey. Her daughter Elena, one of Epa's wives, ignores the visitors while

to make off with pans and hammocks. "We know [the tribes] are around, although no one sees them," explains village chief José Torres Nacimiento, sitting in the open-air community building as women paint traditional designs on visitors' arms with natural plant dyes. "Things are taken, there are footprints, and you hear animal sounds." Nacimiento adds that "people feel angry and abandoned" by a government that seems more concerned with the fate of the isolated peoples than with the welfare of villagers who lack electricity, clean water, and health care.

The villagers along the Curanja are themselves only a generation or two removed from a traditional life in the forest. Christian missionaries encouraged them to settle down starting in the 1950s. Now, they keep chickens and grow peanuts, mango, and cocoa beans while maintaining some traditional practices.

A dozen turns upriver in the village of Nueva Vida, a robust 78-year-old elder named Filomeno Torres Marquez recalls that when he was a child, "we were naked, without clothes, or chickens or salt or sugar." Today, he is just back from a solo hunt for the piglike peccary and a large bird called a curassow—traditional forest staples. In an impromptu demonstration, Marquez pulls out his bow and arrow, both taller than his small but sturdy frame, and demonstrates his mastery by piercing an old shoe several dozen meters away.

Stories of fleeting contact and "harvests" by isolated peoples are echoed in village after village as the group approaches the communal wilderness. Thirteen more turns upriver in Columbiana, a 42-year-old farmer named Maquias Pinero Puricho reports that the isolated peoples appear hungry. "I think these guys don't have a food safety net, such as farms, so they seek out ours," he says. Solano notes that in the communal reserve itself, recent floods limited the supply of turtle eggs, a key food for forest peoples in the summer. And the larger of the two main types of peccaries, which usually travel in packs of 100 or more, is in steep decline for unknown reasons. Last year, Mashco Piro tribespeople appeared on the riverbank near the town of Monte Salvado, demanding, "Where did the peccaries go?"

The next village upstream, Balta, boasts a medical post with a nurse, Miguel Silva. But Silva lacks transportation and basic medical supplies, such as antivenom. "Ask the Ministry of Health why I have no boat or motor," he says. The previous day, a common viper bit the village chief's 9-year-old

ONLINE

Video of recent contacts with isolated peoples in Brazil and Peru

Multimedia story on the history of contact since 1492

http://scim.ag/isotribes

cradling a sick dog and singing a haunting song. Curious foresters and villagers crowd around, snapping photos with their iPhones. As Maria's anxiety increases, Fagan calls everyone to withdraw to the boats, to avoid exacerbating a situation that verges on chaos.

After camping on a wide beach, the next morning the team heads back downriver. A figure appears on the far bank: Epa himself. He wears a knit cap and a blue and yellow striped shirt and has a small circle of metal cut from a tin can suspended from his nostrils. His eyebrows are shaved, and he looks past middle age. He invites some of the visitors to his compound.

Epa—the name means "father" in the Pano language family—says that his real name is Shuri and that although he has no children, he has 10 family members in the forest. "I often visit my family in the forest, and they often come to visit me here," he says through an interpreter. His people do not farm or build canoes, he says. He boasts that he recently shot a tapir, a large snouted mammal, taking half to his family, and he proudly shows off his bow and arrow, skillfully made of local wood and fiber.

When asked about the maloca that Fagan saw from the air, he nods. "Those are our enemies," he says, adding that he fled here in part to avoid their violence. Such clashes among tribes are common and may intensify as the jungle shrinks, anthropologists say.

Epa says his family is reluctant to join him because game and fruit are scarce nearby. "We need cooking oil, sugar, salt, knives, machetes, tobacco, and clothes. If you give me plenty of these things—all the

Mercy on these people, and give us a road

By **Andrew Lawler**, *in Puerto Esperanza, Peru*

When the Peruvian government created the Alto Purús National Park in 2004 to protect biodiversity and isolated peoples (see main story, p. 1072), Miguel Piovesan, the priest in this frontier town, was outraged. He says the park sealed Puerto Esperanza off from the rest of Peru, leaving its people impoverished and ill, without access to medical care or modern conveniences. "People call the Amazon the lungs of the world," he says in an interview at his modest rectory close to the town's quiet landing strip. "But here we have children suffering from tuberculosis."

No roads lead into or out of this town of fewer than 2000, located just upstream from Brazil on the Purús River. The only way to get here is by infrequent flights from the town of Pucallpa, Peru, 450 kilometers away, or by a monthlong river trip through Brazil. Teachers and doctors are reluctant to move to such an isolated place, says Piovesan, a thin and ascetic figure dressed in white. "Many families are leaving for Brazil, since living costs are so high here," he adds.

Piovesan wants a road, as do his allies, who include Catholic bishops, military officers, and local mestizos (people of mixed white and indigenous ancestry), who own most of the small businesses here and are eager for economic growth. The preferred route would hug the Brazilian border and connect the town with the Peruvian city of Iñapari to the southeast. Next to the Puerto Esperanza airport, supporters have erected an optimistic sign pointing down a rutted path: "Iñapari—207 kilometers: Have a Nice Trip!"

A road linking the town of Puerto Esperanza to the outside world would slice through isolated tribes' territory in the Alto Purús National Park.

Piovesan also spreads his message from the pulpit. Behind the altar of his church, above the crucifix, large red and white block letters spell out "Jesuscristo Camino: Apiadate De Este Pueblo y Danos Une Carretera," or "The way of Jesus Christ: Mercy on these people, and give us a road."

Piovesan's message resonates in Lima with some politicians who are keen to develop the Amazon and suspicious of foreign environmental groups. "Three and a half thousand people are living in an unacceptable and unjust situation," lawmaker Carlos Tubino Arias Schreiber told the Peruvian Congress in 2012, citing lack of education and emergency medical care in the province of Purús. "Human beings are worth more than trees and animals."

But advocates for the environment and for indigenous people decry the plan for the road—"the Death Road," as Survival International, a London-based group that defends indigenous rights, calls it. If built, the road would cut through a long swath of the Alto Purús National Park and the Madre de Dios territorial reserve. In the past, such roads have brought economic gains but also a flood of outsiders and pathogens, alcohol, and material goods, anthropologists say. Glenn Shepard of Museu Paraense Emílio Goeldi in the Brazilian city of Belém, who works extensively in the Amazon, notes that a logging road extending west from Iñapari already threatens the isolated Mashco Piro people, who have recently had aggressive interactions with outsiders. The proposed road's only beneficiaries, says one indigenous organization, will be "illegal logging mafias."

Jose Borgo Vasquez, the regional coordinator of the nongovernmental organization ProPurús, argues that a better approach to boosting Puerto Esperanza's fortunes would be to encourage small-scale businesses such as aquaculture or cultivating turtles for export down the river to Brazil and eventually perhaps even China. A road, he argues, will simply destroy the forest on which indigenous people, both isolated and not, depend.

For now, the Peruvian government has declined to approve the road due to its high cost as well as the international pressure. The path from the airport ends in dense jungle. Piovesan and his opponents do agree on one point: Lima's failure to help the indigenous people who make up most of Purús province. "The government is doing nothing for the contacted people," Piovesan says, "so how can they plan to help the uncontacted?" ■

Journeys into the tribes' last refuges are measured not in kilometers but in turns of the river.

things you use in town—then my relatives might move here. … Maybe if there were a large house and a farm to support us, then they might come and settle down."

He offers to exchange a large turtle and two small ones for staples and flashlights. Fagan trades the animals, which are later released in the river, for rice, sugar, and oil. "I know you won't give me the flashlights," Epa grouses, his eyes straying to the photographer's camera gear.

At the mention of the October raids, Epa grows wary. "Yes, some of my family members were involved," he admits. "But the timing was just coincidence. I didn't know everyone would be gone."

But the Curanja villagers say that Epa knew all about the elections. They suspect that he is much more than a naive native seeking safety, sugar, and salt. He is, they believe, studying them as carefully as any anthropologist, noting the ripening of orchard fruits, the quantity of their goods, and their daily movements. He may be, in effect, a spy.

"I've been analyzing the encounters with isolated people since Epa's arrival around 2002," says Tomas Torres Alicio, a 61-year-old schoolteacher back downstream in Columbiana. "There have been 15 or so incidents, almost all on the north bank of the Curanja. … He must be telling his family details about our farms and goods, and when we are absent."

Whatever Epa's precise role in the incidents, he is an agent of contact, and Fagan worries that he may transmit pathogens back to his people in the jungle.

Some villagers and even government foresters lack the dozen or so vaccinations recommended to protect isolated peoples, says reserve chief Solano. Missionaries say that Epa, Maria, and his wives refused vaccinations a decade ago; whether they have been vaccinated since is not clear. "He and his family have consistent contact with their tribe, which still lives in isolation and have not received any immunizations, as well as with nearby villagers who travel to cities, and even with the occasional outsiders who visit the Curanja," Fagan says. "Disease transmission is a significant and immediate threat."

Isolated peoples "are being pushed to the last remnants of intact forest. … We are on the threshold of large extinctions of cultures."

Francisco Estremadoyro, ProPurús

Epa's story shows the need for better planning and health care in these remote regions, Huertas says. "You can't take them to a town," she says of the tribespeople. "You need a small group of specialists to isolate them from villages." This would entail building small centers on the reserve perimeters, as is done in Brazil, to serve as a base for treating or helping isolated people.

Back at the Ministry of Culture in Lima, Prieto acknowledges the need. "We respect the right of the people to be isolated, and we are also pushing to provide health care assistance." But with an annual budget of only $1 million, her 17-member staff is stretched thin. "There is no way to cover this amount of territory on our budget," she says. The government has yet to agree on health protocols for the isolated peoples, much less on the funding to put Prieto's vision into place. Meanwhile, anthropologists agree that more research is desperately needed to understand just why tribes are emerging now.

If isolated people do manage to avoid epidemics, the loss of land, and violence by hostile outsiders, they may find little comfort in the struggling villages along the Curanja. These villagers themselves have yet to reap many of the benefits of modern civilization, including electricity, clean water, or employment opportunities. "After initial contact, these people are often left to their fate, struggling to survive, cut off from other groups, begging for food, and with no land to call their own," Huertas says.

Faced with a shrinking habitat and an influx of outsiders, however, the tribes' time for choosing between the forest and settled life may be drawing to a close as abruptly as the tropical dusk. ■

Reporting for this package was supported in part by a grant from the Pulitzer Center on Crisis Reporting, with logistical assistance from the nonprofit organizations the Upper Amazon Conservancy and ProPurús.

Brazil's Belo Monte Dam will flood part of the Amazon rainforest and threatens the territories of indigenous tribes, who have protested the dam.

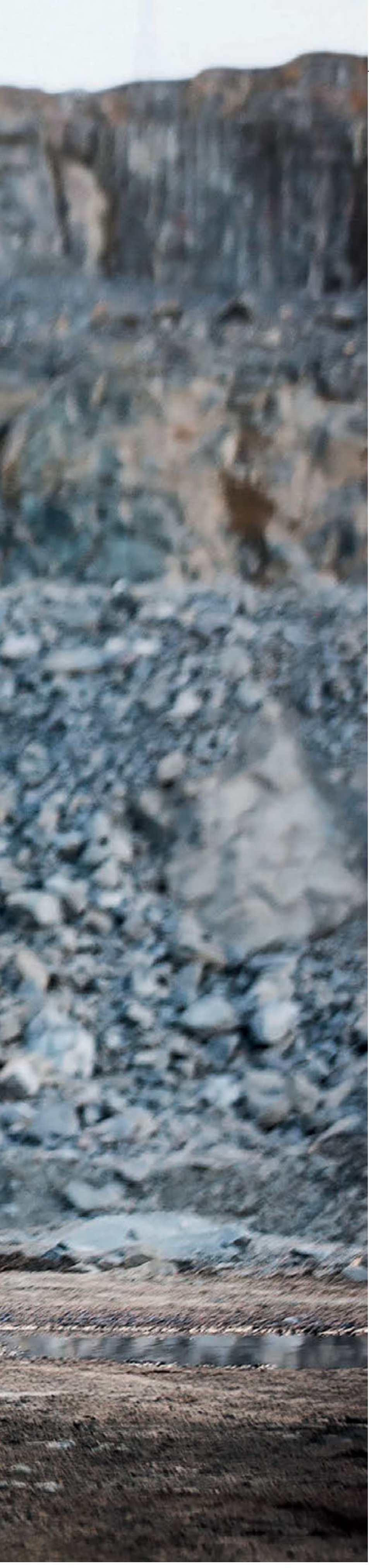

PHOTO: TAYLOR WEIDMAN/LIGHTROCKET/GETTY IMAGES

IN PERIL

As contacts spike, critics fear that Brazil's once-vaunted protection of isolated tribes is crumbling

By **Heather Pringle***, in Brasília*

In a spacious, art-filled apartment in Brasília, 75-year-old Sydney Possuelo takes a seat near a large portrait of his younger self. On the canvas, Possuelo stares with calm assurance from the stern of an Amazon riverboat, every bit the famous sertanista, or Amazon frontiersman, that he once was. But on this late February morning, that confidence is nowhere to be seen. Possuelo, now sporting a beard neatly trimmed for city life, seethes with anger over the dangers now threatening the Amazon's isolated tribespeople. "These are the last few groups of humans who are really free," he says. "But we will kill them."

For decades, Possuelo worked for Brazil's National Indian Foundation (FUNAI), the federal agency responsible for the country's indigenous peoples. In the 1970s and 1980s, he and other sertanistas made contact with isolated tribespeople so they could be moved off their land and into settlements. But Possuelo and others grew alarmed by the human toll. The newly contacted had no immunity to diseases carried by outsiders, and the flu virus, he recalls, "was like a suicide bomber," stealing into a village unnoticed. Among some groups, 50% to 90% died (see sidebar, p. 1084). In 1987, Possuelo and fellow sertanistas met to try to stop this devastation.

> ***"FUNAI is dead. But nobody told it, and nobody held a funeral."***
> **Sydney Possuelo**, retired FUNAI official

In Brasília, a futuristic city whose central urban footprint evokes the shape of an airplane, the frontiersmen agreed that contact was inherently damaging to isolated tribespeople. They drew up a new action plan for FUNAI, based solidly on the principle of no contact unless groups faced extinction. They recommended mapping and legally recognizing the territories of isolated groups, and keeping out loggers, miners, and settlers. If contact proved unavoidable, protecting tribespeople's health should be top priority.

The recommendations became FUNAI policy, and a model for other countries where isolated populations are emerging, such as neighboring Peru (see companion story, p. 1072). In remote regions, FUNAI has designated a dozen "protection fronts"—official front lines in the battle to defend isolated groups, each dotted with one or more frontier bases to track tribes and sound the alarm when outsiders invade. In an interview in February, FUNAI's interim president, Flávio Chiarelli, told *Science* that his agency is "doing great" at protecting the country's isolated tribes.

But some experts say that as the pace of economic activity in the Amazon accelerates, the protection system that was once the envy of South America is falling apart. Brazil has the world's seventh largest economy, with a gross domestic product in 2013 of $2.24 trillion. To fuel this vast economic engine, public and private enterprises are pushing deeper into the Amazon, constructing dams, transmission lines, mines, pipelines, and highways. Meanwhile, drug smugglers cross isolated groups' territories to transport Peruvian cocaine to Brazil, triggering attacks. "There's no part of the Amazon that is not under some kind of pressure," says anthropologist Barbara Arisi of the Federal University of Latin American Integration in Foz do Iguaçu, Brazil.

The rate of contact seems to be rising in both Brazil and Peru. Between 1987 and 2013, FUNAI made contact with five isolated groups. But in the past 18 months alone, three groups initiated contact: the Xinane,

A woman from the isolated Awá Guajá tribe tends to her sick sister after the two chose to make contact with Brazilian officials in January 2015.

the Korubo, and the Awá Guajá. Physician Douglas Rodrigues of the Federal University of São Paulo, a public health specialist who works with indigenous tribes, worries that the recent flurry of contacts is just the beginning. "I fear that we are facing a 'decade of contacts,' " he says. By many accounts, FUNAI—cash-strapped and under pressure from development interests—is not prepared.

DURING THE DRY SEASON in the Amazon last summer, a handful of robust young men emerged from the forest along the Envira River, near the Peru border. They wore thin belts around their waists, had their hair styled in a bowl cut, and carried long bows. They were from an isolated tribe that FUNAI calls the Xinane people, and according to what the tribespeople later told government interpreters, they had survived a violent attack by nonindigenous men along the Envira River in eastern Peru, a border region favored by cocaine smugglers. FUNAI had had a base nearby on the Xinane River, but abandoned it in 2011 after heavily armed drug traffickers surrounded it.

As the dry season progressed last summer, the Xinane moved eastward through the forest to a small indigenous settlement known as Simpatia, where at least 70 contacted Ashaninka people lived. For several days, the young hunters watched and waited in the dense vegetation around the village, calling to one another with bird cries and animal sounds. The Ashaninka feared an attack.

Then on 13 June, Simpatia's schoolteacher radioed FUNAI for help. Four young Xinane men had entered the village, noted a later medical report, and taken machetes, metal pots, and clothing, the latter a potential source of disease transmission. Frightened, the Ashaninka hid in their houses.

The Xinane were not unknown to FUNAI. Since 2008, researchers had been studying the group and tracking their movements from FUNAI's headquarters in a sleek glass office tower in Brasília. Last February, seated at a large conference table there, Leonardo Lenin thumbed through photos taken by FUNAI field teams, which had found vestiges of Xinane camps since at least 2005. Dark-haired and intense, with an urgent way of speaking, Lenin is responsible for the FUNAI division that gathers data on Brazil's isolated groups and tries to protect them.

To date, Lenin explains, FUNAI has confirmed the existence of 26 isolated groups in Brazil, with the greatest concentration located along the Peruvian border. The agency's records suggest that up to 78 additional groups may be in hiding or on the run.

Gathering enough evidence to confirm a suspected group can take years, Lenin says. FUNAI researchers scour historical accounts and examine anthro-pological records on the languages and material culture of nearby contacted groups. They also compile a picture of nearby development projects and any illegal activities, such as the drug trafficking that threatened the Xinane.

In the field, FUNAI workers interview local people and may send a team into the forest. Skirting areas likely to be seasonally occupied, the teams hunt for abandoned camps,

A settled Kayapo man receives rare eye care from a traveling charity. Many indigenous villagers in the Amazon receive scant medical care, and their lack threatens isolated people, too.

PHOTOS: (TOP TO BOTTOM) SURVIVAL INTERNATIONAL; REUTERS/RICARDO MORAES

documenting huts and houses, as well as discarded tools and weapons, food remains, and raw materials. Team members are instructed to leave everything in situ, to win the trust of the isolated groups. "They will know that someone was there, but they will also know that it was a group that doesn't want to harm them," Lenin says.

Back in the FUNAI offices, Lenin and his colleagues analyze the findings and begin mapping territories and estimating populations. "It is an archaeology of the living," Lenin says, adding that even small finds can disclose vital information.

He holds up a photograph of a child's reed toy, found in a hideout used by the Kawahiva, an isolated group in the state of Mato Grosso who are on the run from loggers and farmers. "It was quite emotional to find this," Lenin says. Tribespeople who are constantly evading hostile outsiders often seem to stop having children, a sure path to extinction. The small woven toy, however, indicates that Kawahiva mothers have not yet reached that point.

To monitor isolated populations over time, FUNAI researchers conduct regular flyovers, taking aerial photos of houses and fields, estimating populations, and noting hair styles and patterns of body paint. But flyovers are expensive, so researchers increasingly gather information from remote sensing imagery.

For example, in a paper published in *Royal Society Open Science* in November 2014, scientists led by anthropologist Robert Walker of the University of Missouri, Columbia, used satellite images to survey isolated groups in Brazil. The researchers searched for thatched-roof houses and gardens along the Brazil-Peru border where FUNAI had confirmed the existence of three isolated groups, including the Xinane, through fieldwork and overflights. They found at least five villages and calculated their areal extent.

Using population estimates from FUNAI's published data, they found that the isolated villages had far greater population densities than did the contacted villages—nine people per square hectare versus just 0.7 people in the contacted settlements. Isolated tribespeople may not clear spacious areas because they lack steel tools such as machetes and axes, Walker says—or because of pressure from hostile outsiders. "We need to track these populations over time," Walker says. "They are really fragile groups on the cusp of extinction."

FUNAI's official policies are directed toward preventing rather than managing contact, and neither the agency nor Brazil's Ministry of Health has an official contingency plan for how to protect isolated people's health should contact occur. But contact was exactly what the Xinane seemed to be seeking.

BACK IN SIMPATIA last June, the Ashaninka were growing increasingly anxious as the Xinane calls resounded through the forest. Finally, on 26 June, a small FUNAI team arrived to take charge of the situation, including José Carlos Meirelles, a retired sertanista who advised the state of Acre on indigenous affairs. The Ashaninka knew Meirelles well. The gaunt 66-year-old had supervised FUNAI's protection front in the region for more than 2 decades and had set up the Xinane base.

In all likelihood, the young Xinane men knew Meirelles, too. Anthropologists working in recently settled communities have collected accounts showing that tribespeople carefully observed nonindigenous communities before they made contact, for example learning people's names.

FUNAI researchers had deduced that the Xinane spoke a language in the Panoan family, likely a language closely related to Yaminawa. So Meirelles's team included two Yaminawa interpreters.

Three days after Meirelles arrived, seven Xinane appeared on the opposite riverbank with machetes, arrows, and one rifle in hand. Eventually some waded across the river, and this time the nervous Ashaninka welcomed them with bananas, coconuts, and clothing. The young Xinane men said that they had come from a village deep in the forest, where as many as 60 people lived. They spent several hours in Simpatia that day, walking about and occasionally pilfering goods. It was their first official contact with the Brazilian government.

The next day, however, the situation took a sudden turn for the worse. FUNAI team members noticed that some Xinane were coughing and looked ill. Alarmed, the field team informed FUNAI and Ministry of Health officials in Brasília.

An untreated disease can kill up to 90% of an isolated population, and such illnesses demand a fast response, Lenin says. "We're talking almost a process of extermination of a group," he later told a public hearing in Brasília on public policies and land conflicts concerning indigenous groups.

But while FUNAI and Ministry of Health officials tried to organize and fly in a medical team, the Xinane melted back into the forest, raising concerns that they would carry disease back to their home village. It was not until 6 July that the Ministry of Health flew in the first physician, Rodrigues. He managed to find and examine three tribesmen on 8 July. Each had a fever and an acute respiratory infection. Concerned about preventing secondary infections such as pneumonia, Rodrigues and a small team began treating the Xinane with fluids, antibiotics, and drugs to lower their fevers.

The FUNAI and Ministry of Health workers then located all seven Xinane and convinced them to move upriver with Rodrigues and colleagues to the abandoned Xinane base. There, the young men would be less likely to catch additional diseases or to return to their home village while contagious.

Eight days later, the Xinane had recovered fully. Through an interpreter, Rodrigues asked them to return to the base in a month with their families. On 26 July, 34 Xinane men, women, and children began trickling into the base to receive immunizations for

Seeking safety in Brazil

An isolated Xinane group (left) fled violent attacks by outsiders in Peru last year. Later, young tribesmen made peaceful contact with indigenous villagers across the border in Simpatia, Brazil.

PHOTO: REUTERS/FUNAI

How to court an isolated tribe

By **Heather Pringle**

In June 1909, a Brazilian military engineer instructed his assistant, Severiano Godofredo d'Albuquerque, to tame and pacify the Nambikwara, an isolated group living in the path of a new telegraph line pushing into the upper Amazon River Basin in western Brazil. Albuquerque and his men followed a practice pioneered by missionaries: They set up an "attraction front," building a small frontier post in Nambikwara territory, planting a garden nearby, and allowing the tribe to raid the crops. As the sorties increased, Albuquerque began leaving out metal tools, too. Finally, in August 1910, when a Nambikwara chief appeared during daylight in the garden, Albuquerque made contact, embracing the chief and dressing him and six of his companions in European clothing.

Nearly 60 years later, during a taped interview with American anthropologist David Price of Cornell University, an elderly Nambikwara described what happened next. Vitorino Nambikwara explained that his people initially traded woven ornaments and manioc flour for the newcomers' metal tools. But soon the men at the post demanded more. "When we asked for something, we had to work for it," Nambikwara recalled. If he and others refused to do physical labor, they were cut off from the steel machetes, axes, and other metal goods that they had come to depend on.

Decades after being drawn into contact with outsiders, some Nambikwara still live in poverty.

Such attraction fronts were an engine of sweeping cultural change. Brazilian missionaries used them to draw isolated, animistic societies out of the forest and into missions, where the people could be converted to Christianity. Government officials used the fronts early in the 20th century to transform traditional tribespeople into a settled workforce capable of building telegraph lines and roads in the Amazon's harsh conditions. Many saw the policy as enlightened.

But for indigenous groups, the attraction fronts were the beginning of disease and dependence. Government employees often hugged the tribespeople, ate with them, and gave them "clothes and hammocks," says Antenor Vaz, a former senior official at FUNAI, the federal agency responsible for Brazil's indigenous peoples. In doing so, they also shared their pathogens, to which the newly contacted had no immunity.

The Nambikwara, for example, suffered devastating losses. Price estimated that the group numbered some 5000 people at the beginning of the 20th century. By 1969, that number had plummeted to 550, according to a census he conducted, and by 2010 the count was still only 1950, according to a census by Brazil's National Health Foundation.

In the wake of such repeated tragedies, FUNAI frontiersmen helped convince the Brazilian government to abandon attraction fronts and adopt a no-contact policy in 1988 (see main story, p. 1080). Today, anthropologists consider the fronts a shameful chapter in Brazil's history. "It was a mess," says anthropologist Cristhian Teófilo da Silva of the University of Brasília. "And it has been proven to be genocide." ■

influenza, chickenpox, and other infectious diseases. Today, Lenin reports, the Xinane are doing well and the Xinane base remains open. "They know that if there is any situation of health or territorial invasion, the team is there to help them," he says.

So far, contact has not meant death for the Xinane. But some observers think that last summer's achievement was mostly a matter of luck. In an online report, physician Rodrigues notes that the virus contracted by the Xinane happened to be relatively mild, possibly a rhinovirus or adenovirus; a more serious virus such as influenza might have killed many. And some critics think FUNAI and the Ministry of Health moved much too slowly when disease broke out. The Xinane, Arisi says, "did not receive prompt and proper emergency treatment."

In light of these experiences, Rodrigues thinks that FUNAI and the Ministry of Health need contingency plans that can be activated immediately, with specially trained health teams and stockpiles of vaccines and medicines available on short notice, as well as helicopters to ferry them to inaccessible corners of the Amazon. He adds that the Brazilian government needs to provide better health care in remote indigenous villages such as Simpatia, to help the villagers as well as to reduce the likelihood of disease transmission to isolated groups.

Lenin himself conceded last August in the public hearing in Brasília that more funds and planning are required to protect isolated groups. "Now, our concern is to have … teams ready to make this work in relation to health," Lenin said. "Either we, in fact, do a competent, skilled intervention, or we will be talking about repeating the histories of contacts, where the mortality of indigenous groups was very high."

SITTING IN A shady tropical garden in one of Brasília's middle-class neighborhoods, Antenor Vaz frowns as he considers the tale of the Xinane. A crisp, precise man in his 60s who once trained as a physicist, Vaz is the person who systematized FUNAI's procedures for protecting isolated people after the agency moved to a no-contact policy in 1988. Since leaving the agency in 2013, Vaz has monitored and critiqued its activities, hunting down obscure FUNAI reports and presentations online and publishing his findings.

FUNAI, he says, lacks the funds and human resources it needs. In 2014, the Brazilian government approved just 2.77 million reais ($1.15 million) for finding and protecting isolated groups, 20% of what FUNAI requested; this year, the government again provisionally approved 2.77 million reais, less than 15% of the amount FUNAI re-

This sawmill, on a cleared patch of Amazon forest in Brazil, trades in wood taken illegally from an indigenous reserve.

quested, according to documents presented at the 2014 public hearing.

FUNAI officials stated in 2014 that they needed 30 staffed frontier posts, each outfitted with communications equipment and transportation. But according to a document presented at the hearing, they had just 15 posts operating in 2014, suggesting that their front lines are operating at half strength.

Vaz notes that most of FUNAI's protection fronts now lack the specialized field teams needed to find isolated groups and map territories. At the 2014 public hearing, FUNAI officials reported that they needed 14 specialized field teams; at present the agency has two. Vaz is furious. "Why do we have protection bases being closed?" he asks. "Why are there protection fronts that are no longer able to implement the procedures for protection? There is something wrong."

He thinks the problem boils down to a highly coveted commodity in Brazil today: land. The data gathered by FUNAI's specialist field teams lay the groundwork for legally demarcating land for the sole use of isolated indigenous groups. Once the land is protected, the Brazilian government can no longer auction it off to public and private development enterprises.

Vaz digs out a chart published by the Brazilian nonprofit Povos Indígenas no Brasil, which itemizes indigenous land demarcation over the past 2 decades. Between 1995 and 2002, the government of Fernando Henrique Cardoso demarcated and ratified 118 applications for indigenous land. From 2003 to 2010, Luiz Inácio Lula da Silva's government ratified another 81 applications. But from 2011 to 2015, Dilma Rousseff's government ratified just 11 applications, and only one since 2013; that application was signed on 29 May 2015. Several demarcation documents "are sitting on the desk of the minister of justice, and he is not signing them," Vaz says.

Vaz contends that the current government is demarcating very little land for indigenous groups and has largely abandoned its responsibilities to them, placing their lives in danger, primarily because it "sees the Indians as hampering the agricultural business, hampering the expansion of mining, and hampering the extraction of natural resources."

João Paulo Gomes, a representative for the Secretariat for Social Communication of the Presidency of Brazil, does not dispute Vaz's numbers. "It is natural that the number of demarcations should decrease over time as the demand for them is met," he wrote by e-mail. Most of the indigenous lands now awaiting ratification, he adds, "are concentrated in the center-south and northeast regions of Brazil," where there is still major social conflict over the demarcation of indigenous lands.

Gomes also dismisses charges that President Rousseff and her government favor economic development on the territories of isolated tribes. The Ministry of Justice is now using legal mediation measures to resolve disputes over land between indigenous communities and rural producers, he says. The government "is keenly interested in bringing the conflicts in indigenous lands to an end," he says.

In his sunlit apartment, Sydney Possuelo agrees with Vaz's contention that the current government has reneged on its responsibilities to isolated peoples. The legendary protection system that Possuelo helped build is crumbling, as abandoned protection bases molder in the forest. The once efficient system of radio communication between FUNAI riverboats and bases is falling apart. The isolated people who once preserved traditional knowledge of Amazonian plants as well as a rich diversity of cultures and languages face new threats. And in their glass towers in Brasília, federal officials are veering dangerously close to repeating the mistakes of the past, Possuelo says.

"FUNAI is dead," he says. "But nobody told it, and nobody held a funeral." ■

Indigenous leaders gathered at Brazil's National Congress in Brasília in April, demanding more land for isolated tribes and settled communities.

PHOTOS: (TOP TO BOTTOM) RICARDO MORAES/REUTERS/CORBIS; REUTERS/UESLEI MARCELINO

Reporting for these stories was supported in part by a grant from the Pulitzer Center on Crisis Reporting.

INSIGHTS

The large and small of friction *p. 1087 and p. 1089*

Brain methylation *p. 1094*

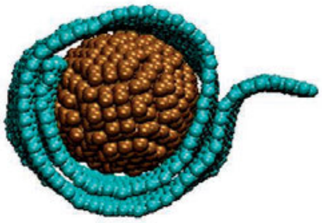

PERSPECTIVES

OCEANS

Invisible barriers to dispersal

Physiological properties constrain future range expansions of marine organisms

By **Joan Kleypas**

Climate change is causing organisms to migrate into new geographic areas, with most organisms tracking the movement of suitable temperatures poleward (*1*). The movements appear to be more rapid for marine than for terrestrial fauna (*2*), perhaps because marine organisms have fewer barriers to dispersal (*3*), but many marine organisms do encounter barriers that inhibit their ability to colonize new habitats. On page 1135 of this issue, Muir *et al.* (*4*) show that low wintertime irradiance limits the poleward expansion of staghorn corals. On page 1132, Deutsch *et al.* (*5*) identify another barrier to marine species: the ratio of oxygen supply and metabolic demand, which determines in which parts of the ocean fish and invertebrates have enough oxygen to support their metabolic needs. These two studies remind us that climate change will reshape marine species habitats but not necessarily expand them.

Some barriers to range expansions are essentially static with respect to climate change (see the figure, panel A). For organisms that depend on photosynthesis, light availability is one of those barriers. The amount of solar

Climate and Global Dynamics, National Center for Atmospheric Research, Boulder, CO 80307, USA. E-mail: kleypas@ucar.edu

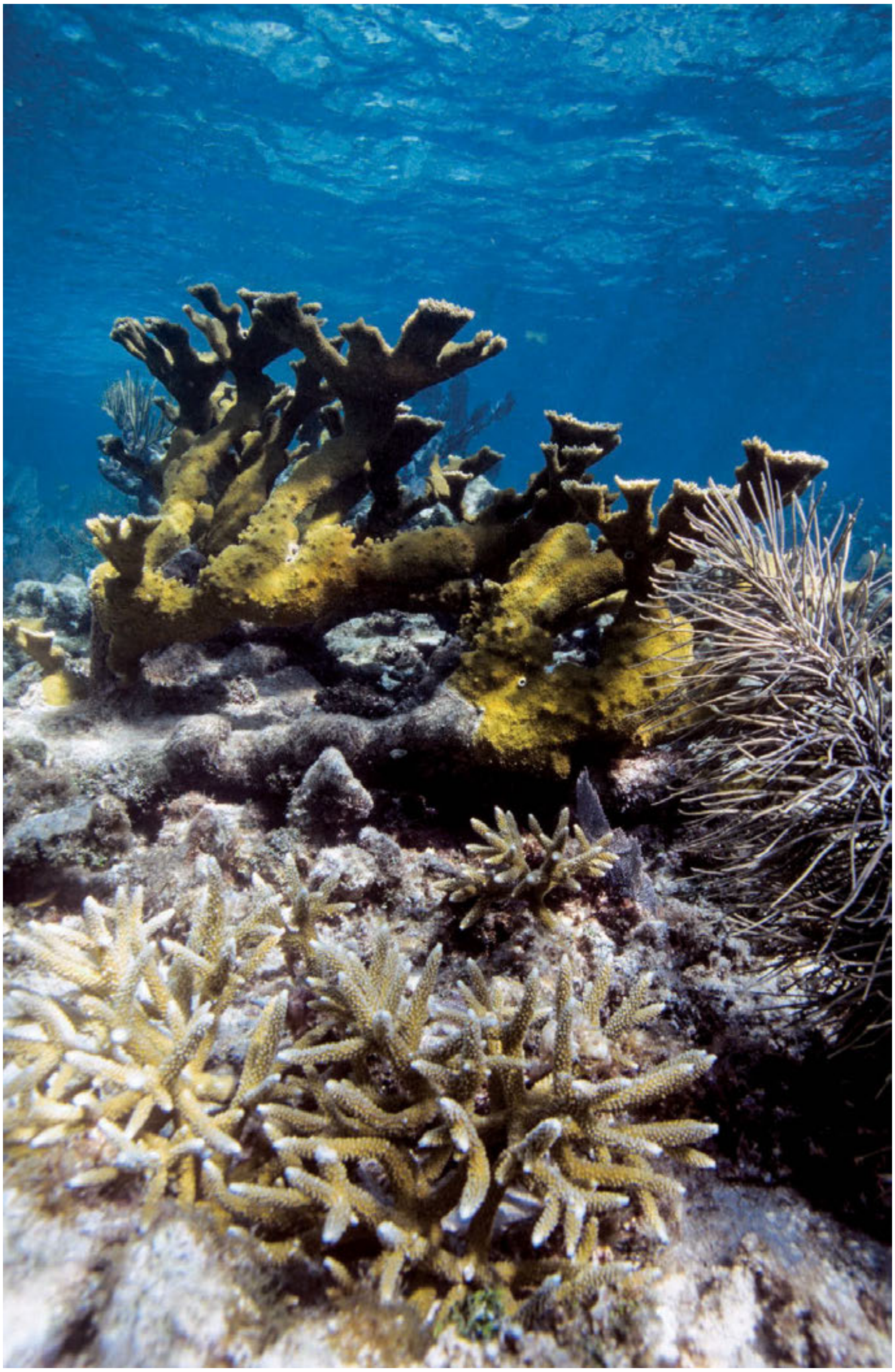

Warmer but dimmer. Acroporid corals, such as staghorn (foreground) and elkhorn (background) corals in the Florida Keys, thrive in warm well-lit waters. As ocean temperatures increase, they may be able to colonize at higher and higher latitudes but as they do so, the depth of wintertime light penetration will limit them to progressively shallower waters. Many marine species will encounter similar barriers as their habitats are reshaped by changes in temperature, oxygen, nutrients and other ocean properties.

PHOTO: RICK POLEY/VISUALS UNLIMITED

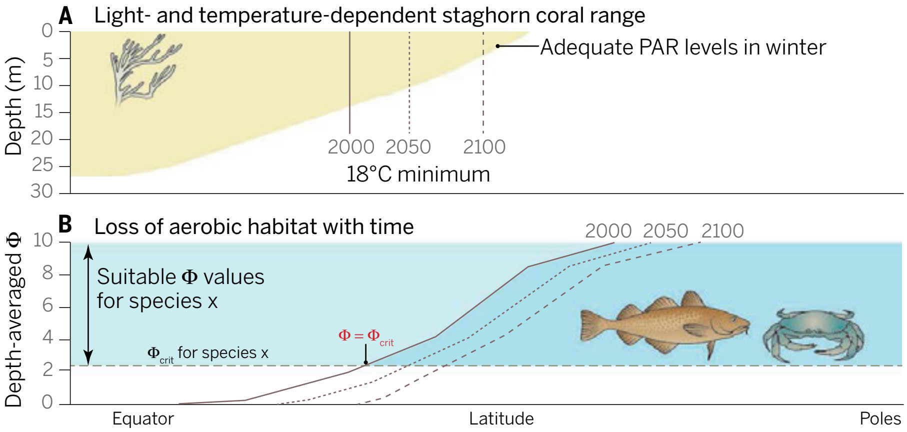

Invisible barriers. Muir *et al*. show that even though higher water temperatures will allow corals to colonize higher latitudes, low wintertime light levels will restrict them to progressively shallower depths (**A**). Furthermore, Deutsch *et al*. show how the depth-averaged metabolic index (Φ) for a given marine species decreases from higher latitudes to lower latitudes, often to levels that fall below the critical metabolic limit (Φ_{crit}) (**B**). With future increases in temperature and decreases in O_2 concentrations, the metabolic boundary of the species (where $\Phi = \Phi_{crit}$) is shifted poleward. Both panels are conceptual and should not be used to extract numerical values.

irradiance reaching the ocean surface and its attenuation with depth are not expected to change much with changes in climate. Reef-building corals, such as the staghorn corals studied by Muir *et al.*, depend on photosynthetic symbionts, limiting them to depths with sufficient levels of photosynthetically available radiation (PAR) throughout the year. Near the equator, this depth is typically around 25 to 30 m. Outside the tropics, it shallows by about 0.6 m per degree latitude, and so do the depths at which these corals are found. Muir *et al.* show that as reef-building corals settle at higher and higher latitudes in response to warming temperatures (*6–10*), they will eventually be confined to waters too shallow to support growth. Low PAR also appears to similarly limit the poleward expansions of other benthic photosynthesizers (*11*).

Other barriers to range extensions are dynamic (see the figure, panel B). Although rising temperature can lower barriers to poleward dispersal, such as minimum temperature limits, it also raises others. Warmer waters hold less oxygen, and warming at the ocean surface increases stratification, which leads to less oxygen at depth. At the same time, the metabolic oxygen demand of organisms increases with rising temperature. Using physiological data for various fish and invertebrate species, Deutsch *et al.* apply an energetics approach to determine how these changes affect the habitable space of several marine species. They define a metabolic index Φ, which is the ratio of O_2 supply and metabolic O_2 demand, and thus captures the minimal physiological requirements for survival. Φ_{crit} is the sum of Φ and the additional energy required for key ecological activities. For the species studied, Φ_{crit} ranged from 2 to 5, suggesting that species are limited to environments where they can sustain metabolic rates that are 2 to 5 times their resting rates. These values are quite close to those for terrestrial organisms and may thus reflect basic metabolic requirements of organisms. Deutsch *et al.* find that if climate change proceeds along its current path, the habitats for the species they studied will contract by ~20% by the end of this century.

Both studies highlight little-recognized barriers to future range expansions in the oceans. Each is based on physiological limitations of marine organisms that are quantifiable and thus increase our ability to predict species habitats into the future. More difficult to quantify are the consequences of climate change on species interactions, which will reshape marine communities and the ranges of their species in complex nonlinear ways (*12*). Thus, although studies such as Muir *et al.* and Deutsch *et al.* increase scientists' confidence to pencil in the lines around future species distributions, we still need to keep the erasers handy. ■

REFERENCES

1. M. T. Burrows *et al.*, *Science* **334**, 652 (2011).
2. M. L. Pinsky *et al.*, *Science* **341**, 1239 (2013).
3. J. M. Sunday *et al.*, *Nature Climate Change* **2**, 686 (2012).
4. P. R. Muir *et al.*, *Science* **348**, 1135 (2015).
5. C. Deutsch *et al.*, *Science* **348**, 1132 (2015).
6. A. H. Baird *et al.*, *Coral Reefs* **31**, 1063 (2012).
7. B. J. Greenstein, J. M. Pandolfi, *Glob. Change Biol.* **14**, 513 (2008).
8. W. F. Precht, R. B. Aronson, *Front. Ecol. Environ* **2**, 307 (2004).
9. K. Sugihara *et al.*, *J. Jap. Coral Reef Soc.* **11**, 51 (2009).
10. H. Yamano *et al.*, *Geophys. Res. Lett.* **38**, L04601 (2011).
11. S. A. Manuel, K. A. Coates, W. J. Kenworthy, J. W. Fourqurean, *Mar. Environ. Res.* **89**, 63 (2013).
12. G.-R. Walther, *Philos. Trans. R. Soc. Lond. B Biol. Sci.* **365**, 2019 (2010).

10.1126/science.aab4122

FRICTION

Slippery when dry

Stiff nanodiamond particles encapsulated in graphene can substantially reduce friction for water-free macroscopic surfaces

By **James Hone**[1] *and* **Robert W. Carpick**[2]

Friction and wear account for massive amounts of wasted energy annually (estimates run in the hundreds of billions of dollars in the United States), in addition to unwanted and even unsafe failures of vehicles, machines, and devices (*1*). For example, nearly one-third of a vehicle's fuel energy is spent on overcoming engine, transmission, and tire friction (*2*). Engineers have devised many ways to reduce and control friction and wear, but it remains unknown whether superlubricity—the reduction of friction forces to nearly immeasurable levels—can be achieved with practical materials. On page 1118 of this issue, Berman *et al.* (*3*) describe an approach that combines the advantages of two nanomaterials with very different mechanical properties—stiff nanodiamonds and bendable graphene—to achieve apparent superlubricity on the macroscopic scale.

Superlubricity has been observed for a range of materials including practical amorphous diamondlike carbon (DLC) coatings (*4*). However, most reports describe very well-controlled nanoscale contacts or specific experimental conditions (e.g., ultrasmooth surfaces) for limited durations with coatings that must be applied with advanced thin-film deposition methods. Graphene's distinctive properties make it a promising material in the search for practical superlubricity. It is extremely rigid in-plane and is not likely to form bonds with other materials it contacts, which suggests that it should shear across itself (or other materials) with ease. Indeed, graphite flakes work as a lubricant for this primary reason, and isolated domains of single graphene on substrates have been shown to exhibit order-of-magnitude reductions in friction relative to the surrounding substrate (*5*).

Graphene's surface is crystalline, which allows it to achieve a condition known as "structural lubricity," a type of superlubric-

ity in which surfaces with different atomic lattices are incommensurate, like egg cartons for different-sized eggs. The potential energy between the two surfaces is almost completely independent of position, so that the two surfaces never lock together and slide easily. Previous investigations, first in nanoscale contacts (*6*) and more recently on the scale of 1 μm (*7*), showed that superlubricity can exist between misaligned graphitic surfaces. In addition, concentric carbon nanotubes, in which the inner and outer shells are by nature incommensurate, have been shown to exhibit ultralow friction arising from structural lubricity up to lengths of centimeters (*8*).

Large-area graphene sheets (grown by chemical vapor deposition) and liquid suspensions of micrometer-scale graphene flakes have both been investigated for their potential as tribological coatings. However, initial studies have so far not shown great promise, likely because single-layer graphene weakly adheres to surfaces and easily delaminates (*9*, *10*). Recently, graphene flakes deposited in suspension on steel were shown to be durable across a range of environments, but the friction coefficient of ~0.15 to 0.2 was not as low as can be achieved with graphite. Another complication is that the low friction seen for few-layer graphene at the nanoscale deformation actually goes up, by nearly 50%, as the number of layers reduces to one, because the thinner the sheet, the greater its ability to flex and wrap around an asperity to increase contact area and friction (*11*).

Motivated by the potential for superlubricity between the incommensurate lattices of DLC and graphene, Berman *et al.* explored the frictional properties of SiO_2 coated with graphene flakes deposited from liquid suspension, against a large (1 cm) steel ball coated with DLC. However, the friction coefficient was well above the regime of superlubricity. In examining the wear tracks from these experiments, they observed that the graphene had delaminated from the surface and rolled up into "nanoscrolls," similar to previously observed fullerene "onions" and consistent with the ease with which graphene, given its thinness, can flex, bend, and roll up.

[1]Department of Mechanical Enginnering, Columbia University, New York, NY 10027, USA. [2]Department of Mechanical Engineering and Applied Mechanics, University of Pennsylvania, Philadelphia, PA 19104, USA. E-mail: jh2228@columbia.edu

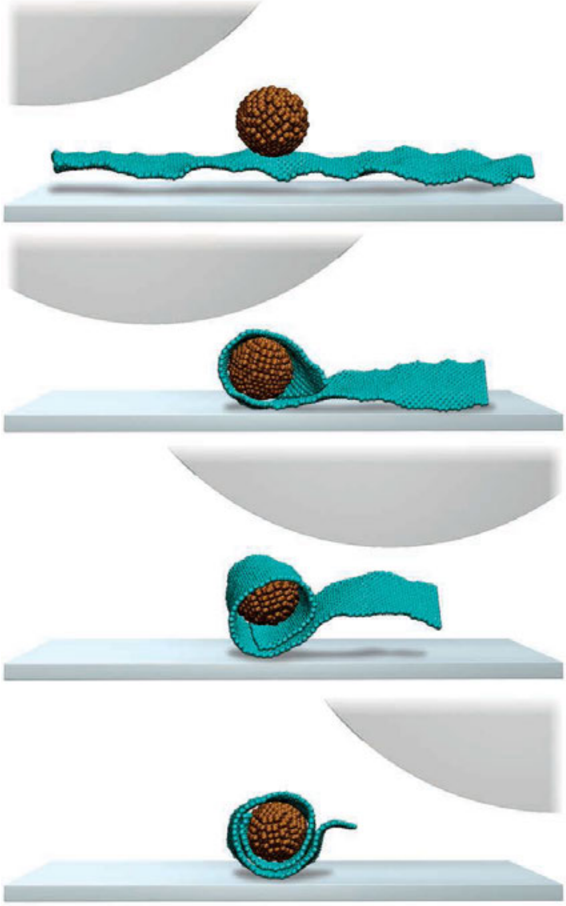

Squeeze wrap. Berman *et al*. found that huge reductions in macroscopic friction ("superlubricity") were achieved where nanodiamonds slid against graphene. The nanodiamonds bonded to graphene nanoplatelets and became wrapped in them, allowing them to slide easily through incommensurate surface effects.

Berman *et al.* recognized that such nanoscrolls might in themselves be quite useful as an antifriction coating if it were not for their easy deformability under pressure. Thus, they added nanodiamond particles, 3 to 5 nm in diameter, to the graphene suspension as a way to mechanically stabilize the nanoscrolls. The frictional coefficient was initially similar to that achieved with graphene only, but upon repeated cycling, the coefficient of friction dramatically decreased to 0.004. This reduction was not observed with either the graphene or nanodiamond alone, and was also only seen in a dry environment—the friction coefficient was nearly 100 times greater in high humidity.

Investigations by Raman spectroscopy, transmission electron microscopy, and detailed molecular dynamics simulations enabled Berman *et al.* to describe the process by which superlubricity is achieved. First, sliding of the nanodiamonds across the graphene platelets induces bonding between the graphene nanoplatelets and the diamond (see the figure). This process is facilitated both by the dangling bonds on the diamond surface and defects in the solution-produced graphene, such as those at the edges of the isolated graphene particles. The graphene then rolls around the diamond to make spheres ~10 nm in diameter. These spheres are nearly rigid, providing mechanical stability. Furthermore, the ordered surface provides an incommensurate atomic contact with the DLC-coated sphere, leading to superlubricity from the structural mismatch.

Unfortunately, water interrupts this rolling process by increasing adhesion of the graphene to the surface and by stabilizing defective sites in the graphene that provide bonding to the nanodiamond. Still, achieving such low friction for sustained times under macroscopic conditions, where roughness, irregularities, and high local stresses at nanoscale contact points could easily trigger failure of such thin coatings, is surprising and promising. Moreover, the solution-based deposition methods are relatively simple. Taken together, these findings suggest that practical coatings that take advantage of graphene's remarkable properties may be practically attainable.

Although more work is needed to fully verify the hypotheses behind the remarkable observations, the results of Berman *et al.* are intriguing for many reasons. Other combinations of two-dimensional materials (such as molybdenum disulfide) with other types of nanoparticles may prove more tolerant of water, or could open up their use as additives in lubricant fluids to reduce the large and undesirable amount of friction in vehicles. The potential for reduced energy consumption renders the result important in itself, and worthy of inspiring further studies that build upon it. ■

REFERENCES

1. H. P. Jost, *Tribol. Lubrication Technol.* **61**, 18 (2005).
2. K. Holmberg, P. Andersson, A. Erdemir, *Tribol. Int.* **47**, 221 (2012).
3. D. Berman, S. A. Deshmukh, S. K. R. S. Sankaranarayanan, A. Erdemir, A. V. Sumant, *Science* **348**, 1118 (2015).
4. A. Erdemir, J. M. Martin, *Superlubricity* (Elsevier, Amsterdam, 2007).
5. P. Egberts, G. H. Han, X. Z. Liu, A. T. C. Johnson, R. W. Carpick, *ACS Nano* **8**, 5010 (2014).
6. M. Dienwiebel *et al.*, *Phys. Rev. Lett.* **92**, 126101 (2004).
7. Z. Liu *et al.*, *Phys. Rev. Lett.* **108**, 205503 (2012).
8. R. Zhang *et al.*, *Nat. Nanotechnol.* **8**, 912 (2013).
9. D. Marchetto *et al.*, *Tribol. Lett.* **48**, 77 (2012).
10. F. Wählisch, J. Hoth, C. Held, T. Seyller, R. Bennewitz, *Wear* **300**, 78 (2013).
11. C. Lee *et al.*, *Science* **328**, 76 (2010).

10.1126/science.aab3233

ILLUSTRATION: ADAPTED BY P. HUEY/*SCIENCE*

PHYSICS

Controlling friction atom by atom

A cold-atom system is used to probe atomic friction on the scale of single atoms

By **Ernst Meyer**

Friction is a phenomenon of great technological relevance. The empirical laws of friction date back to the investigations of Leonardo da Vinci (1452 to 1519) and Guillaume Amontons (1663 to 1705). Thus, we have known for a long time that friction is proportional to the force normal to a surface and independent of the geometrical contact area. We also know that friction is one of major sources of energy loss, whereby a large amount of energy is dissipated into heat. In some cases, suitable surface preparation can lead to superlubricity, which corresponds to a state with extremely low frictional forces, where energy dissipation is at a minimum (*1*). On page 1115 of this issue, Bylinskii *et al.* (*2*) describe a cold-atom system that takes us to the ultimate limit of friction. They show that a defined number of ions, from one to six, can be moved across an optical lattice to study the elementary processes of atomic friction.

The mechanism behind superlubricity has remained unknown so far. It is possible that the surface chemistry—for example, coverage with thin molecular layers or structural properties of the interface—might play an important role. Although the Frenkel-Kontorova (FK model) (*3*, *4*) predicts that two incommensurate crystals (*5*) might lead to superlubric conditions, little is known about the influence of the atomic structure of the sliding interfaces under real experimental conditions. This subject has become the focus of fundamental research, where a number of modern experimental setups, such as quartz microbalance, surface force apparatus, or atomic force microscopy, were applied and advanced models were developed to unveil the secrets of the fundamental processes of friction (*6*).

The technique presented by Bylinskii *et al.* uses a small number of ions trapped to form an ion crystal in a linear Paul trap (see the figure). This ionic crystal is then positioned close to a periodic optical lattice, and can be pulled across the periodic lattice, analogous to pulling a sledge across the ground. In contrast to the macroscopic sledge, however, the authors have full control over the number of ions in the trap, which they varied between one and six. A stick-slip motion was observed for the commensurate cases, where the ions stick in the valleys of the periodic lattice until the applied force is large enough for the ions to slide together to the next valley. When the degree of commensurability was reduced, a transition to smooth sliding, or superlubricity, was seen. In this case, the ions move asynchronously, and the overall frictional force is drastically reduced. From the FK model, the transition from stick-slip to smooth sliding is expected for the incommensurate case. However, the FK model was developed for a crystal of infinite size, and it was expected that small crystals might show a different behavior. Therefore, it is surprising that such a drastic reduction of friction in the incommensurate case compared to the commensurate case (by a factor of 10 for two ions to 100 for six ions) is observable with only a few atoms.

The present experimental setup is a versatile atomic friction simulator, which allows the experimentalist to control the number of atoms, the interaction strength, and the degree of commensurability between ion lattice and optical lattice. Although the temperature of the ions was only in the sub-millikelvin regime, it was observed that thermal excitation plays an appreciable role. Comparison with simulations showed that a model without thermal excitation would lead to discrepancies, which validates the thermal lubricity model introduced by Krylov and Frenken (*7*).

The experiments by Bylinskii *et al.* have shown that atomic friction can be controlled by the use of ion traps. The relevant parameters, such as the number of atoms in contact and the periodicities of the slider and the surface, are determined, and subsequently the effects of commensurability can be controlled with high accuracy. The limits of the experiments are the pure one-dimensional character and the quite artificial way to create physical interactions with optical lattices, which is rather far removed from the world of material science. However, the experiments have shown that the concept of commensurability can be realized with only a few atoms. Future experiments may further elucidate the fundamental processes of friction. Possibly, novel regimes may be explored, where quantum-mechanical tunneling becomes important, and the fascinating world of quantum mechanics comes into reach. ■

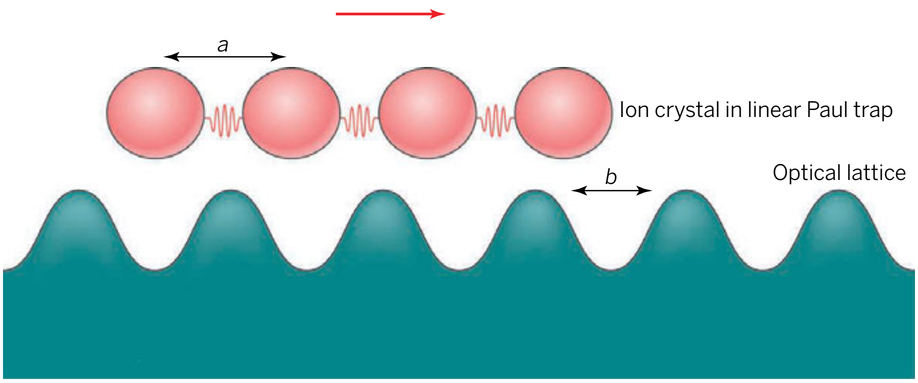

The atomic friction simulator. An ion crystal confined in a linear Paul trap is moved across a periodic optical lattice. Friction is found to depend strongly on the commensurability of these two lattices, even for systems with only two to six ions included in the trap.

ILLUSTRATION: ADAPTED BY P. HUEY/*SCIENCE*

Department of Physics, University of Basel, Klingelbergstrasse 82, CH-4056 Basel, Switzerland.
E-mail: ernst.meyer@unibas.ch

REFERENCES AND NOTES

1. A. Erdemir, J.-M. Martin, Eds., *Superlubricity* (Elsevier Science, Amsterdam, 2007).
2. A. Bylinskii, D. Gangloff, V. Vuletić, *Science* **348**, 1115 (2015).
3. Y. I. Frenkel, T. Kontorova, *Zh. Eksp. Teor. Fiz.* **8**, 1340 (1938).
4. Y. I. Frenkel, T. Kontorova, *J. Phys. Moscow* **1**, 137 (1939).
5. Commensurability: The ratio of the periodicity of the optical lattice *a* and the periodicity of the ion crystal *b* is equal to a ratio of integer numbers: $a/b = p/q$, where $p,q \in \mathbb{N}$. Incommensurability: a/b is not a ratio of integer values.
6. M. Urbakh, E. Meyer, *Nat. Mater.* **9**, 8 (2010).
7. S. Y. Krylov, J. W. M. Frenken, *Phys. Status Solidi B* **251**, 711 (2014).

10.1126/science.aab3539

SOCIAL SCIENCES

The rise of the social algorithm

Does content curation by Facebook introduce ideological bias?

By **David Lazer**[1,2]

Humanity is in the early stages of the rise of social algorithms: programs that size us up, evaluate what we want, and provide a customized experience. This quiet but epic paradigm shift is fraught with social and policy implications. The evolution of Google exemplifies this shift. It began as a simple deterministic ranking system based on the linkage structure among Web sites—the model of algorithmic Fordism, where any color was fine as long as it was black (*1*). The current Google is a very different product, personalizing results (*2*) on the basis of information about past searches and other contextual information, like location. On page 1130 of this issue, Bakshy *et al.* (*3*) explore whether such personalized curation on Facebook prevents users from accessing posts presenting conflicting political views.

The rise of the social algorithm is rather less transparent than the post–Model T choice in automobiles. Today's social algorithms are so complex that no single person can fully understand them. It is illustrative in this regard to consider that Bakshy *et al.* are Facebook researchers studying the impact of Facebook algorithms. You might imagine that they could just go into the next building and look directly at the code. However, looking at the algorithms will not yield much insight, because the interplay of social algorithms and behaviors yields patterns that are fundamentally emergent. These patterns cannot be gleaned from reading code.

Social algorithms are often quite helpful; when searching for pizza in Peoria, it helps not to get results about Famous Ray's in Manhattan. However, personalization might not be so benign in other contexts, raising questions about equity, justice, and democracy. Bakshy *et al.* focus on the last, asking whether the curation of news feeds by Facebook undermines the role that Facebook plays as a forum for public deliberation.

For the Facebook-uninitiated, much of the activity of Facebook is in the form of news that users post to their feed, which their friends have some access to and can like and comment on. When you open Facebook, you see a list of recent posts by friends; however, you typically will not see all posts, which are algorithmically sorted. The rationale for such curation is that in its absence, users would be deluged by uninteresting content from their friends. Facebook tries to pick out the gems from the detritus, anticipating what you will like and click on. But what are we missing? And are these computational choices troubling?

There are many facets to these questions, but one important one is how this curation affects Facebook as a deliberative sphere regarding public issues. Habermas (*4*) wrote of the role of the Parisian salons in the 19th century in offering a public space for such deliberations. The salons enabled intense conversation, with leakage across conversations creating a broader, systemic discussion. Facebook has many of these same qualities, and the issue is whether the curation process accentuates or undermines the quality of deliberation.

The specific deliberative issue that Bakshy *et al.* examine is whether Facebook's curation of news feeds prevents the intersection of conflicting points of view. That is, does a "filter bubble" emerge from this algorithmic curation process, so that individuals only see posts that they agree with (*5*)? Such an algorithmic sorting has the potential to be unhealthy for our democracy, fostering polarization and undermining the construction of a vision of the common good.

Their answer, after parsing the Facebook pages of ~10 million U.S. individuals with self-declared ideologies, is that the curation does ideologically filter what we see. However, this effect is modest relative to choices people make that filter information, including who their friends are and what they choose to read given the curation. The deliberative sky is not yet falling, but the skies are not completely clear either.

This is an important finding and one that requires continued vigilance. A small effect today might become a large effect tomorrow, depending on changes in the algorithms and human behavior. Ironically, these findings suggest that if Facebook incorporated ideology into the features that the algorithms pay attention to, it would improve engagement with content by removing dissonant ideological content. It is also notable, for example, that Facebook announced April 21st—well after the analysis conducted in this paper—three major changes to the curation of newsfeeds.

[1]*Department of Political Science and College of Computer and Information Science, Northeastern University.* [2]*John F. Kennedy School of Government, Harvard University, Cambridge, MA, USA. E-mail: d.lazer@neu.edu*

ILLUSTRATION: PETER AND MARIA HOEY/WWW.PETERHOEY.COM

These changes had benign objectives, such as ensuring that one sees updates from "the friends you care about" (*6*). It is plausible, however, that friends that Facebook infers you to care about also tend to be more ideologically aligned with you as well, accentuating the filtering effect. Furthermore, the impact of curation on other dimensions of deliberative quality on Facebook remains to be examined. Open questions include whether the curation privileges some voices over others, and whether certain types of subjects are highlighted by the curation in a way that systematically undermines discussions of the issues of the day (pets over politics).

The impacts of social algorithms are a subject with rich scientific possibilities, not least because of the enormous data streams captured by these socio-technical systems (*7*). It is not possible to determine definitively whether Facebook encourages or hinders political discussion across partisan divides relative to a pre-Facebook world, because we do not have nearly the same quality or quantity of data for the pre-Facebook world. The existence of Facebook, Twitter, etc., should be a boon to the study of political deliberation, because it is now possible to study these systems at a societal scale.

Important normative implications will follow from a clearer understanding of these systems. For example, a recent paper on price discrimination and steering that I coauthored (*8*) revealed that people sometimes get different prices and different products prioritized on e-commerce sites. This work has spurred substantial public discourse, as well as discussions with European Union regulators. Research such as that of Bakshy *et al.* has similar potential to inform a vigorous debate about the role that social media play in our society.

It is laudable that Facebook supported this research (*3*) and has invested in the public good of general scientific knowledge. Indeed, the information age hegemons should proactively support research on the ethical implications of the systems that they build. Facebook deserves great credit for building a talented research group and for conducting this research in a public way. But there is a broader need for scientists to study these systems in a manner that is independent of the Facebooks of the world. There will be a need at times to speak truth to power, for knowledgeable individuals with appropriate data and analytic skills to act as social critics of this new social order (*9*).

And although these systems are permeable and offer some entry points for study, this permeability is revocable and arguably decreasing. Facebook, for example, allows some access to user data via applications within the Facebook ecosystem. The relatively broad access creates the risk of third parties siphoning off large amounts of data from users, but has also allowed researchers to collect data to study Facebook.

The amount of data that can be collected via this route was sharply reduced on 30 April 2015 (*10*), with benefits to privacy, but undercutting independent research. This creates the risk that the only people who can study Facebook are researchers at Facebook—an unhealthy weighting of the dice of scientific exploration.

The fact that human lives are regulated by code is hardly a new phenomenon. Organizations run on their own algorithms, called standard operating procedures. And anyone who has been told that "it's a rule" knows that social rules can be as automatic and thoughtless as any algorithm. Our friends generally are a lot like us (*11*) and news media have always had to choose to pay attention to some stories and not others, in part based on financial and cultural imperatives (*12*, *13*). Social and organizational codes have always resulted in filter bubbles. However, every system of rules and every filtering process has potentially quite different dynamics and normative implications. Therein lies the most important lesson of Bakshy *et al.*'s report: the need to create a new field around the social algorithm, which examines the interplay of social and computational code. ■

REFERENCES AND NOTES

1. S. Brin, L. Page, *Comput. Netw. ISDN Syst.* **30**, 107 (1998).
2. A. Hannak *et al.*, in *Proceedings of the 22nd International Conference on World Wide Web* (International World Wide Web Conferences Steering Committee, Geneva, Switzerland, 2013), pp. 527–538.
3. E. Bakshy *et al.*, *Science* **348**, 1130 (2015).
4. J. Habermas, *The Structural Transformation of he Public Sphere: An Inquiry into a Category of Bourgeois Society* (MIT Press, Harvard, MA, 1991).
5. E. Pariser, *The Filter Bubble: What the Internet Is Hiding from You* (Penguin, London, 2011).
6. http://newsroom.fb.com/news/2015/04/news-feed-fyi-balancing-content-from-friends-and-pages
7. D. Lazer *et al.*, *Science* **323**, 721 (2009).
8. A. Hannak, G. Soeller, D. Lazer, A. Mislove, C. Wilson, in *Proceedings of the 2014 Conference on Internet Measurement Conference* (Association for Computing Machinery, New York, 2014), pp. 305–318.
9. Z. Tufekci, *First Monday* 10.5210/fm.v19i7.4901 (2014).
10. Go to https://developers.facebook.com/docs/apps/upgrading and click on "What happens on April 30, 2015".
11. M. McPherson *et al.*, *Annu. Rev. Sociol.* **27**, 415 (2001).
12. P. J. Shoemaker, T. P. Vos, *Gatekeeping Theory* (Routledge, New York, 2009).
13. J. W. Dimmick, *Media Competition and Coexistence: The Theory of the Niche* (Erlbaum Associates, Mahwah, NJ, 2003).

ACKNOWLEDGMENTS

This article has benefited from feedback from B. Keegan, D. Margolin, K. Ognyanova, M. Wasserman, B. F. Welles, and C. Wilson, and was supported by NSF grant no. 1408345. The views and conclusions contained herein are the author's alone.

10.1126/science.aab1422

CELL BIOLOGY

Centrioles, in absentia

What is the link between centrioles and cell proliferation?

By **Tim Stearns**

The centriole is one of the organelles that defines eukaryotes. It was present in the last universal common eukaryotic ancestor (*1*), and persists in all major branches of the eukaryotic tree. The centriole nucleates the cilium, which is involved in sensory signaling and in cell motility. In animal cells, the centriole is also the hub of the centrosome, an accumulation of microtubule-nucleating and -organizing proteins that determine the spatial arrangement of the microtubule cytoskeleton. Duplication and segregation of the centrioles are strictly controlled such that each cell begins the cell division cycle with a single pair of centrioles, which duplicate only once and are then segregated on the poles of the mitotic spindle (*2*). On page 1155 of this issue, Wong *et al.* (*3*) describe a small-molecule inhibitor of centriole duplication that allowed them to probe the effects of centriole loss. Surprisingly, it appears that some cancer cells can proliferate indefinitely without centrioles, whereas normal cells cannot.

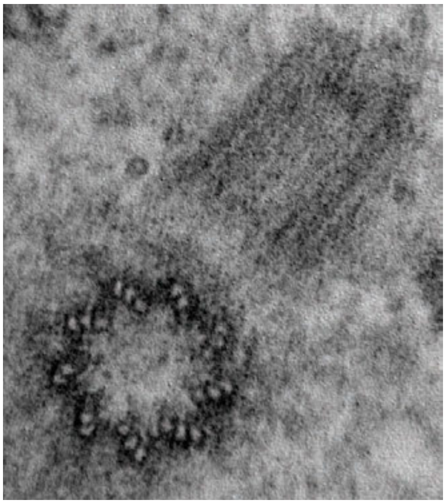

Ninefold symmetric structure. Electron micrograph shows two centrioles in cross section (lower left) and longitudinal section (upper right).

MICROGRAPH: MARK VAN BREUGEL/MRC LABORATORY OF MOLECULAR BIOLOGY

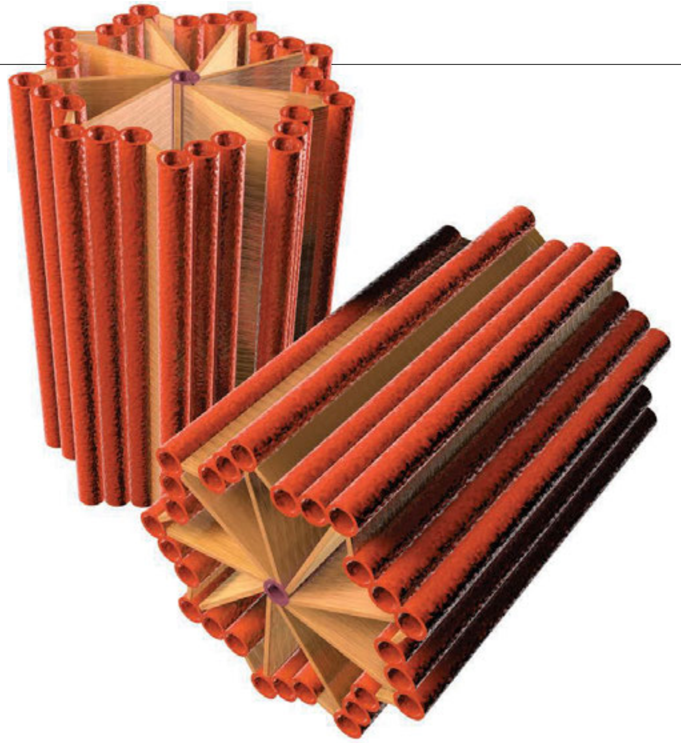

Exalted status. Centrioles are found in organisms in all branches of the eukaryotic tree, They organize microtubules in the cilium and in the mitotic spindle. Centrioles are linked to cell proliferation, but the mechanism is unclear.

Centrioles are made of tubulins, and their characteristic ninefold symmetric structure is unique to eukaryotes (see both figures). The beginnings of a molecular basis for this structure are now known (*4*), but the evolutionary origin of the centriole is still unclear. The presence of a pair of centrioles at each mitotic spindle pole in many organisms has strongly influenced thought about spindle mechanisms. In this regard, the natural events leading to loss of the centrioles during evolution are particularly interesting: Centrioles are absent from higher plants but present in many lower plants, which have gametes that swim by ciliary motility. Similarly, they are absent from higher fungi but present in the basal chytrid fungi, which have swimming zoospores. In each case, lack of the centriole is accompanied by loss of the cilium that grows from it. Presumably, the signaling and motility functions of the cilium can be dispensed with when, as in the higher plants, gametes can be distributed by wind and animals, and a different set of cilium-independent signaling pathways predominates. Even within animals, which universally have centrioles and cilia, the centriole is lost from the female gamete during meiosis, to be reintroduced in most cases by the sperm cell.

Centrioles in animals would seem to be critical for the formation of a cilium, but what of the other suspected functions in microtubule organization and mitotic spindle formation? This question has led to attempted elimination of centrioles in animal cells or in entire organisms to assess the resulting phenotype. Other studies have sought to increase centriole number to mimic the situation observed in many cancer cells (*5*).

Methods of centriole elimination have included direct manipulation of cells with a glass microneedle (*6*), ablation of one or both centrioles with a laser (*7*), and mutation or inhibition of genes essential for centriole formation (*8–10*). In organisms that normally have centrioles, their loss eliminates the ability to make a cilium, with the known organismal consequences that are largely based on the cilium's sensory functions. However, many other aspects of cell function still occur. Spindles form and chromosomes segregate, albeit with lower fidelity. In *Drosophila melanogaster*, flies in which centrioles are removed genetically, after the early embryonic divisions, develop relatively normally, but die soon after hatching due to sensory cilia defects (*8*). In mice, the primary cilium is required for early embryonic development, but genetic loss of the centrioles led to a phenotype distinct from cilium dysfunction, in which acentriolar cells underwent an apoptotic cell death dependent on p53, a cellular stress sensor (*9*). This was a strong hint that at least in the context of mammalian development, acentriolar cells are somehow defective.

In all of the previous centriole-loss experiments, the effect of loss is confounded by de novo formation of new centrioles (after physical removal), or in the case of genetic manipulation, by the relatively long time over which the effect is brought to bear, and the irreversible nature of the change. Compensatory changes also take effect over time (*11*). Wong *et al.* address these problems by identifying a potent inhibitor of Polo-like kinase 4 (Plk4), a protein kinase that is essential for centriole duplication. The compound was identified by starting with a molecule that could inhibit several kinases, including Plk4. Modeling was used to make modifications to the small molecule, paired with a very specific biological assay measuring inhibition of centriole duplication. The final compound, called centrinone, is highly selective for Plk4 and causes loss of centrioles by failure of centriole duplication, as expected for Plk4 inhibition. The effect was fully reversible, such that 10 days after removing centrinone, centriole number returned to normal. Many cancer cell lines have an increase in centriole number. Remarkably, removal of centrioles by centrinone in such cells, followed by washout and reestablishment of centriole equilibrium, yielded cells with essentially the same centriole number as that of the parental cells, suggesting that some form of homeostasis exists even in cells with a defective number of centrioles.

The most important difference between the study of Wong *et al.* and previous cell culture experiments on centriole loss is that centrinone-treated cells undergo a permanent p53-dependent arrest in the G_1 phase of the cell division cycle after one or two cycles. P53 is a well-characterized tumor suppressor, and P53-deficient cells can proliferate indefinitely without centrioles. What about centriole loss is being sensed by p53? The authors check all known p53 response pathways—DNA damage, mitotic delay, aneuploidy due to decreased mitotic fidelity—with negative results in all cases.

A provocative proposal by Wong *et al.* is that a link between a functional centrosome and proliferation might be part of a normal mechanism that prevents cell cycle reentry. Centrosomes are often inactivated in differentiated cells, and in some cases centrioles are absent. Thus, such a link might both explain how multicellular organisms separate differentiated from proliferating cells, and also provide an opportunity for intervention in cancer—for example, by targeting cells proliferating without normal centrosome function. The challenge now is to understand what it is about an acentriolar cell that p53 senses as defective. ■

Department of Biology, Stanford University, Stanford, CA, USA.
E-mail: stearns@stanford.edu

REFERENCES

1. Z. Carvalho-Santos, J. Azimzadeh, J. B. Pereira-Leal, M. Bettencourt-Dias, *J. Cell Biol.* **194**, 165 (2011).
2. E. N. Fırat-Karalar, T. Stearns, *Philos. Trans. R. Soc. Lond. B Biol. Sci.* **369**, 20130460 (2014).
3. Y. L. Wong *et al.*, *Science* **348**, 1155 (2015).
4. D. Kitagawa *et al.*, *Cell* **144**, 364 (2011).
5. S. A. Godinho, D. Pellman, *Philos. Trans. R. Soc. Lond. B Biol. Sci.* **369**, 20130467 (2014).
6. E. H. Hinchcliffe, F. J. Miller, M. Cham, A. Khodjakov, G. Sluder, *Science* **291**, 1547 (2001).
7. A. Khodjakov *et al.*, *J. Cell Biol.* **158**, 1171 (2002).
8. R. Basto *et al.*, *Cell* **125**, 1375 (2006).
9. H. Bazzi, K. V. Anderson, *Proc. Natl. Acad. Sci. U.S.A.* **111**, E1491 (2014).
10. J.-H. Sir *et al.*, *J. Cell Biol.* **203**, 747 (2013).
11. J. S. Poulton, J. C. Cuningham, M. Peifer, *Dev. Cell* **30**, 731 (2014).

10.1126/science.aac4860

MEDICINE

Progeria accelerates adult stem cell aging

Diseases resembling premature aging model naturally aging mesenchymal stem cells

By **Regina Brunauer** and **Brian K. Kennedy**

Aging is a multimodal process involving accumulation of macromolecular damage, genomic instability, and loss of heterochromatin, leading to stem cell exhaustion and reduced tissue-regenerative capability. Still highly debated are the extent to which loss of adult stem cell regenerative potential drives the organismal aging process and, more broadly, the relationship between cellular and organismal aging. On page 1160 of this issue, Zhang *et al.* (*1*) report the disruption of the *WRN* gene, mutations of which cause Werner syndrome (WS), in embryonic stem cells (ESCs). The dramatic phenotype of the WRN-deficient ESCs resembles aspects of aging but only after differentiation of the ESCs into mesenchymal stem cells (MSCs). The findings provide insights into the molecular events driving WS pathology, reveal similarities between Werner and Hutchinson-Gilford progeria syndromes (HGPS), and hint at the potential reversibility of the aging process, at least at the cellular level.

Diseases resembling accelerated aging, termed progerias, are widely used as models of normal aging, yet the extent to which the molecular events leading to these diseases overlap with aging, or even with each other, remain unclear. WS, or "adult progeria" (with an early adulthood onset), and HGPS, or "childhood progeria," are segmental in nature; that is, patients present with only a subset of aging pathologies, including cataracts, frequent neoplasia (often sarcomas), and diabetes in the case of WS. HGPS is generally more severe, with a mean life span in the mid-teens and cardiovascular disease as the major cause of mortality. In HGPS, a truncated form of the nuclear structure protein lamin A, termed progerin, is expressed and interferes with several nuclear processes (*2*).

Among the progerias, initial studies attempted to recapitulate progeria in the petri dish by reprogramming HGPS fibroblasts to form induced pluripotent stem cells (iPSCs) (*3*). Although generated with a lower efficiency compared to healthy samples, iPSCs derived from patient fibroblasts appeared normal, in part because ESCs and iPSCs express A-type lamins at very low levels. Differentiation into vascular smooth muscle cells, a cell type severely affected in HGPS, activated progerin expression and led to premature senescence. In a second study of iPSC differentiation in HGPS, this time looking at many cell types, MSCs, along with vascular smooth muscle cells, were found to induce the highest levels of, and be among the most sensitive to, progerin particularly under conditions of stress (*4*).

WS patients exhibit pathologies associated with degeneration of mesenchymal tissues, and transplantation of healthy MSCs into a WS mouse model improved mean life span and bone density (*5*). Therefore, Zhang *et al.* chose to examine the properties of MSCs derived from ESCs lacking WRN (*1*). The results show clear overlap with the HGPS studies described above, with normally behaving ESCs differentiating into MSCs that displayed progressive defects in proliferation and premature senescence, as well as an elevated DNA damage response. Furthermore, WRN-deficient MSCs show decreased survival when transplanted into mouse skeletal muscle. Together the studies suggest that impairment of adult stem cell function, particularly of MSCs, may be common attributes of different progeria syndromes.

Both A-type lamins and WRN have numerous roles in the nucleus. Progerin expression and loss of WRN change the structure of both the nuclear membrane and heterochromatin, lead to telomere attrition, and invoke DNA damage response pathways (*1*, *4*, *6*), all of which have been linked to normal aging (*7*). A major challenge, however, is to link specific molecular alterations to progeroid pathologies. The notion that loss of heterochromatin could be a cause of aging and a potential target for anti-aging interventions has arisen from work in nonvertebrate model organisms (*8*). In general, a decrease in heterochromatin levels has been observed during aging, and life-span extension occurs when heterochromatin levels are genetically restored. In mammalian fibroblasts and MSCs, cellular senescence is also associated with loss of heterochromatin and increased transcriptional noise (*9*, *10*).

It is unknown whether in the course of aging, it is DNA damage that induces het-

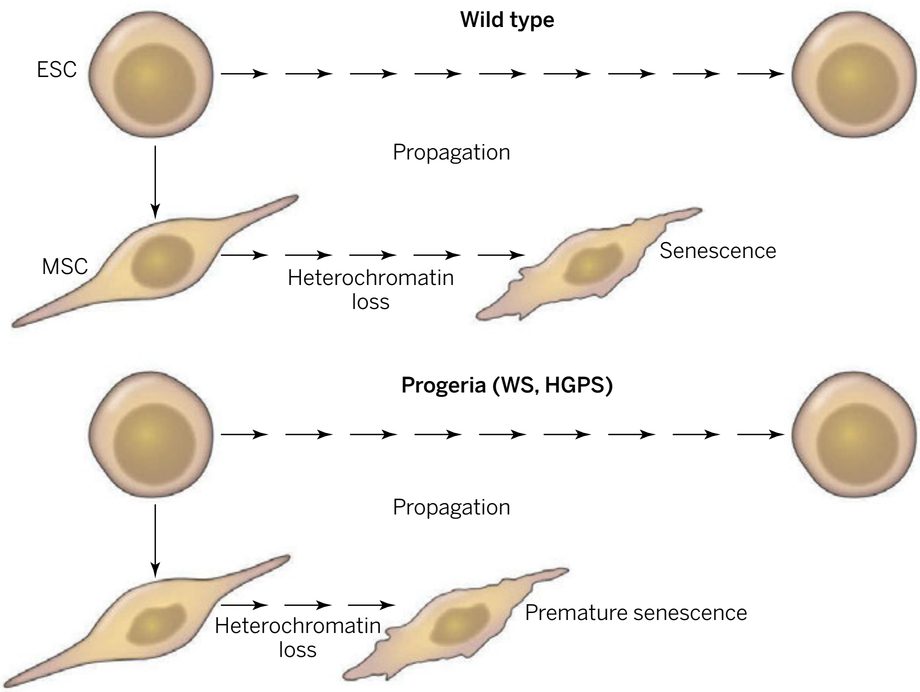

A stem cell model of progeria. Mesenchymal stem cells (MSCs) lacking the WRN helicase undergo premature senescence due to loss of heterochromatin. Similarly, MSCs expressing progerin exhibit accelerated replicative aging in vitro. The role of heterochromatin therein remains to be elucidated.

ILLUSTRATION: P. HUEY/*SCIENCE*

Buck Institute for Research on Aging, Novato, CA, USA. E-mail: bkennedy@buckinstitute.org

erochromatin changes, or loss of heterochromatin that facilitates DNA damage (*11*). Zhang *et al.* discovered a role of WRN in stabilizing heterochromatin in MSCs (*1*). Absence of WRN resulted in loss of heterochromatin mainly in subtelomeric and subcentromeric regions and aberrant transcription of repetitive satellite DNA. Overexpression of the heterochromatin protein HP1α, which interacts with WRN, increased heterochromatin levels and suppressed MSC senescence, but did not prevent DNA damage (*1*). Thus, in the WS setting, DNA damage may precede loss of heterochromatin and cannot be reversed by restoration of heterochromatin. Nevertheless, restoration of heterochromatin suppressed the senescent phenotype, indicating that repair of DNA damage may not be required to reverse the cellular phenotypes of the WRN-deficient ESCs. Because progerin has been shown to alter the cellular identity and differentiation potential of MSCs and to induce chromatin defects in fibroblasts, it is possible that restoration of heterochromatin would also restore MSC function in the HGPS context (*12*).

Strikingly, both HGPS and WS may phenocopy aging on the molecular level. Prior studies have detected elevated progerin expression in cells and tissues with age (*6*). In the current study, Zhang *et al.* report reduced WRN expression in MSCs isolated from aging individuals. These findings, which require further confirmation, raise the possibility that a subset of the pathologies of normal aging is driven by modification of pathways linked to progeria, thereby validating progeria aging models. More importantly, they raise the possibility that reversal of age-associated MSC dysfunction may be a valid mechanism to slow aging and prevent associated diseases. A major outstanding question is whether the restoration of heterochromatin organization seen in tissue culture cells would translate into a means to rescue the regenerative ability of the aged—thereby preventing pathology and extending life span. ■

REFERENCES

1. W. Zhang *et al.*, *Science* **348**, 1160 (2015).
2. C. R. Burtner, B. K. Kennedy, *Nat. Rev. Mol. Cell Biol.* **11**, 567 (2010).
3. G. H. Liu *et al.*, *Nature* **472**, 221 (2011).
4. J. Zhang *et al.*, *Cell Stem Cell* **8**, 31 (2011).
5. L. Singh *et al.*, *Stem Cells* **31**, 607 (2013).
6. P. Scaffidi, T. Misteli, *Science* **312**, 1059 (2006).
7. C. López-Otín, M. A. Blasco, L. Partridge, M. Serrano, G. Kroemer, *Cell* **153**, 1194 (2013).
8. A. Tsurumi, W. X. Li, *Epigenetics* **7**, 680 (2012).
9. M. De Cecco *et al.*, *Aging Cell* **12**, 247 (2013).
10. S. Bork *et al.*, *Aging Cell* **9**, 54 (2010).
11. G. Pegoraro, T. Misteli, *Aging* **1**, 1017 (2009).
12. P. Scaffidi, T. Misteli, *Nat. Cell Biol.* **10**, 452 (2008).

10.1126/science.aac4214

EPIGENETICS

Exceptional epigenetics in the brain

Non-CG DNA methylation modulates gene expression in the adult brain

By **Chongyuan Luo** *and* **Joseph R. Ecker**

Cytosine (C) methylation, or mC, is a modification of DNA that regulates gene expression in various contexts such as development, cancer, and imprinting. In most mammalian somatic tissues, mC arises only when C is in a dinucleotide context followed by the nucleotide guanine (G), and the vast majority of these sites are methylated (mCG). However, in the adult mammalian brain, noncanonical cytosine methylation in a non-CG context occurs at a high level [mCH; H = adenine (A), C, or thymine (T)]. The quantity of non-CG methylation is inversely correlated with gene expression, but the mechanism by which mCH controls transcription has not been clear. Two recent studies (*1*, *2*) suggest a mechanistic link between mCH and gene expression and substantially revise our view of gene regulation by DNA methylation in the brain, which was previously formed only on the basis of studies of mCG.

Non-CG methylation has been found in human embryonic stem cells (*3*, *4*) and more recently in the mammalian brain (*5*–*7*), and is present at a much higher level in neurons than in glia, a group of non-neuronal brain cell types. Non-CG methylation predominantly occurs at CA dinucleotides, with mCA accounting for more than 70% of non-CG methylation in the frontal cortex. Intriguingly, mCH is absent or present at very low levels in the brains of newborn mice or humans, respectively, but gradually amasses between birth and adolescence. mCH accumulation coincides temporally with the period of synaptogenesis when connections between neurons proliferate in the developing frontal cortex (*7*).

Gabel *et al.* (*1*) and Chen *et al.* (*2*) identify a possible mechanism whereby mCH may regulate neuronal gene expression through its recognition by methyl-CpG binding protein 2 (MeCP2), a factor whose disruption causes the neurological disorder Rett syndrome (*8*). Gabel *et al.* observed that human or mouse genes repressed by MeCP2 tend to have greater physical length (number of nucleotides) and are also associated with a greater amount of mCA. The finding was supported by an independent study showing that disruption of MeCP2 is more likely to affect long genes in distinct neuron types (*9*). With previous reports that MeCP2 can bind mCH (*10*), Gabel *et al.* further refined an in vitro binding assay and found that mCAC is a preferred binding target of MeCP2, with comparable or greater affinity than that for mCG. Gabel *et al.* and Chen *et al.* performed a series of correlative analyses that led to a model where mCA targets MeCP2 to its genomic binding sites in the adult mammalian brain (see the figure). Chen *et al.* used transgenic mice expressing a tagged version of MeCP2 and chromatin immunoprecipitation to generate a high-coverage map of MeCP2 binding sites in the mouse genome. Notably, the authors have found that the locations of mCH as well as MeCP2 binding sites are enriched in genes whose expression is both up-regulated and down-regulated when MeCP2 is disrupted, suggesting a more diverse regulatory role of MeCP2. The model in which mCA targets

"It is tempting to speculate on the importance of this epigenetic mechanism in… normal brain function or…disorders such as Rett syndrome."

MeCP2 binding is supported by Gabel *et al.*'s study showing that the elimination of mCH accumulation, through the ablation of de novo DNA methyltransferase Dnmt3a in the nervous system, led to a derepression of long genes similar to that caused by disruption of MeCP2.

The mechanism uncovered by these two studies provides new insights into the spatial scale and amplitude of the regulation by DNA methylation and the targeting of epigenetic regulatory machinery. Many previous studies focused on correlations between apparent gene expression changes and DNA methylation (primarily mCG) patterns at discrete regulatory elements such as promoters, CpG islands, or distal enhancers. By contrast, MeCP2 preferentially binds mCA

Genomic Analysis Laboratory and Howard Hughes Medical Institute, Salk Institute for Biological Studies, La Jolla, CA 92037, USA.
E-mail: ecker@salk.edu

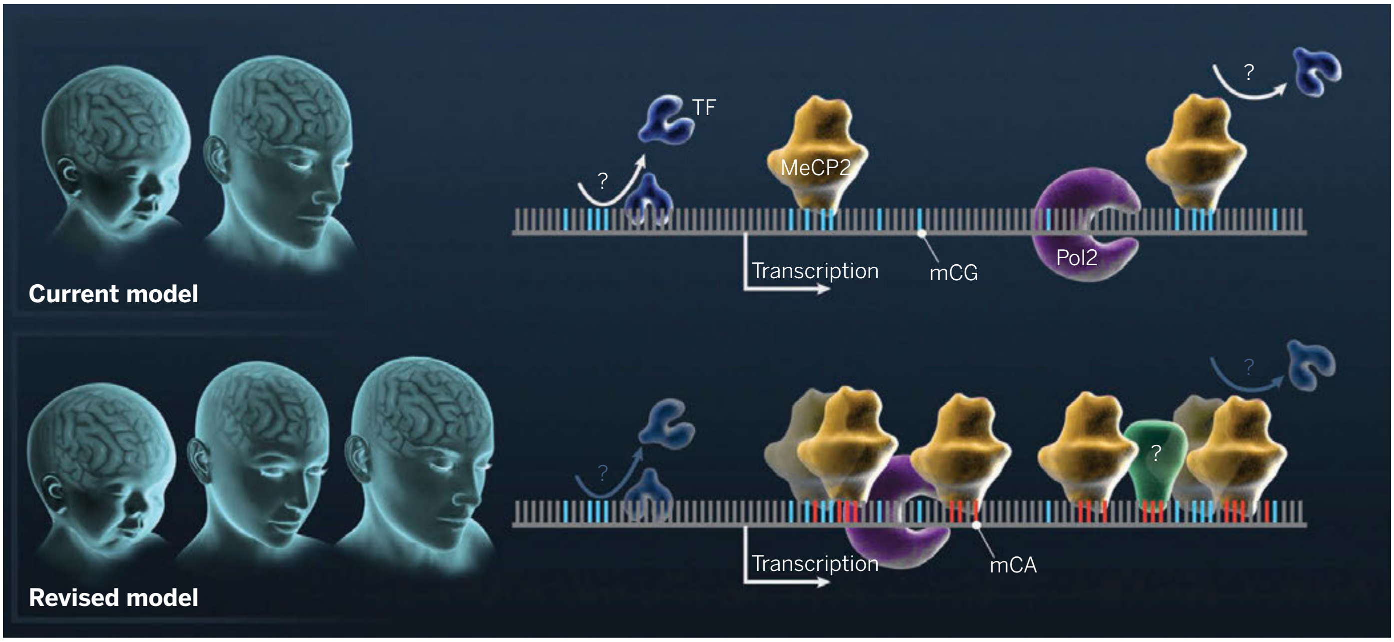

Brain methylation. The current model focuses on mCG at discrete regulatory elements in the genome, where it may block the binding of a transcription factor (TF) or bind to MeCP2, which represses transcription. The model does not inform about epigenomic differences between newborn and adult brains. The revised model highlights the accumulation of mCH, which is initiated at birth and continues throughout adolescence, resulting in a distinct state in the adult brain with high-affinity interaction between mCA and MeCP2. The recruitment of MeCP2 (and perhaps other mCH "readers" indicated with "?") by non-CG methylation represses the expression of genes enriched in mCA, possibly by affecting transcription elongation. Pol2, RNA polymerase 2.

deposited along gene bodies (the region of a gene that is transcribed by RNA polymerase) that can span hundreds of kilobases, which may allow fine tuning of gene expression at the level of individual genes. The currently pervasive view, based on correlations observed in large-scale epigenomic profiling analyses between local depletion of mCG and transcription factor binding, is that the initiation or targeting of epigenetic regulation likely involves sequence-specific transcription factors. Although this may well be true, the generality of this view is now challenged by the selective targeting of MeCP2 to mCA on genes with greater length, which is a spatial property of the genome and is unlikely to be associated with specific cis elements. Specifically, the recruitment of MeCP2 may be directly mediated by the epigenomic mark mCA.

Extending the profiling and perturbation of mCA and MeCP2 binding to specific neuron subtypes will be crucial to further unraveling mCA patterns that are currently measured with whole tissues (e.g., cortex) or mixed neuron populations. For example, ablating MeCP2 leads to cell type–specific gene misregulation (*9*). Such experiments will test whether cell type–specific MeCP2 regulation is associated with differential mCA deposition across distinct brain cell types. The contribution of mCA (versus other possible marks such as mCG) in recruiting MeCP2 remains to be quantified; this could be accomplished by profiling MeCP2 binding in specific neurons that are conditionally depleted of mCH. If mCA is indeed the primary mark for targeting MeCP2 and/or other effectors, what are mechanisms by which mCH is targeted to long genes and excluded from actively expressed neuronal genes? Although a cogent explanation for the former is unknown, for the latter it is possible that DNMT3a is excluded by the elongating RNA polymerase II or certain histone modifications associated with transcription elongation. An opposite mechanism was recently discovered by which DNA methyltransferase DNMT3b interacts with histone mark H3K36me3, which is characteristic of the transcription elongation leading to the preferential deposition of mC at actively transcribed genes in embryonic stem cells and primordial germ cells (*11, 12*).

It is tempting to speculate on the importance of this epigenetic mechanism in the context of normal brain function or for the understanding of neurological disorders such as Rett syndrome. mCH in the adult brain could provide a docking platform to direct the binding of a variety of factors (e.g., MeCP2) that could mediate distinct functions in the adult versus juvenile brain. Chen *et al.* have begun to explore this link by finding increased binding of MeCP2 at the *brain-derived neurotrophic factor* (*Bdnf*) locus in the adult relative to the juvenile mouse brain. Consistent with the enhanced MeCP2 recruitment, *Bdnf* expression is misregulated only in adult but not juvenile brains when MeCP2 is disrupted. The authors postulated that the gradual accumulation of mCA between birth and adolescence may provide an explanation of the late onset of Rett syndrome.

The pervasive accumulation of mCH in the adult brain as well as in pluripotent stem cells suggests the possibility that, in addition to MeCP2, other proteins not yet identified may bind to mCAC and mCAG, thereby mediating additional regulatory functions. Finding additional effectors or "readers" of mCH in tissues with abundant non-CG methylation will expand our understanding of the functions of this distinct epigenomic mark. We anticipate that further exploration of epigenomic mechanisms will lead to a more complete picture of the potential exceptionalism of gene regulation in the brain (*13*). ■

REFERENCES

1. H. W. Gabel *et al.*, *Nature* 10.1038/nature14319 (2015).
2. L. Chen *et al.*, *Proc. Natl. Acad. Sci. U.S.A.* **112**, 5509 (2015).
3. B. H. Ramsahoye *et al.*, *Proc. Natl. Acad. Sci. U.S.A.* **97**, 5237 (2000).
4. R. Lister *et al.*, *Nature* **462**, 315 (2009).
5. J. Zeng *et al.*, *Am. J. Hum. Genet.* **91**, 455 (2012).
6. W. Xie *et al.*, *Cell* **148**, 816 (2012).
7. R. Lister *et al.*, *Science* **341**, 1237905 (2013).
8. R. E. Amir *et al.*, *Nat. Genet.* **23**, 185 (1999).
9. K. Sugino *et al.*, *J. Neurosci.* **34**, 12877 (2014).
10. J. U. Guo *et al.*, *Nat. Neurosci.* **17**, 215 (2014).
11. T. Baubec *et al.*, *Nature* **520**, 243 (2015).
12. M. Morselli *et al.*, *eLife* **4**, 10.7554/eLife.06205 (2015).
13. T. R. Insel, S. C. Landis, F. S. Collins, *Science* **340**, 687 (2013).

10.1126/science.aac5832

ILLUSTRATION: NICOLLE R. FULLER

ATMOSPHERE

Challenges of a lowered U.S. ozone standard

Source attribution science can help areas of the U.S. west

By **Owen R. Cooper,**[1,2]* **Andrew O. Langford,**[2] **David D. Parrish,**[1,2] **David W. Fahey**[2]

At Earth's surface, ozone is an air pollutant that causes respiratory health effects in humans and impairs plant growth and productivity (*1*). The Clean Air Act (CAA) of 1970 mandates that the U.S. Environmental Protection Agency (EPA) assess the ozone standard every 5 years and revise when necessary to protect human health. With a decision expected in October 2015 as to whether the standard will be toughened, we discuss limitations of ozone and precursor observations that hinder the ability of state and local air pollution–control agencies to accurately attribute sources of ozone within their jurisdictions. Attaining a lower standard may be particularly challenging in high elevations of the western United States, which are more likely to be affected by ozone that has been transported long distances or that originated in the stratosphere.

POLICY

Understanding the origins of surface ozone is complicated by its multitude of sources. Ozone is transported to the surface from the natural reservoir in the stratosphere or produced from precursor gases [nitrogen oxides (NO_x) and volatile organic compounds] that react in the presence of sunlight. Ozone precursors have natural sources—such as vegetation, wildfires, and lightning—and are also emitted by human activity—such as combustion of fossil fuels and human-caused biomass burning.

The current primary (health-based) EPA standard is 75 parts per billion by volume (ppbv), with 227 U.S. counties, home to 123 million people, classified as not having attained the standard (www.epa.gov/airquality/greenbook/index.html). In November 2014, EPA proposed a revised primary ozone standard in the range of 65 to 70 ppbv in order to improve public health protection (*2*). The most recent ozone "design values" were used to determine whether ozone observations comply with the standard (which is based on the 3-year average of the fourth-highest daily maximum 8-hour ozone average in each year) at all EPA-approved ozone-monitoring sites (see the chart). The highest values are in large urban areas. Recent data from 2011 to 2013 reveal that 358 and 558 counties have design values that would exceed a revised ozone standard of 70 and 65 ppbv, respectively (www.epa.gov/groundlevelozone/maps.html). The good news is that ozone design values are declining because of ongoing reductions in precursor emissions resulting from regulations such as the "NO_x SIP Call," a state implementation plan that took effect across 22 eastern states in 2003, and the nationwide Tier 2 Vehicle and Gasoline Sulfur Program that began in 2004. EPA expects these emissions trends to continue through 2025 owing to already promulgated regulations (*3*).

Although ozone design values are generally declining across the United States, the trends are weakest at rural high-elevation sites in the western United States (>1.5 km above sea level) (*4*). One potential reason is greater exposure to enhanced "baseline" ozone that flows across the North Pacific Ocean or is transported downward from the lower stratosphere (*5*–*9*). Baseline ozone is transported from all upwind sources (natural and anthropogenic) before modification by recent, localized emissions; it includes aged ozone, produced many days earlier from U.S. emissions, that is returned to the United States after circling the globe. Baseline ozone can be directly observed by surface or airborne instrumentation along the West Coast or U.S. political borders and above inland regions of the western United States in air masses not influenced by recent U.S. emissions. Note that baseline ozone plumes produced from routine anthropogenic emissions outside of the United States cannot be classified as exceptional events, which are unusual exceedances of the ozone standard that EPA removes from consideration when classifying an area as having nonattainment.

Observed springtime baseline ozone 3 to 8 km above western North America has increased significantly since the 1980s and 1990s, and the trend is strongest in air masses that are transported directly from South and East Asia (*4*). High-elevation regions of the western United States are more strongly influenced by baseline ozone than locations at lower elevations, especially in springtime (*7*–*9*). However, model studies

EPA-approved ozone monitoring sites

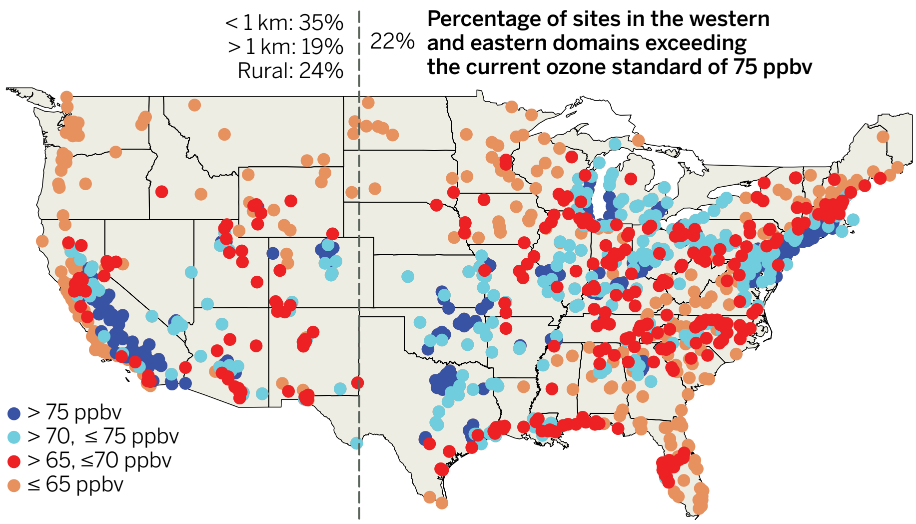

Ozone design values at all EPA ozone monitors operating during 2011–2013. The vertical dashed line separates the high-elevation regions (>1.5 km) of the west from the east. Western sites are divided into those above and below 1 km above sea level, with a separate overlapping category of rural sites. [Ozone values source: www.epa.gov/airtrends/values.html]

[1]Cooperative Institute for Research in Environmental Sciences, University of Colorado, Boulder, CO 80309, USA. [2]Chemical Sciences Division, NOAA Earth System Research Laboratory, Boulder, CO 80305, USA.
*Corresponding author. E-mail: owen.r.cooper@noaa.gov

(*10–12*) and ozone observations above the California coast (*9*) and rural Nevada (*6*) also indicate substantial baseline ozone at low-elevation rural and urban (<1.5 km) sites in the western United States.

EPA is aware of ozone variations across the western United States and has conducted targeted research for the latest ozone standard review (*1*, *3*) by focusing on the estimation of North American background ozone levels (*10*, *11*). This is ozone that would exist in the absence of any anthropogenic ozone precursor emissions from North America. Although background ozone is a large component of baseline ozone, it differs from baseline ozone because it cannot be measured by instruments but must be calculated by global-scale atmospheric chemistry–transport models. Background ozone indicates the proportion of observed North American ozone that is beyond the control of domestic air pollution–control measures; these estimates also inform U.S. air-quality managers how much domestic emissions must be reduced in order to attain the ozone standard. Although the CAA requires EPA to set the ozone standard at levels requisite to protect public health and welfare without regard to the source of the pollutant, EPA does view background ozone as an important concept to understand and quantify in developing implementation policies. Using two separate global-to-regional air-quality modeling approaches, EPA estimated that background ozone makes substantial contributions to surface ozone in the western United States (*1*, *3*). Seasonal (April to October) mean background levels ranged from 40 to 45 ppbv across much of Arizona, Colorado, Nevada, New Mexico, Utah, and Wyoming, with some individual days approaching the range of the proposed standard (i.e., 65 to 70 ppbv).

EPA has stated that "[e]xisting and upcoming EPA regulations and guidance will assist states in ensuring background ozone does not create unnecessary control obligations" (*13*). However, these mechanisms require states and EPA to be able to quantify the overall contribution and sources of background ozone. The role of scientists is to inform the decision-making by conducting research to accurately quantify background ozone. The challenges are model accuracy and limited observations of baseline ozone, which require further development and enhancement in order to improve the quantification of background ozone. A comparison of two global models shows that they differ in their estimates of monthly mean background ozone by as much as 10 ppbv and produce different seasonal cycles (*12*). Global models also have deficiencies in reproducing long-term observed ozone trends at northern mid-latitudes, which indicates the need for model improvements related to production or transport of ozone (*14*). Although the U.S. surface-ozone observation network is extensive, the observations for evaluating model estimates of surface and free troposphere baseline ozone along the 1800-km U.S. West Coast are extremely limited. There are only two measurement sites representative of marine boundary layer ozone (Trinidad Head, CA, and Cheeka Peak, WA), and two coastal mountain sites representative of lower tropospheric baseline ozone [Mt. Bachelor, OR (*15*), and Chews Ridge, CA]. The only routine ozone profiles from sea level to the stratosphere on the West Coast are made just once per week at Trinidad Head.

"Background ozone... estimates also inform U.S. air-quality managers how much domestic emissions must be reduced..."

From both scientific and regulatory points of view, a lower ozone standard will motivate air quality–control planners to seek more accurate and precise attribution of observed ozone to local, upwind, and stratospheric sources of ozone to determine how much domestic emissions must be reduced in order to attain that standard. A lower ozone standard will also increase the probability that the standard will be exceeded in springtime, which would require the attribution of ozone episodes beyond the typical summertime period of concern. Accurate quantification of background ozone under this new paradigm would require enhanced baseline ozone observations at a spatial density and temporal frequency adequate for evaluating and improving the models. Once the models can replicate baseline ozone, greater confidence can be placed in their estimates of background and locally produced ozone.

Additional observations include routine vertical ozone profiles at multiple coastal and inland sites using balloon-borne ozonesondes, ground-based ozone lidars, or, possibly, commercial aircraft. Related options include augmenting the U.S. Tropospheric Ozone Lidar Network (TOLNet), the U.S. National Oceanic and Atmospheric Administration (NOAA) Global Greenhouse Gas Reference Network aircraft program, or the European In-Service Aircraft for a Global Observing System (IAGOS). New ozone and precursor monitoring sites at inland rural locations (especially high elevation) would be useful for gauging the descent of baseline ozone from the free troposphere into the boundary layer.

These additional observations would improve detection of interannual variability (*12*) and long-term trends in baseline ozone. The observations would be used to improve the coarse-scale global models needed for the routine estimation of background ozone and precursors that are subsequently downscaled and included in the best regional air-quality models covering the United States. Along these lines, the United Nations Task Force on Hemispheric Transport of Air Pollution is evaluating multiple global- and regional-scale model estimates of baseline and background ozone across the western United States—but only for a very limited time period when sufficient observations are available. If a revised ozone standard is adopted, air quality–control programs will have a greater need to precisely and accurately attribute ozone sources on a continuous basis, and systematic and long-term efforts of scientists will be required to help identify and fill gaps in observations and modeling capabilities in coming years. ■

REFERENCES AND NOTES

1. EPA, *Policy Assessment for Ozone* (EPA-452/R-14-006, EPA, Washington, DC, 2014); www.epa.gov/ttn/naaqs/standards/ozone/s_o3_index.html.
2. Office of Air and Radiation, EPA, "National ambient air quality standards for ozone: Proposed rule." **45** Code of Federal Regulations (C.F.R.). Parts 50, 51, 52, 53, and 58 (2014).
3. EPA, *Regulatory Impact Analysis of the Proposed Revisions to the National Ambient Air Quality Standards for Ground-Level Ozone* (EPA-452/P-14-006, EPA, Washington, DC, 2014); www.epa.gov/ttn/naaqs/standards/ozone/s_o3_2008_ria.html.
4. O. R. Cooper, R.-S. Gao, D. Tarasick, T. Leblanc, C. Sweeney, *J. Geophys. Res.* **117** (D22), D22307 (2012).
5. F. Dentener, T. Keating, H. Akimoto, Eds., *Hemispheric Transport of Air Pollution 2010, Part A: Ozone and Particulate Matter, Air Pollution Studies No. 17* (United Nations, New York and Geneva, 2011).
6. A. O. Langford *et al.*, *Atmos. Environ.* **109**, 305 (2015).
7. M. Lin *et al.*, *J. Geophys. Res.* **117**(D21), 10.1029/2011JD016961 (2012). 10.1029/2011JD016961
8. M. Lin *et al.*, *J. Geophys. Res.* **117**(D21), 10.1029/2012JD018151 (2012). 10.1029/2012JD018151
9. O. R. Cooper *et al.*, *J. Geophys. Res.* **116**, D00V03 (2011).
10. L. Zhang *et al.*, *Atmos. Environ.* **45**, 6769 (2011).
11. C. Emery *et al.*, *Atmos. Environ.* **47**, 206 (2012).
12. A. M. Fiore *et al.*, *Atmos. Environ.* **96**, 284 (2014).
13. EPA, *Tools for Addressing Background Ozone* (EPA, Washington, DC, 2014); www.epa.gov/airquality/ozonepollution/pdfs/20141125fs-tools.pdf.
14. D. D. Parrish *et al.*, *J. Geophys. Res. Atmos.* **119**, 5719 (2014).
15. L. E. Gratz, D. A. Jaffe, J. R. Hee, *Atmos. Environ.* **109**, 323 (2015).

ACKNOWLEDGMENTS

The opinions expressed here are those of the authors and not their institutions. The authors acknowledge support from NOAA's Health of the Atmosphere and Atmospheric Chemistry and Climate Programs. T. Keating and G. Tonnesen, U.S. EPA, provided comments.

10.1126/science.aaa5748

BOOKS *et al.*

PALEOANTHROPOLOGY

Understanding our origins

How a long tradition of exceptionalism distorted our perception of human evolution

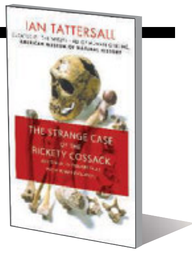

The Strange Case of the Rickety Cossack
And Other Cautionary Tales from Human Evolution
Ian Tattersall
Palgrave Macmillan, 2015. 256 pp.

By **Erika Lorraine Milam**

What would happen if, tomorrow, scientists were to rediscover the entire hominid (*1*) fossil record, without any preconceptions inherited from the last century? According to Ian Tattersall, curator emeritus of anthropology at the American Museum of Natural History (AMNH), the resulting picture of human evolution would differ dramatically from that bequeathed to today's paleontologists by their predecessors. In *The Strange Case of the Rickety Cossack*, he traces the contingencies, false starts, and diversity of opinions that have characterized the intellectual history of paleoanthropology from Darwin to today.

The Piltdown debacle from the early decades of the 20th century—in which an unknown perpetrator buried a cranium from a modern human with the mandible of a chimpanzee, leading people to believe that the remains might be an ancient British ape-man—provides Tattersall with an object lesson he repeats throughout the book. Preconceptions matter. They shape scientific ideas with as much force as fossils and facts. Piecing together skeletons from bones found in close association requires a leap of faith. This, he notes, constitutes most fossil finds, as specimens preserved in lifelike articulation are a great rarity.

Another misstep lends the book its title. Quarrymen in the mid-19th century, working in the Neander Valley outside of Düsseldorf, found an unusually shaped skull and associated bones. Pathologist Rudolf Virchow and retired physiologist August Franz Mayer postulated that they represented, not an anatomically distinct "primitive" ancestor (as claimed by Hermann Schaaffhausen, the comparative anatomist who first described the bones), but the relics of a diseased Russian horseman. New specimens discovered in subsequent decades, however, shared the same peculiar morphologies and demonstrated the error made by Virchow and Mayer.

For Tattersall, the greatest villain in the history of paleoanthropology was also one of the most respected evolutionary theorists of the century. Ernst Mayr initially made a name for himself studying the taxonomy and biogeography of living birds. In 1942, he published *Systematics and the Origin of Species* (*2*), in which he defined species as actually or potentially interbreeding populations, reproductively isolated from other related groups.

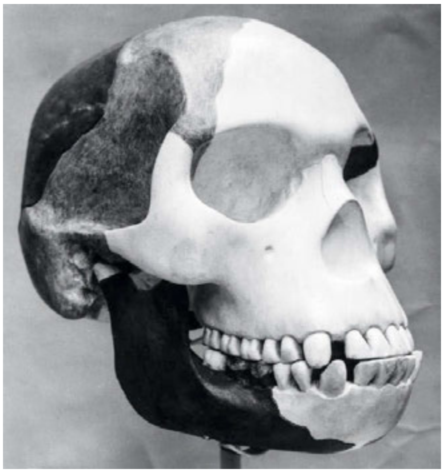

Once believed to be the remains of an early human, the "Piltdown man" was exposed as a hoax in 1953.

Reproductive isolation worked well for delimiting extant bird species but, according to Tattersall, set an impossible standard by which to judge fossils. Mayr dismissed morphology as a basis for diagnosing taxonomic relationships, yet morphological differences between specimens were all paleoanthropologists had to work with at the time.

At a conference on "The Origin and Evolution of Man" at Cold Spring Harbor Laboratory in 1950, Mayr accused the assembled paleoanthropologists of taxonomic splitting. The numerous hominid genera they had created, he argued, were not warranted. Tattersall claims that Mayr's self-assurance and theoretical heft inspired a generation of English-speaking paleoanthropologists to commit to a vision of human evolution as a "saga of a lone hero battling from primitiveness to perfection over the eons, armed with nothing but natural selection and its own wits." After World War II, this framework proved persuasive in part because it became associated with an antiracist commitment to variation within a singular, progressive human lineage.

Tattersall devotes the bulk of the book to documenting how paleoanthropologists, himself included, struggled in subsequent decades to transcend this linear account of human evolution and rethink assumptions ingrained by their own training. He describes an emerging appreciation for the widespread diversity of mostly extinct hominid genera, built on a wealth of fossil discoveries, radiocarbon and potassium-argon dating, and molecular genetic techniques.

Embedded in this larger narrative, we catch vibrant glimpses of Tattersall's own history. He spent his undergraduate years at the University of Cambridge, working with the "simultaneously intimidating and inspiring" David Pilbeam. He then earned his doctorate under the hands-off genial tutelage of Elwyn Simons in Yale's Department of Geology and Geophysics (which housed the paleontologists). By the mid-1970s, as a junior curator at the AMNH, he arrived at the Comoro Islands in search of lemurs and found political turmoil. When his interest in lemurs waned, Tattersall turned once again to human evolution. Readers follow him to Djibouti, where he hides from a "drunken gang of Yugoslav sailors" who ransacked the hotel where he was staying. These almost cinematic renderings of life behind the scenes add personal texture to his otherwise scientific chronicle.

History, Tattersall reminds us, defines who we think we are. In his retelling, this rings true both for the scientific debates and convergences that comprise his narrative and for the long, complex history of hominids that paleoanthropologists are still piecing together.

REFERENCES AND NOTES

1. Because Tattersall uses "hominid" to refer to the taxonomic group that "contains humans, plus all their extinct relatives that lived after the common ancestor," I follow the same terminological convention in this review.
2. E. Mayr, *Systematics and the Origin of Species from the Viewpoint of a Zoologist* (Columbia Univ. Press, New York, 1942).

10.1126/science.aab1020

The reviewer is at the Department of History, Princeton University, Princeton, NJ 08544, USA. E-mail: emilam@princeton.edu

ECONOMICS

Irrational actors

Embracing the mystifying choices that flummox the field of economics

By **Andrew J. Oswald**

Imagine that it is the first day of the final semester of your undergraduate studies. You have just discovered that there is a perfect clash in your scheduling: The economics course and the psychology course you need to graduate are held at the same time. You decide you have no choice but to leave halfway through every economics lecture to dash to the psychology lecture. Then imagine that you are asked to take a single final exam on what you have learned. Your exam answers turn out to be thought-provoking and wide-ranging, more canny and interesting than those given by the more conventional students, full of good ideas—sometimes muddled and inconsistent—and broader than they are deep. Welcome to behavioral economics.

Although optimistic, Richard Thaler believes that most of economics is a mess. First, it treats people as though they are cold-blooded, shrewd optimizers (think Mr. Spock from *Star Trek*). Real humans, he argues, are routinely gripped by biases and errors of passion, and it is here that conventional economic theory goes wrong. Second, it has failed to predict important events like the financial crash of the 2000s. Third, he believes that economists should spend more time on observation and fact gathering. Here, the discipline of psychology is ahead of Thaler's curve.

If you buy this book, turn initially to the last page. Here, Thaler argues that most economists stubbornly cling "to an imaginary world" and that one day it will not be necessary to have a field called behavioral economics because all of economics will fall under that heading. He is largely right. However, given the verve with which he attacks traditional economics, it is not surprising to learn that Thaler's first published article on the topic was repeatedly turned down by prestigious journals, although it later went on to become hugely cited in a then-new and

The reviewer is at the Department of Economics, University of Warwick, Coventry CV47AL, UK. E-mail: andrew.oswald@warwick.ac.uk

PHOTO: ASSOCIATED PRESS

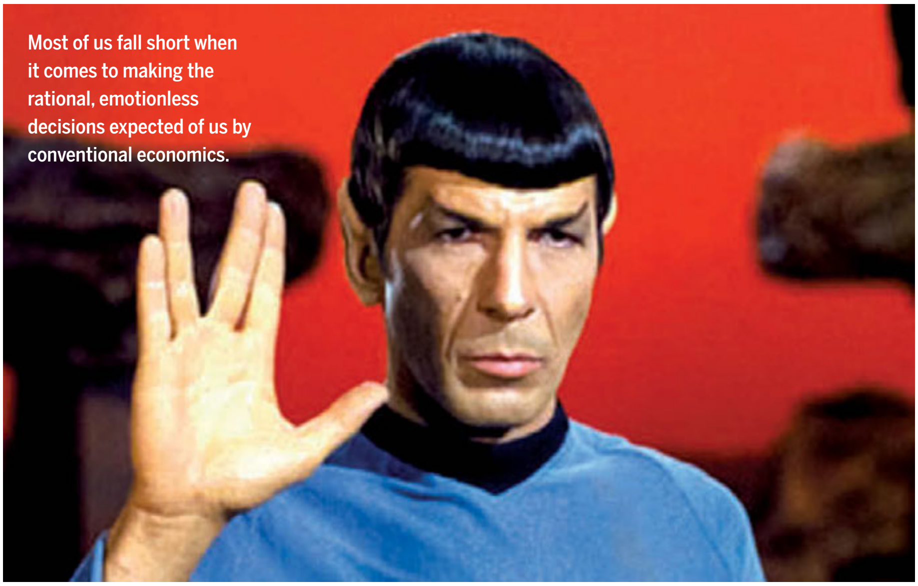

Most of us fall short when it comes to making the rational, emotionless decisions expected of us by conventional economics.

Misbehaving
The Making of Behavioral Economics
Richard H. Thaler
Norton, 2015. 431 pp.

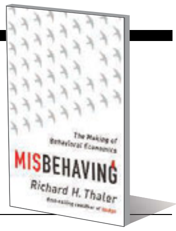

little-known journal (*1*).

According to Thaler, loss aversion—the idea that a loss hurts more than an equivalent gain—is "the single most powerful tool in the behavioral economist's arsenal." This is why, for example, firms on the verge of bankruptcy do not cut their workers' pay, even though wage cuts would arguably be the most rational choice, saving jobs and benefiting everyone involved. It explains why homeowners fruitlessly cling for years to the hope of selling their colonial for \$300,000 rather than \$280,000 and molds the behavior of scared but otherwise sensible stock market investors.

Thaler suggests that, in contrast to these real-life human behaviors, conventional economics equals optimization plus equilibrium, which, although not a meaningful equation, does actually convey the spirit of the underlying theory. He means by this that if we blend the assumption of rational decision-making (optimization) with that of stability (equilibrium), we end up with a calm, ordered world of the kind that is currently described in standard economics courses. Unfortunately, this is not the world we live in. Such an equation is hard to square with house-price booms and stock market crashes, for example.

Behavioral economics seeks to combine the best elements of the fields of psychology and economics. In his pithy and still-valuable introduction to the field in 1999 (*2*), Camerer wrote that to the typical economist, a theory is a body of mathematical tools, whereas to a psychologist, a theory is a verbal construct that organizes experimental regularity. Many psychologists use mathematical models, and I therefore do not agree with the details of this characterization, but there is something to the idea of unifying these two approaches.

If I were asked for criticisms, I might point gently to the fact that Thaler does not mention George Katona, a founding father of behavioral economics who worked three decades before Richard Thaler; nor are any of his 100 writings on the topic referenced [see selected publications (*3*, *4*); see also (*5*)]. Moreover, given that behavioral economics is meant to be the marriage of psychology and economics, one might wonder what psychologists will make of the fact that the references to economics journals vastly outnumber those to psychology journals. Apart from one brief nod to Dutch television, the book is also American-centered, in a way that may put off readers from the rest of the world's population.

Perhaps, finally, the book might have been even more cogent and rounded if it had explained that battles between scholars over a theoretical framework that does not fit the observed facts are normal in science. Viewed from a distance, nothing unusual is going on in modern economics. It is bending to the data. The tetchiness, howls, and misbehavior of those whose ideas are out of date are just what has been happening for centuries in other disciplines. Scientific progress hurts.

REFERENCES

1. R. H. Thaler, *J. Econ. Behav. Organ.* **1**, 39 (1980).
2. C. Camerer, *Proc. Natl. Acad. Sci. U.S.A.* **96**, 10575 (1999).
3. G. Katona, *J. Am. Stat. Assoc.* **42**, 449 (1947).
4. G. Katona, *Psychol. Rev.* **60**, 307 (1953).
5. K.-E. Wärneryd, *J. Econ. Psychol.* **2**, 1 (1982).

10.1126/science.aab1365

Published by AAAS

LETTERS

Edited by **Jennifer Sills**

Editor's note

ON 20 MAY, in response to questions about the validity of the methods and data in the 2014 Report by M. J. LaCour and D. P. Green, *Science* published online an Editorial Expression of Concern on the Report. On 28 May, *Science* released online an Editorial Retraction of the paper. Articles first published online are typically published in print a few weeks after online posting. Because of the rapid chain of events in this case, both the Editorial Retraction and the Editorial Expression of Concern are printed here. The Editorial Retraction is *Science*'s final decision on this paper and supersedes the earlier Editorial Expression of Concern.

Marcia McNutt
Editor-in-Chief

Editorial retraction

SCIENCE, WITH THE concurrence of author Donald P. Green, is retracting the 12 December 2014 Report "When contact changes minds: An experiment on transmission of support for gay equality" by LaCour and Green (*1*).

The reasons for retracting the paper are as follows: (i) Survey incentives were misrepresented. To encourage participation in the survey, respondents were claimed to have been given cash payments to enroll, to refer family and friends, and to complete multiple surveys. In correspondence received from Michael J. LaCour's attorney, he confirmed that no such payments were made. (ii) The statement on sponsorship was false. In the Report, LaCour acknowledged funding from the Williams Institute, the Ford Foundation, and the Evelyn and Walter Haas Jr. Fund. Per correspondence from LaCour's attorney, this statement was not true.

In addition to these known problems, independent researchers have noted certain statistical irregularities in the responses (*2*). LaCour has not produced the original survey data from which someone else could independently confirm the validity of the reported findings.

Michael J. LaCour does not agree to this Retraction.

Marcia McNutt
Editor-in-Chief

REFERENCES

1. M. J. LaCour, D. P. Green, *Science* **346**, 1366 (2014).
2. D. Broockman, J. Kalla, P. Aronow, "Irregularities in LaCour (2014)" (2015); http://stanford.edu/~dbroock/broockman_kalla_aronow_lg_irregularities.pdf.

Published online 28 May 2015
DOI: 10.1126/science.aac6638

Editorial expression of concern

IN THE 12 December 2014 issue, *Science* published the Report "When contact changes minds: An experiment on transmission of support for gay equality" by Michael J. LaCour and Donald P. Green (*1*). On 19 May 2015, author Green requested that *Science* retract the paper because of the unavailability of raw data and other irregularities that have emerged in the published paper. *Science* is urgently working toward the appropriate resolution, while ensuring that a fair process is followed. In the meantime, *Science* is publishing this Editorial Expression of Concern to alert our readers to the fact that serious questions have been raised about the validity of findings in the LaCour and Green paper.

Marcia McNutt
Editor-in-Chief

REFERENCE

1. M. J. LaCour, D. P. Green, *Science* **346**, 1366 (2014).

Published online 20 May 2015
DOI 10.1126/science.aac6184

Antibiotics crisis in China

Antibiotics have been found in pork in China.

PHOTO: LI BIN/IMAGINECHINA/AP IMAGES

THE EMERGENCE OF antibiotic-resistant pathogens has become a global public health crisis. A new and serious crisis is emerging in China: Antibiotics have polluted the food and drinking water supply. Antibiotics are detectable in the residential tap water of Chinese homes (*1*). Urban water supplies present multiclass antibiotic residues, including those of fluoroquinolones (broad-spectrum antibiotics whose use is discouraged except in treating serious bacterial infections). Antibiotic residues have been found in foods, including pork (*2*), aquatic products (*3*), vegetables (*4*), and milk (*5*). For instance, the Shanghai Food and Drug Administration found 7.7% of aquatic products to be unacceptable for human consumption because of antibiotic residues (*6*). Antibiotic residues are also found in vegetable samples, especially those grown in manure-amended soil (*7*). In one study, 47% of raw milk samples from 10 provinces of China were found positive for antibiotic residues (*5*).

At least three factors are responsible for this new antibiotic-related crisis in China. First, the country is the largest producer and consumer of antibiotics, reaching about 210,000 tons of antibiotics annually (*8*). Antibiotics are misused and discharged into the environment, where they pollute crop-producing soil and groundwater and rivers that are sources of drinking water, such as the Yangtze River (*7*). Second, an important source of antibiotics in food is antibiotic residues present in the agricultural and livestock industries (*9*). In China, about 97,000 tons of antibiotics [46% of all antibiotics used in the country (*8*)] are used in its livestock to prevent disease and improve production (*8*). In addition to residues present in livestock food products, misuse of antibiotics results in 29,000 to 87,000 tons of antibiotic residues annually in livestock waste, which is used as manure soil amendment for crop production, thereby causing contamination of agricultural products with antibiotics (*10*). Third, a main reason for this emerging crisis is the lack of effective supervision over the production, use, and disposal of antibiotics. For instance, one of

Published by AAAS

the largest antibiotic-producing manufacturers in China was found to be secretly discharging antibiotic-containing sewage, increasing the antibiotic concentration in nearby rivers to 10,000 times that of uncontaminated rivers (*1*).

Effective measures are urgently needed to control the antibiotic-related crisis in China while it is still at an early stage. It is important to control the sources of antibiotic pollution through prohibiting nontherapeutic use of antibiotics in the livestock industry and the arbitrary discharge of wastewater containing antibiotics. China should also establish more effective systems through strengthening the enforcement of its regulations to monitor and evaluate the safety and adverse reactions of food and drugs, including veterinary pharmaceuticals. Moreover, it is necessary to develop safer food additive products, as well as improve veterinary vaccines so as to eliminate the use of antibiotics in animal feed.

Rongzhang Hao, Rongtao Zhao, Shaofu Qiu, Ligui Wang, Hongbin Song*

Institute of Disease Control and Prevention, Academy of Military Medical Sciences, Beijing 100071, China.

*Corresponding author.
E-mail: hongbinsong@263.net

REFERENCES

1. L. Sha, *Global Times*, "High levels of antibiotics in China's rivers" (2014); www.globaltimes.cn/content/898705.shtml.
2. Q. Wang *et al*., *Food Addit. Contam. Part A Chem. Anal. Control Expo. Risk Assess.* **31**, 1177 (2014).
3. F. Y. Hu *et al*., *J. Chromatogr. B Analyt. Technol. Biomed. Life Sci.* **79**, 949 (2014).
4. B. Chen *et al*., *J. AOAC Int.* **95**, 523 (2012).
5. N. Zheng *et al*., *Food Addit. Contam. Part B Surveill.* **6**, 84 (2013).
6. Z. Lin, "Shanghai: 13 batches of substandard fish on the shelf involve a number of large supermarkets," Xinhua (2014); http://news.ifeng.com/a/20141231/42838674_0.shtml [in Chinese].
7. X. Hu, Q. Zhou, Y. Luo, *Environ. Pollut.* **158**, 2992 (2010).
8. Y. G. Zhu *et al*., *Proc. Natl. Acad. Sci. U.S.A.* **110**, 3435 (2013).
9. N. Wang *et al*., *J. Environ. Sci. Health B* **49**, 468 (2014).
10. L. Zhao, Y. H. Dong, H. Wang, *Sci. Total Environ.* **408**, 1069 (2010).

TECHNICAL COMMENT ABSTRACTS

Comment on "Human-like hand use in *Australopithecus africanus*"

Sergio Almécija, Ian J. Wallace, Stefan Judex, David M. Alba, Salvador Moyà-Solà

Skinner and colleagues (Research Article, 23 January 2015, p. 395), based on metacarpal trabecular bone structure, argue that *Australopithecus africanus* employed human-like dexterity for stone tool making and use 3 million years ago. However, their evolutionary and biological assumptions are misinformed, failing to refute the previously existing hypothesis that human-like manipulation preceded systematized stone tool manufacture, as indicated by the fossil record.

Full text at http://dx.doi.org/10.1126/science.aaa8414

Response to Comment on "Human-like hand use in *Australopithecus africanus*"

Matthew M. Skinner, Nicholas B. Stephens, Zewdi J. Tsegai, Alexandra C. Foote, N. Huynh Nguyen, Thomas Gross, Dieter H. Pahr, Jean-Jacques Hublin, Tracy L. Kivell

Almécija and colleagues claim that we apply a simplified understanding of bone functional adaptation and that our results of human-like hand use in *Australopithecus africanus* are not novel. We argue that our results speak to actual behavior, rather than potential behaviors, and our functional interpretation is well supported by our methodological approach, comparative sample, and previous experimental data.

Full text at http://dx.doi.org/10.1126/science.aaa8931

TECHNICAL COMMENT

HUMAN EVOLUTION

Comment on "Human-like hand use in *Australopithecus africanus*"

Sergio Almécija,[1,2,3]* Ian J. Wallace,[4] Stefan Judex,[5] David M. Alba,[3] Salvador Moyà-Solà[6]

Skinner and colleagues (Research Article, 23 January 2015, p. 395), based on metacarpal trabecular bone structure, argue that *Australopithecus africanus* employed human-like dexterity for stone tool making and use 3 million years ago. However, their evolutionary and biological assumptions are misinformed, failing to refute the previously existing hypothesis that human-like manipulation preceded systematized stone tool manufacture, as indicated by the fossil record.

Skinner *et al.* (*1*) analyze metacarpal trabecular bone structure in the 3-million-year-old hominin *Australopithecus africanus* and infer based on these data that this taxon "was capable of habitual and forceful human-like opposition of the thumb and fingers during [...] tool-related behaviors, providing morphological evidence of committed tool use in a hominin hitherto considered not to be capable of these behaviors" (*1*). Specifically, they found that the trabecular organization of the pollical metacarpal of *A. africanus* is, in some respects, more human-like than chimpanzee-like, which they interpret as "morphological evidence…that can be linked to behavior and hand use during life" (*1*), with clear allusions to stone tool making and use throughout the article. Although we appreciate their effort to investigate a novel aspect of fossil morphology like trabecular structure, we note here limitations in the proposed evolutionary importance of their findings, which together with misinformed assumptions about bone mechanobiology make many of their conclusions unwarranted. We hope that the concerns that we raise will help promote a constructive discussion dealing with the complex topic of the relationships between form and function and redirect future research studies in human evolution.

It is well known that, like humans, all living great apes make and use tools, and some chimpanzees and capuchin monkeys even engage in regular stone tool use (*2*). Humans, however, display especially advanced manual dexterity facilitated by a unique (among modern hominoids) type of interaction between the proximal pulps of our thumb and fingers (*3*). The primary anatomical requirement for this pad-to-pad precision grasping is having a long thumb relative to finger lengths (*3–5*). Previous analyses of hand bone morphology in australopiths (*4*, *6–8*) and the Miocene hominin *Orrorin* (*5*) have provided compelling evidence for pad-to-pad precision grasping before the widespread occurrence of flaked stone tools, which indicates that a basic human-like hand structure is plesiomorphic for modern humans (Fig. 1). The emerging evolutionary picture is that increased reliance on bipedalism and enhanced manipulation were very early apomorphies of the hominin lineage, as a part of our original adaptive shift from apes in relation to new foraging strategies (*5*, *7*). Thus, the eventual application of human-like hand structure to stone tool flaking and use was almost certainly an exaptation, not an adaptation (*4*). In this light, the inference by Skinner *et al.* of human-like hand use among australopiths is neither unprecedented nor unexpected.

Skinner *et al.* downplay previous evidence for human-like hand use among australopiths by arguing that because earlier studies were focused exclusively on external (cortical) bone features, they do not necessarily provide insight into how hominins were actually using their hands during life. As they see it, "external morphology can be ambiguous, as some features can be retentions from the ancestral condition and may not be functionally important" (*1*). The structure of internal trabecular bone, they argue, is a truer reflection of in vivo loading than cortical structure and less influenced by nonmechanical factors such as phylogeny. This claim is based on a simplified account of bone functional adaptation that trabecular remodeling throughout life is optimized to add and preserve bone where loading occurs and resorb bone where it does not. However, it is important to recognize that trabecular structure alone has little bearing on individual capacity to achieve human-like hand grips. In fact, no type of trabecular organization will enable an individual to attain human-like grips if the external morphology of their hand bones does not permit it. Therefore, Skinner and colleagues' conclusions rely on the circular reasoning that the external morphology of australopith hands actually allowed human-like grips, which weakens the basic premise of their study that trabecular structure is a more informative signal than external features.

Furthermore, Skinner *et al.*'s interpretation of trabecular bone functional adaptation is problematic for at least three reasons. First, while trabecular bone clearly can respond to mechanical signals, loads must be dynamic to be osteogenic (*9*). Relatively static loads associated with tool grasping [like those shown for the pollical metacarpal in figure 1 in (*1*)] have not been associated with enhanced trabecular morphology, independent of the magnitude of the applied force. Second, there is little evidence that trabecular bone is less influenced by genetics, or more influenced by loading, than cortical bone. Heritability estimates for trabecular density in humans range between 59 and 73%, whereas estimates for cortical density are between 17 and 42% [see references in (*10*)]. Moreover, human studies have shown that cortical morphology of weight-bearing elements scales far better with body mass (a proxy for mechanical loading) than trabecular architecture [e.g., (*11*)]. Third, if trabecular organization indeed correlates strongly with predicted loading conditions, then this should be evident throughout the skeleton, especially in weight-bearing elements. However, numerous previous attempts to identify functional loading signals in the trabecular structure of weight-bearing elements in humans and other primates have most often been unsuccessful (*12*). Thus, why mechanical signals induced by object manipulation should be uniquely discernible in hominin pollical metacarpals is unclear. Skinner *et al.* base their conclusions on their previous comparative analysis of trabecular structure in the hominoid third metacarpal (*13*). However, this analysis was unable to separate humans from gibbons or orangutans [figure 4 in (*13*)], and it failed to provide any direct evidence that observed differences between taxa were actually due to variation in lifetime mechanical loading. Inherently, extrapolating from this potentially phylogenetically dependent correlation in the third metacarpal to all metacarpals renders the conclusions of Skinner *et al.* even more speculative.

Nevertheless, even if one assumes that metacarpal trabecular structure closely reflects lifetime loading, Skinner *et al.*'s comparative evidence linking form to function is limited. Although the authors found that "[d]ifferences in the distribution of trabecular bone across apes and humans were also found in Mc3 and Mc5" (*1*), their pairwise comparisons [table S3 in (*1*)] indicate that this is only true for the fifth metacarpal head, for which no australopiths were sampled [table 1 in (*1*)]. For the third metacarpal head, differences in trabecular organization were only found between humans and African apes [table S3 in

[1]Department of Anatomical Sciences, Stony Brook University, Stony Brook, NY 11794, USA. [2]Center for the Advanced Study of Human Paleobiology, Department of Anthropology, The George Washington University, Science and Engineering Hall, 800 22nd Street NW, Washington, DC 20052, USA. [3]Institut Català de Paleontologia Miquel Crusafont, Universitat Autònoma de Barcelona, Edifici ICTA-ICP, Carrer de les Columnes s/n, Campus de la UAB, 08193 Cerdanyola del Vallès, Barcelona, Spain. [4]Department of Anthropology, Stony Brook University, Stony Brook, NY 11794, USA. [5]Department of Biomedical Engineering, Stony Brook University, Stony Brook, NY 11794, USA. [6]ICREA at Institut Català de Paleontologia Miquel Crusafont and Unitat d'Antropologia Biològica (Departament BABVE), Universitat Autònoma de Barcelona, Edifici ICTA-CP, Carrer de les Columnes s/n, Campus de la UAB, 08193 Cerdanyola del Vallès, Barcelona, Spain.
***Corresponding author. E-mail: sergio.almecija@gmail.com**

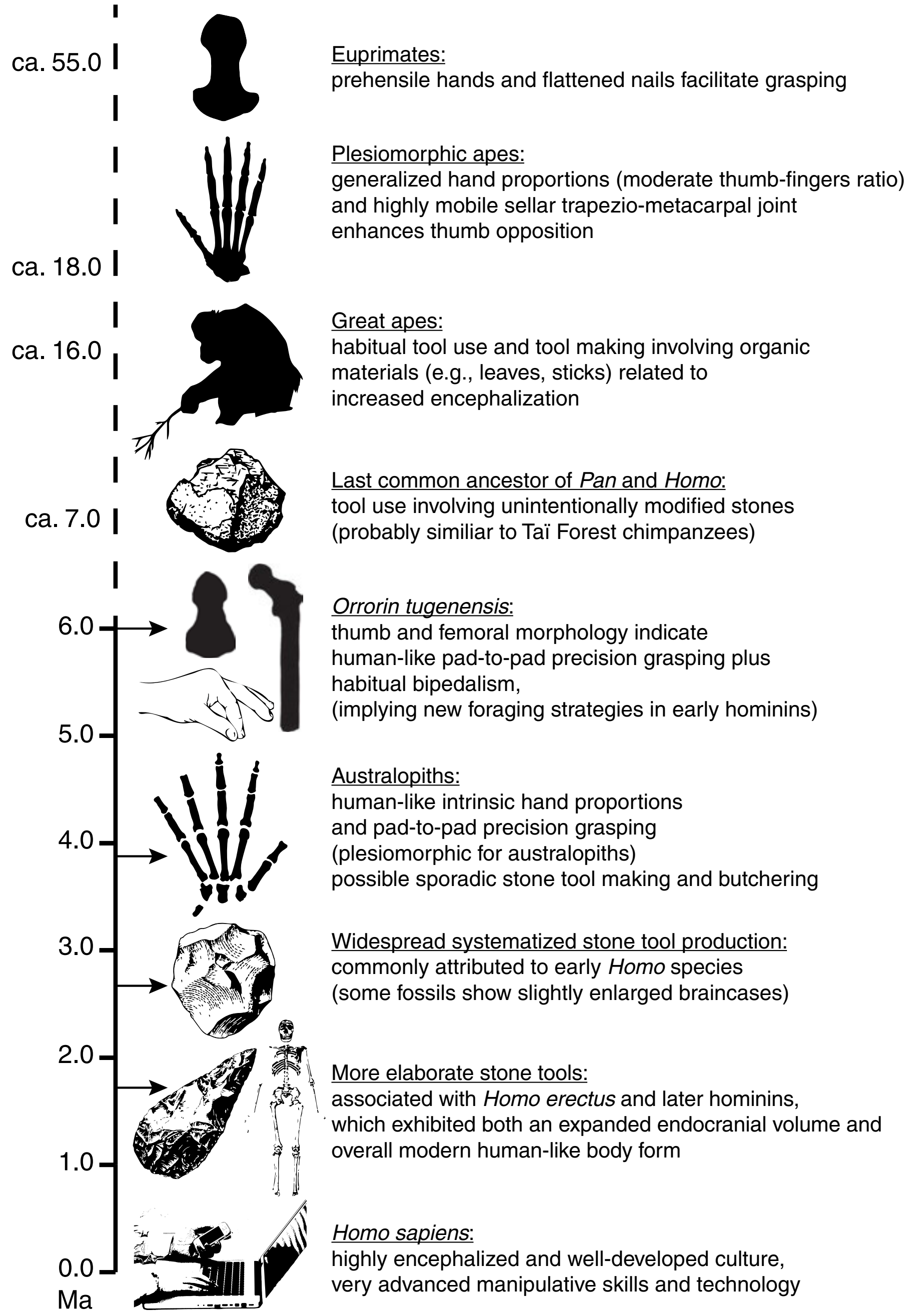

Fig. 1. Simplified timeline showing major evolutionary advents in human manipulative capabilities. The fossil record indicates that the story of human advanced manipulation has very early origins, predating the widespread appearance of systematized flaked stone tool manufacture. Basic human-like hand proportions allowing for refined manipulation have been inferred in *Orrorin* and all australopith species and confirmed by the virtually complete hand of *Australopithecus sediba*. The morphological results of Skinner *et al*. merely support these previous findings. Ma, million years ago.

(*1*)], with *A. africanus* showing values closer to apes than humans. Ultimately, Skinner *et al.*'s numerical results support human-like hand use in *A. africanus* based only on certain similarities with the trabecular pattern of the pollical metacarpal base of humans as compared to chimpanzees. In our opinion, it is overly risky to draw profound conclusions about hominin paleobiology based solely on a comparative sample of two taxa (*Pan* versus *Homo*). It is noteworthy that a previous inference (*14*) of australopith stone tool manufacture based on pollical metacarpal external morphology that relied on a comparative sample of only chimpanzees and humans was no longer supported once gorillas were included in the analysis [i.e., gorillas were similar to hominins (*15*)]. A more credible test relating pollical metacarpal trabecular structure to manipulative behaviors would incorporate not only gorillas (as they did with rays three and five) but also other primates with dexterous hands like *Theropithecus* (specialized forager) or the Taï Forest chimpanzees and *Cebus* (stone tool users). Such a strategy would permit evaluation of whether the observed morphological signatures of Skinner *et al.* are ecophenotypic (as they argue) instead of merely representing a hominin phylogenetic signal.

Ultimately, the results of Skinner *et al.*, far from demonstrating strong evidence of stone tool manufacture and use among australopiths, support previous observations reached on the basis of external morphology that australopith hands were, in some ways, more similar to those of humans than to apes, and thus were likely capable of human-like manipulation (*4*–*8*). However, this does not mean that human hands evolved for the sole purpose of making and using stone tools, for which cognitive capabilities should be also considered, as Napier and others indicated before (*3*).

Note added in proof: The recently described lithic artifacts from Lomekwi 3, northwestern Kenya, are claimed to represent the earliest evidence of intentional stone tool production at 3.3 Ma [S. Harmand *et al.* (*16*)]. This discovery is consistent with human-like manual dexterity being an ancient adaptation among hominins. Even so, as Harmand *et al.* argue, and in agreement with our view, the decisive adaptation enabling "Lomekwian" stone knapping (to yet-unidentified hominins) was likely neurological.

REFERENCES AND NOTES

1. M. M. Skinner *et al.*, *Science* **347**, 395–399 (2015).
2. M. A. Panger, A. S. Brooks, B. G. Richmond, B. Wood, *Evol. Anthropol.* **11**, 235–245 (2002).
3. J. Napier, *Nature* **196**, 409–411 (1962).
4. D. M. Alba, S. Moyà-Solà, M. Köhler, *J. Hum. Evol.* **44**, 225–254 (2003).
5. S. Almécija, S. Moyà-Solà, D. M. Alba, *PLOS ONE* **5**, e11727 (2010).
6. D. J. Green, A. D. Gordon, *J. Hum. Evol.* **54**, 705–719 (2008).
7. S. Almécija, D. M. Alba, *J. Hum. Evol.* **73**, 88–92 (2014).
8. T. L. Kivell, J. M. Kibii, S. E. Churchill, P. Schmid, L. R. Berger, *Science* **333**, 1411–1417 (2011).
9. T. Sugiyama, J. S. Price, L. E. Lanyon, *Bone* **46**, 314–321 (2010).
10. L. M. Yerges *et al.*, *J. Bone Miner. Res.* **25**, 330–338 (2010).
11. J. D. Schipilow, H. M. Macdonald, A. M. Liphardt, M. Kan, S. K. Boyd, *Bone* **56**, 281–289 (2013).
12. C. N. Shaw, T. M. Ryan, *Am. J. Phys. Anthropol.* **147**, 187–200 (2012).
13. Z. J. Tsegai *et al.*, *PLOS ONE* **8**, e78781 (2013).
14. R. L. Susman, *Science* **265**, 1570–1573 (1994).
15. W. C. McGrew *et al.*, *Science* **268**, 586–589 (1995).
16. S. Harmand *et al.*, *Nature* **521**, 310–315 (2015).

ACKNOWLEDGMENTS

We thank M. Skinner, T. Kivell, and their coauthors for their willingness to contribute to a collegial discussion on this interesting (although complex) topic.

8 February 2015; accepted 19 March 2015
10.1126/science.aaa8414

TECHNICAL RESPONSE

HUMAN EVOLUTION

Response to Comment on "Human-like hand use in *Australopithecus africanus*"

Matthew M. Skinner,[1,2,3,4]* Nicholas B. Stephens,[3] Zewdi J. Tsegai,[3] Alexandra C. Foote,[2] N. Huynh Nguyen,[3] Thomas Gross,[5] Dieter H. Pahr,[5] Jean-Jacques Hublin,[3] Tracy L. Kivell[1,3,4]*

Almécija and colleagues claim that we apply a simplified understanding of bone functional adaptation and that our results of human-like hand use in *Australopithecus africanus* are not novel. We argue that our results speak to actual behavior, rather than potential behaviors, and our functional interpretation is well supported by our methodological approach, comparative sample, and previous experimental data.

Almécija *et al.* (*1*) challenge our conclusions on three points: (i) we do not give sufficient credence to published studies on the external morphology of australopith hand bones that are consistent with precision grip capabilities; (ii) we overstate the evidence for a form-function signal in trabecular bone; and (iii) our comparative sample and analyses do not support differences in trabecular patterning between humans and extant apes. Their critique suffers from a lack of recognition that (i) our study provides evidence for hand postures actually adopted by australopiths, rather than those they were potentially capable of; (ii) we base our conclusions on the three-dimensional distribution of trabecular bone throughout the epiphysis rather than on particular measures of subregions of trabecular structure; and (iii) our comparative sample, which includes stone tool–using Taï chimpanzees, indicates that humans have a distinctive trabecular pattern that is shared with Neandertals and *Australopithecus africanus* (*2*).

We do not claim that our results "refute the previously existing hypothesis that human-like manipulation preceded systematized stone tool manufacture" (*1*); to the contrary, we state that our results are consistent with the use of "forceful hand grips for any number of manipulative behaviors" (*2*). Almécija *et al.* (*1*) refer to previous studies (mainly their own) based on the relative lengths and external morphology of hand bones that "have provided compelling evidence for pad-to-pad precision grasping before the widespread occurrence of flaked stone tools" (*1*) and that australopiths and earlier hominins "were likely capable of human-like manipulation" (*1*). We agree; however, Almécija *et al.* (*1*) fail to acknowledge that our results are novel because they reflect (i) actual behavior, rather than the capability for particular behaviors and (ii) forceful pad-to-pad precision grasping, which is what separates human dexterity from that of other primates (*3*). The asymmetric distribution of trabecular bone within the base of the thumb and metacarpal heads in humans, Neandertals, and *A. africanus* (and the absence of this pattern in apes) provides evidence for habitual, forceful opposition of the thumb to the fingers. We agree that inferences for human-like hand use among australopiths referred to by Almécija *et al.* are neither "unprecedented nor unexpected" (*1*). However, the inferences we can now make, based on the trabecular bone distribution and the well-accepted concept that trabeculae remodel in response to habitual load during an individual's lifetime (*4*, *5*), are much stronger than they and others have been able to make based on external morphology of hand bones alone.

Almécija *et al.* (*1*) also take issue with our statement that "external morphology can be ambiguous, as some features can be retentions from the ancestral condition and may not be functionally important" (*2*). This is an often-recognized, fundamental problem of any researcher trying to reconstruct behavior in the past in palaeoanthropology (*6*) and beyond (*7*), and we stand by this assertion. Their claim that we suggest that "trabecular organization will enable an individual to attain human-like grips" (*1*) is simply incorrect. Clearly, the range of motion of each finger and thumb and the possibilities for their relative positions during manipulation are largely dictated by the size and shape of the bones themselves, as well as soft tissues, and not by trabecular bone. We assert that the trabecular pattern indicates whether or not individual australopiths were actually adopting these grips with enough force to maintain an appropriate distribution of trabecular bone [i.e., a physiological adaptation, *sensu* (*8*)].

Almécija *et al.* (*1*) highlight three reasons that our interpretation of trabecular bone functional adaption is problematic. First, they note that trabecular bone remodels under dynamic loads and not static loads, such as when one is "tool grasping" (*1*). Not only does experimental evidence show that gripping force varies during static holding, and thus that loads experienced by the hand are dynamic (*9*), but when one uses an object, gripping force will fluctuate throughout the duration of the task (*10*, *11*).

Second, they claim that "there is little evidence that trabecular bone is less influenced by genetics, or more influenced by loading, than cortical bone" (*1*). The authors ignore substantial experimental evidence that trabecular bone structure can adapt to longer-term (i.e., minimum 8 to 10 weeks) cyclic loading [e.g., (*4*, *5*)] and appears to do so better than cortical bone (*12*). Indeed, one of the authors themselves has recently used trabecular bone to infer function in fossil hominins (*13*).

Third, they claim that the failure of previous studies to find a strong link between trabecular structure and inferred patterns of loading weakens our argument. These previous studies examine a volume of interest within the epiphysis and quantify characteristics of trabecular structure such as the ratio of bone volume to total volume (BV/TV), trabecular spacing, or trabecular number. Our analysis differs from these studies in that we quantify the distribution of BV/TV throughout the entire epiphysis, and the key finding of our study is based not on the "density" of trabecular bone but on its relative distribution throughout the epiphyses. This includes the distribution of trabeculae just beneath the articular joint surface, where joint reaction forces are initially incurred, which allows us to infer the joint position during predominant loading.

Finally, Almécija *et al.* (*1*) suggest that a lack of differences in pairwise comparisons in BV/TV in the third metacarpal (Mc3) between humans and Asian apes weakens our argument for a link between form and function. Unfortunately, they are conflating two sets of results: those for average BV/TV throughout the epiphysis and the distribution of trabecular bone throughout the epiphysis. Furthermore, we acknowledge the shared high BV/TV values between *Pan* and *A. africanus*, suggesting that this may reflect that "the hands of these early hominins may still be used for arboreal locomotion" (*2*). Contrary to Almécija *et al.*'s (*1*) claim, our comparative sample does include tool-using Taï chimpanzees [*Pan troglodytes verus*; original table S1 (*2*)], and their metacarpals do not show any similarity to the trabecular distribution found in humans, Neandertals, and *A. africanus*. We agree that examining other nonhuman primates is likely to further elucidate links between hand use and trabecular structure, but the limited trabecular bone in the epiphyses of smaller-bodied hominoids and

[1]School of Anthropology and Conservation, University of Kent, Canterbury CT2 7NR, UK. [2]Department of Anthropology, University College London, London WC1H 0BW, UK. [3]Department of Human Evolution, Max Planck Institute for Evolutionary Anthropology, Deutscher Platz 6, 04103 Leipzig, Germany. [4]Evolutionary Studies Institute and Centre for Excellence in PalaeoSciences, University of the Witwatersrand, Private Bag 3, Wits 2050, South Africa. [5]Institute of Lightweight Design and Structural Biomechanics, Vienna University of Technology, Gusshausstrasse 27-29, 1040 Wien, Vienna, Austria.
***Corresponding author. E-mail: m.skinner@kent.ac.uk (M.M.S.); t.l.kivell@kent.ac.uk (T.L.K.)**

monkeys (*14*) suggests caution in applying either our method or traditional volume-of-interest approaches to broad comparative samples. For example, hylobatids have very few trabecular struts in their hand bone epiphyses. This yields similar average BV/TV values in hylobatids and humans, as Almécija *et al.* (*1*) highlight, even though the trabecular structure itself is very different between the two taxa.

Based on our understanding of Almécija and colleagues' (*1*) critique, we see no reason to alter the conclusions of our study (*2*). Although we agree that such forceful human-like grips could have been used for various manipulative behaviors, experimental evidence suggests that tool use and tool production [albeit current studies (*10*, *11*) are biased toward these behaviors] induce some of the highest nonlocomotor loading on the hands. Thus, it is parsimonious, based on current evidence, to conclude that these hand grips (forceful precision and power squeeze) were adopted during tool use (be it of wood, bone, or stone), and this derived, human-like pattern is consistent with evidence for stone flake use by *A. afarensis* (*15*). Future analyses of trabecular structure in earlier hominins may indeed reveal that such forceful precision grips were actually used long before evidence of tool use, supporting the claims of Almécija *et al.* (*1*), but until then, such gripping behaviors can only be considered a potential capability.

Note added in proof: Recently described pre-Oldowan stone tools from Kenya, named the Lomekwian [S. Harmand *et al.* (*16*)], are relevant to this discussion and particularly interesting, as they occur at least 0.5 Ma before the appearance of the genus *Homo*. The large size of hammers, anvils, and flakes that characterize the Lomekwian are suggestive of considerable loading of the thumb and fingers during flake production, and this is consistent with our evidence for high BV/TV and the distribution of trabecular bone in the base of the thumb consistent with forceful precision grips in *Australopithecus*. Biomechanical analyses of hand loading during simulated Lomekwian tool production would shed light on potential links between this behavior and the patterns of trabecular bone distribution in the hands of pre-*Homo* hominins.

REFERENCES AND NOTES

1. S. Almécija, I. J. Wallace, S. Judex, D. M. Alba, S. Moyà-Solà, *Science* **348**, 1101 (2015).
2. M. M. Skinner *et al.*, *Science* **347**, 395–399 (2015).
3. M. W. Marzke, *Am. J. Phys. Anthropol.* **102**, 91–110 (1997).
4. M. M. Barak, D. E. Lieberman, J.-J. Hublin, *Bone* **49**, 1141–1151 (2011).
5. F. M. Lambers *et al.*, *Bone* **55**, 325–334 (2013).
6. C. V. Ward, *Am. J. Phys. Anthropol.* **119** (suppl. 35), 185–215 (2002).
7. J. G. M. Thewissen, S. T. Hussain, M. Arif, *Science* **263**, 210–212 (1994).
8. W. J. Bock, G. von Wahlert, *Evolution* **19**, 269–299 (1965).
9. T. Sugiyama, J. S. Price, L. E. Lanyon, *Bone* **46**, 314–321 (2010).
10. C. Rolian, D. E. Lieberman, J. P. Zermeno, *J. Hum. Evol.* **61**, 26–41 (2011).
11. E. M. Williams, A. D. Gordon, B. G. Richmond, *J. Hum. Evol.* **62**, 520–532 (2012).
12. I. J. Wallace, S. Gupta, J. Sankaran, B. Demes, S. Judex, *J. Anat.* **226**, 224–228 (2015).
13. A. Su, I. J. Wallace, M. Nakatsukasa, *J. Hum. Evol.* **64**, 667–677 (2013).
14. Z. J. Tsegai *et al.*, *PLOS ONE* **8**, e78781 (2013).
15. S. P. McPherron *et al.*, *Nature* **466**, 857–860 (2010).
16. S. Harmard *et al.*, *Nature* **521**, 310–315 (2015).

ACKNOWLEDGMENTS

We thank the authors for raising these issues and their collegial discussion of this complex topic. This research is supported by the Max Planck Society (M.M.S., T.L.K., N.B.S., Z.J.T., and J.-J.H) and the European Research Council Starting Grant 336301 (T.L.K. and M.M.S.).

24 February 2015; accepted 19 March 2015
10.1126/science.aaa8931

RESEARCH

High resolution cryo–electron microscopy within sight

Bartesaghi et al., *p. 1147*

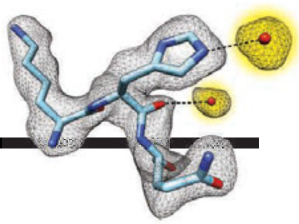

IN *SCIENCE* JOURNALS

Edited by **Stella Hurtley**

Honey bees (*Apis mellifera*) form complex societies

SOCIAL EVOLUTION

For bees, many roads lead to social harmony

Eusociality, where workers sacrifice their reproductive rights to support the colony, has evolved repeatedly and represents the most evolved form of social evolution in insects. Kapheim *et al.* looked across the genomes of 10 bee species with varying degrees of sociality to determine the underlying genomic contributions. No one genomic path led to eusociality, but similarities across genomes were seen in features such as increases in gene regulation and methylation. It also seems that selection pressures relaxed after the emergence of complex sociality. — SNV

Science, this issue p. 1139

HUMAN OOCYTES

Earliest stages of human development revealed

Most of our knowledge about meiosis in mammalian oocytes stems from studies of mouse oocytes. However, chromosome segregation in mouse oocytes is much more reliable than in human oocytes. Working with the clinic that first pioneered IVF, Holubcová *et al*. studied freshly harvested human oocytes. They used high-resolution fluorescence microscopy to watch more than 100 human oocytes as they went through each step of meiosis. — SMH

Science, this issue p. 1143

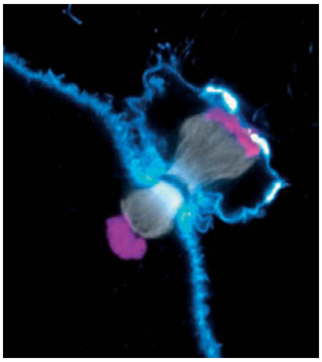

Human meiosis in living color

NITROGEN CYCLING

More N_2O is no laughing matter

Because N_2O is a potent greenhouse gas, tracking its sources and sinks—including those from natural processes—is imperative. Babbin *et al*. developed an isotopic tracer method to measure biological N_2O reduction rates directly in the Eastern Tropical North Pacific Ocean. Incomplete denitrification results in the rapid cycling and net accumulation of N_2O. As oxygen minimum zones expand in the global ocean, more N_2O may enter the atmosphere than previously expected. — NW

Science, this issue p. 1127

FRICTION

A frigid simulator for friction

Friction can be a friend or a foe, depending on whether we are trying to brake on a slippery road or to protect moving parts in industrial equipment. It results from the forces between atoms on the two surfaces in contact, but the details of the process are not well understood. Bylinskii *et al*. constructed a tunable friction simulator out of a handful of cold trapped ions that move in the potential of an optical lattice (see the Perspective by Meyer). They could vary the friction force experienced by the ions from maximal to nearly zero simply by changing the spatial arrangement of the ion array with respect to the optical lattice. — JS

Science, this issue p. 1115; see also p. 1089

POLITICAL SCIENCE

Not getting all sides of the news?

People are increasingly turning away from mass media to social media as a way of learning news

CREDITS: (TOP TO BOTTOM) BARTESAGHI *ET AL.*; © PHIL DEGGINGER/ALAMY; ZUZANA HOLUBCOVA AND MELINA SCHUH/MRC LABORATORY OF MOLECULAR BIOLOGY

and civic information. Bakshy *et al*. examined the news that millions of Facebook users' peers shared, what information these users were presented with, and what they ultimately consumed (see the Perspective by Lazer). Friends shared substantially less cross-cutting news from sources aligned with an opposing ideology. People encountered roughly 15% less cross-cutting content in news feeds due to algorithmic ranking and clicked through to 70% less of this cross-cutting content. Within the domain of political news encountered in social media, selective exposure appears to drive attention. — BJ

Science, this issue p. 1130; see also p. 1090

ECOPHYSIOLOGY

Double trouble

It is well known that climate change will warm ocean waters, but dissolved oxygen levels also decrease as water warms. Deutsch *et al*. combined data on metabolism, temperature, and demographics to determine the impact of marine deoxygenation on a variety of fish and crustacean species (see the Perspective by Kleypas). Predicted climate and oxygen conditions can be expected to contract the distribution of marine fish poleward, as equatorward waters become too low in oxygen to support their energy needs. Furthermore, even the more-poleward waters will have reduced oxygen levels. — SNV

Science, this issue p. 1132; see also p. 1086

CELL BIOLOGY

Giving an old organelle the old heave-ho

Centrioles are ancient cellular organelles that build centrosomes, the major microtubule-organizing centers in animal cells. Duplication of centrioles is tightly controlled to ensure that each dividing cell has precisely two centrosomes. Human cancer cells often have extra centrosomes, which has been hypothesized to confer a proliferative advantage. Wong *et al*. developed small molecules (centrinones) that allowed them to reversibly "delete" centrioles from cells (see the Perspective by Stearns). Surprisingly, cancer cells continued to divide in the absence of centrosomes, whereas normal cells stopped dividing. — PAK

Science, this issue p. 1155; see also p. 1091

DINOSAUR DENTITION

Was triceratops in need of a good dentist?

Reptiles and mammalian herbivores tend to differ in the way their teeth align. Ericksson *et al.* combined nanomechanics and paleontology to study the dental structure of herbivorous dinosaurs. Triceratops and duck-billed dinosaur teeth evolved for efficient chewing of plant matter, resulting in a dental complexity and tooth wear patterns similar to those seen in mammals. — BJP

Sci. Adv. 10.1126/sciadv.1500055 (2015).

PREECLAMPSIA

Drugs play a PPARt against preeclampsia

Preeclampsia is a life-threatening complication of pregnancy, with symptoms including high blood pressure and protein in the urine. The underlying causes of preeclampsia are not yet understood. The only effective treatment for preeclampsia is preterm delivery, which poses risks for the child. Holobotovskyy *et al.* show that a vascular protein called RGS5 plays an important role in the regulation of blood pressure during pregnancy. The absence of this protein caused a preeclampsia-like syndrome in mouse models. The mice were treated effectively with drugs called PPAR agonists, some of which are already approved for use in humans with diabetes. — YN

Sci. Transl. Med. **7**, 290ra88 (2015).

IN OTHER JOURNALS

Edited by **Kristen Mueller** *and* **Jesse Smith**

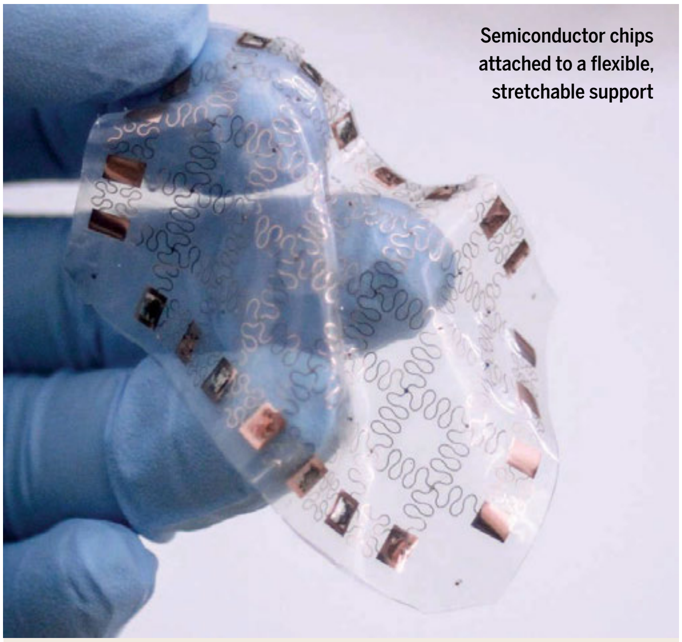

Semiconductor chips attached to a flexible, stretchable support

MATERIALS SCIENCE

Faster ways to flexible electronics

Stretchable electronics that combine both inorganic and organic parts require processing methods compatible with both types of materials. Writing semiconductors directly onto flexible substrates is possible only at low temperatures. If one fabricates the semiconductors first, precise alignment steps are needed, including deposition of the interconnects. Park *et al.* developed a process of directed self-assembly where light-emitting diodes (LEDs) can be fluidically deposited onto a stretchable substrate, so that they bond to regions that are isolated from deformation. The bottom substrate contained regions of solder that directed the LED assembly. A top conductive layer was designed for rapid attachment without critical alignment. Thus, flexible solid-state lighting could be made in a continuous roll-to-roll process. — MSL

Adv. Mat. 10.1002/adma.201500839 (2015).

AGING

In search of an anti-aging drug

As organisms age, they accumulate cells that can no longer proliferate. Such cells—termed "senescent"—persist and appear to promote aging by producing and secreting a variety of proteins. Zhu *et al*. tested whether drugs that inhibit cellular signaling pathways that make senescent cells resistant to stress and cell death could deplete senescent cells in mice. A combination of two drugs that inhibit such pathways selectively killed senescent cells in vitro, improved heart and vascular function in aging mice, and improved symptoms in a mouse model of accelerated aging. Although pinpointing the relevant targets of these drugs is difficult, the studies indicate that

EVOLUTION

Maintaining a massive mitochondrial genome

Even within the same species, flowering plants exhibit extreme differences in genome size, composition, and organization of their mitochondrial genomes. The coding sequence, however, is a different story. Wu *et al*. sequenced the mitochondrial genome of the plant *Silene noctiflora* and found that the genome consisted of 54 genes mapping to 59 circular chromosomes of varying size, many of which lacked genes. When compared with an individual from another population, both mitochondrial genomes contained the same number and organization of genes. However, variation was observed in total chromosome number (59 versus 63), suggesting that noncoding sequence had both been lost and gained between the populations but that selection maintains genetic information in the mitochondria. — LMZ

Proc. Natl. Acad. Sci. U.S.A. 10.1073/pnas.1421397112 (2015).

Silene noctiflora plants have an unusually large mitochondrial genome

selectively targeting senescent cells with small molecules may be feasible. — LBR

Aging Cell 10.1111/acel.12344 (2015).

TRANSLATION

Special proteins for stressed cells

Stress, in the form of high temperatures, causes cells to shut down the translation of most messenger RNAs (mRNAs). At the same time, stress activates the synthesis of a small number of proteins needed for cell survival and recovery, but how? To find out, Zhang *et al*. exposed human tissue culture cells to heat stress and found that they produced an alternative form of the protein MRPL18, which is normally part of mitochondrial ribosomes. When stressed, cells express this alternative form of MRPL18 and incorporate it into cytosolic ribosomes, large protein complexes required for translation. These modified ribosomes can engage and efficiently translate mRNAs needed for stress survival. — GR

Nat. Struct. Mol. Biol. **22**, 404 (2015).

MICROBIOTA

A new normal for the microbiota

Many surfaces of the human body, including the genital tract, harbor bacteria collectively referred to as the microbiota. Previous studies suggested that a healthy vaginal microbiota is lactobacillus-dominant and has low bacterial diversity. Anahtar *et al*. now challenge this. Studying young healthy women in South Africa, they identified four clusters of vaginal microbiomes. Only 37% of the women fell into lactobacillus-dominant clusters. The rest had more diverse microbiomes dominated by other genera. One diverse cluster associated strongly with genital inflammation. Because genital inflammation can place women at higher risk for acquiring sexually transmitted infections (STIs), such as HIV, these results suggest that the vaginal microbiome may influence rates of STI acquisition. — KLM

Immunity **42**, 965 (2015).

GREEN CHEMISTRY

Savvy solvent swaps to make artemisinin

Solvents greatly influence the course of chemical reactions. More indirectly, they constrain the accessible temperature and pressure conditions and frequently constitute the bulk of waste left over when reactions are finished. Amara *et al.* explored the advantages of using environmentally friendly solvents in the photochemical oxidation process used to make the antimalarial drug artemisinin. In particular, they developed one protocol using liquefied carbon dioxide and another using mixtures of water and either ethanol or tetrahydrofuran. The latter protocol operated at room temperature, and the solvents could be recycled after directly delivering crystallized product. — JSY

Nat. Chem. **7**, 10.1038/NCHEM.2261 (2015).

EDUCATION

Review sessions: From passive to active

Most science lectures begin with a 5- to 10-min review of what was covered previously, but is this time well spent? Using trained observers, Maxwell *et al.* showed that students lose focus during review sessions, ultimately leading to more time being lost as students attempt to reengage when new material is presented. To alleviate this, a "two-stage" review session, where students work on problems relating to the review material first alone and then in groups, was introduced. Results show that the active review sessions increased student engagement, allowed instructors to immediately know with what content students were or were not struggling, and allowed students to participate in active learning. — MM

J. Coll. Sci. Teach. **44**, 48 (2015).

PHOTO: © FLORALIMAGES/ALAMY

ALSO IN *SCIENCE* JOURNALS

Edited by **Stella Hurtley**

VIRAL IMMUNOLOGY

Viral exposure—the complete history

In addition to causing illness, viruses leave indelible footprints behind, because infection permanently alters the immune system. Blood tests that detect antiviral antibodies can provide information about both past and present viral exposures. Typically, such tests measure only one virus at a time. Using a synthetic representation of all human viral peptides, Xu *et al.* developed a blood test that identifies antibodies against all known human viruses. They studied blood samples from nearly 600 people of differing ages and geographic locations and found that most had been exposed to about 10 viral species over their lifetime. Despite differences in the rates of exposure to specific viruses, the antibody responses in most individuals targeted the same viral epitopes. — PAK

Science, this issue p. 1105

NEURODEGENERATION

A mouse model for ALS

A G4C2 repeat expansion in C9ORF72 is known to be the major genetic cause of frontotemporal dementia and amyotrophic lateral sclerosis (c9FTD/ALS). However, a lack of animal models recapitulating key disease features has hindered efforts to understand and prevent c9FTD/ALS-related neurodegeneration. Until now. Chew *et al.* describe a mouse model that mimics both neuropathological and clinical phenotypes of c9FTD/ALS. — SMH

Science, this issue p. 1151

ANTIBIOTICS

New for old—TB drug development

Tuberculosis (TB) is a global health threat for which there is only lengthy drug treatment. Patients need to consume multiple tablets over several months and frequently fail to complete their treatment. Consequently, drug-resistant strains of the pathogen have emerged, which add to the threat. Kling *et al.* revisited a natural product called griselimycin, extracted from the same organism that produced the prototype anti-TB drug, streptomycin. Unmodified griselimycin has poor pharmacological properties. However, one synthetic derivative had improved oral uptake and penetrated cells of the immune system that harbor the TB mycobacterium. In combination with other drugs, the griselimycin derivative showed high potency in mice with TB. — CA

Science, this issue p. 1106

MULTIFERROICS

Visualizing ferroelectric domains

Multiferroic materials support intertwined ferromagnetic and ferroelectric orders, with the magnetic field capable of controlling the electric order and vice versa. Matsubara *et al.* used second harmonic generation microscopy to visualize what happens to the ferroelectric domains in the multiferroic $TbMnO_3$ when an externally applied magnetic field changes the direction of electric polarization by 90°. Unexpectedly, the domain walls, initially parallel to the polarization vector, did not change their shape or position. The resulting transition from neutral to charged domain walls may help in the development of future ferroelectric devices. — JS

Science, this issue p. 1112

FRICTION

Slip sliding away

Many applications would benefit from ultralow friction conditions to minimize wear on the moving parts such as in hard drives or engines. On the very small scale, ultralow friction has been observed with graphite as a lubricant. Berman *et al.* achieved superlubricity using graphene in combination with crystalline diamond nanoparticles and diamondlike carbon (see the Perspective by Hone and Carpick). Simulations showed that sliding of the graphene patches around the tiny nanodiamond particles led to nanoscrolls with reduced contact area that slide easily against the amorphous diamondlike carbon surface. – MSL

Science, this issue p. 1118; see also p. 1087

ORGANIC THIN FILMS

Standing at order

Thin films of organic molecules on solid substrates tend to nucleate at many sites and grow multiple domains. However, one large uniform film would be much more desirable in device applications. Seiki *et al.* designed organic molecules that filled space in a hexagonal tiling; a propeller-like triptycene base adhered to crystalline surfaces and alkyl tails extended away from it. The authors could make well-ordered multilayer films up to centimeter length scales. — PDS

Science, this issue p. 1122

CORAL REEFS

Not as deep

As our climate warms, many species ranges are predicted to shift toward the warmer poles. Focusing solely on temperatures, however, ignores many factors that change across latitudes, such as the intensity of solar radiation. Muir *et al.* looked at global distributions of two groups of reef-building corals (see the Perspective by Kleypas). Most reef-building corals occur deep enough to be protected from surge. However, corals require sunlight to sustain their symbiotic photosynthetic algae. Because solar radiation is more limited farther away from the equator, future populations might be limited to more turbulent shallow waters. — SNV

Science, this issue p. 1135; see also p. 1086

ELECTRON MICROSCOPY

Pushing the limits of electron microscopy

Recent advances in cryo–electron microscopy (cryo-EM) allow structures of large macromolecules to be determined at near-atomic resolution. So far, though, resolutions approaching 2 Å, where features key to drug design are revealed, remain the province of x-ray crystallography. Bartesaghi *et al.* achieved a resolution of 2.2 Å for a 465-kD ligand-bound protein complex using cryo-EM. The density map is detailed enough to show close to 800 water molecules, magnesium and sodium ions, and precise side-chain conformations. These results bring routine use of cryo-EM in rational drug design a step closer. — VV

Science, this issue p. 1147

AGING STEM CELLS

Heterochromatin in aging stem cells

Analysis of human aging syndromes, such as Werner syndrome (WS), may lead to greater understanding of both premature and normal aging. Zhang *et al.* generated isogenic WS-specific human embryonic stem cell lines (see the Perspective by Brunauer and Kennedy). WS-mesenchymal stem cells displayed features characteristic of premature aging, including heterochromatin disorganization. WRN protein thus functions in the maintenance of heterochromatin, and heterochromatin alterations may represent a driving force of human aging. — BAP

Science, this issue p. 1160; see also p. 1093

BONE BIOLOGY

A scaffold for directing bone breakdown

Too much bone breakdown by osteoclasts and not enough bone formation by osteoblasts can lead to osteoporosis. The cytokine RANKL and the kinase p38 stimulate precursor cells in the bone to become osteoclasts. Lin *et al.* found that the binding of RANKL to its receptor complex recruited the scaffold protein RACK1, leading to the activation of p38. RANKL was less effective at stimulating osteoclast formation and bone loss in those portions of mouse skulls treated to reduce RACK1 levels than in untreated parts. These results provide a potential therapeutic target for osteoporosis. — JFF

Sci. Signal. **8**, ra54 (2015).

RESEARCH ARTICLE SUMMARY

VIRAL IMMUNOLOGY

Comprehensive serological profiling of human populations using a synthetic human virome

George J. Xu, Tomasz Kula, Qikai Xu, Mamie Z. Li, Suzanne D. Vernon, Thumbi Ndung'u, Kiat Ruxrungtham, Jorge Sanchez, Christian Brander, Raymond T. Chung, Kevin C. O'Connor, Bruce Walker, H. Benjamin Larman, Stephen J. Elledge*

INTRODUCTION: The collection of viruses found to infect humans can have profound effects on human health. In addition to directly causing acute or chronic illness, viral infection can alter host immunity in more subtle ways, leaving an indelible footprint on the immune system. This interplay between virome and host immunity has been implicated in the pathogenesis of complex diseases such as type 1 diabetes, inflammatory bowel disease, and asthma. Despite the growing appreciation for the importance of interactions between the virome and host, a comprehensive method to systematically characterize these interactions has yet to be developed.

RATIONALE: Current serological methods to detect viral infections are predominantly limited to testing one pathogen at a time and are therefore used primarily to address specific clinical hypotheses. A method that could simultaneously detect responses to all human viruses would allow hypothesis-free analysis to detect associations between past viral infections and particular diseases or population structures. Humoral responses to infection typically arise within 10 to 14 days of initial exposure and can persist over years or decades, thus providing a rich source of the history of pathogen encounters. In this work, we present VirScan, a high-throughput method that allows comprehensive analysis of antiviral antibodies in human sera. VirScan uses DNA microarray synthesis and bacteriophage display to create a uniform, synthetic representation of peptide epitopes comprising the human virome. Immunoprecipitation and high-throughput DNA sequencing reveal the peptides recognized by antibodies in the sample. The analysis requires less than 1 μl of blood.

RESULTS: We screened sera from 569 human donors across four continents, assaying a total of over 10^8 antibody-peptide interactions for reactivity to 206 human viral species and >1000 strains. We found that VirScan's performance in detecting known infections and distinguishing between exposures to related viruses is comparable to that of classical serum antibody tests for single viruses. We detected antibodies to an average of 10 viral species per person and 84 species in at least two individuals. Our approach maps antibody targets at 56–amino acid resolution, and our results nearly double the number of previously established viral B cell epitopes. Although rates of specific virus exposure varied depending on age, HIV status, and geographic location of the donor, we observed strong similarities in antibody responses across individuals. In particular, we found multiple instances of single peptides that were recurrently recognized by antibodies in the vast majority of donors. We performed tiling mutagenesis and found that these antibody responses targeted substantially conserved "public epitopes" for each virus, suggesting that antibodies with highly similar specificities, and possibly structures, are elicited across individuals.

CONCLUSION: VirScan is a method that enables human virome-wide exploration, at the epitope level, of immune responses in large numbers of individuals. We have demonstrated its effectiveness for determining viral exposure and characterizing viral B cell epitopes in high throughput and at high resolution. Our preliminary studies have revealed intriguing general properties of the human immune system, both at the individual and the population scale. VirScan may prove to be an important tool for uncovering the effect of host-virome interactions on human health and disease and could easily be expanded to include new viruses as they are discovered, as well as other human pathogens, such as bacteria, fungi, and protozoa. ■

ON OUR WEB SITE

Read the full article at http://dx.doi.org/10.1126/science.aaa0698

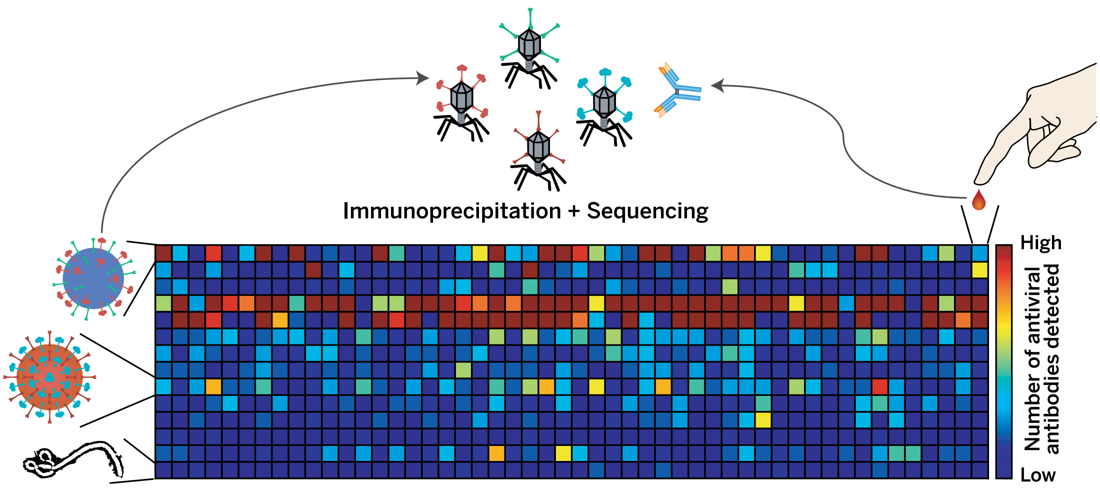

Systematic viral epitope scanning (VirScan). This method allows comprehensive analysis of antiviral antibodies in human sera. VirScan combines DNA microarray synthesis and bacteriophage display to create a uniform, synthetic representation of peptide epitopes comprising the human virome. Immunoprecipitation and high-throughput DNA sequencing reveal the peptides recognized by antibodies in the sample. The color of each cell in the heatmap depicts the relative number of antigenic epitopes detected for a virus (rows) in each sample (columns).

The list of author affiliations is available in the full article online.

*Corresponding author. E-mail: selledge@genetics.med.harvard.edu

Cite this paper as G. J. Xu *et al.*, *Science* **348**, aaa0698 (2015). DOI: 10.1126/science.aaa0698

RESEARCH ARTICLE

VIRAL IMMUNOLOGY

Comprehensive serological profiling of human populations using a synthetic human virome

George J. Xu,[1,2,3,4]* Tomasz Kula,[3,4,5]* Qikai Xu,[3,4] Mamie Z. Li,[3,4] Suzanne D. Vernon,[6] Thumbi Ndung'u,[7,8,9,10] Kiat Ruxrungtham,[11] Jorge Sanchez,[12] Christian Brander,[13] Raymond T. Chung,[14] Kevin C. O'Connor,[15] Bruce Walker,[8,9] H. Benjamin Larman,[16] Stephen J. Elledge[3,4,6]†

The human virome plays important roles in health and immunity. However, current methods for detecting viral infections and antiviral responses have limited throughput and coverage. Here, we present VirScan, a high-throughput method to comprehensively analyze antiviral antibodies using immunoprecipitation and massively parallel DNA sequencing of a bacteriophage library displaying proteome-wide peptides from all human viruses. We assayed over 10^8 antibody-peptide interactions in 569 humans across four continents, nearly doubling the number of previously established viral epitopes. We detected antibodies to an average of 10 viral species per person and 84 species in at least two individuals. Although rates of specific virus exposure were heterogeneous across populations, antibody responses targeted strongly conserved "public epitopes" for each virus, suggesting that they may elicit highly similar antibodies. VirScan is a powerful approach for studying interactions between the virome and the immune system.

The collection of viruses found to infect humans (the "human virome") can have profound effects on human health (*1*). In addition to directly causing acute or chronic illness, viral infection can also alter host immunity in more subtle ways, leaving an indelible footprint on the immune system (*2*). For example, latent herpesvirus infection has been shown to confer symbiotic protection against bacterial infection in mice through prolonged production of interferon-γ and systemic activation of macrophages (*3*). This interplay between virome and host immunity has also been implicated in the pathogenesis of complex diseases such as type 1 diabetes, inflammatory bowel disease, and asthma (*4*). Despite this growing appreciation for the importance of interactions between the virome and host, a comprehensive method to systematically characterize these interactions has yet to be developed (*5*).

Viral infections can be detected by serological or nucleic acid–based methods (*6*). However, nucleic acid tests fail in cases where viruses have already been cleared after causing or initiating tissue damage and can miss viruses of low abundance or viruses not normally present in the sampled fluid or surface. In contrast, humoral responses to infection typically arise within 2 weeks of initial exposure and can persist over years or decades (*7*). Tests detecting antiviral antibodies in peripheral blood can therefore identify ongoing and cleared infections. However, current serological methods are predominantly limited to testing one virus at a time and are therefore only used to address specific clinical hypotheses. Scaling serological analyses to encompass the complete human virome poses substantial technical challenges, but would be of great value for better understanding host-virus interactions and would overcome many of the limitations associated with current clinical technologies. In this work, we present VirScan, a programmable, high-throughput method to comprehensively analyze antiviral antibodies using immunoprecipitation and massively parallel DNA sequencing of a bacteriophage library displaying proteome-wide coverage of peptides from all human viruses.

[1]Program in Biophysics, Harvard University, Cambridge, MA 02115, USA. [2]Harvard-Massachusetts Institute of Technology (MIT) Division of Health Sciences and Technology, Cambridge, MA 02139, USA. [3]Division of Genetics, Department of Medicine, Howard Hughes Medical Institute, Brigham and Women's Hospital, Boston, MA 02115, USA. [4]Department of Genetics, Harvard University Medical School, Boston, MA 02115, USA. [5]Program in Biological and Biomedical Sciences, Harvard University, Cambridge, MA 02115, USA. [6]Solve ME/CFS Initiative, Los Angeles, CA 90036, USA. [7]KwaZulu-Natal Research Institute for Tuberculosis and HIV, Nelson R. Mandela School of Medicine, University of KwaZulu-Natal, Durban, South Africa. [8]HIV Pathogenesis Programme, Doris Duke Medical Research Institute, Nelson R. Mandela School of Medicine, Durban, South Africa. [9]Ragon Institute of Massachusetts General Hospital, MIT, and Harvard University, Cambridge, MA 02139, USA. [10]Max Planck Institute for Infection Biology, Chariteplatz, D-10117 Berlin, Germany. [11]Vaccine and Cellular Immunology Laboratory, Department of Medicine, Faculty of Medicine; and Chula-Vaccine Research Center, Chulalongkorn University, Bangkok, Thailand. [12]Asociación Civil IMPACTA Salud y Educación, Lima, Peru. [13]AIDS Research Institute-IrsiCaixa and AIDS Unit, Hospital Germans Trias i Pujol, Universitat Autònoma de Barcelona, Badalona, Spain Institució Catalana de Recerca i Estudis Avançats (ICREA), Barcelona, Spain. [14]Division of Gastroenterology, Massachusetts General Hospital, Boston, MA 02114, USA. [15]Department of Neurology, Yale School of Medicine, New Haven, CT 06520, USA. [16]Division of Immunology, Department of Pathology, Johns Hopkins University, Baltimore, MD 21205, USA.
*These authors contributed equally to this work. **†Corresponding author. E-mail: selledge@genetics.med.harvard.edu**

Results

The VirScan platform

VirScan uses the phage immunoprecipitation sequencing (PhIP-seq) technology previously developed in our laboratory (*8*). Briefly, we used a programmable DNA microarray to synthesize 93,904 200-mer oligonucleotides, encoding 56-residue peptide tiles, with 28-residue overlaps, that together span the reference protein sequences (collapsed to 90% identity) of all viruses annotated to have human tropism in the UniProt database (Fig. 1A, a and b) (*9*). This library includes peptides from 206 species of virus and over 1000 different strains. We cloned the library into a T7 bacteriophage display vector for screening (Fig. 1A, c).

To perform a screen, we incubate the library with a serum sample containing antibodies, recover the antibodies by using a mixture of protein A– and G–coated magnetic beads, and remove unbound phage particles by washing (Fig. 1A, d and e). Last, we perform polymerase chain reaction (PCR) and massively parallel sequencing on the phage DNA to quantify enrichment of each library member resulting from antibody binding (Fig. 1A, f). Each sample is screened in duplicate to ensure reproducibility. VirScan requires only 2 μg of immunoglobulin (<1 μl of serum) per sample and can be automated on a 96-well liquid handling robot (*10*). PCR product from 96 immunoprecipitations can be individually barcoded and pooled for sequencing, reducing the cost for a comprehensive viral antibody screen to about $25 per sample.

After sequencing, we tally the read count for each peptide before ("input") and after ("output") immunoprecipitation. We then fit a zero-inflated generalized Poisson model to the distribution of output read counts for each input read count and regress the parameters as a function of input read count (fig. S1). With use of this model, we calculate a $-\log_{10}(P\text{ value})$ for the significance of each peptide's enrichment. Last, we call a peptide significantly enriched if its $-\log_{10}(P\text{ value})$ is greater than the reproducibility threshold of 2.3 in both replicates (fig. S2).

Characterizing VirScan's sensitivity and specificity

Figure 1B shows the antibody profiles of a set of human viruses in sera from a typical group of individuals in a heat map format that illustrates the number of enriched peptides from each virus. We frequently detected antibodies to multiple peptides from common human viruses, such as Epstein-Barr virus (EBV), cytomegalovirus (CMV), and rhinovirus. As expected, we observed more peptides to be enriched from viruses with larger proteomes, such as EBV and CMV, likely because

there are more epitopes available for recognition. We noticed fewer enriched peptides in samples from individuals less than 10 years of age compared with their geographically matched controls, in line with an accumulation of viral infections throughout adolescence and adulthood. However, there were occasional samples from young donors with very strong responses to viruses that cause childhood illness, such as parvovirus B19 and herpesvirus 6B, which cause the "fifth disease" and "sixth disease" of the classical infectious childhood rashes, respectively (11). These observations are examined in greater detail in Fig. 2.

We developed a computational method to identify the set of viruses to which an individual has been exposed, based on the number of enriched peptides identified per virus. Briefly, we set a threshold number of significant non-overlapping enriched peptides for each virus. We empirically determined that a threshold of three non-overlapping enriched peptides gave the best performance for detecting herpes simplex virus 1 (HSV1) compared with a commercial serologic test, described below (Table 1). For other viruses, we adjusted the

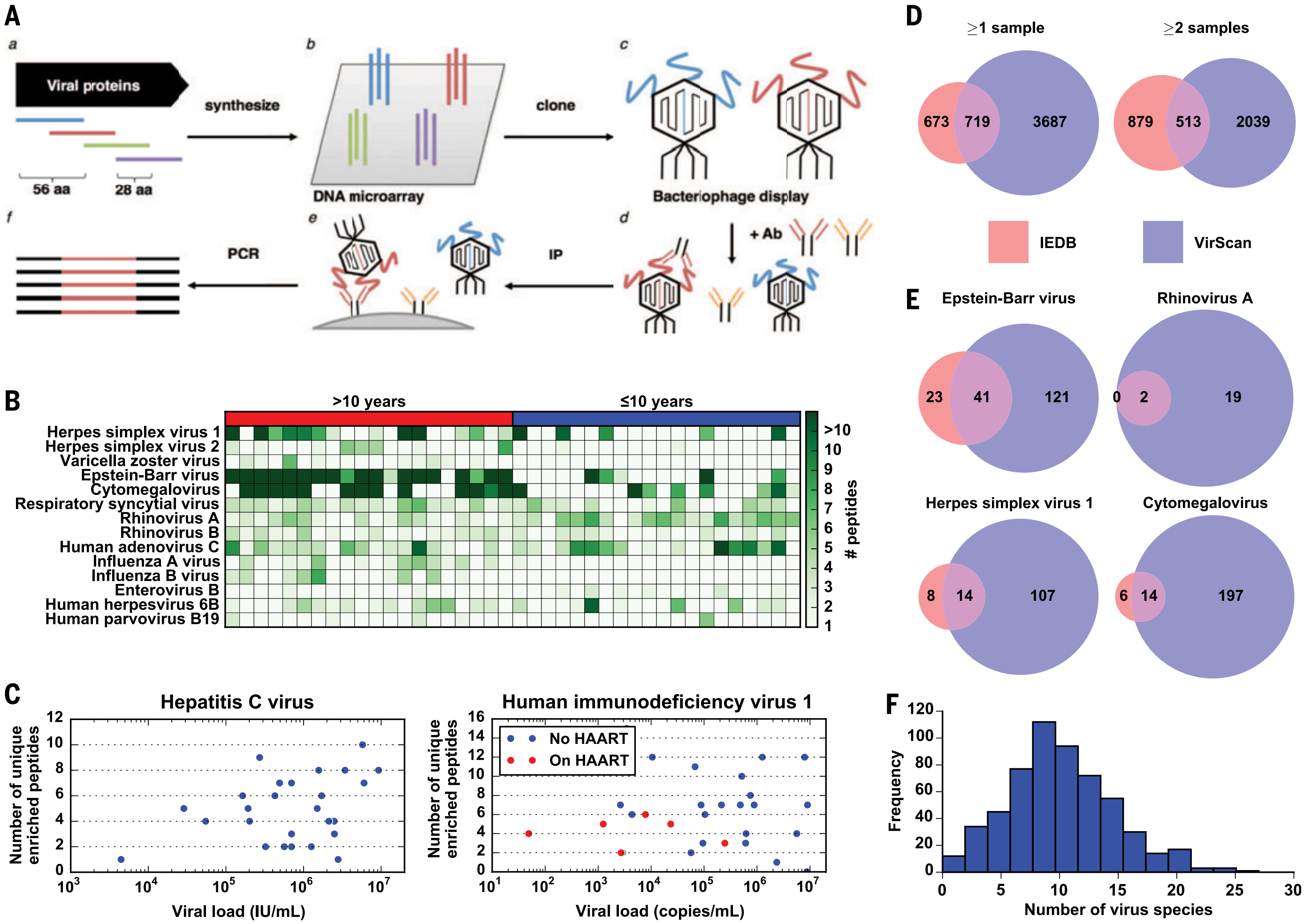

Fig. 1. General VirScan analysis of the human virome. (**A**) Construction of the virome peptide library and VirScan screening procedure. (a) The virome peptide library consists of 93,904 56–amino acid peptides tiling, with 28–amino acid overlap, across the proteomes of all known human viruses. (b) The 200-nt DNA sequences encoding the peptides were printed on a releasable DNA microarray. (c) The released DNA was amplified and cloned into a T7 phage display vector and packaged into virus particles displaying the encoded peptide on its surface. (d) The library is mixed with a sample containing antibodies that bind to their cognate peptide antigen on the phage surface. (e) The antibodies are immobilized, and unbound phage are washed away. (f) Last, amplification of the bound DNA and high-throughput sequencing of the insert DNA from bound phage reveals peptides targeted by sample antibodies. Ab, antibody; IP, immunoprecipitation. (**B**) Antibody profile of randomly chosen group of donors to show typical assay results. Each row is a virus; each column is a sample. The label above each chart indicates whether the donors are over 10 years of age or at most 10 years of age. The color intensity of each cell indicates the number of peptides from the virus that were significantly enriched by antibodies in the sample. (**C**) Scatter plot of the number of unique enriched peptides (after applying maximum parsimony filtering) detected in each sample against the viral load in that sample. Data are shown for the HCV-positive and HIV-positive samples for which we were able to obtain viral load data. For the HIV-positive samples, red dots indicate samples from donors currently on highly active antiretroviral therapy (HAART) at the time the sample was taken, whereas blue dots indicate different donors before undergoing therapy. IU, international units. (**D**) Overlap between enriched peptides detected by VirScan and human B cell epitopes from viruses in IEDB. The entire pink circle represents the 1392 groups of nonredundant IEDB epitopes that are also present in the VirScan library (out of 1559 clusters total). The overlap region represents the number of groups with an epitope that is also contained in an enriched peptide detected by VirScan. The purple-only region represents the number of nonredundant enriched peptides detected by VirScan that do not contain an IEDB epitope. Data are shown for peptides enriched in at least one (left) or at least two (right) samples. (**E**) Overlap between enriched peptides detected by VirScan and human B cell epitopes in IEDB from common human viruses. The regions represent the same values as in (D) except only epitopes corresponding to the indicated virus are considered, and only peptides from that virus that were enriched in at least two samples were considered. (**F**) Distribution of number of viruses detected in each sample. The histogram depicts the frequency of samples binned by the number of virus species detected by VirScan. The mean and median of the distribution are both about 10 virus species.

threshold to account for the size of the viral proteome (fig. S3). Next, we tally the number of enriched peptides from each virus. Antibodies generated against a specific virus can cross-react with similar peptides from a related virus. This would lead to false positives, because an antibody targeted to an epitope from one virus to which a donor was exposed would also enrich a homologous peptide from a related virus to which the donor may not have been exposed. In order to address this issue, we adopted a maximum parsimony approach to infer the fewest number of virus exposures that could elicit the observed spectrum of antiviral peptide antibodies. Groups of enriched peptides that share a seven–amino acid subsequence may be recognized by a single specific antibody, so we only count them as one epitope for the virus that has the greatest number of other enriched peptides. If this adjusted peptide count is greater than the threshold for that virus, the sample is considered positive for the virus. For this analysis, we also filtered out peptides that were enriched in only 1 of the 569 samples to avoid spurious hits.

With this analytical framework, we measured the performance of VirScan by using serum samples from individuals known to be infected or not infected with human immunodeficiency virus (HIV) and hepatitis C virus (HCV), based on commercial enzyme-linked immunosorbent assay (ELISA) and Western blot assays. For both viruses, VirScan achieves very high sensitivities and specificities of ~95% or higher (Table 1) over a wide range of viral loads (Fig. 1C). The viral genotype was also known for the HCV-positive samples. Despite the over 70% amino acid sequence conservation among HCV genotypes (12), which poses a problem for all antibody-based detection methods, VirScan correctly reported the HCV genotype in 69% of the samples. We also compared VirScan to a commercially available serology test that is type-specific for the highly related HSV1 and HSV2 (Table 1). These results demonstrate that VirScan performs well in distinguishing between closely related viruses and viruses that range in size from small (HIV and HCV) to very large (HSV1 and HSV2) with high sensitivity and specificity.

Population-level analysis of viral exposures

After ascertaining the performance of VirScan for a panel of viruses, we undertook a large-scale screening of samples with unknown exposure history. By using our multiplex approach, we assayed over 106 million antibody-peptide interactions with samples from 569 human donors in duplicate. We detected antibody responses to an average of 10 species of virus per sample (Fig. 1F). Each person is likely exposed to multiple distinct strains of some viral species. We detected antibody responses to 62 of the 206 species of virus in our library in at least five individuals and 84 species in at least two individuals. The most frequently detected viruses are generally those known to commonly infect humans (Table 2 and table S1). We occasionally detected what appear to be false positives that may be due to antibodies that cross-react with nonviral peptides. For example, 29% of the samples positive for cowpox virus were right at the threshold of detection and had antibodies against a peptide from the *C4L* gene that shares an eight–amino acid sequence (SESDSDSD; D, Asp; E, Glu; S, Ser) with the clumping factor B protein from *Staphylococcus aureus*, against which humans are known to generate antibodies (13). This will become less of an issue when we test more examples of sera from individuals with known infections to determine the set of likely antigenic peptides for a given virus. However, the fact that we do not detect

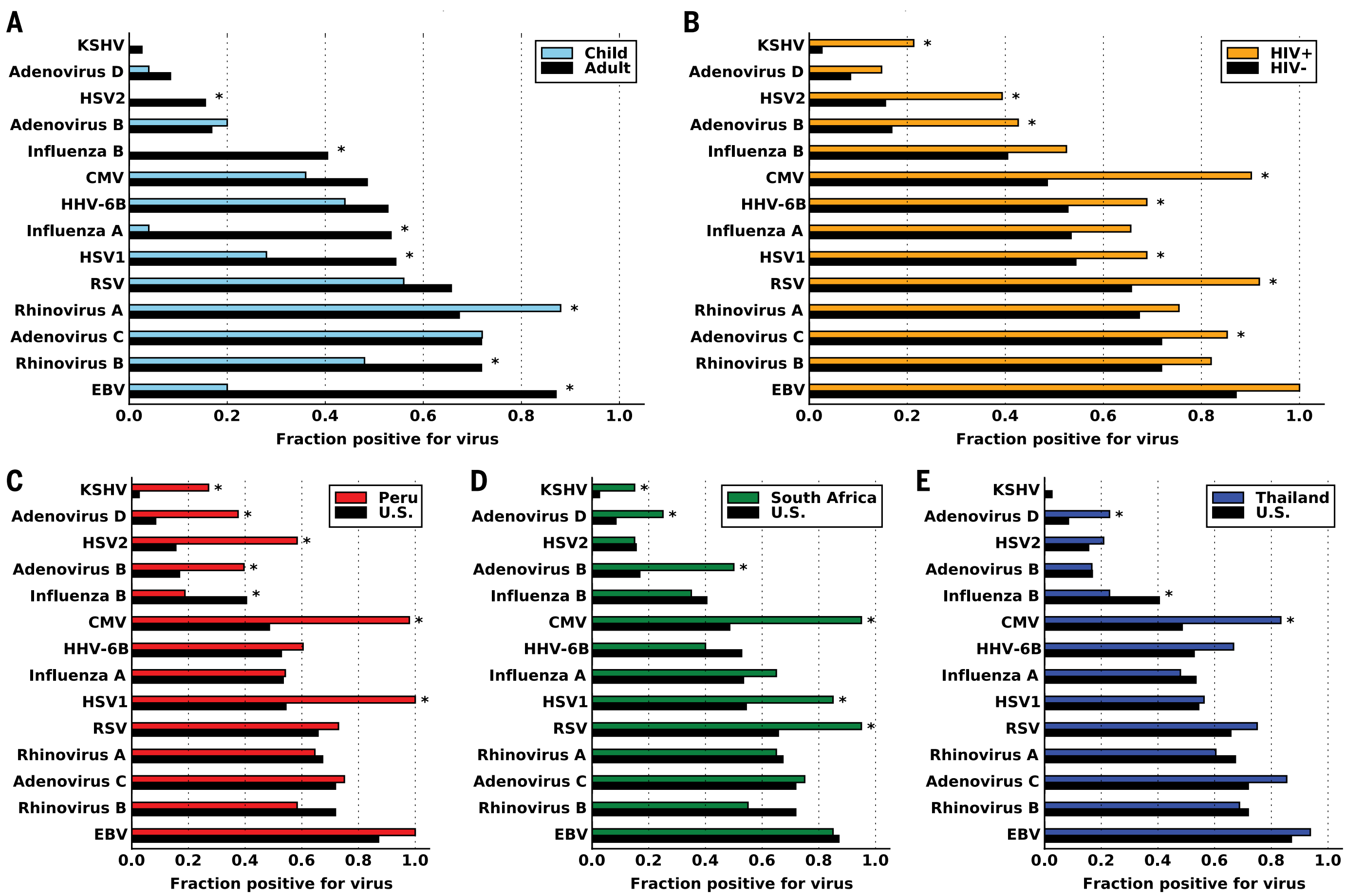

Fig. 2. Population stratification of the human virome immune response. The bar graphs depict the differences in exposure to viruses between donors who are (**A**) less than 10 years of age versus over 10 years of age, (**B**) HIV-positive versus HIV-negative, residing in the United States (**C**) residing in Peru versus residing in the United States, (**D**) residing in South Africa versus residing in the United States, and (**E**) residing in Thailand versus residing in the United States. Asterisks indicate false discovery rate < 0.05.

Table 1. VirScan's sensitivity and specificity on samples with known viral infections. Sensitivity is the percentage of samples positive for the virus as determined by VirScan out of all *n* known positives. Specificity is the percentage of samples negative for the virus by VirScan out of all *n* known negatives.

Virus	Sensitivity (*n*)	Specificity (*n*)
HCV	92% (26)*	97%** (34)
HIV1	95% (61)*	100% (33)
HSV1	97% (38)	100% (6)
HSV2	90% (20)	100% (24)

*We found that, although the false negative samples did not meet our stringent cutoff for enriching multiple unique peptides, they had detectable antibodies to a recurrent epitope. By modifying the criterion to allow for samples that enrich multiple homologous peptides that share a recurrent epitope as described in the text, the sensitivity of detecting HCV increases to 100%, and the sensitivity for detecting HIV increases to 97%. This modified criterion does not significantly affect specificity (fig. S13). **The one false positive was from an individual whose HCV-negative status was self-reported, but who had antibodies to as many HCV peptides as 23% of the true HCV-positive individuals and is likely to be HCV-positive now or in the past. It is possible that this individual was exposed to HCV but cleared the infection. If true, the observed specificity for HCV is 100%.

Table 2. Frequently detected viruses. The % column indicates the percentage of samples that were positive for the virus by VirScan. Known HIV- and HCV-positive samples were excluded when performing this analysis.

Virus species	%
Human herpesvirus 4	87.1%
Rhinovirus B	71.8%
Human adenovirus C	71.8%
Rhinovirus A	67.3%
Human respiratory syncytial virus	65.7%
Human herpesvirus 1	54.4%
Influenza A virus	53.4%
Human herpesvirus 6B	52.8%
Human herpesvirus 5	48.5%
Influenza B virus	40.5%
Poliovirus	33.7%
Human herpesvirus 3	24.3%
Human adenovirus F	20.4%
Human adenovirus B	16.8%
Human herpesvirus 2	15.5%
Enterovirus A	15.2%
Enterovirus B	13.3%

high rates of very rare viruses strengthens our confidence in VirScan's specificity (see supplementary discussion).

We frequently detected antibodies to rhinovirus and respiratory syncytial virus, which are normally found only in the respiratory tract, indicating that VirScan using blood samples is still able to detect viruses that do not cause viremia. We also detected antibodies to influenza, which is normally cleared, and poliovirus, to which most people in modern times generate antibodies through vaccination. Because the original antigen is no longer present, we are likely detecting antibodies secreted by long-lived memory B cells (*14*).

We detected antibodies to certain viruses less frequently than expected based on previous seroprevalence studies that used optimized serum ELISAs. For example, the frequency at which we detect influenza (53.4%) and poliovirus (33.7%) is lower than expected given that the majority of the population has been exposed to or vaccinated against these viruses. This may be due to reduced sensitivity because of a gradual narrowing and decrease of the long-lived B cell response in the absence of persistent antigen. We also rarely detected antibody responses to small viruses, such as JC virus (JCV) and torque teno virus, which are frequently detected by using specific tests. We believe that the disparity is due to low titers of antibodies to unmodified, linear epitopes from these viruses. For example, serum antibodies against the major capsid protein of JCV are reported to only recognize conformational epitopes (*15*). Last, the frequency of detecting varicella zoster virus (chicken pox) antibodies is also lower than expected (24.3%), even though the frequency of detecting other latent herpesviruses, such as EBV (87.1%) and CMV (48.5%), is similar to the prevalence reported in epidemiological studies (*16*–*18*). This may reflect differences in how frequently these viruses shed antigens that stimulate B cell responses or a more limited humoral response that relies on epitopes that cannot be detected in a 56-residue peptide. It might also be possible to increase the sensitivity of detection of these viral antibodies by stimulating memory B cells in vitro to probe the history of infection more deeply.

To assess differences in viral exposure between populations, we split the samples into different groups based on age, HIV status, and geography. We first compared results from children under the age of 10 to adults within the United States (HIV-positive individuals were excluded from this analysis) (Fig. 2A). Fewer children were positive for most viruses, including EBV, HSV1, HSV2, and influenza virus, which is consistent with our preliminary observations comparing the number of enriched peptides (Fig. 1B). In addition to the fact that children may generate lower antibody titers in general, these younger donors probably have not yet been exposed to certain viruses, for example, HSV2, which is sexually transmitted (*19*).

When comparing results from HIV-positive to HIV-negative samples, we found more of the HIV-positive samples to also be seropositive for additional viruses, including HSV2, CMV, and Kaposi's sarcoma–associated herpesvirus (KSHV) (false discovery rate $q < 0.05$, Fig. 2B). These results are consistent with prior studies indicating higher risk of these co-infections in HIV positive patients (*20*–*22*). Patients with HIV may engage in activities that put them at higher risk for exposure to these viruses. Alternatively, these viruses may increase the risk of HIV infection. HIV infection may reduce the immune system's ability to control reactivation of normally dormant resident viruses or to prevent opportunistic infections from taking hold and triggering a strong adaptive immune response.

Last, we compared evidence of viral exposure among samples taken from adult HIV-negative donors residing in countries (United States, Peru, Thailand, and South Africa) from four different continents. In general, donors outside the United States had higher frequencies of seropositivity (Fig. 2, C to E). For example, CMV antibodies were found in significantly higher frequencies in samples from Peru, Thailand, and South Africa. Other viruses, such as KSHV and HSV1, were detected more frequently in donors from Peru and South Africa but not Thailand. The observed detection frequency of different adenovirus species varies across populations. Adenovirus C seropositivity was found at similar frequencies in all regions, but adenovirus D seropositivity was generally higher outside the United States, whereas adenovirus B seropositivity was higher in Peru and South Africa but not in Thailand. The higher rates of virus exposure outside the United States could be due to differences in population density, cultural practices, sanitation, or genetic susceptibility. Additionally, influenza B seropositivity was more common in the United States compared with other countries, especially Peru and Thailand. The global incidence of influenza B is much lower than influenza A, but the standard influenza vaccination contains both influenza A and B strains, so the elevated frequency of individuals with seroreactivity may be due to higher rates of influenza vaccination in the United States. Other viruses, such as rhinovirus and EBV, were detected at very similar frequencies in all the geographic regions.

Analysis of viral epitope determinants

After analyzing responses on the whole-virus level, we focused our attention on the specific peptides targeted by these antibodies. We detected antibodies to a total of 8425 peptides in at least two samples, and 15,052 in at least one sample. Because of the presence of many related peptides in our library and the Immune Epitope Database (IEDB), for the following analysis we consider a peptide unique only if it does not contain a continuous seven-residue subsequence, the estimated size of a linear epitope, in common with another peptide. Analyzed as such, our VirScan database nearly doubles the 1559 unique human B cell epitopes from human viruses in the IEDB (*23*). The epitopes identified in our unbiased analysis demonstrate a significant overlap with those contained in the IEDB ($P < 10^{-30}$, Fisher's exact text, Fig. 1D). The amount of overlap is even greater for epitopes from viruses that commonly cause infection (Fig. 1E). We would likely have detected even more antigenic peptides in common with the IEDB if we had tested more samples from individuals infected with rare viruses. We next analyzed the amino acid composition of recurrently enriched peptides. Enriched peptides tend to have more proline and charged amino acids and fewer hydrophobic amino acids, which is consistent with a previous analysis of B cell epitopes in the IEDB (fig. S4) (*24*). This trend

likely reflects enrichment for amino acids that are surface-exposed or can form stronger interactions with antibodies.

B cell responses target highly similar viral epitopes across individuals

We compared the profile of peptides recognized by the antibody response in different individuals. We found that, for a given protein, each sample generally only had strong responses against one to three immunodominant peptides (Fig. 3). Unexpectedly, we found that the vast majority of seropositive samples for a given virus recognized the same immunodominant peptides, suggesting that the antiviral B cell response is highly stereotyped across individuals. For example, in glycoprotein G from respiratory syncytial virus, there is only a single immunodominant peptide comprising positions 141 to 196 that is targeted by all samples with detectable antibodies to the protein, regardless of the country of origin (Fig. 3A).

For other antigens, we observed interpopulation serological differences. For example, two overlapping peptides from positions 309 to 364 and 337 to 392 of the penton base protein from adenovirus C frequently elicited antibody responses (Fig. 3B). However, donors from the United States and South Africa had much stronger responses to peptide 309-364 ($P < 10^{-6}$, t test) relative to donors from Thailand and Peru. We observed that, for the EBNA1 protein from EBV, donors from all four countries frequently had strong responses to peptide 393-448 and occasionally to peptide 589-644. However, donors from Thailand and Peru had much stronger responses to peptide 57-112 ($P < 10^{-6}$, t test) (Fig. 3C). These differences may reflect variation in the strains endemic in each region. In addition, polymorphism of major histocompatibility complex (MHC) class II alleles, immunoglobulin genes, and other modifiers that shape immune responses in each population likely play a role in defining the relative immunodominance of antigenic peptides.

To determine whether the humoral responses that target an immunodominant peptide are actually targeting precisely the same epitope, we constructed single-, double-, and triple-alanine scanning mutagenesis libraries for eight commonly recognized peptides. These were introduced into the same T7 bacteriophage display vector and subjected to the same immunoprecipitation and sequencing protocol using samples from the United States. Mutants that disrupt the epitope diminish antibody binding affinity and peptide enrichment. We found that, for all eight peptides tested, there was a single, largely contiguous subsequence in which mutations disrupted binding for the majority of samples. As expected, the triple mutants abolished antibody binding to a greater extent, and the enrichment patterns were similar among single, double, and triple mutants of the same peptide (Fig. 4 and figs. S5 to S11).

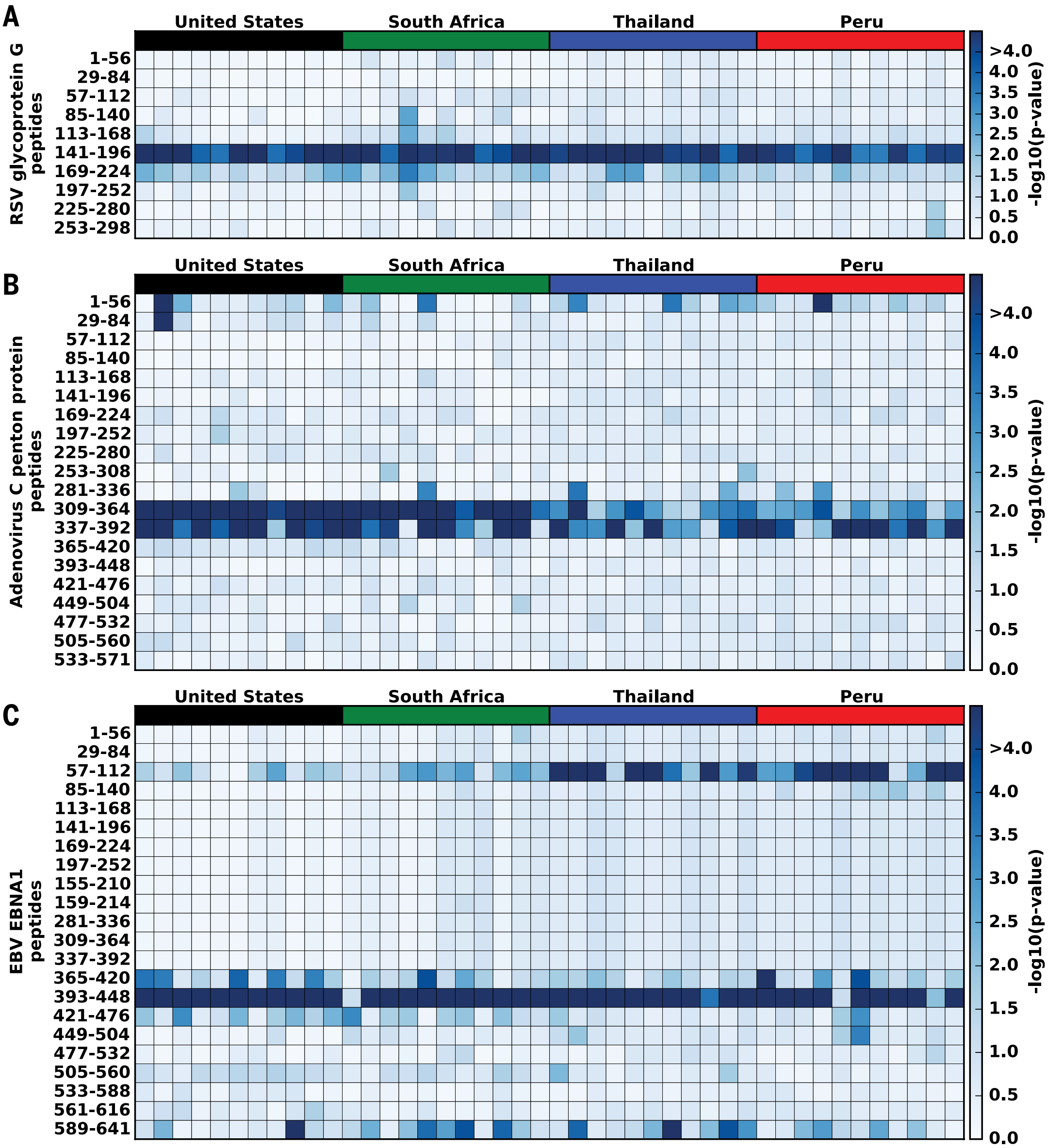

Fig. 3. The human antivirome response recognizes a similar spectrum of peptides among infected individuals. In the heat-map charts, each row is a peptide tiling across the indicated protein, and each column is a sample. The colored bar above each column, labeled at the top of the panels, indicates the country of origin for that sample. The samples shown are a subset of individuals with antibodies to at least one peptide from the protein. The color intensity of each cell corresponds to the $-\log_{10}(P$ value) measure of significance of enrichment for a peptide in a sample (greater values indicates stronger antibody response). Data are shown for (**A**) human RSV attachment glycoprotein G (*G*), (**B**) human adenovirus C penton protein (*L2*), and (**C**) EBV nuclear antigen 1 (*EBNA1*). Data shown are the mean of two replicates.

For four of the eight peptides, a 9- to 15-amino acid region was critical for antibody recognition in >90% of samples (Fig. 4 and figs. S5 to S7). One other peptide had a region of similar size that was critical in about half of the samples (fig. S8). In another peptide, a single region was important for antibody recognition in the majority of the samples, but the extents of the critical region varied slightly for different samples, and occasionally there were donors that recognized a completely separate epitope (fig. S9). The remaining two peptides contained a single triple mutant that abolished binding in the majority of samples, but the critical region also extended further to different extents depending on the sample (figs. S10 and S11). Unexpectedly, in one of these peptides, in addition to the main region surrounding positions 13 and 14 that is critical for binding, a single $Gly^{36} \rightarrow Ala^{36}$ (G36A) mutation disrupted binding in almost half of the samples, whereas none of the double- or triple-alanine mutants that also included the adjacent positions [Lys^{35} (L35) and G37] affected binding (fig. S11). It is possible that G36 plays a role in helping the peptide adopt an antigenic conformation and multiple mutants containing the adjacent Leu or Gly residues rescue this ability. We occasionally saw other examples of mutations that resulted in patterns of disrupted binding with no simple explanation, illustrating the complexity of antibody-antigen interaction.

The discovery of recurring targeted epitopes led us to ask whether we could apply this knowledge to improve the sensitivity of viral detection with VirScan. We hypothesized that samples showing a strong response to a recurrently targeted "diagnostic" peptide, which we defined as a peptide enriched in at least 30% of known positive samples, are likely to be seropositive even if they do not meet our stringent cutoff requiring at least two non-overlapping enriched peptides. We tested how this modified criterion affected our sensitivity and specificity in detecting HIV and HCV and found that it reduced the number of false negatives without affecting the specificity of the assay (fig. S13). We next turned our attention to respiratory syncytial virus (RSV), a virus for which our detected seroprevalence was lower than reported epidemiological rates, suggesting imperfect sensitivity of our assay. We tested sera from 60 individuals for antibodies to RSV by ELISA and found that 95% were positive, above the reported sensitivity of the assay and consistent with near-universal exposure to this pathogen. Applying the modified criterion to these samples increased our rate of detection by VirScan from 63% to 97% (table S2). These data suggest that assigning more weight to recurrently targeted epitopes can enhance the sensitivity of VirScan and that the performance of the assay can be improved by screening known positives for a particular virus.

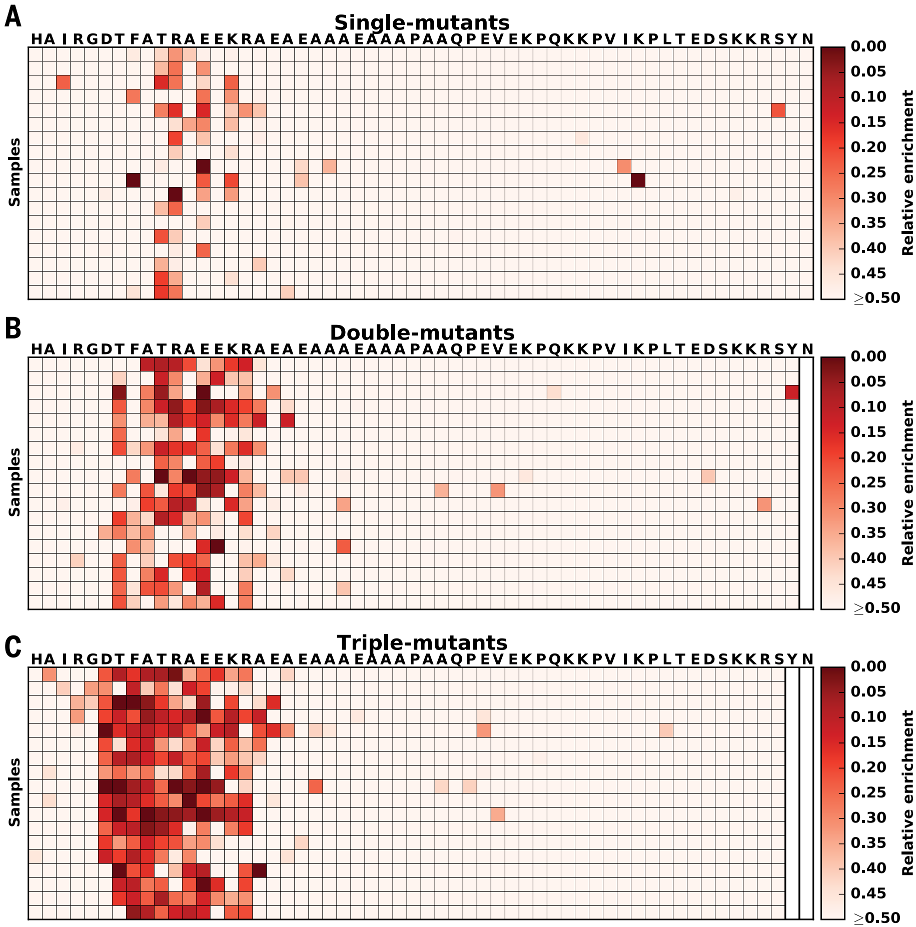

Fig. 4. Recognition of common epitopes within an antigenic peptide from human adenovirus C penton protein (*L2*) across individuals. Each row is a sample. Each column denotes the first mutated position for the (**A**) single-, (**B**) double-, and (**C**) triple-alanine mutant peptide starting with the N terminus on the left. Each double- and triple-alanine mutant contains two or three adjacent mutations, respectively, extending toward the C terminus from the colored cell. The color intensity of each cell indicates the enrichment of the mutant peptide relative to the wild-type. For double-mutants, the last position is blank. The same is true for the last two positions for triple mutants. Data shown are the mean of two replicates. Single-letter amino acid abbreviations are as follows: F, Phe; H, His; I, Ile; K, Lys; N, Asn; P, Pro; Q, Gln; R, Arg; T, Thr; V, Val; and Y, Tyr.

Discussion

We have developed VirScan, a technology for identifying viral exposure and B cell epitopes across the entire known human virome in a single, multiplex reaction using less than a drop of blood. VirScan uses DNA microarray synthesis and bacteriophage display to create a uniform, synthetic representation of peptide epitopes comprising the human virome. Immunoprecipitation and high-throughput DNA sequencing reveals the peptides recognized by antibodies in the sample. VirScan is easily automated in 96-well format to enable high-throughput sample processing. Barcoding of samples during PCR enables pooled analysis that can dramatically reduce the per-sample cost. The VirScan approach has several advantages for studying the effect of viruses on the host immune system. By detecting antibody responses, it can identify infectious agents that have been cleared after an effective host response. Current serological methods of antiviral antibody detection typically use the selection of a single optimized antigen in order to achieve high accuracy. In contrast, VirScan's unique approach does not require such optimization in order to obtain similar performance. VirScan achieves sensitive detection by assaying each virus's complete proteome to detect any antibodies directed to epitopes that can be captured in a 56-residue fragment and specificity by computationally eliminating cross-reactive antibodies. This unbiased approach identifies exposure to less well-studied viruses for which optimal serological antigens are not known and can be rapidly extended to include new viruses as they are discovered (25).

Although sensitive and selective, VirScan has a few limitations. First, it cannot detect epitopes that require post-translational modifications. Secondly, it cannot detect epitopes that involve discontinuous sequences on protein fragments greater than 56 residues. In principle, the latter can be overcome by using alternative technologies that allow for the display of full-length proteins, such as parallel analysis of translated open reading frames (PLATO) (26). Third, VirScan is likely

to be less specific compared with certain nucleic acid tests that discern highly related virus strains. However, VirScan demonstrates excellent serological discrimination among similar virus species, such as HSV1 and HSV2, and can even distinguish the genotype of HCV 69% of the time. We envision that VirScan will become an important tool for first-pass unbiased serologic screening applications. Individual viruses or viral proteins uncovered in this way can subsequently be analyzed in further detail by using more focused assays, as we have demonstrated for a panel of immunodominant epitopes.

We have demonstrated that VirScan is a sensitive and specific assay for detecting exposure to viruses across the human virome. Because it can be performed in high-throughput and requires minimal sample and cost, VirScan enables rapid and cost-effective screening of large numbers of samples to identify population-level differences in virus exposure across the human virome. In this work, we analyzed over 106 million antibody-viral peptide interactions in a comprehensive study of pan-virus serology in a large, diverse population. In doing so we detected 84 different viral species in two or more individuals. This is likely to be an underestimate of the history of viral infection, because only low levels of circulating antibodies may remain from infections that were cleared in the distant past. In addition, an individual could be infected by multiple distinct strains of each viral species. We identified known and novel differences in virus exposure between groups differing in age, HIV status, and geographic location across four different continents. Our results are largely consistent with previous studies, validating the effectiveness of VirScan. For example, CMV antibodies were found in significantly higher frequencies in Peru, Thailand, and South Africa, whereas KSHV and HSV1 antibodies were detected more frequently in Peru and South Africa but not in Thailand (*16*, *27*–*31*). We also uncovered previously undocumented serological differences, such as an increased rate of antibodies against adenovirus B and RSV in HIV-positive individuals compared with HIV-negative individuals. These differences may provide insight into how HIV co-infection alters the balance between host immunity and resident viruses, as well as help to identify pathogens that may increase susceptibility to HIV and other heterologous infections. HIV infection may reduce the immune system's ability to control reactivation of normally dormant resident viruses or to prevent opportunistic infections from taking hold and triggering a strong adaptive immune response. Beyond the epidemiological applications demonstrated here, VirScan could also be applied to identify viral exposures that correlate with disease or other phenotypes in virome-wide association studies.

Our results identified a large number of novel B cell epitopes, cumulatively nearly doubling the number of all previously identified viral epitopes. We have used our data to identify globally immunodominant and commonly recognized "public" epitopes. For most species of viruses, one or more peptides are individually recognized in over 70% to 95% of samples positive for that species (table S3). We identified a set of two peptides that together are recognized by >95% of all screened samples and a set of five peptides that together are recognized in >99% of screened samples. These public epitopes could be used to improve vaccine design by piggybacking on the existing antibody response against them. Fusing a public B cell epitope to a protein in a vaccine to which we hope to induce an immune response may increase a vaccine's efficacy among a broad population by improving presentation of that protein and aiding affinity maturation. Preexisting B cells recognizing the public epitope can act as antigen presenting cells to process and present T cell epitopes of the fused vaccine target on MHC class I and II (*32*). Antibodies secreted by these B cells can also participate in immune complexes with the fused vaccine target, which are critical for follicular dendritic cells to prime class switching and affinity maturation of B cells recognizing other epitopes on the fused antigen (*33*). Last, we demonstrated that applying more weight to these public epitopes increases the sensitivity of VirScan without significantly affecting specificity, suggesting that this limited subset of peptides can serve as the basis for the next generation of our assay or for other novel diagnostics.

We also found that the precise epitopes recognized by the B cell response are highly similar among individuals across many viral proteins. One possible model for this notable similarity is that these regions possess properties favorable for antigenicity, such as accessibility. Another model is that the same or highly similar B cell receptor sequences that recognize these epitopes are commonly generated. Identical T cell receptor sequences ("public" clonotypes) have been found in multiple individuals and are thought to be the result of biases during the recombination process that favor certain amino acid sequences (*34*). V(D)J recombination of the immunoglobulin heavy- and light-chain loci is also heavily biased (*35*). Highly similar or even identical complementarity determining region 3 (CDR3) sequences have been observed in dengue virus–specific antibodies from different individuals (*36*). It is possible that, rather than being an exception for dengue-specific antibodies, this represents a general phenomenon: Inherent biases in V(D)J recombination generate the same or similar antibodies in multiple individuals that recognize highly similar epitopes. Slight differences in the antibody CDR3 sequence may subtly alter antibody-antigen interaction, leading to the slight variations observed in the extent of critical epitope regions. Sequencing of antigen-specific antibody genes will be required to investigate these possibilities. The same principle may also apply to T cell epitopes and their cognate T cell receptors.

VirScan is a method that enables human virome-wide exploration—at the epitope level—of immune responses in large numbers of individuals. We have demonstrated its effectiveness for determining viral exposure and characterizing viral B cell epitopes in high throughput and at high resolution. Our preliminary studies have revealed intriguing general properties of the human immune system, both at the individual and population scale. VirScan will be an important tool in uncovering the effect of host-virome interactions on human health and disease and could easily be expanded to include other human pathogens such as bacteria, fungi, and protozoa.

Materials and methods

Human donor samples

Specimens originating from human donors were collected after informed written consent was obtained and under a protocol approved by the local governing human research protection committee. Secondary use of all samples for the purposes of this work was exempted by the Brigham and Women's Hospital Institutional Review Board (protocol number 2013P001337). Samples included donors residing in Thailand (n = 48), Peru (n = 48), South Africa (n = 48), and the Unites States, including HIV^+ donors (n = 61) and HCV^+ donors (n = 26). All serum and plasma samples were stored in aliquots at –80°C until use.

Design and cloning of viral peptide and scanning mutagenesis library sequences

For the virome peptide library, we first downloaded all protein sequences in the UniProt database from viruses with human host and collapsed on 90% sequence identity [www.uniprot.org/uniref/?query=uniprot:(host: "Human+[9606]")+identity:0.9]. The clustering algorithm UniProt represents each group of protein sequences sharing at least 90% sequence similarity with a single representative sequence. Then, we created 56–amino acid (aa) peptide sequences tiling through all the proteins with 28-aa overlap. We reverse-translated these peptide sequences into DNA codons optimized for expression in *Escherichia coli*, making synonymous mutations when necessary to avoid restriction sites used in subsequent cloning steps (EcoRI and XhoI). Last, we added the adapter sequence AGGAATTCCGCTGCGT to the 5′ end and CAGGGAAGAGCTCGAA to the 3′ end to form the 200-nucleotide (nt) oligonucleotide sequences.

For the scanning mutagenesis library, we first took the sequences of the peptides to be mutagenized. For each peptide, we made all single-mutant, and consecutive double- and triple-mutant, sequences scanning through the whole peptide. Non-alanine amino acids were mutated to alanine, and alanines were mutated to glycine. We reverse-translated these peptide sequences into DNA codons, making synonymous mutations when necessary to avoid restriction sites used in subsequent cloning steps (EcoRI and XhoI). We also made synonymous mutations to ensure that the 50 nt at the 5′ end of peptide sequence is unique to allow unambiguous mapping of the sequencing results. Last, we added the adapter sequence AGGAATTCCGCTGCGT to the 5′ end and CAGGGAAGAGCTCGAA to the 3′ end to form the 200-nt oligonucleotide sequences.

The 200-nt oligonucleotide sequences were synthesized on a releasable DNA microarray. We PCR-amplified the DNA with the primers T7-PFA AATGATACGGCGGGAATTCCGCTGCGT) and T7-PRA (CAAGCAGAAGACTCGAGCTCTTCCCTG), digested the product with EcoRI and XhoI, and cloned the fragment into the EcoRI/SalI site of the T7FNS2 vector (8). The resulting library was packaged into T7 bacteriophage by using the T7 Select Packaging Kit (EMD Millipore) and amplified by using the manufacturer suggested protocol.

Phage immunoprecipitation and sequencing

We performed phage immunoprecipitation and sequencing by using a slightly modified version of previously published PhIP-Seq protocols (8, 10). First, we blocked each well of a 96-deep-well plate with 1 ml of 3% bovine serum albumin in TBST overnight on a rotator at 4°C. To each preblocked well, we added sera or plasma containing about 2 μg of immunoglobulin G (IgG) [quantified using a Human IgG ELISA Quantitation Set (Bethyl Laboratories)] and 1 ml of the bacteriophage library diluted to ~2×10^5 fold representation (2×10^{10} plaque-forming units for a library of 10^5 clones) in phage extraction buffer (20 mM Tris-HCl, pH 8.0, 100 mM NaCl, 6 mM $MgSO_4$). We performed two technical replicates for each sample. We allowed the antibodies to bind the phage overnight on a rotator at 4°C. The next day, we added 20 μl each of magnetic protein A and protein G Dynabeads (Invitrogen) to each well and allowed immunoprecipitation to occur for 4 hours on a rotator at 4°C. With a 96-well magnetic stand, we then washed the beads three times with 400 μl of PhIP-Seq wash buffer (50 mM Tris-HCl, pH 7.5, 150 mM NaCl, 0.1% NP-40). After the final wash, we resuspended the beads in 40 μl of water and lysed the phage at 95°C for 10 m. We also lysed phage from the library before immunoprecipitation ("input") and after immunoprecipitation with beads alone.

We prepared the DNA for multiplexed Illumina sequencing by using a slightly modified version of a previously published protocol (36). We performed two rounds of PCR amplification on the lysed phage material using hot start Q5 polymerase according to the manufacturer-suggested protocol (NEB). The first round of PCR used the primers IS7_HsORF5_2 (ACACTCTTTCCCTACACGACTCCAGTCAGGTGTGATGCTC) and IS8_HsORF3_2 (GTGACTGGAGTTCAGACGTGTGCTCTTCCGATCCGAGCTTATCGTCGTCATCC). The second round of PCR used 1 μl of the first-round product and the primers IS4_HsORF5_2 (AATGATACGGCGACCACCGAGATCTACACTCTTTCCCTACACGACTCCAGT) and a different unique indexing primer for each sample to be multiplexed for sequencing (CAAGCAGAAGACGGCATACGAGATxxxxxxxGTGACTGGAGTTCAGACGTGT, where "xxxxxxx" denotes a unique 7-nt indexing sequence). After the second round of PCR, we determined the DNA concentration of each sample by quantitative PCR and pooled equimolar amounts of all samples for gel extraction. After gel extraction, the pooled DNA was sequenced by the Harvard Medical School Biopolymers Facility using a 50–base pair read cycle on an Illumina HiSeq 2000 or 2500. We pooled up to 192 samples for sequencing on each lane and generally obtained ~100 million to 200 million reads per lane (500,000 to 1,000,000 reads per sample).

Informatics and statistical analysis

We performed the initial informatics and statistical analysis by using a slightly modified version of the previously published technique (8, 10). We first mapped the sequencing reads to the original library sequences by using Bowtie and counted the frequency of each clone in the "input" and each sample "output" (37). Because the majority of clones are not enriched, we used the observed distribution of output counts as a null distribution. We found that a zero-inflated generalized poisson distribution fits our output counts well. We used this null distribution to calculate a P value for the likelihood of enrichment for each clone. The probability mass function for the zero-inflated generalized poisson distribution is

$$P(Y = y) = \begin{cases} \pi + (1 - \pi)[\theta(\theta + \lambda)^{x-1} e^{-\theta - x\lambda}], y = 0 \\ (1 - \pi)[\theta(\theta + \lambda)^{x-1} e^{-\theta - x\lambda}], y > 0 \end{cases}$$

We used maximum likelihood estimation to regress the parameters π, θ, and λ to fit the distribution of counts after immunoprecipitation for all clones present at a particular frequency count in the input. We repeated this procedure for all of the observed input counts and found that θ and λ are well fit by linear regression and π by an exponential regression as a function of input count (fig. S1). Last, for each clone we used its input count and the regression results to determine the null distribution based on the zero-inflated generalized poisson model, which we used to calculate the $-\log_{10}(P$ value) of obtaining the observed count.

To call hits, we determined the threshold for reproducibility between technical replicates based on a previously published method (10). Briefly, we made scatter plots of the $\log_{10}$ of the $-\log_{10}$ (P values) and used a sliding window of width 0.005 from 0 to 2 across the axis of one replicate. For all the clones that fell within each window, we calculated the median and median absolute deviation of the $\log_{10}$ of the $-\log_{10}$ (P values) in the other replicate and plotted it against the window location (fig. S2). We called the threshold for reproducibility the first window in which the median was greater than the median absolute deviation. We found that the distribution of the threshold $-\log_{10}$ (P value) was centered around a mean of ~2.3 (fig. S12). So we called a peptide a hit if the $-\log_{10}$ (P value) was at least 2.3 in both replicates. We eliminated the 593 hits that came up in at least 3 of the 22 immunoprecipitations with beads alone (negative control for nonspecific binding). We also filtered out any peptides that were not enriched in at least two of the samples.

To call virus exposures, we grouped peptides according to the virus the peptide is derived from. We grouped all peptides from individual viral strains for which we had complete proteomes. The sample was counted as positive for a species if it was positive for any strain from that species. For viral strains that had partial proteomes, we grouped them with other strains from the same species to form a complete set and bioinformatically eliminated homologous peptides (see next paragraph). We set a threshold number of hits per virus based on the size of the virus. We found that there is approximately a power-law relationship between size of the virus and the average number of hits per sample (fig. S3). In comparing results from VirScan to samples with known infection, we empirically determined that a threshold of three hits for HSV1 worked the best. We used this value and the slope of the best fit line to scale the threshold for other viruses. We also set a minimum threshold of at least two hits in order to avoid false positives from single spurious hits.

To bioinformatically remove cross-reactive antibodies, we first sorted the viruses by total number of hits in descending order. We then iterated through each virus in this order. For each virus, we iterated through each peptide hit. If the hit shared a subsequence of at least 7 aa with any hit previously observed in any of the viruses from that sample, that hit was considered to be from a cross-reactive antibody and would be ignored for that virus. Otherwise, the hit is considered to be specific, and the score for that virus is incremented by one. In this way, we summed only the peptide hits that do not share any linear epitopes. We compared the final score for each virus to the threshold for that virus to determine whether the sample is positive for exposure to that virus.

To identify differences between populations, we first used Fisher's exact test to calculate a P value for the significance of association of virus exposure with one population versus another. Then, we constructed a null distribution of Fisher's exact P values by randomly permuting the sample labels 1000 times and recalculating the Fisher's exact P value for each virus. With use of this null distribution, we calculated the false discovery rate by dividing the number of permutation P values more extreme than the one observed by the total number of permutations.

IEDB epitope overlap analysis

We downloaded data for all continuous human B cell epitopes from IEDB and filtered out all nonviral epitopes (22). To avoid redundancy in these 4549 viral epitopes, we grouped together epitopes that are 100% identical or share a 7-aa subsequence, giving us 1559 nonredundant epitope groups. Of these groups, 1392 contain a member epitope that is also a subsequence of a peptide in the VirScan library. This represents the total number of epitopes we could detect by VirScan. To determine the number of epitopes we detected, we tallied the number of epitope groups with at least one member that is contained in a peptide that was enriched in one or two samples. Last, to determine the number of nonredundant new epitopes we detected, we grouped non-IEDB

epitopes containing peptides that share a seven-residue subsequence and counted the number of these nonredundant peptide groups.

Scanning mutagenesis data analysis

First, we estimated the fractional abundance of each peptide by dividing the number of reads for that peptide by the total number of reads for the sample. Then, we divided the fractional abundance of each peptide after immunoprecipitation by the fractional abundance before immunoprecipitation to get the enrichment. To calculate relative enrichment, we divided enrichment of the mutated peptide by enrichment of the wild-type peptide. Because most of the single-mutant peptides had wild-type levels of enrichment, we averaged enrichment of the wild-type peptide enrichment with the middle two quartiles of enrichment of single-mutant peptides to get a better estimate of the wild-type peptide enrichment.

RSV and HSV1 and 2 serology

Serum from 44 donors was tested for HSV1 and HSV2 antibodies by using the HerpeSelect 1 and 2 Immunoblot IgG kit (Focus Diagnostics) according to manufacturer's protocol. Serum from 60 donors was tested for RSV antibodies by using anti-RSV IgG Human ELISA Kit (ab108765) according to manufacturer's protocol.

REFERENCES AND NOTES

1. K. M. Wylie, G. M. Weinstock, G. A. Storch, Emerging view of the human virome. *Transl. Res.* **160**, 283–290 (2012). doi: 10.1016/j.trsl.2012.03.006; pmid: 22683423
2. B. A. Duerkop, L. V. Hooper, Resident viruses and their interactions with the immune system. *Nat. Immunol.* **14**, 654–659 (2013). doi: 10.1038/ni.2614; pmid: 23778792
3. E. S. Barton *et al*., Herpesvirus latency confers symbiotic protection from bacterial infection. *Nature* **447**, 326–329 (2007). doi: 10.1038/nature05762; pmid: 17507983
4. E. F. Foxman, A. Iwasaki, Genome-virome interactions: Examining the role of common viral infections in complex disease. *Nat. Rev. Microbiol.* **9**, 254–264 (2011). doi: 10.1038/nrmicro2541; pmid: 21407242
5. M. Lecuit, M. Eloit, The human virome: New tools and concepts. *Trends Microbiol.* **21**, 510–515 (2013). doi: 10.1016/j.tim.2013.07.001; pmid: 23906500
6. I. De Vlaminck *et al*., Temporal response of the human virome to immunosuppression and antiviral therapy. *Cell* **155**, 1178–1187 (2013). doi: 10.1016/j.cell.2013.10.034; pmid: 24267896
7. E. Hammarlund *et al*., Duration of antiviral immunity after smallpox vaccination. *Nat. Med.* **9**, 1131–1137 (2003). doi: 10.1038/nm917; pmid: 12925846
8. H. B. Larman *et al*., Autoantigen discovery with a synthetic human peptidome. *Nat. Biotechnol.* **29**, 535–541 (2011). doi: 10.1038/nbt.1856; pmid: 21602805
9. UniProt Consortium, Activities at the Universal Protein Resource (UniProt). *Nucleic Acids Res.* **42**, D191–D198 (2014). doi: 10.1093/nar/gkt1140; pmid: 24253303
10. H. B. Larman *et al*., PhIP-Seq characterization of autoantibodies from patients with multiple sclerosis, type 1 diabetes and rheumatoid arthritis. *J. Autoimmun.* **43**, 1–9 (2013). doi: 10.1016/j.jaut.2013.01.013; pmid: 23497938
11. C. Bialecki, H. M. Feder Jr., J. M. Grant-Kels, The six classic childhood exanthems: A review and update. *J. Am. Acad. Dermatol.* **21**, 891–903 (1989). doi: 10.1016/S0190-9622(89)70275-9; pmid: 2681288
12. J. H. Lee, W. K. Roth, S. Zeuzem, Evaluation and comparison of different hepatitis C virus genotyping and serotyping assays. *J. Hepatol.* **26**, 1001–1009 (1997). doi: 10.1016/S0168-8278(97)80108-0; pmid: 9186830
13. H. F. L. Wertheim *et al*., Key role for clumping factor B in Staphylococcus aureus nasal colonization of humans. *PLOS Med.* **5**, e17 (2008). doi: 10.1371/journal.pmed.0050017; pmid: 18198942
14. R. A. Manz, A. E. Hauser, F. Hiepe, A. Radbruch, Maintenance of serum antibody levels. *Annu. Rev. Immunol.* **23**, 367–386 (2005). doi: 10.1146/annurev.immunol.23.021704.115723; pmid: 15771575
15. M. Wang *et al*., Human anti-JC virus serum reacts with native but not denatured JC virus major capsid protein VP1. *J. Virol. Methods* **78**, 171–176 (1999). doi: 10.1016/S0166-0934(98)00180-3; pmid: 10204707
16. S. A. S. Staras *et al*., Seroprevalence of cytomegalovirus infection in the United States, 1988-1994. *Clin. Infect. Dis.* **43**, 1143–1151 (2006). doi: 10.1086/508173; pmid: 17029132
17. M. A. Reynolds, D. Kruszon-Moran, A. Jumaan, D. S. Schmid, G. M. McQuillan, Varicella seroprevalence in the U.S.: Data from the National Health and Nutrition Examination Survey, 1999-2004. *Public Health Rep.* **125**, 860–869 (2010).pmid: 21121231
18. J. I. Cohen, Epstein-Barr virus infection. *N. Engl. J. Med.* **343**, 481–492 (2000). doi: 10.1056/NEJM200008173430707; pmid: 10944566
19. L. Dong *et al*., A combination of serological assays to detect human antibodies to the avian influenza A H7N9 virus. *PLOS ONE* **9**, e95612 (2014). doi: 10.1371/journal.pone.0095612; pmid: 24755627
20. P. Patel *et al*., Prevalence and risk factors associated with herpes simplex virus-2 infection in a contemporary cohort of HIV-infected persons in the United States. *Sex. Transm. Dis.* **39**, 154–160 (2012). doi: 10.1097/OLQ.0b013e318239d7fd; pmid: 22249305
21. C. T. Stover *et al*., Prevalence of and risk factors for viral infections among human immunodeficiency virus (HIV)-infected and high-risk HIV-uninfected women. *J. Infect. Dis.* **187**, 1388–1396 (2003).pmid: 12717619
22. E. A. Engels *et al*., Risk factors for human herpesvirus 8 infection among adults in the United States and evidence for sexual transmission. *J. Infect. Dis.* **196**, 199–207 (2007). doi: 10.1086/518791; pmid: 17570106
23. R. Vita *et al*., The immune epitope database 2.0. *Nucleic Acids Res.* **38**, D854–D862 (2010). doi: 10.1093/nar/gkp1004; pmid: 19906713
24. H. Singh, H. R. Ansari, G. P. S. Raghava, Improved method for linear B-cell epitope prediction using antigen's primary sequence. *PLOS ONE* **8**, e62216 (2013). doi: 10.1371/journal.pone.0062216; pmid: 23667458
25. J. L. Mokili, F. Rohwer, B. E. Dutilh, Metagenomics and future perspectives in virus discovery. *Curr. Opin. Virol.* **2**, 63–77 (2012). doi: 10.1016/j.coviro.2011.12.004; pmid: 22440968
26. J. Zhu *et al*., Protein interaction discovery using parallel analysis of translated ORFs (PLATO). *Nat. Biotechnol.* **31**, 31–334 (2013). doi: 10.1038/nbt.2539; pmid: 23503679
27. Y. Urwijitaroon, S. Teawpatanataworn, A. Kitjareontarm, Prevalence of cytomegalovirus antibody in Thai-northeastern blood donors. *Southeast Asian J. Trop. Med. Public Health* **24** (suppl. 1), 180–182 (1993). pmid: 7886568
28. M. J. Cannon, D. S. Schmid, T. B. Hyde, Review of cytomegalovirus seroprevalence and demographic characteristics associated with infection. *Rev. Med. Virol.* **20**, 202–213 (2010). doi: 10.1002/rmv.655; pmid: 20564615
29. S. Mohanna *et al*., Human herpesvirus-8 in Peruvian blood donors: A population with hyperendemic disease? *Clin. Infect. Dis.* **44**, 558–561 (2007). doi: 10.1086/511044; pmid: 17243060
30. D. Ablashi *et al*., Seroprevalence of human herpesvirus-8 (HHV-8) in countries of Southeast Asia compared to the USA, the Caribbean and Africa. *Br. J. Cancer* **81**, 893–897 (1999). doi: 10.1038/sj.bjc.6690782; pmid: 10555764
31. J. S. Smith, N. J. Robinson, Age-specific prevalence of infection with herpes simplex virus types 2 and 1: A global review. *J. Infect. Dis.* **186** (suppl. 1), S3–S28 (2002). doi: 10.1086/343739; pmid: 12353183
32. A. Heit *et al*., CpG-DNA aided cross-priming by cross-presenting B cells. *J. Immunol.* **172**, 1501–1507 (2004). doi: 10.4049/jimmunol.172.3.1501; pmid: 14734727
33. Y. Aydar, S. Sukumar, A. K. Szakal, J. G. Tew, The influence of immune complex-bearing follicular dendritic cells on the IgM response, Ig class switching, and production of high affinity IgG. *J. Immunol.* **174**, 5358–5366 (2005). doi: 10.4049/jimmunol.174.9.5358; pmid: 15843533
34. M. F. Quigley *et al*., Convergent recombination shapes the clonotypic landscape of the naive T-cell repertoire. *Proc. Natl. Acad. Sci. U.S.A.* **107**, 19414–19419 (2010). doi: 10.1073/pnas.1010586107; pmid: 20974936
35. K. J. L. Jackson, M. J. Kidd, Y. Wang, A. M. Collins, The shape of the lymphocyte receptor repertoire: Lessons from the B cell receptor. *Front. Immunol.* **4**, 263 (2013). doi: 10.3389/fimmu.2013.00263; pmid: 24032032
36. P. Parameswaran *et al*., Convergent antibody signatures in human dengue. *Cell Host Microbe* **13**, 691–700 (2013). doi: 10.1016/j.chom.2013.05.008; pmid: 23768493
37. B. Langmead, C. Trapnell, M. Pop, S. L. Salzberg, Ultrafast and memory-efficient alignment of short DNA sequences to the human genome. *Genome Biol.* **10**, R25 (2009). doi: 10.1186/gb-2009-10-3-r25; pmid: 19261174

ACKNOWLEDGMENTS

We thank E. Unger and S. Buranapraditkun for providing reagents, K. Wucherpfennig (Harvard) and H. Ploegh (MIT) for critical reading of the manuscript, and TWIST Bioscience for providing access to their advanced oligonucleotide synthesis technology. The cohort in Durban, South Africa, was funded by the NIH (R37AI067073) and the International AIDS Vaccine Initiative (UKZNRSA1001). T.N. received additional funding from the South African Research Chairs Initiative, the Victor Daitz Foundation, and an International Early Career Scientist Award from the Howard Hughes Medical Institute. R.T.C. was funded by grants NIH DA033541 and AI082630. C.B. and J.S. were supported by NIH N01-AI-30024 and N01-AI-15422, NIH–National Institute of Dental and Craniofacial Research R01 DE018925-04, the HIVACAT program, and CUTHIVAC 241904. K.R. is supported by TRF Senior Research Scholar, the Thailand Research Fund; the Chulalongkorn University Research Professor Program, Thailand; and NIH grant N01-A1-30024. G.J.X. and T.K. were supported by the NSF Graduate Research Fellowships Program. S.J.E. and B.W. are Investigators with the Howard Hughes Medical Institute. G.J.X., T.K., H.B.L., and S.J.E. are inventors on a patent application (application no. PCT/US14/70902) filed by Brigham and Women's Hospital, Incorporated that covers the use of phage display libraries to detect antiviral antibodies.

SUPPLEMENTARY MATERIALS

www.sciencemag.org/content/348/6239/aaa0698/suppl/DC1
Supplementary Text
Figs. S1 to S14
Tables S1 to S3

12 October 2014; accepted 24 April 2015
10.1126/science.aaa0698

RESEARCH ARTICLE

ANTIBIOTICS

Targeting DnaN for tuberculosis therapy using novel griselimycins

Angela Kling,[1,2*] Peer Lukat,[1,2,3*] Deepak V. Almeida,[4,5] Armin Bauer,[6] Evelyne Fontaine,[7] Sylvie Sordello,[7] Nestor Zaburannyi,[1,2] Jennifer Herrmann,[1,2] Silke C. Wenzel,[1,2] Claudia König,[6] Nicole C. Ammerman,[4,5] María Belén Barrio,[7] Kai Borchers,[6] Florence Bordon-Pallier,[8] Mark Brönstrup,[3,6] Gilles Courtemanche,[7] Martin Gerlitz,[6] Michel Geslin,[7] Peter Hammann,[9] Dirk W. Heinz,[2,3] Holger Hoffmann,[6] Sylvie Klieber,[10] Markus Kohlmann,[6] Michael Kurz,[6] Christine Lair,[7] Hans Matter,[6] Eric Nuermberger,[4] Sandeep Tyagi,[4] Laurent Fraisse,[7] Jacques H. Grosset,[4,5] Sophie Lagrange,[7] Rolf Müller[1,2]†

The discovery of *Streptomyces*-produced streptomycin founded the age of tuberculosis therapy. Despite the subsequent development of a curative regimen for this disease, tuberculosis remains a worldwide problem, and the emergence of multidrug-resistant *Mycobacterium tuberculosis* has prioritized the need for new drugs. Here we show that new optimized derivatives from *Streptomyces*-derived griselimycin are highly active against *M. tuberculosis*, both in vitro and in vivo, by inhibiting the DNA polymerase sliding clamp DnaN. We discovered that resistance to griselimycins, occurring at very low frequency, is associated with amplification of a chromosomal segment containing *dnaN*, as well as the *ori* site. Our results demonstrate that griselimycins have high translational potential for tuberculosis treatment, validate DnaN as an antimicrobial target, and capture the process of antibiotic pressure-induced gene amplification.

The discovery of streptomycin, a natural antibiotic produced by *Streptomyces griseus*, marked the beginning of two formative disciplines within the field of infectious diseases—namely, the study of bacterial-derived (rather than fungal- or plant-derived) medicinal compounds and the drug treatment of tuberculosis (TB) (*1*). This achievement initiated decades of research in the discovery and use of anti-TB drugs, ultimately leading to the development of the 6-month, multidrug regimen currently used for the cure of drug-susceptible TB (*2*). Unfortunately, failures in the implementation of this curative regimen, which are partly due to the challenges of its complex and lengthy nature, have led to the development and transmission of drug-resistant strains of *Mycobacterium tuberculosis*. Today, TB remains an enormous global health burden, causing an estimated 1.3 million deaths and 8.7 million new cases in 2012, and a growing percentage of TB (more than 30% of new cases in some countries) is multidrug-resistant (*3*). Thus, new drugs addressing novel *M. tuberculosis* targets are needed to provide different therapy options for patients with drug-resistant TB and also to both shorten and simplify treatment of drug-sensitive TB. Ideally, these new drugs should be combined in regimens tackling both drug-sensitive and drug-resistant TB, representing a paradigm shift toward more universally useful TB treatment regimens.

Bacterial-derived natural products remain a rich source for antibacterial lead compounds. In fact, ~80% of the currently used antibiotics are either directly derived from bacterial metabolic pathways or represent structural derivatives of metabolites with improved pharmaceutical properties (*4*). However, due to the reduced interest in development of antibacterial drugs in the last decades of the 20th century, quite a number of promising natural product leads were not advanced to clinical development. Recently, natural product and antibiotic research has been revitalized, not only because of the urgent need to identify novel antibiotics but also owing to advanced technologies becoming available. Thus, researchers are now enabled to overcome hurdles in natural product research, such as target identification by deciphering the self-resistance mechanisms in producer strains through whole-genome sequencing and compound optimization by genetic engineering. Successful recent applications of these capabilities include the derivation of semisynthetic spectinamides found to be highly active against both drug-resistant and -susceptible *M. tuberculosis* strains (*5*) and the identification of InhA as the mycobacterial target of the *Dactylosporangium fulvum*–produced pyridomycin (*6*).

In a search for neglected antibiotics with high anti-TB potential, Sanofi reinvestigated griselimycin (GM) (Fig. 1), a cyclic peptide that was isolated from two strains of *Streptomyces* identified in the 1960s (*7*). GM was found to have antibacterial activity specifically against organisms within the *Corynebacterineae* suborder, notably including *Mycobacterium* species, which prompted the company Rhône-Poulenc to pursue development of GM as an anti-TB drug. The first human studies were promising but revealed poor pharmacokinetics of GM, in particular short plasma elimination half-life after oral administration (*8*, *9*). Following elucidation of the compound's structure (*10*, *11*), a derivatization program was initiated to find GM analogs with improved pharmacokinetic properties (*12*, *13*); however, this program was terminated in the 1970s after rifampin (RIF) became available for TB treatment. Because of earlier reports of the effectiveness of GM against drug-resistant *M. tuberculosis* (*14*, *15*), we recently reinitiated studies on this natural product lead with the ultimate goal of introducing a highly active, stable, and safe derivative of this compound class into the TB drug development pipeline.

Development of GM analogs

Our primary optimization goals for GM were to increase its potency, metabolic stability, and exposure. Metabolic stability profiling of natural, less abundant analogs of GM identified Pro^8 as a main site of metabolic degradation, supported by the finding that the methyl derivative [methyl-griselimycin (MGM)] (Fig. 1) was markedly more stable than GM itself after incubation with human liver microsomes (Table 1). Because only very small amounts of MGM are produced naturally, a total synthesis route was elaborated to provide access to MGM and related analogs (see supplementary text). Structure-activity relationships of new synthetic GM analogs resulting from this approach confirmed that incorporation of substituents at Pro^8 led to metabolically highly stable compounds and also indicated that increasing lipophilicity considerably increased in vivo exposure in plasma and lungs of mice, as well as in vitro activity against *M. tuberculosis* (see supplementary text). From these efforts, cyclohexyl-griselimycin (CGM) (Fig. 1) was identified. The minimum inhibitory concentration (MIC) values of CGM were 0.06 and 0.2 μg/ml for the drug-susceptible *M. tuberculosis* strain H37Rv in broth culture and within macrophage-like (RAW264.7) cells, respectively (Table 1). CGM exhibited time-dependent bactericidal activity in vitro (Fig. 2A). Although the unbound fraction of CGM in plasma was low (0.3 and 0.4% in human and mouse plasma, respectively), the MIC shift of CGM in the presence of human or mouse sera was only

[1]Department of Microbial Natural Products, Helmholtz Institute for Pharmaceutical Research Saarland (HIPS), Helmholtz Centre for Infection Research and Pharmaceutical Biotechnology, Saarland University, 66123 Saarbrücken, Germany. [2]German Centre for Infection Research (DZIF), Partner Site Hannover-Braunschweig, Hannover, Germany. [3]Helmholtz Centre for Infection Research (HZI), 38124 Braunschweig, Germany. [4]Center for Tuberculosis Research, Johns Hopkins University School of Medicine, Baltimore, MD 21231, USA. [5]KwaZulu-Natal Research Institute for Tuberculosis and HIV (K-RITH), Durban 4001, South Africa. [6]Sanofi-Aventis R&D, LGCR/Chemistry, Industriepark Höchst, 65926 Frankfurt am Main, Germany. [7]Sanofi-Aventis R&D, Infectious Diseases Therapeutic Strategic Unit, 31036 Toulouse, France. [8]Sanofi-Aventis R&D, Strategy, Science Policy & External Innovation (S&I), 75008 Paris, France. [9]Sanofi-Aventis R&D, Infectious Diseases Therapeutic Strategic Unit, 65926 Frankfurt, Germany. [10]Sanofi-Aventis R&D, Disposition Safety and Animal Research, 34184 Montpellier, France.
*These authors contributed equally to this work.
†Corresponding author. E-mail: rolf.mueller@helmholtz-hzi.de

around five- or sevenfold, respectively (Table 1). The MIC values of CGM were similar for a range of *M. tuberculosis* strains from different lineages (representing geographical and evolutionary diversity), as well as for strains monoresistant to first- or second-line anti-TB drugs (table S1), demonstrating a lack of cross-resistance. GM, MGM, and CGM were not active against *M. tuberculosis* under hypoxic conditions in which the bacteria were not actively multiplying (Table 1). CGM exhibited optimized adsorption, distribution, metabolism, and excretion properties; that is, high oral bioavailability (89%), moderate total plasma clearance (1.1 liter/hour per kilogram), and a large volume of distribution (5.5 liter/kg). Exposure and half-life in mice (supportive of once-daily dosing) were higher than for GM and MGM. In addition, over the 30- to 100-mg/kg dose range, CGM exposure in plasma and lung increased roughly with dose proportionality and continued to increase over the 100- to 600-mg/kg dose range (table S2). Moreover, CGM exhibited limited potential for drug-drug interactions, as neither CYP induction nor inhibition was observed, and the contribution of CYP to degradation was balanced, indicating that induction of CYPs by other drugs should not affect CGM exposures (Table 1). CGM (at concentrations up to 5000 μg/ml) did not increase the number of revertant colonies in Ames II testing with TA98 and mixed strains of *Salmonella typhimurium*, indicating a lack of mutagenicity. Additionally, no chromosomal aberrations were observed in CGM-exposed mammalian cells, as tested with L5178Y cells (at CGM concentrations up to 1000 μg/ml, with or without metabolic activation) and with CHO-K1 cells (fig. S1), indicating a lack of genotoxicity.

Fig. 1. Chemical structure of GM and derivatives. Substitutions at Pro[8] increased metabolic stability.

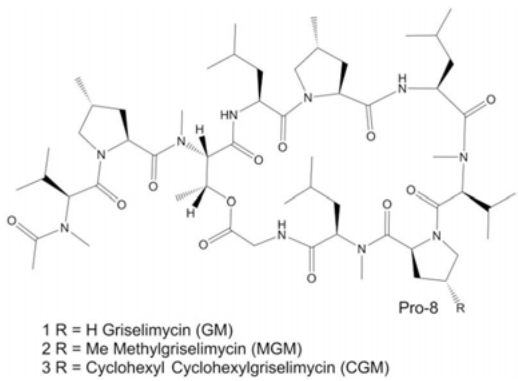

Table 1. Optimization parameters for GM and derivatives. C_{max}, maximum concentration; AUC, area under the concentration curve; V_{ss}, volume of distribution; $t_{1/2}$, half-life; nd, not determined. Pharmacokinetic parameters (C_{max}, AUC, and $t_{1/2}$) were determined after a single oral administration of 30 mg/kg of the test compound in mice. For oral bioavailability, a single oral dose was compared to a single intravenous dose of 3 mg/kg. $F = [AUC_{oral}]/[AUC_{iv}]$, the ratio of exposure of an equivalent dose after nonintravenous (in this case, oral) and intravenous administration as a measure of bioavailability.

Optimization parameter	**Compound**		
	GM	**MGM**	**CGM**
MIC (μg/ml) for *M. tuberculosis* in liquid culture	1	0.6	0.06
MIC (μg/ml) for *M. tuberculosis* in liquid culture containing 25% human serum	1.2	0.9	0.3
MIC (μg/ml) for *M. tuberculosis* in liquid culture containing 25% mouse serum	1.2	0.8	0.4
MIC (μg/ml) for *M. tuberculosis* in liquid culture under anaerobic conditions	>33	>33	>35
MIC (μg/ml) for *M. tuberculosis* in macrophages	6.2	2.1	0.2
Unbound fraction (%) in human plasma	nd	7.9	0.3
Unbound fraction (%) in mouse plasma	nd	11.9	0.4
Metabolic stability in human liver microsomes (% remaining compound after 20 min)	62	100	86
Metabolic degradation/clearance from human liver microsomes (μl/min per mg)	187.5	3	6.75
CYP1A2, CYP2B6, and CYP3A induction (Yes/No)	nd	nd	No
CYP3A4 inhibition (μg/ml)	>33	>33	>35
Contribution of CYP3A4 to degradation in human liver microsomes (%)	38	nd	19
C_{max} (ng/ml) in plasma	3900	2820	2620
C_{max} (ng/g) in lung tissue	2580	8550	8850
AUC (ng·hour/ml) in plasma	5100	6600	23,000
AUC (ng·hour/ml) in lung tissue	5900	12,000	70,000
Clearance (liters/hour per kg)	2.4	2.1	1.1
V_{ss} (liters/kg)	1.2	1.6	5.5
$t_{1/2}$ (hours) in plasma	2.0	2.4	4.3
$t_{1/2}$ (hours) in lung tissue	3.9	4.3	4.3
Oral bioavailability (F) (%)	48	47	89

CGM activity in mouse models of TB

To assess the in vivo activity of CGM, we conducted dose-ranging experiments using mouse models of acute and chronic TB (see supplementary materials and methods). In the acute model, which is used to test the antimicrobial activity of compounds and regimens against bacteria actively multiplying in vivo, mice were aerosol-infected with *M. tuberculosis*, and oral administration of CGM (at daily doses ranging from 10 to 600 mg/kg) was initiated on the day after infection. After 4 weeks, all of the untreated control mice had died, whereas all of the mice treated with any dose of CGM survived. As expected, mice treated with isoniazid (INH) at 10 mg/kg experienced a decrease of ~3 $\log_{10}$ colony-forming units (CFUs) in the lungs, whereas mice receiving RIF at 10 mg/kg, which is expected to have poor initial activity in this model (*16*), did not die but did experience bacterial growth in the lungs (Fig. 2B). In mice receiving 10 and 25 mg/kg of CGM, neither the development of gross lung lesions (fig. S2) nor bacterial growth could be prevented (Fig. 2B). Total prevention of bacterial growth and gross lung lesions occurred in mice treated with 50 mg/kg, defining the minimal effective dose of CGM. The CFU count decreased by ~2 $\log_{10}$ in the lungs compared with the CFU count at initiation of treatment with a daily 100-mg/kg dose, defining the minimal bactericidal dose. In mice treated with 200-, 400-, and 600-mg/kg doses, a dose-dependent decline in lung CFU counts was observed (P < 0.0001), and the lungs of mice receiving the 600-mg/kg daily dose were culture-negative after 4 weeks of treatment. In the chronic model, which is used to test for antimicrobial activity against a stable bacterial population in vivo, mice were aerosol-infected, achieving a low implantation of 2.21 $\log_{10}$ CFU per lung, and treatment was initiated 4 weeks later when a stable, host-contained infection was established at nearly 7 $\log_{10}$ CFU per lung. After 4 weeks of treatment, all doses of CGM exhibited some degree of activity, with doses of 50 mg/kg and higher resulting in statistically significant differences in lung CFU counts from the untreated control (P ≤ 0.01) (Fig. 2C and fig. S2). Treatment with CGM at 100 mg/kg resulted in a decrease in lung CFU counts similar to that observed with RIF at 10 mg/kg. In both

of these experiments, no overt adverse effects of CGM administration were observed in treated mice.

Due to the promising bactericidal activity of CGM when administered as monotherapy, we evaluated the activity of this compound when administered together with first-line anti-TB drugs in the mouse model of TB chemotherapy. Standard TB treatment comprises a 2-month intensive phase of daily RIF, INH, pyrazinamide (PZA), and ethambutol, followed by a 4-month continuation phase of daily RIF and INH. We designed an experiment to assess the bactericidal activity of CGM (at the minimal bactericidal dose of 100 mg/kg per day) used alone and in combination during the first 3 months of treatment. Mice were aerosol-infected with *M. tuberculosis* (implantation of 3.26 $\log_{10}$ CFU per lung), and treatment was initiated 2 weeks after infection, when the lung CFU count had reached 7.43 $\log_{10}$. In these experimental conditions, CGM alone was as active as INH (the most bactericidal first-line drug), reducing CFU counts in the lungs of mice by 3.78 $\log_{10}$ over 3 months, indicating that on a molar basis, CGM (1196 g/mol) had equivalent potency to INH (137 g/mol). However, at any time point, the combination of INH and CGM was as active as either INH or CGM alone. The combination of CGM with PZA was as active as the standard combination of INH, RIF, and PZA, reducing lung CFU counts in the mice by 5.5 $\log_{10}$ over 3 months (table S3). Additionally, the combination of CGM with RIF was much more active than the standard combination (additional 2 $\log_{10}$ CFU decline), nearly resulting in mouse lung culture conversion by week 12 of treatment. Even more impressive was the activity of the three-drug combination of RIF, PZA, and CGM that resulted in mouse lung culture conversion after only 8 weeks of treatment, representing killing of >7 $\log_{10}$ CFU in the lungs. In contrast and as expected, in the mice receiving the standard drug combination, lung CFU counts declined by ~4.4 and ~5.7 $\log_{10}$ by weeks 8 and 12, respectively (Fig. 2D and table S3). To assess the activity of CGM (at 100 mg/kg per day) during the continuation phase, mice received the standard regimen for the first 8 weeks of treatment, and then CGM was administered alone or in combination during weeks 8 to 20. The bacterial population remaining during the continuation phase had survived the initial 8 weeks of treatment and may have been enriched for organisms that are phenotypically tolerant to the antibiotics (i.e., the so-called "persisters"). The replacement of either of the drugs in the standard continuation regimen (RIF and INH) with CGM did not affect the time to mouse lung culture conversion (20 weeks), and no statistically significant differences were observed in lung CFU counts between these groups at any time point (table S4). The bactericidal activity of the combination of INH with CGM was not significantly different from that of CGM alone at any time point. However,

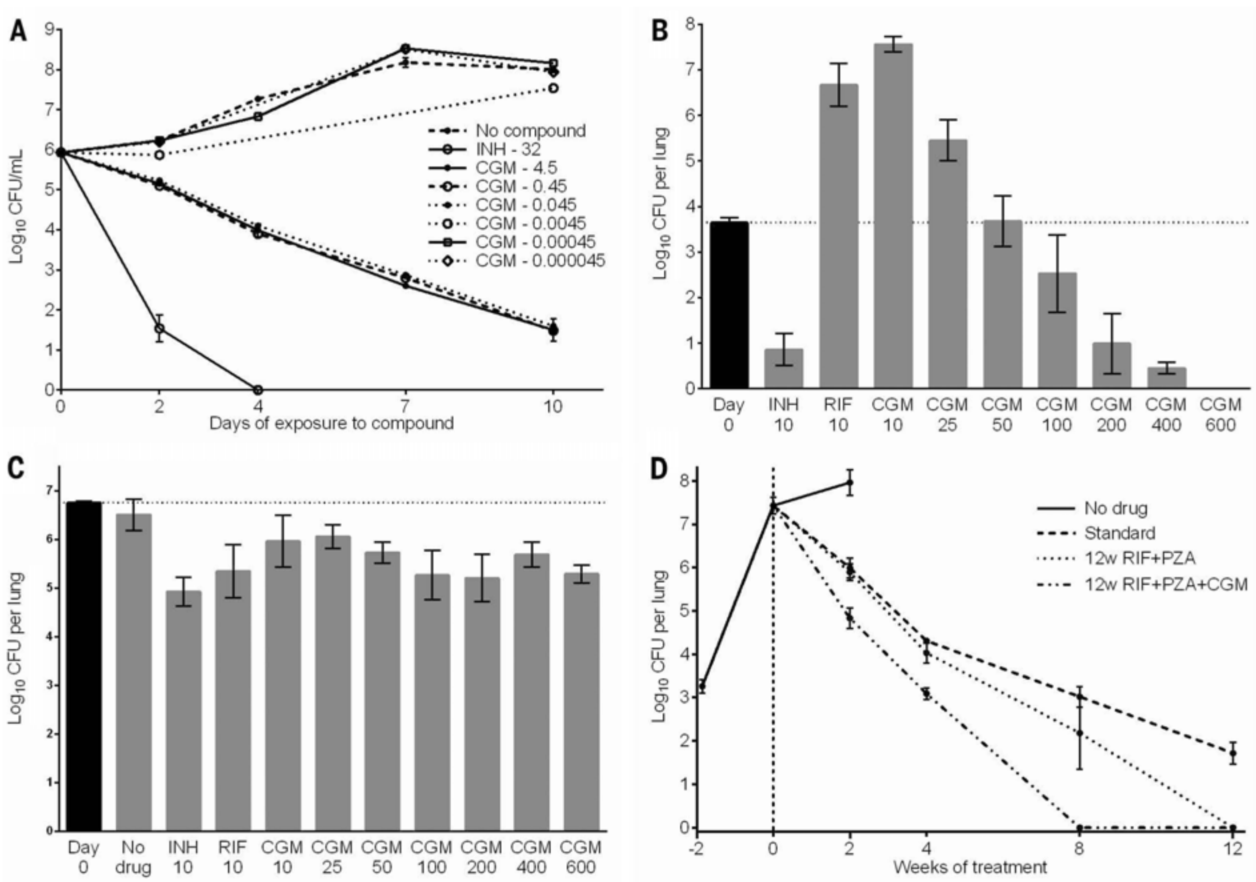

Fig. 2. In vitro and in vivo CGM activity against *M. tuberculosis*. (**A**) Activity of CGM against *M. tuberculosis* in 7H9 broth culture. The number following the compound abbreviation indicates the concentration in micrograms per milliliter. (**B**) CGM dose-ranging in the mouse model of acute TB: CFU counts after 4 weeks of treatment. Data represent the mean lung $\log_{10}$ CFU counts (five mice per group). Day 0 indicates lung CFU counts at treatment initiation (the day after infection). The number following the compound abbreviation indicates the dose in milligrams per kilogram per day. (**C**) CGM dose-ranging in the mouse model of chronic TB: CFU counts after 4 weeks of treatment. Data represent the mean lung $\log_{10}$ CFU counts (5 mice per group). Day 0 indicates lung CFU counts at treatment initiation (28 days after infection). The number following the compound abbreviation indicates the dose in milligrams per kilogram per day. (**D**) CGM administered in combination with anti-TB drugs during the intensive phase of treatment in a mouse model of TB. Data represent the mean lung $\log_{10}$ CFU counts (5 to 10 mice per group). Drug doses: RIF, 10 mg/kg per day; INH, 10 mg/kg per day; PZA, 150 mg/kg per day; CGM, 100 mg/kg per day. w, weeks. Standard treatment is 8 weeks of daily RIF + INH + PZA, followed by daily RIF + INH. Error bars in all panels represent SD. Dotted lines in (B) and (C) indicate the CFU counts in the lungs when treatment was initiated.

this combination was significantly more bactericidal than INH alone after 16 ($P \leq 0.05$) and 20 ($P \leq 0.0001$) weeks of treatment, with the effect being additive. Thus, taken together, our data indicate that CGM is highly active against actively replicating *M. tuberculosis*, both in vitro and in vivo, and also exhibits bactericidal activity against nonreplicating bacteria in vivo.

Self-resistance to GM in *Streptomyces*

The demonstrated activity of CGM against both drug-susceptible and -resistant *M. tuberculosis* (*14*, *15*) and the notable enhancement of the bactericidal activity of the standard TB drug regimen with the addition of CGM in mice suggested that the mechanism of action of CGM may be different from other anti-TB drugs. GM and MGM are naturally produced by some species of *Streptomyces*, and we identified the biosynthetic gene cluster responsible for GM and MGM production in *S.* sp. DSM-40835 (*17*), a strain naturally resistant to GM, and examined it for the presence of a possible resistance-conferring component. We found a homolog of the *dnaN* gene, which encodes the sliding clamp (also called the β clamp) of DNA polymerase, within the nonribosomal peptide megasynthetase cassette for GM synthesis (fig. S3A and table S5). This *dnaN* homolog, annotated as *griR*, encoded a protein with 51% identity to DnaN from the same strain (fig. S3, B and C). To examine the effect of GriR on susceptibility to GM, we introduced the gene into *Streptomyces coelicolor* A3(2), a strain susceptible to this natural product (and naturally lacking the entire GM biosynthesis cassette) (*18*). The presence of the *griR*-expressing plasmid allowed the strain to survive in the presence of GM (fig. S3D and table S6), suggesting that overexpression of *griR* mediated GM resistance. Comparison of the DnaN sequence from different microbial species revealed a clear cluster break between GM-sensitive and -resistant bacteria based on homology of the sliding clamp (fig. S3C and table S6). Taken together, these data suggest that GM and its derivatives target DnaN and may thus interfere with DNA replication.

GM resistance in mycobacteria

The intriguing relationship between *dnaN* sequence, copy number of the gene, and resistance to GM observed in *Streptomyces* compelled us to examine the mechanism(s) of resistance to this compound in mycobacteria. Using the fast-growing, nonpathogenic, and GM-sensitive (MIC: 4.5 μg/ml) *M. smegmatis*, we selected GM-resistant bacteria in vitro. The GM-resistant *M. smegmatis* (which occurred at an extremely low frequency; at a GM concentration of 10 μg/ml the frequency was 5×10^{-10}) exhibited an altered, elongated cellular morphology (Fig. 3A), as has been previously observed in GM-exposed *M. tuberculosis* (*9*). The GM-resistant bacteria were cross-resistant to MGM and CGM, but not to RIF or any other tested antibiotic (table S7). Genome sequence comparisons between the wild-type (WT) parent strain and mutants generated via stepwise exposure to increasing concentrations of GM (up to 40 μg/ml) revealed amplification of a chromosomal segment containing *dnaN*, with a single point mutation in the Pribnow box of the promoter region (115 G > A) (*19*) (tables S8 and S9), suggesting that mycobacterial resistance to GM, like that of *Streptomyces*, is mediated by amplification of DnaN. A number of inconsistent single-nucleotide polymorphisms (SNPs) were also observed. All mutants analyzed contained head-to-tail repeats of a chromosomal segment, but these segments or amplicons varied in size (ranging from 12 to 28 kb in length) and copy number (ranging from 3 to 49 copies), and occurrence of the amplicons was observed at different steps in the selection process (Fig. 3B, fig S4, and table S8). In addition to *dnaN* and its promoter, the amplicons contained *dnaA*, *recF*, *gyrB*, and up to more than 20 additional genes (table S9); they also all included the *ori* site. Amplification of a chromosomal segment was confirmed by Southern blot (Fig. 3, C and D). Based on the high copy number of the amplicons that include the *ori* site, formation of an extrachromosomal element could not be ruled out. However, plasmids were not detected by either standard plasmid isolation methods or agarose gel analysis. Yet in both *M. smegmatis* and *M. tuberculosis*, plasmids containing the same *ori* as the chromosome are usually maintained at a relatively low copy number (*20*, *21*), and naturally occurring plasmids in mycobacteria are known to be difficult to isolate (*22*).

Although the exact sequence of the amplicons varied among GM-resistant mutants, the 115 G > A transition mutation in the *dnaN* promoter occurred in all mutants at the 2.5-μg/ml GM exposure

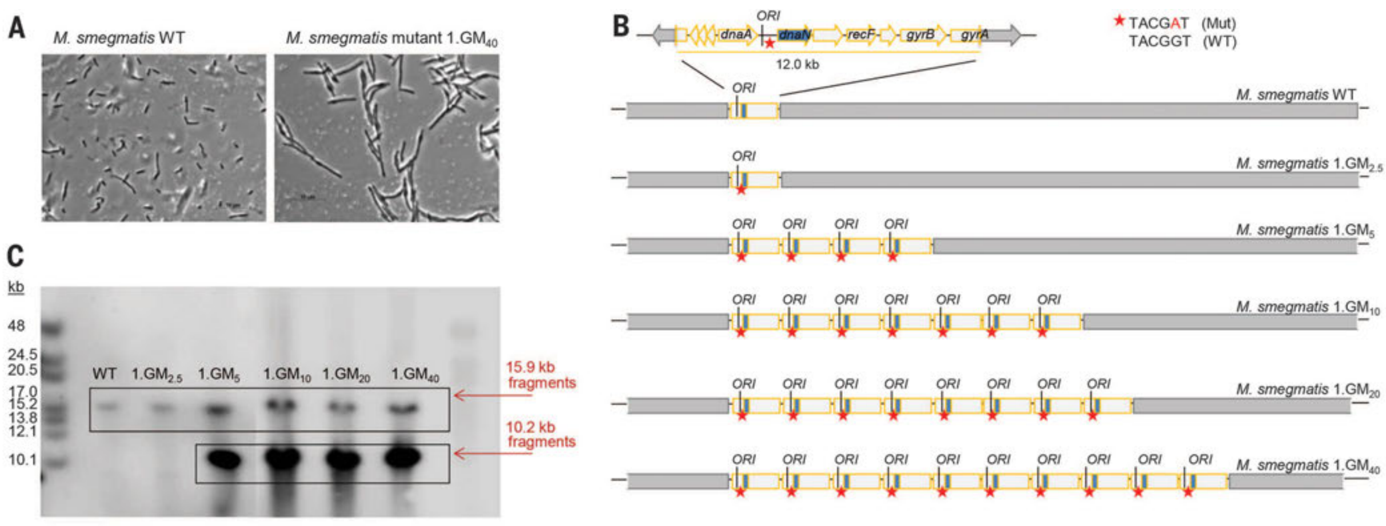

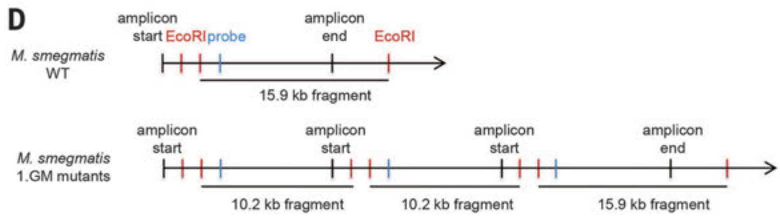

Fig. 3. Emergence of GM resistance in *M. smegmatis* by target amplification. (**A**) Phase-contrast images of WT and GM-resistant *M. smegmatis* cells. Scale bars, 10 μm. (**B**) Overview of the genetic changes associated with increased exposure to GM for *M. smegmatis* mutants $1.GM_{2.5}$ to $1.GM_{40}$ (subscripts indicate GM concentration in micrograms per milliliter when the mutant was obtained). Red stars represent the 115 G > A mutation in the Pribnow box of the *dnaN* promoter region. (**C**) Southern blot and (**D**) fragmentation pattern of *Eco*RI-digested genomic DNA of WT *M. smegmatis* and GM-resistant mutants. *Eco*RI cuts downstream of the *dnaN* gene inside the amplicon and upstream of the *dnaN* gene outside the amplicon, resulting in a 15.9-kb fragment for samples without amplicons and 15.9-kb and 10.2-kb fragments for samples with amplicons. *Eco*RI restriction sites are indicated in red; the binding site of the probe (in the *dnaN* gene) is indicated in blue.

step, leading to an MIC upshift from the baseline 4 μg/ml to 8 to 16 μg/ml (table S8). This point mutation was not consistently maintained in all steps of increasing GM concentration, being either replaced or complemented in mutants exposed to higher GM concentrations by amplification of a *dnaN*-containing chromosomal segment, which led to resistance up to or greater than 64 μg/ml. Resistance to GM was accompanied by considerable fitness costs, whereby *M. smegmatis* growth was negatively correlated with increasing levels of resistance (fig. S5), in some cases growing so poorly that we could not determine MIC values (table S8). Our data indicate that when GM is removed from the growth media, these genetic and phenotypic modifications begin to be reversed, including a decrease in amplicon copy number, a downshift in MIC, and less growth retardation (fig. S5 and table S8).

The unprecedented mechanism of gaining resistance to GM in our in vitro experiments with *M. smegmatis* prompted us to determine the relevance of these findings during in vivo infection with *M. tuberculosis*. To select resistant bacteria in vivo, nude mice were aerosol-infected with the fully drug-susceptible *M. tuberculosis* strain H37Rv and then treated by monotherapy with either INH (5 mg/kg) or CGM (100 mg/kg). Without the pressure from a functional immune system, monotherapy (when administered once daily, 5 days per week) with even the most bactericidal drug (INH) cannot prevent bacterial multiplication in these mice when drug levels in the blood fall below the therapeutic concentration, which, based on the half-life of INH (~1.5 hours) (*23*) and CGM (~4 hours) (Table 1) in the mouse, should occur daily and over the weekends. As anticipated, after 4 weeks of treatment, the lung bacterial loads began to increase in mice receiving either INH or CGM (fig. S6A). CFUs isolated from the CGM-treated mice were more than 10 times less sensitive to CGM (MIC: 1 to 2 μg/ml) (see proportion of CFUs growing on CGM-containing agar plates in table S10). Using the agar proportion method, the CGM-resistant *M. tuberculosis* were found to be fully susceptible to INH and RIF, as well as moxifloxacin and streptomycin. Genomic analysis of CGM-resistant colonies revealed an amplification of a 10.3-kb chromosomal segment containing the *dnaN* gene, together with four other genes and the *ori* site (fig. S6B and table S11), which was present in the CGM-resistant *M. tuberculosis* but absent in the WT parent strain. No SNPs were observed in the CGM-resistant bacteria compared with the WT parent strain. Thus, the mechanism of resistance observed in vitro with *M. smegmatis* was also observed in vivo with *M. tuberculosis*.

Characterization and crystal structure analysis of the GM-DnaN interaction

To confirm our genomic-based findings that DnaN is the target of GM and its derivatives, we used surface plasmon resonance (SPR) to characterize the binding of GM, MGM, and CGM with DnaN from *M. smegmatis*, *M. tuberculosis*, and *Escherichia coli*, as well as with the human sliding clamp [proliferating cell nuclear antigen (PCNA)]. Binding was also characterized with GriR, the DnaN homolog from the GM biosynthesis cluster in *Streptomyces*. SPR analysis demonstrated binding of GM to the mycobacterial sliding clamps with high affinity (equilibrium dissociation constant K_D: 8.3×10^{-11} M and 1.0×10^{-10} M for *M. smegmatis* and *M. tuberculosis* DnaN proteins, respectively) and a fast recognition rate and slow dissociation from the protein (*M. smegmatis*, association rate constant k_a: 2.2×10^7 M^{-1} s^{-1}, dissociation rate constant k_d: 1.9×10^{-3} s^{-1}; *M. tuberculosis*, k_a: 8.6×10^6 M^{-1} s^{-1}, k_d: 8.4×10^{-4} s^{-1}) (Table 2 and fig. S7). No binding was detected between GM and the human sliding clamp, but binding was observed at a significantly lower level with the *E. coli* clamp (K_D: 6.5×10^{-7} M), despite the lack of in vitro activity of GM against this organism (table S6). This lack of activity could be associated with the fast dissociation of GM from the *E. coli* DnaN compared with the mycobacterial sliding clamps (fig. S7), or it may be caused by efflux and/or impaired penetration in *E. coli*. Binding of GM was also observed to the GM resistance-conferring GriR, but at a significantly lower level compared with the mycobacterial DnaN proteins. It is possible that this weaker binding may be sufficient for self-resistance in *Streptomyces*. Binding of GM to GriR showed a kinetic profile similar to that of the *E. coli* DnaN, with fast association and dissociation rates but with somewhat lower affinity. MGM and CGM exhibited kinetic profiles similar to GM when interacting with the *M. tuberculosis* sliding clamp, whereas the interaction of *M. smegmatis* DnaN with CGM was characterized by a slower dissociation rate (k_d: 4.1×10^{-4} s^{-1}) and a slightly slower recognition rate (k_a: 4.5×10^6 M^{-1} s^{-1}). Thus, it may be the increasing lipophilicity (thus influencing the ability to traverse the cell wall) of the GM derivatives, rather than changes in

Table 2. SPR-based kinetic parameters of sliding clamp interactions with GM, MGM, and CGM. For *M. smegmatis* and *M. tuberculosis* DnaN, the K_D values were determined from the ratio between the kinetic rate constants (k_a/k_d), and the dissociative half-life $t_{1/2}$ was calculated by $\ln 2/k_d$. For interactions with fast on and off rates (*E. coli* and *S.* sp. DSM-40835 DnaN proteins), K_D values were determined by steady-state affinity analyses from the dependence of steady-state binding levels on analyte concentrations. Data represent mean and SD from three independent experiments. SPR sensorgrams are presented in fig. S7. na, not applicable.

Interactants		K_D (M) [SD]	k_a (M^{-1} s^{-1}) [SD]	k_d (s^{-1}) [SD]	$t_{1/2}$ (s) [SD]
Protein	**Compound**				
DnaN *M. smegmatis*	GM	8.3×10^{-11} [3.9×10^{-11}]	2.2×10^7 [5.4×10^5]	1.9×10^{-3} [8.7×10^{-4}]	450 [160]
	MGM	9.9×10^{-10} [5.7×10^{-11}]	1.6×10^7 [5.5×10^6]	1.3×10^{-3} [1.9×10^{-4}]	545 [179]
	CGM	1.2×10^{-11} [4.2×10^{-11}]	4.5×10^6 [3.4×10^6]	4.1×10^{-4} [1.7×10^{-4}]	1998 [785]
DnaN *M. tuberculosis*	GM	1.0×10^{-10} [8.1×10^{-10}]	8.6×10^6 [2.5×10^6]	8.4×10^{-4} [1.9×10^{-4}]	863 [183]
	MGM	1.1×10^{-10} [1.1×10^{-11}]	6.5×10^6 [2.1×10^6]	7.1×10^{-4} [2.1×10^{-4}]	1080 [361]
	CGM	2.0×10^{-10} [7.9×10^{-11}]	2.6×10^6 [7.8×10^5]	4.7×10^{-4} [1.4×10^{-4}]	1659 [643]
DnaN *E. coli*	GM	6.5×10^{-7} [9.5×10^{-8}]	na	na	na
	MGM	8.4×10^{-7} [5.2×10^{-8}]	na	na	na
	CGM	6.6×10^{-7} [3.0×10^{-8}]	na	na	na
GriR *S.* sp. DSM-40835	GM	5.8×10^{-6} [1.4×10^{-6}]	na	na	na
	MGM	6.6×10^{-6} [6.8×10^{-7}]	na	na	na
	CGM	6.5×10^{-6} [3.2×10^{-7}]	na	na	na
PCNA	GM	No binding detected			
	MGM	No binding detected			
	CGM	No binding detected			

binding kinetics, that explains their more potent antimycobacterial activity compared with GM.

To gain a better understanding of the molecular interactions responsible for GM-DnaN complex formation, cocrystal structures of GM and CGM bound to mycobacterial DnaN proteins were determined. The structures of *M. smegmatis* DnaN with GM and CGM were refined to resolutions of 2.1 and 2.3 Å, respectively, whereas the structures of the *M. tuberculosis* DnaN with bound GM and CGM were refined to resolutions of 2.2 and 1.9 Å, respectively (table S12). Both inhibitors were well defined in the electron density maps (fig. S8). GM and CGM bound to a hydrophobic cleft between domains II and III of the sliding clamp (Fig. 4A), which has been identified previously as the peptide interaction site responsible for the binding of DNA polymerases and other DNA-modifying enzymes (*24*, *25*). Binding of GM is mainly accomplished via hydrophobic interactions. Only two amino acid residues are involved in direct hydrogen bonding: Arg^{181} (or Arg^{183}) for *M. smegmatis* (or *M. tuberculosis*) forms two hydrogen bonds to the ligand, one via its backbone carbonyl oxygen and one via its guanidine moiety, whereas Arg^{394} (or Arg^{399}) for *M. smegmatis* (or *M. tuberculosis*) is involved in hydrogen bonding through its backbone amide nitrogen. Additionally, a bridging water molecule is coordinated between the ligand and Pro^{392} (or Pro^{397}) for *M. smegmatis* (or *M. tuberculosis*) (Fig. 4B and fig. S9). Subsite one of the peptide-binding pocket is occupied by the cyclic part of the ligand, whereas subsite two harbors the linear part of the GM molecule (Fig. 4C). This linear section and the adjacent half of the macrocycle superimpose very well for GM and CGM, whereas differences are visible on the opposite side of the macrocycle (figs. S10 and S11A). The ligands seem to be less tightly bound in this area, thus exhibiting a higher degree of flexibility (fig. S11B). The additional cyclohexyl moiety of CGM protrudes into the solvent and is involved in the formation of crystal contacts (fig. S12); the crystal packing might induce the observed differences in CGM binding as compared with GM and thus may not be physiologically relevant.

Binding of GM to the peptide interaction site of DnaN should lead to inhibition of the DnaN interaction with the polymerase III α subunit (DnaE1). To test this, we used SPR to assess the effect of GM on the binding of DnaN with a DnaE1 peptide that contains the internal DnaN binding motif and is known to be essential for processive replication in *E. coli* (*26*). Binding of this peptide decreased by half when the sliding clamp was saturated with GM (fig. S13). Inhibition of DnaE1 binding to DnaN should result in inefficient replication with decreased processivity and may lead to DNA strand breaks. Induction of the SOS response was observed in GM-exposed *M. smegmatis* (fig. S14).

Several functional and structural studies have indicated that the sliding clamp may be a feasible antibacterial target that can be addressed by small molecules and peptidic inhibitors (*24*, *27*–*29*). Although inhibition of DNA replication does not necessarily lead to immediate bacterial cell death, blocking the replication process may induce other lethal damage within the cell, such as induction of the SOS response (fig. S14) and/or toxin-antitoxin–like stress, as in the case of the quinolones, which block DNA replication by targeting topoisomerases but kill bacteria rapidly (*30*). In fact, DnaN was recently shown to be targeted by a toxin-antitoxin system in *Caulobacter crescentus* (*31*). The cell-elongation phenotype of GM-exposed mycobacteria indicates that blocking DNA replication induces a wider cellular response; this cell-elongation effect has also been reported in *M. fortuitum* upon exposure to the fluoroquinolone ofloxacin (*32*). Furthermore, in both Gram-positive and Gram-negative bacteria, the sliding clamp has been demonstrated to interact with DNA repair proteins, including many induced during the SOS response (*33*). Thus, the interaction of GMs with DnaN could also affect DNA repair, contributing to the bactericidal activity of the compounds. Whereas previously reported DnaN binders inhibited bacterial growth with only moderate potency, GM and its derivatives represent the first DnaN inhibitors with picomolar affinity to the target and high efficacy (MIC values ≤1.0 μg/ml) against mycobacteria. Known small-molecule DnaN binders targeted the deep hydrophobic pocket of subsite one, whereas subsite two remained empty. Peptidic inhibitors and the natural interacting peptides target both subsites; the linear segment and part of the macrocycle of GM superimposed very well with their backbone, thereby mimicking the conformation of a linear peptide bound to DnaN (fig. S15). The specific inhibition of mycobacteria by GM, which should leave commensal microbiota intact, constitutes an additional advantage with respect to the selection of resistance.

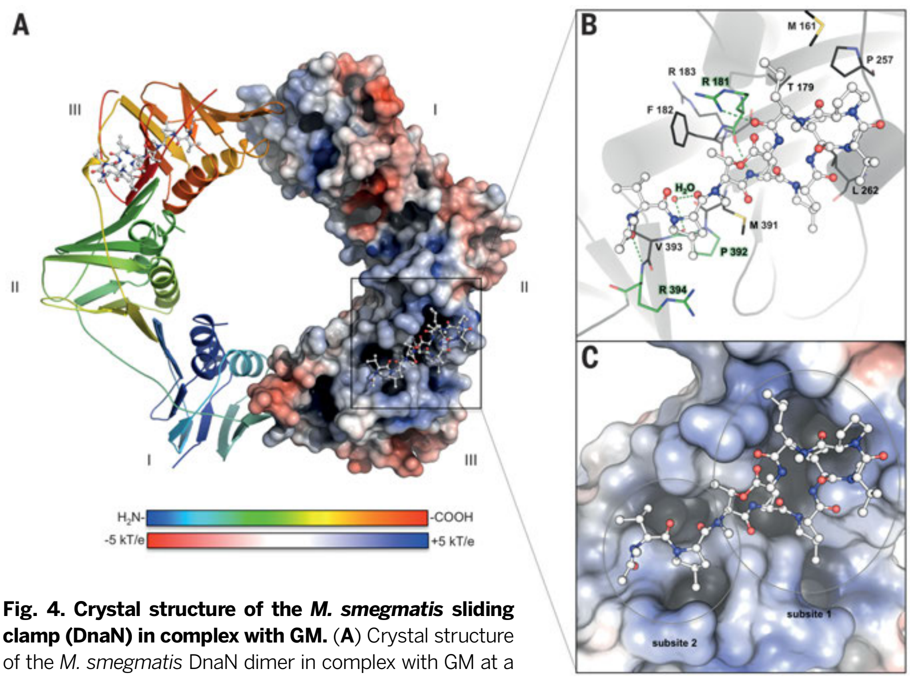

Fig. 4. Crystal structure of the *M. smegmatis* sliding clamp (DnaN) in complex with GM. (**A**) Crystal structure of the *M. smegmatis* DnaN dimer in complex with GM at a resolution of 2.1 Å. GM binds to a hydrophobic pocket between domains II and III, which is known as the protein-protein interaction site responsible for the recruitment of DNA polymerases by the sliding clamp. The cartoon representation of the left half of the homodimeric ring is colored from the N terminus (blue) to the C terminus (red). The second half of the ring is shown as surface representation colored according to the electrostatic surface potential, ranging from −5 *kT/e* (red) to +5 *kT/e* (blue) (*k*, Boltzmann's constant; *T*, temperature; *e*, charge of an electron). (**B**) Interactions between the ligand and the protein. The residues involved in hydrophobic contacts with GM are represented as gray sticks. The residues also involved in hydrogen bonding with the ligand are represented as green sticks. Hydrogen bonds are indicated by dashed green lines. F, Phe; R, Arg; M, Met; P, Pro; T, Thr; L, Leu; V, Val. (**C**) Surface representation of the binding pocket. The surface is colored according to the electrostatic surface potential. Both subsites of the binding pocket are indicated by circles.

Conclusion

Total synthesis of new GMs led to the optimized CGM, which demonstrated a clear potential for TB treatment by targeting the DNA polymerase sliding clamp. Currently, CGM and a few other GM derivatives are being further profiled to select the best drug candidate to move forward in development, with CGM being one of the lead compounds pursued in late preclinical studies involving broad toxicity testing. In this work, we have demonstrated the validity of DnaN as a drug target and have identified direct small-molecule–DnaN interactions that probably interrupt essential polymerase and DNA repair activities in mycobacteria, leading to killing both in vitro and in vivo. Through the selection of GM-or CGM-resistant bacteria, we discovered that resistance to these compounds is possible, albeit at a very

low frequency, and is mediated through multiplication of *dnaN*, whereby the resistance to GMs increases with increasing *dnaN* amplification. The nature of the amplicons, consisting of clonal repeats that differ slightly between bacterial isolates but all include the *ori* site, and the observed decrease in target amplification in the absence of GM suggest that the amplification is connected to severe fitness costs, as observed by the slow growth of the mutants. As exposure to GM triggered chromosomal duplications in a concentration-dependent manner in vitro, GM could possibly serve as a tool to study the mechanism of chromosomal duplication events in mycobacteria that have contributed to the natural variation between different lineages. Because there is no preexisting resistance to GMs due to the different mode of action compared with that of existing TB drugs, and because resistance occurs at an extremely low frequency and is associated with a severe fitness cost, this new series has the potential to contribute to drug regimens with utility for patients with both drug-sensitive and drug-resistant TB. In addition, our work has confirmed the sliding clamp as an antimicrobial target and revealed an unusual mechanism of conferring drug resistance that is applicable to the wider antibiotic discovery field.

REFERENCES AND NOTES

1. A. Smith, Ed., *Br. Med. J.* **1**, 278–279 (1946).
2. British Thoracic Society, *Br. J. Dis. Chest* **78**, 330–336 (1984).
3. World Health Organization, "Antimicrobial resistance: Global report on surveillance" (World Health Organization Press, Geneva, Switzerland, 2014).
4. D. J. Newman, G. M. Cragg, *J. Nat. Prod.* **75**, 311–335 (2012).
5. R. E. Lee *et al.*, *Nat. Med.* **20**, 152–158 (2014).
6. R. C. Hartkoorn *et al.*, *EMBO Mol. Med.* **4**, 1032–1042 (2012).
7. B. Terlain, J. P. Thomas, *Bull. Soc. Chim. Fr.* **6**, 2349–2356 (1971).
8. F. Bénazet *et al.*, in *Antibiotics – Advances in Research, Production and Clinical Use: Proceedings of the Congress on Antibiotics held in Prague, 15-19 June, 1964,* M. Herold, Z. Gabriel, Eds. (Butterworths, London, 1966), pp. 262–264.
9. H. Noufflard-Guy-Loé, S. Berteaux, *Rev. Tuberc. Pneumol. (Paris)* **29**, 301–326 (1965).
10. B. Terlain, J. P. Thomas, *C. R. Hebd. Seances Acad. Sci. Ser. C* **269**, 1546–1549 (1969).
11. B. Terlain, J. P. Thomas, *Bull. Soc. Chim. Fr.* **6**, 2357–2362 (1971).
12. G. Jolles, New cyclopeptides, G.B. Patent 1,252,553 (1971).
13. J. Bouchaudon, Nouveau cyclopeptide, sa préparation et les médicaments qui le contiennent, Fr. Patent 2,469,395 (1981).
14. Anonymous, New antibiotic product, its preparation and compositions containing it, G.B. Patent 966,124 (1964).
15. M. Toyohara, *Ann. Inst. Pasteur Microbiol.* **138**, 737–744 (1987).
16. E. L. Nuermberger, "The role of the mouse model in the evaluation of new antituberculosis drugs," in *Antituberculosis Chemotherapy*, P. R. Donald, P. D. Van Helden, Eds. (Karger, Basel, Switzerland, 2011), pp. 145–152, vol. 40, chap. 15.
17. M. Broenstrup *et al.*, Gene cluster for biosynthesis of griselimycin and methylgriselimycin. PCT Int. Appl. WO 2013/053857 (2013).
18. S. D. Bentley *et al.*, *Nature* **417**, 141–147 (2002).
19. L. Salazar, E. Guerrero, Y. Casart, L. Turcios, F. Bartoli, *Microbiology* **149**, 773–784 (2003).
20. M. H. Qin, M. V. Madiraju, M. Rajagopalan, *Gene* **233**, 121–130 (1999).
21. L. Salazar *et al.*, *Mol. Microbiol.* **20**, 283–293 (1996).
22. F. Movahedzadeh, W. Bitter, *Methods Mol. Biol.* **465**, 217–228 (2009).
23. J. Grosset, B. Ji, in *Mycobacteria Volume II Chemotherapy*, P. R. J. Gangadharam, P. A. Jenkins, Eds. (Chapman and Hall, New York, 1998), pp. 51–97.
24. K. A. Bunting, S. M. Roe, L. H. Pearl, *EMBO J.* **22**, 5883–5892 (2003).
25. D. Y. Burnouf *et al.*, *J. Mol. Biol.* **335**, 1187–1197 (2004).
26. P. R. Dohrmann, C. S. McHenry, *J. Mol. Biol.* **350**, 228–239 (2005).
27. G. Wijffels *et al.*, *J. Med. Chem.* **54**, 4831–4838 (2011).
28. Z. Yin *et al.*, *J. Med. Chem.* **57**, 2799–2806 (2014).
29. R. E. Georgescu *et al.*, *Proc. Natl. Acad. Sci. U.S.A.* **105**, 11116–11121 (2008).
30. K. Drlica, M. Malik, R. J. Kerns, X. Zhao, *Antimicrob. Agents Chemother.* **52**, 385–392 (2008).
31. C. D. Aakre, T. N. Phung, D. Huang, M. T. Laub, *Mol. Cell* **52**, 617–628 (2013).
32. H. Saito, T. Watanabe, T. Hirata, *Zentralbl. Bakteriol. Mikrobiol. Hyg. A* **268**, 448–455 (1988).
33. G. Wijffels, B. Dalrymple, K. Kongsuwan, N. E. Dixon, *IUBMB Life* **57**, 413–419 (2005).

ACKNOWLEDGMENTS

We thank the staff at beamlines P11 at PETRA III (DESY, Hamburg, Germany), X06DA at the Swiss Light Source (PSI, Villigen, Switzerland), and BL14.1 at BESSY II (Berlin, Germany) for assistance during data collection. R.M.'s research laboratory was supported by the German Ministry for Education and Research (BMBF) with grant fZ031598. Sanofi funded its contribution. D.V.A., N.C.A., and J.H.G. are supported by the KwaZulu-Natal Research Institute for Tuberculosis and HIV and the Howard Hughes Medical Institute. D.V.A., S.T., E.N., and J.H.G. were supported by two grants from Sanofi-Aventis (Amd. 14, grant 111937, and Amd. 7, grant 103671). We thank C. Wylegalla for technical assistance. We acknowledge the GMAK group at HZI for assistance with genome sequencing of bacterial mutants; S. Franzblau from the University of Illinois at Chicago for performing the in vitro MIC assays both under hypoxic conditions and with different strains of *M. tuberculosis* (testing agreement) and for the gift of luciferase-expressing *M. tuberculosis*; and P. Brodin from the Pasteur Institute, Lille, France, for the gift of GFP-expressing *M. tuberculosis* H37Rv. We thank A. Upton from the TB Alliance for analysis of the manuscript. The sequence of the *Streptomyces* sp. DSM-40835 GM biosynthetic gene cluster has been deposited in GenBank (accession number KP211414). Atomic coordinates and structure factors for the reported crystal structures have been deposited in the Protein Data Bank (identification numbers listed in table S12). A.B., E.F., S.S., M.B.B., F.B.-P., M.B., G.C., M.G., P.H., S.K., C.L., H.M., C.K., K.B., M.Ger., H.H., M.Ko., M.Ku., L.F., and S.L. are employed by Sanofi-Aventis R&D. Sanofi has filed patent applications on GM derivatives. Author contributions: A.K. performed resistance studies and DnaN expression and physicochemical analysis of the interaction of the protein with GM derivatives. P.L. performed expression of *M. smegmatis* DnaN and all structural biology experiments. P.L. and D.W.H. were involved in structural analyses and data interpretation. P.H. and F.B.P. identified the GM series from the Rhône-Poulenc archives. G.C., M.Ges., H.H., A.B., and E.F. designed and synthesized all GM derivatives. S.S., M.B.B., E.F., and A.B. managed the drug optimization program. S.L., M.B., and L.F. supervised the overall GM program at Sanofi. C.L. and M.B.B. designed and performed the in vitro experiments with *M. tuberculosis* H37Rv. S.K. and M.Ko. designed and performed the pharmacokinetic evaluations. M.Ko. and K.B. elucidated the metabolic degradation of GM and its derivatives. M.Ger. and M.Ku. performed analytics and structure confirmation of GM and its derivatives. M.Ku. and H.M. performed conformational analysis and designed models for GM derivatives with improved pharmacokinetic properties. D.V.A., N.C.A., E.N., S.T., and J.H.G. designed and performed all animal infection experiments, including associated assays, and analyzed all resulting data. N.Z. analyzed all genome data. J.H. performed activity assays and identified and analyzed resistant *M. smegmatis* strains. S.C.W. and C.K. identified and characterized the GM biosynthetic gene cluster. A.K., P.L., A.B., N.C.A., S.L., M.B., and R.M. conceived the studies and wrote the paper. A.K. and P.L. contributed equally to the study. All authors discussed the results and commented on the manuscript.

SUPPLEMENTARY MATERIALS

www.sciencemag.org/content/348/6239/1106/suppl/DC1
Materials and Methods
Supplementary Text
Figs. S1 to S15
Tables S1 to S12
References (*34*–*76*)

12 December 2014; accepted 16 April 2015
10.1126/science.aaa4690

REPORTS

MULTIFERROICS

Magnetoelectric domain control in multiferroic $TbMnO_3$

Masakazu Matsubara,[1,2*†] Sebastian Manz,[1*†] Masahito Mochizuki,[3,4] Teresa Kubacka,[5] Ayato Iyama,[6] Nadir Aliouane,[7] Tsuyoshi Kimura,[6] Steven L. Johnson,[5] Dennis Meier,[1] Manfred Fiebig[1]

The manipulation of domains by external fields in ferroic materials is of major interest for applications. In multiferroics with strongly coupled magnetic and electric order, however, the magnetoelectric coupling on the level of the domains is largely unexplored. We investigated the field-induced domain dynamics of $TbMnO_3$ in the multiferroic ground state and across a first-order spin-flop transition. In spite of the discontinuous nature of this transition, the reorientation of the order parameters is deterministic and preserves the multiferroic domain pattern. Landau-Lifshitz-Gilbert simulations reveal that this behavior is intrinsic. Such magnetoelectric correlations in spin-driven ferroelectrics may lead to domain wall–based nanoelectronics devices.

The entanglement of magnetic and electric long-range orders in magnetically induced ferroelectrics is a key to the manipulation of dielectric properties by magnetic fields and vice versa. Long believed to be a low-temperature phenomenon, these strong magnetoelectric correlations are now gaining importance in the light of recent studies that report spin-driven ferroelectricity in conditions approaching room temperature (*1*–*3*).

Present discussions on magnetoelectric phase control focus on the conversion of a state with one orientation of the magnetic and/or ferroelectric order parameter into a state with another orientation of these order parameters in the appropriate external fields. The end products of this operation—before and after the transition—are considered (*4–11*), whereas the actual switching process is not further discussed. It is this switching process, though, that is the key to practical magnetoelectric phase control. The switching occurs through transient states that are highly inhomogeneous, with many domains and domain walls interacting with one another in a complex fashion; this is in contrast to the single-domain end states. This process of transition determines functional issues such as hardness or durability or the speed of the magnetoelectric switching. Investigations of the multidomain equilibrium distribution of domains and their response to external fields in multiferroics are also rare (*12*, *13*).

Two aspects determine the magnetoelectric phase control of such a multidomain state: (i) the response of the domain pattern to small perturbations such as a gradual increase of the external field, and (ii) the response to a large perturbation such as a field-induced phase transition. In this work, we investigated examples for both types of perturbation. Our test case was multiferroic $TbMnO_3$, as the probably best-known compound with magnetically induced ferroelectricity.

In the archetypal spin-spiral ferroelectric $TbMnO_3$, a cycloidal spin structure emerges below the transition temperature T_C = 27 K and breaks inversion symmetry, giving rise to a spontaneous electric polarization, $\boldsymbol{P}_c$, along the *c* axis (*14*, *15*). This mechanism distinguishes the orthorhombic from the hexagonal multiferroics, in which the magnetic and electric order emerge independently so that they display a much weaker coupling (*16*). The polarization in $TbMnO_3$ is described as the product of the unit vector $\boldsymbol{e}_{ij}$ that connects neighboring spins at sites *i* and *j*, and their vector chirality, $\boldsymbol{S}_i \times \boldsymbol{S}_j$, according to $\boldsymbol{P} \propto \boldsymbol{e}_{ij} \times (\boldsymbol{S}_i \times \boldsymbol{S}_j)$ (*17*, *18*). Thus, changes in the spin arrangement and the polarization are rigidly connected. For example, a polarization flop ($\boldsymbol{P}_c \rightarrow \boldsymbol{P}_a$) can be triggered by spin reordering in a magnetic field along the *b* axis. This occurs as a first-order phase transition and has been studied for more than a decade (*14*, *19–21*). Data documenting the actual reorientation in the form of the evolving magnetoelectric domains are, however, unavailable. It remains an open question to which extent the transition and the associated functionalities are controllable.

We addressed this fundamental question by tracking the evolution of ferroelectric spin-cycloidal domains under external electric and magnetic fields in noninvasive imaging experiments. As the starting point for our analysis, we spatially resolved the as-grown domain structure of $TbMnO_3$. Imaging was done after zero-field cooling below T_C, using second harmonic generation (SHG) microscopy (*22*). SHG, the frequency doubling of a light wave in a material, is an optical process allowed in the leading order only in materials without inversion symmetry. It thus became an established, spatially resolving tool for probing the ferroelectric state (*23*). Domains with the spontaneous polarization $\pm\boldsymbol{P}$ emit SHG light waves $\pm\boldsymbol{E}_P(2\omega)$ with a relative 180° phase shift. If a SHG reference light wave is superimposed according to $\boldsymbol{E}_{ref}(2\omega) \pm \boldsymbol{E}_P(2\omega)$, opposite ferroelectric domain states can be imaged as regions of different brightness. This technique is used throughout our work (*24*).

The domain structure in Fig. 1A shows a stripe-like pattern of bright and dark regions, with a preferred orientation along the polar *c* axis. To demonstrate that these regions correspond to ferroelectric $\pm\boldsymbol{P}_c$ domains, we applied an electric field, E_c, as presented in Fig. 1, B to I. The image sequence documents a complete hysteretic poling cycle (Fig. 1J) and shows that E_c transforms the initial multidomain state (Fig. 1A) into either single-domain state (Fig. 1, D and G). This behavior, as well as the intermediate switching (including domain nucleation, forward growth with walls parallel to the electric field and $\boldsymbol{P}_c$, and subsequent sideways growth) corroborates the ferroelectric aspect of the domains (*25*). X-ray–imprinted domains deviate from this equilibrium state by forming walls perpendicular to $\boldsymbol{P}_c$ (*8*).

In each poling cycle, we observed new domain patterns. All images reflect the aforementioned preference for electrically neutral and hence energetically favorable "side-by-side" domain walls (Fig. 2C). The magnetic exchange interaction, too, is most pronounced along the *c* direction, so that both electric and magnetic energy can be lowered by establishing domain walls parallel to this axis. The areal ratio of $+\boldsymbol{P}_c$ and $-\boldsymbol{P}_c$ domains in Fig. 1, A to I, is presented in Fig. 1J and yields a symmetric hysteresis loop with a coercive field of 7.5 kV/cm at 22 K. Figure 1 thus demonstrates

[1]Department of Materials, ETH Zurich, Vladimir-Prelog-Weg 4, 8093 Zurich, Switzerland. [2]Department of Physics, Tohoku University, Sendai 980-8578, Japan. [3]Department of Physics and Mathematics, Aoyama Gakuin University, Sagamihara, Kanagawa 229-8558, Japan. [4]PRESTO, Japan Science and Technology Agency, Kawaguchi, Saitama 332-0012, Japan. [5]Department of Physics, ETH Zurich, Auguste-Piccard-Hof 1, 8093 Zurich, Switzerland. [6]Division of Materials Physics, Graduate School of Engineering Science, Osaka University, Toyonaka, Osaka 560-8531, Japan. [7]Laboratory for Neutron Scattering and Imaging, Paul Scherrer Institute, 5232 Villigen, Switzerland.
***Corresponding author. E-mail: m-matsubara@m.tohoku.ac.jp (M.M.); sebastian.manz@mat.ethz.ch (S.M.)** †These authors contributed equally to this work.

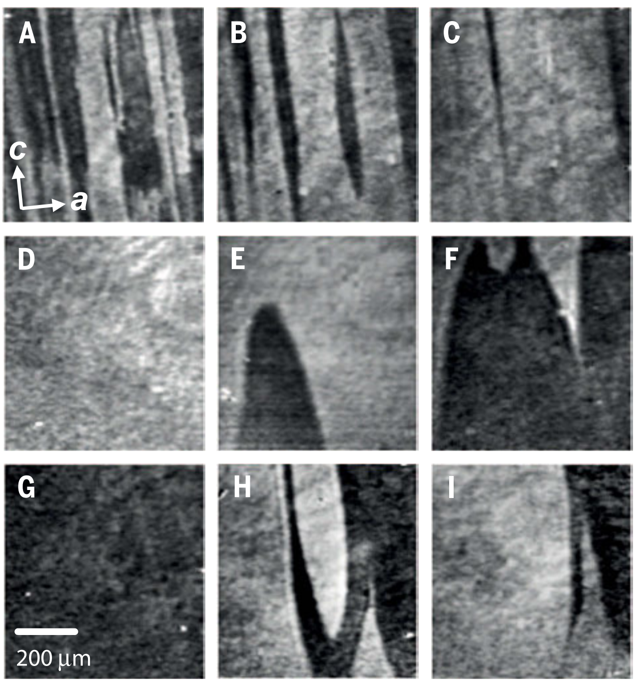

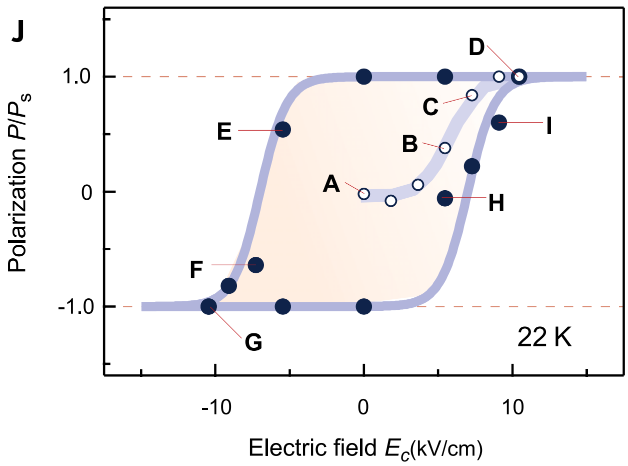

Fig. 1. Electric-field control of domains in $TbMnO_3$. (**A** to **I**) Progression of multiferroic domain structure in a cycled electric field E_c along the *c* axis (temperature = 22 K). Bright and dark regions correspond to $+\boldsymbol{P}_c$ and $-\boldsymbol{P}_c$ domains, respectively. (**J**) Ferroelectric hysteresis loop $\boldsymbol{P}_c(E_c)$ derived from the areal ratio of $+\boldsymbol{P}_c$ to $-\boldsymbol{P}_c$ domains in SHG images (A) to (I).

that we can access the ferroelectric domain pattern by SHG and control it by application of an electric field. The imaging data reveal that the domain walls move easily in the field.

At about $\mu_0 H_b = 5$ T at 9 K (*14*), the bulk polarization changes from $\boldsymbol{P}_c$ to $\boldsymbol{P}_a$, passing through a first-order phase transition. This polarization flop is driven by a reorientation of the spin-cycloidal plane from *bc* to *ab* (*26*). For a single-domain state, it was shown that the direction of the flop can be enforced by an appropriately tilted magnetic field (*5*, *27*). Here, we are interested in the intrinsic reorientation behavior of a multidomain state. We therefore minimized the angle between the magnetic field and the *b* axis below the one controlling the field-tilt–promoted polarization flop in (*27*). In Fig. 2, we present the corresponding SHG domain images obtained at 0 and 10 T, with $\boldsymbol{P}$ pointing along the *c* and *a* axis, respectively. The pattern of $\pm\boldsymbol{P}_c$ domains at 0 T (Fig. 2A) exhibits the same features as in Fig. 1A; i.e., stripe-like domains and predominance of side-by-side domain walls. We then increased the magnetic field to 10 T while tracking the polarization flop with SHG signals sensitive to $\boldsymbol{P}_c$ and $\boldsymbol{P}_a$, respectively (*24*). At 10 T, we imaged the distribution of $\pm\boldsymbol{P}_a$ domains, with the result shown in Fig. 2B. We find that the $\pm\boldsymbol{P}_c$ and $\pm\boldsymbol{P}_a$ domain structures, displayed in Fig. 2, A and B, respectively, are identical within the resolution limit of our experiment of a few micrometers. Because of the first-order nature of the traversed phase transition, this correspondence is unexpected. The discontinuity of a first-order phase transition usually involves isolated growth of domains of the new phase, which replaces the original domain structure (*28*). In the present case, however, all domain walls remain in position, which is particularly surprising because the walls move easily and without memory, according to Fig. 1. The persistence of the domain pattern further implies that neutral side-by-side domain walls are transformed into nominally charged head-to-head and tail-to-tail walls (Fig. 2, C and D). The transformation might respect the strong magnetic exchange along the *c* axis and could be energetically less costly than a reorientation of the domain walls retaining a neutral side-by-side state. It thus reflects the secondary nature of the magnetically induced ferroelectric order (*29*). Such energy considerations, however, cannot explain why $+\boldsymbol{P}_c$ and $-\boldsymbol{P}_c$ domains both flop deterministically; i.e., with a unique correspondence $+\boldsymbol{P}_c \leftrightarrow +\boldsymbol{P}_a$ and $-\boldsymbol{P}_c \leftrightarrow -\boldsymbol{P}_a$ and without additional domains and domain walls when the $\boldsymbol{P}_a$-related domains nucleate and grow.

To understand this exotic switching behavior, we performed Landau-Lifshitz-Gilbert (LLG) simulations based on the microscopic spin Hamiltonian developed in (*30*, *31*). We applied this formalism for modeling and resolving the reorientation dynamics of the magnetic field–driven polarization flop. For details on the validity and application of the LLG simulation and on the role of the ions carrying the spin and the polarization, see (*24*).

The simulations reveal that the magnetic field H_b leads to a local effective field $\boldsymbol{H}_{i,\mathrm{eff}}$, exerting a torque $\boldsymbol{\tau}_i \propto -\boldsymbol{m}_i \times \boldsymbol{H}_{i,\mathrm{eff}}$ on the magnetization $\boldsymbol{m}_i$ at site *i*. Thanks to this torque, spin textures of positive and negative chirality both rotate counterclockwise around the *b* axis, giving rise to intrinsically identical flop directions for $+\boldsymbol{P}_c$ and $-\boldsymbol{P}_c$ domains (Fig. 3, A and B). Figure 3C shows a calculated spatiotemporal map documenting the transition from the $-\boldsymbol{P}_c$ to the $-\boldsymbol{P}_a$ domain state on an arbitrary time scale from 0 to 1 (from start to end of the spin rotation). The polarization rotation progresses in a spatially inhomogeneous way, which nicely reflects the inhomogeneous nucleation-based nature of the first-order phase transition. Areas in which the flop occurs first drag neighboring regions along, so that additional domain walls are not formed. Each domain undergoes a quasi-coherent deterministic polarization reorientation.

The deterministic nature of the multiferroic phase transition and the stability of the associated multiferroic domains allow us to convert neutral walls into nominally charged domain walls. This dynamical degree of freedom may enable domain wall–based nanoelectronics devices in magnetically induced ferroelectrics. Our results apply to noncollinear spin-order–driven ferroelectrics in general. They provide a proof of concept for domain engineering in these materials. This is matched by ongoing successful attempts to increase their ordering temperature and spontaneous polarization (*32*, *33*). Resonant excitations (*34*, *35*) may lead to polarization flops within a picosecond, which could be a foundation for ultrafast deterministic magnetoelectric phase control.

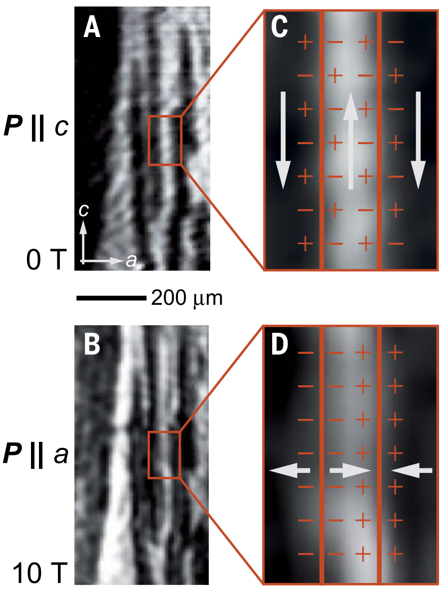

Fig. 2. Domain structure across the first-order polarization flop. (**A** and **B**) Multiferroic domain structure at 9 K in the ground state ($H_b = 0$ T, $\boldsymbol{P}_a = 0$, $\boldsymbol{P}_c \neq 0$) and excited state ($H_b = 10$ T, $\boldsymbol{P}_a \neq 0$, $\boldsymbol{P}_c = 0$), respectively. The resulting domain structures are identical. Thus, the polarization flop occurs in a deterministic way; i.e., with a unique correlation $+\boldsymbol{P}_c \leftrightarrow +\boldsymbol{P}_a$ and $-\boldsymbol{P}_c \leftrightarrow -\boldsymbol{P}_a$ of the domain states. (**C** and **D**) The magnified regions show that side-by-side domain walls are changed to head-to-head/tail-to-tail walls by the polarization flop, leading to nominally charged domain walls.

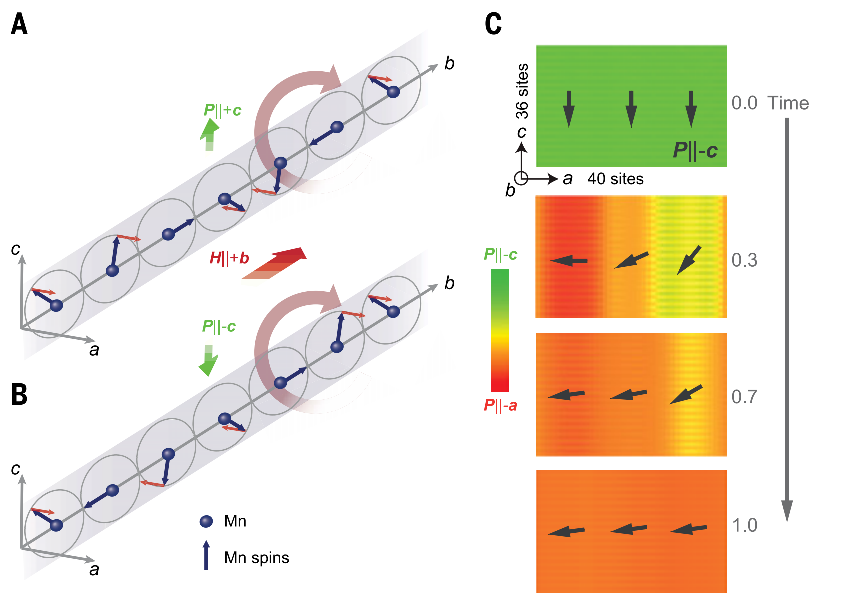

Fig. 3. LLG simulation of the deterministic polarization switching. (**A** and **B**) *bc*-plane spin cycloid with $+\boldsymbol{P}_c$ and $-\boldsymbol{P}_c$, respectively. The local spin torque $\boldsymbol{\tau}_i \propto -\boldsymbol{m}_i \times \boldsymbol{H}$ for $\boldsymbol{H} \parallel +b$ is represented by solid red arrows. For both domain states, the torque forces the cycloidal plane to rotate counterclockwise around the *b* axis. Thus, an intrinsically deterministic polarization flop is acquired. (**C**) Simulated spatiotemporal maps of the local polarization in the *ac* plane for the polarization switching from $-\boldsymbol{P}_c$ at time 0 to $-\boldsymbol{P}_a$ at time 1. The polarization rotates in a spatially inhomogeneous way, yet quasi-coherently without generating additional domain walls.

REFERENCES AND NOTES

1. S. Picozzi, C. Ederer, *J. Phys. Condens. Matter* **21**, 303201 (2009).
2. T. Kimura, *Annu. Rev. Condens. Matter Phys.* **3**, 93–110 (2012).
3. X. Rocquefelte, K. Schwarz, P. Blaha, S. Kumar, J. van den Brink, *Nat. Commun.* **4**, 2511 (2013).
4. K. Noda, M. Akaki, T. Kikuchi, D. Akahoshi, H. Kuwahara, *J. Appl. Phys.* **99**, 08S905 (2006).
5. N. Abe *et al.*, *Phys. Rev. Lett.* **99**, 227206 (2007).
6. H. Murakawa *et al.*, *Phys. Rev. Lett.* **101**, 197207 (2008).
7. F. Kagawa *et al.*, *Phys. Rev. Lett.* **102**, 057604 (2009).
8. E. Schierle *et al.*, *Phys. Rev. Lett.* **105**, 167207 (2010).
9. N. Abe, K. Taniguchi, H. Sagayama, H. Umetsu, T. Arima, *Phys. Rev. B* **83**, 060403(R) (2011).
10. F. Kagawa, Y. Onose, Y. Kaneko, Y. Tokura, *Phys. Rev. B* **83**, 054413 (2011).
11. I. Fina, L. Fàbrega, X. Martí, F. Sánchez, J. Fontcuberta, *Phys. Rev. Lett.* **107**, 257601 (2011).
12. D. Meier *et al.*, *Phys. Rev. Lett.* **102**, 107202 (2009).
13. T. Hoffmann, P. Thielen, P. Becker, L. Bohatý, M. Fiebig, *Phys. Rev. B* **84**, 184404 (2011).
14. T. Kimura *et al.*, *Nature* **426**, 55–58 (2003).
15. M. Kenzelmann *et al.*, *Phys. Rev. Lett.* **95**, 087206 (2005).
16. B. Lorenz, *ISRN Condens. Matter Phys.* **2013**, 497073 (2013).
17. H. Katsura, N. Nagaosa, A. V. Balatsky, *Phys. Rev. Lett.* **95**, 057205 (2005).
18. M. Mostovoy, *Phys. Rev. Lett.* **96**, 067601 (2006).
19. H. C. Walker *et al.*, *Phys. Rev. B* **88**, 214415 (2013).
20. D. Meier, N. Aliouane, D. N. Argyriou, J. A. Mydosh, T. Lorenz, *New J. Phys.* **9**, 100 (2007).
21. D. Senff, P. Link, N. Aliouane, D. N. Argyriou, M. Braden, *Phys. Rev. B* **77**, 174419 (2008).
22. M. Fiebig, V. V. Pavlov, R. V. Pisarev, *J. Opt. Soc. Am. B* **22**, 96–118 (2005).
23. S. A. Denev, T. T. A. Lummen, E. Barnes, A. Kumar, V. Gopalan, *J. Am. Ceram. Soc.* **94**, 2699–2727 (2011).
24. See the supplementary materials on *Science* Online.
25. A. K. Tagantsev, L. Eric Cross, J. Fousek, *Domains in Ferroic Crystals and Thin Films* (Springer, New York, 2010).
26. N. Aliouane *et al.*, *Phys. Rev. Lett.* **102**, 207205 (2009).
27. N. Abe, K. Taniguchi, S. Ohtani, H. Umetsu, T. Arima, *Phys. Rev. B* **80**, 020402(R) (2009).
28. A. N. Kolmogorov, *Bull. Acad. Sci. USSR Phys. Ser.* **1**, 355–359 (1937).
29. P. Tolédano, *Phys. Rev. B* **79**, 094416 (2009).
30. M. Mochizuki, N. Furukawa, *Phys. Rev. Lett.* **105**, 187601 (2010).
31. M. Mochizuki, N. Furukawa, N. Nagaosa, *Phys. Rev. B* **84**, 144409 (2011).
32. T. Kimura, Y. Sekio, H. Nakamura, T. Siegrist, A. P. Ramirez, *Nat. Mater.* **7**, 291–294 (2008).
33. T. Aoyama *et al.*, *Nat. Commun.* **5**, 4927 (2014).
34. M. Mochizuki, N. Nagaosa, *Phys. Rev. Lett.* **105**, 147202 (2010).
35. T. Kubacka *et al.*, *Science* **343**, 1333–1336 (2014).

ACKNOWLEDGMENTS

We thank M. Trassin and T. Arima for fruitful discussions. This work was supported by the Swiss National Science Foundation (SNSF) (grant nos. 200021_147080/1 and 200021_144115), the NCCR Molecular Ultrafast Science and Technology (NCCR MUST) research instrument of the SNSF, and Grants-in-Aid for Scientific Research, Japan Society for the Promotion of Science (JSPS KAKENHI) (grant nos. 24244058, 25870169, and 25287088), MEXT, Japan. M.Mo. was supported by JSPS KAKENHI (grant nos. 25870169 and 25287088).

SUPPLEMENTARY MATERIALS

www.sciencemag.org/content/348/6239/1112/suppl/DC1
Materials and Methods
Supplementary Text
Figs. S1 to S4
References (*36–38*)

28 August 2014; accepted 5 May 2015
10.1126/science.1260561

FRICTION

Tuning friction atom-by-atom in an ion-crystal simulator

Alexei Bylinskii,* Dorian Gangloff,* Vladan Vuletić†

Friction between ordered, atomically smooth surfaces at the nanoscale (nanofriction) is often governed by stick-slip processes. To test long-standing atomistic models of such processes, we implemented a synthetic nanofriction interface between a laser-cooled Coulomb crystal of individually addressable ions as the moving object and a periodic light-field potential as the substrate. We show that stick-slip friction can be tuned from maximal to nearly frictionless via arrangement of the ions relative to the substrate. By varying the ion number, we also show that this strong dependence of friction on the structural mismatch, as predicted by many-particle models, already emerges at the level of two or three atoms. This model system enables a microscopic and systematic investigation of friction, potentially even into the quantum many-body regime.

Stick-slip friction is a nonlinear phenomenon in which two surfaces stick to each other owing to a static friction force and accumulate potential energy under increasing applied shear force, then slip suddenly. As the released energy is dissipated, the surfaces stick again, and the process repeats (*1*). This phenomenon occurs on length scales ranging from nanometers [biological molecules and atomic contacts (*1–3*)] to the kilometer scales of earthquakes (*4*). Interestingly, at the nanoscale, lattice mismatch between surfaces can cancel the sticking forces, resulting in continuous and almost frictionless sliding termed superlubricity (*5*). Despite their fundamental and technological importance, stick-slip and superlubricity are not fully understood because of the difficulty of probing an interface with microscopic resolution and control.

The simplest atomistic friction model is the single-particle stick-slip model by Prandtl and Tomlinson (PT) (*6*, *7*). The particle, held in a harmonic potential of an elastic object crystal, is driven across a sinusoidal potential of a rigid substrate crystal. This one-particle model, however, fails to capture the effects of structural mismatch between the crystal surfaces. The Frenkel-Kontorova (FK) model (*8*, *9*) instead treats the object as an infinite array of atoms joined by springs. This model is governed by the commensurability of the unperturbed array and the substrate and exhibits nontrivial kink dynamics (*8*), the pinned-to-sliding Aubry phase transition (*10*), and the related superlubricity (*5*).

Tools based on atomic force microscopy (*11*) can measure atomic-scale slips between surfaces comprising down to a few atoms (*12–14*). This has enabled the observation of superlubricity by varying the normal load (*15*) or the relative orientation of crystal lattices forming the interface (*16*, *17*). Most observations in these systems can be qualitatively explained via variants of the PT or FK models but without direct access to microscopic dynamics. Kink propagation dynamics, however, was observed in a macroscopic friction simulator with colloidal polystyrene beads in an optical lattice (*18*).

Here, following recent proposals (*19–22*), and enabled by the recent trapping of an ion in an optical lattice (*23–25*), we introduce an experimental system that allows us to study and control nanofriction at the individual-atom level. We form a nanofriction interface (Fig. 1A) by transporting a trapped-ion crystal with tunable spacings (*26*) over the sinusoidal potential of an optical standing wave (optical lattice), emulating an elastic crystal moving over a rigid periodic substrate. We measure the static friction force and the dissipated energy for each individual ion by tracking its position with sublattice spatial resolution and time resolution below the thermal relaxation time scale.

$^{174}Yb^{+}$ ions, laser cooled to sub-millikelvin temperatures, are held in a linear Paul trap with harmonic confinement (*27*), where they self-organize into an inhomogeneous one-dimensional crystal owing to their mutual Coulomb repulsion. Adding the sinusoidal optical-lattice potential (*23*, *28*) produces a corrugated external potential V for each ion, given by $V/(m\omega_0^2a^2) = \frac{1}{2}\left(\frac{x_i - X}{a}\right)^2 + \eta \cdot \frac{1}{4\pi^2}\cos\left(\frac{2\pi}{a}x_i\right)$ (Fig. 1A). Here, m is the ion's mass, a = 185 nm is the optical-lattice period, x_i is the ion's position, and X is the center of the Paul trap. This potential is characterized by the dimensionless corrugation parameter η, equal to the confinement ratio $(\omega_L/\omega_0)^2$ of the lattice site vibrational frequency $\omega_L/(2\pi)$ to the Paul trap longitudinal vibrational frequency $\omega_0/(2\pi)$, both of which can be tuned over a wide range via laser intensity and static electric fields, respectively. The translation $X(t) = F(t)/(m\omega_0^2)$ of the Paul trap with respect to the optical lattice transports the ion crystal at adjustable speed, when the uniform electric force $F(t)$ is linearly ramped. The distribution of ion positions relative to the lattice can be tuned with nanometer precision via ω_0, allowing us to introduce a controlled structural mismatch between object (ion

Department of Physics, Massachusetts Institute of Technology, 77 Massachusetts Avenue, Cambridge, MA 02139, USA.
*These authors contributed equally to this work. **†Corresponding author. E-mail: vuletic@mit.edu**

crystal) and substrate (optical lattice). To remove the heat generated by friction, the ions are continuously laser cooled to temperatures much lower than the optical-lattice depth (*23*). We observe that the scattering of light by an ion is proportional to the ion's optical-lattice potential energy as a result of the lattice-assisted Raman cooling scheme (*23*, *28*). Thus, we can deduce the ion's position with subwavelength resolution during transport while its kinetic energy remains below its displacement-dependent potential energy—i.e., we can measure an ion's position before a slip and when it has cooled down again after a slip (*28*).

We first benchmark our nanofriction simulator against the PT model by transporting a single trapped ion in the corrugated potential V. Under intermediate corrugation, stick-slip results from the applied-force–induced switching between the two minima of a bistable potential (Fig. 1B). As the force $F(t)$ is linearly ramped up, the ion sticks in the initial site (no. 1), riding up the lattice potential and increasing in fluorescence (no. 2), until a critical maximum static friction force F_s is reached. At that point, the barrier vanishes and the initial minimum disappears, resulting in a fold catastrophe (*1*). The ion discontinuously slips from its initial site to the global minimum one site over (no. 3). The ion then dissipates the released energy ΔW via laser cooling, while localization in the lattice potential reduces its fluorescence again. The positions of fluorescence peaks in Fig. 2A thus correspond to the maximum static friction force F_s, when the ion slips. As the force ramp is reversed, hysteresis can be clearly observed in the shift $2F_s$ between the forward and reverse slips (Fig. 2A). The fluorescence increase leading up to each slip is converted to the ion's position to reconstruct the force-displacement curve enclosing the area $2\Delta W$ (Fig. 2B). We repeat the measurement at different values of the corrugation parameter $\eta = (\omega_L/\omega_0)^2$ and plot in Fig. 2C the maximum static friction force F_s versus η. For $\eta < 1$, friction vanishes, as there is no bistability, and the unique potential minimum is continuously translated by the applied force. For $1 < \eta < 4.60$, the potential is bistable and F_s increases with η (linearly in the large η limit). These results are in excellent agreement with the PT model (solid line in Fig. 2C). The regime with multiple minima $\eta > 4.60$

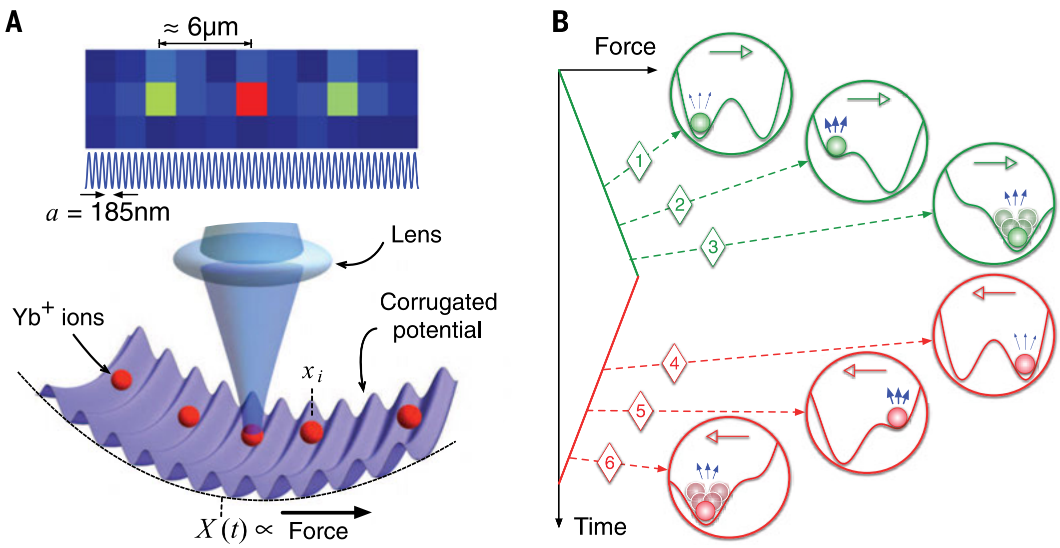

Fig. 1. Ion-crystal simulator of stick-slip friction. (**A**) Synthetic nanofriction interface between a Coulomb crystal of $^{174}Yb^+$ ions and an optical lattice, with single-ion-resolving microscope. The typical ion spacing is 6 μm, and the lattice period is a = 185 nm. In the bottom illustration of the corrugated potential, the lattice period and the corrugation are strongly exaggerated. (**B**) Stick-slip results from bistability, illustrated here for a single ion. We linearly ramp a shear force, causing the ion to jump between the minima, and we extract its position from its fluorescence, proportional to the lattice potential energy: (no. 1) ion initialized in the left site; (no. 2) the applied force pushes the ion up the lattice potential, eventually causing the slip; (no. 3) immediately after the slip, the ion is optically recooled and localizes to the right site; (no. 4), (no. 5), and (no. 6), the force ramp reverses and the ion sticks at the right site before slipping back to the left. Slips are identified by maxima in the ion's fluorescence.

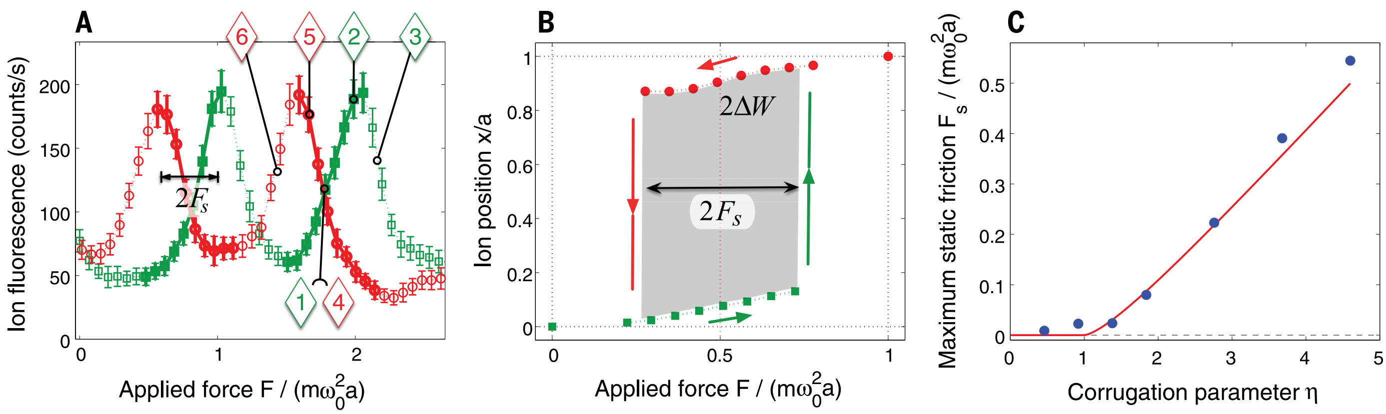

Fig. 2. Measured stick-slip hysteresis cycle of a single ion. (**A**) Fluorescence versus applied force during the forward transport (green squares) and reverse transport (red circles), showing hysteresis that is used to measure the maximum static friction force F_s. The stages of the stick-slip process (no. 1) to (no. 6) correspond to the illustrations in Fig. 1B. The bold data points indicate the ion's position before a slip, and only those data are used to reconstruct the force-displacement curve. (**B**) The force-displacement hysteresis loop encloses an area equal to twice the dissipated energy per slip ΔW. The unit $m\omega_0^2a$ of the applied force corresponds to 2.8×10^{-19} N; here, $\omega_0 = 2\pi \times 364$ kHz. (**C**) The static friction force disappears for corrugations $\eta < 1$ and increases linearly with corrugation for $\eta > 1$, in excellent agreement with the Prandtl-Tomlinson model with no free parameters (red solid line). In (A), error bars indicate 1 SD, and for (B) and (C), statistical error bars are smaller than the symbols. The data in (A) and (B) were measured at $\eta = 2.8$.

results in more complicated multiple-slip patterns (*29*), sensitive to the recooling time constant, and is not explored here.

To study multiparticle models with a trapped ion crystal, we load a desired number of ions up to $N = 6$ and control their matching to the periodic optical-lattice potential via the electrostatic harmonic confinement ω_0. In the FK model, mismatch is manifested as incommensurability of the (infinite) object and substrate lattices. Although our ion crystals are finite and inhomogeneous, we find that the essence of the FK model can be captured by introducing a matching parameter q that quantifies the alignment of the ions with equivalent points on the lattice when unperturbed by it. We define $q = \max_X \left[\frac{1}{N}\sum_i \sin(2\pi(x_{i0} - X)/a)\right]$, the maximum possible normalized averaged force of the optical lattice on the ions, when considering their lattice-free (unperturbed) equilibrium positions x_{i0} as the harmonic trap is displaced relative to the lattice. q is also related to the normalized potential barrier in the bistable energy landscape seen by the unperturbed ion crystal. By adjusting the Paul trap vibration frequency ω_0, we can continuously vary the q value (*28*) between $q = 1$, where each ion experiences an identical lattice force and the crystal behaves like a single particle (corresponding to the commensurate case in the FK model), and $q = 0$, where the lattice forces on the unperturbed crystal cancel out (analogous to an incommensurate arrangement).

For a selected matching parameter q, we drive the ion crystal across the lattice by linearly increasing the applied force and measure for each ion separately the stick-slip hysteresis, extracting F_s and ΔW. This is performed for crystal sizes from $N = 2$ to $N = 6$ ions at a value of η just below 4.60. As we switch from the matched case $q = 1$ to the mismatched case $q = 0$, we observe the friction change from maximal, corresponding to strong one-ion stick-slip friction for each ion, to nearly zero, corresponding to a superlubric regime, as shown in Fig. 3 for $N = 3$. Fluorescence of all three ions is plotted against the applied force in the forward and reverse directions, and the fluorescence peaks indicate the moment when each ion passes the barrier between two lattice sites. The data reveal that in the matched case, ions stick and slip together as a rigid body, with strong hysteresis between the forward and reverse transport, resulting in the maximal force-displacement hysteresis loop for each ion (middle ion shown), and maximal friction. By contrast, in the mismatched case, the ions move over the lattice in a staggered kink-like fashion, and each ion experiences almost no hysteresis or friction. Thus,

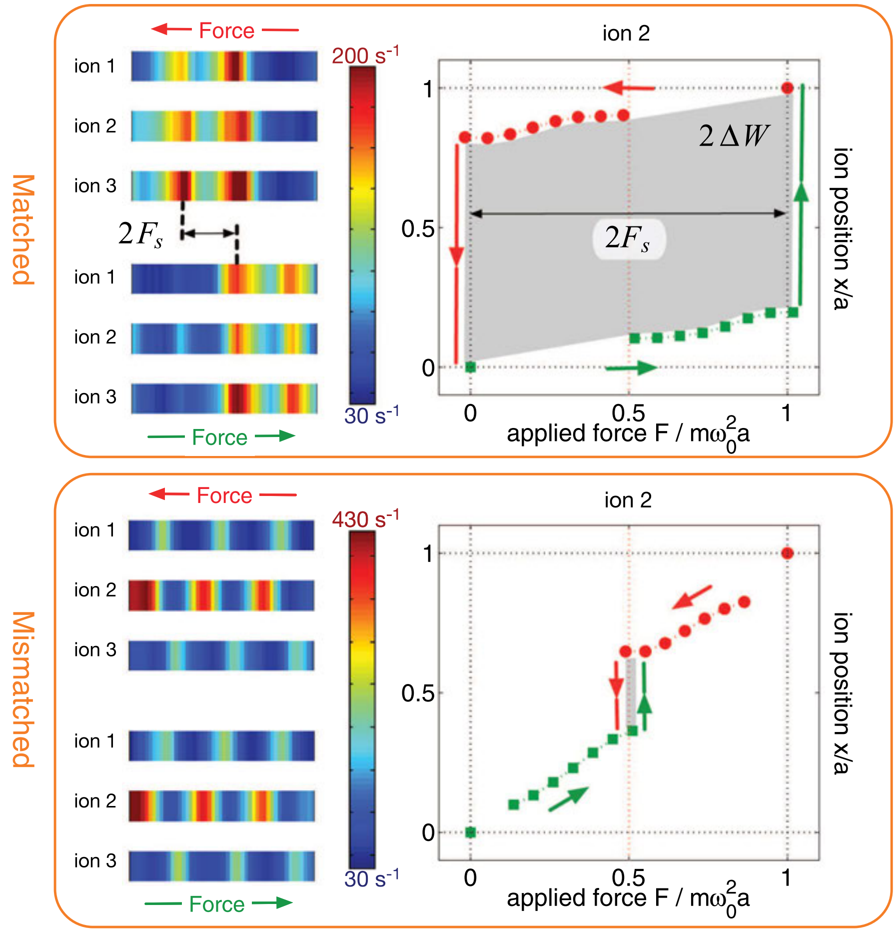

Fig. 3. Changing friction in a 3-ion crystal from maximal to nearly frictionless (superlubric) by structural mismatch. In the matched case (top), the ions stick and slip synchronously during transport (the observed photon detection rate for each ion, expressed in color, is maximum when the given ion slips over a potential barrier). The large hysteresis corresponds to large friction, shown here for the middle ion. In the mismatched case (bottom), the different ions slide over lattice barriers one at a time, and the friction and hysteresis nearly vanish.

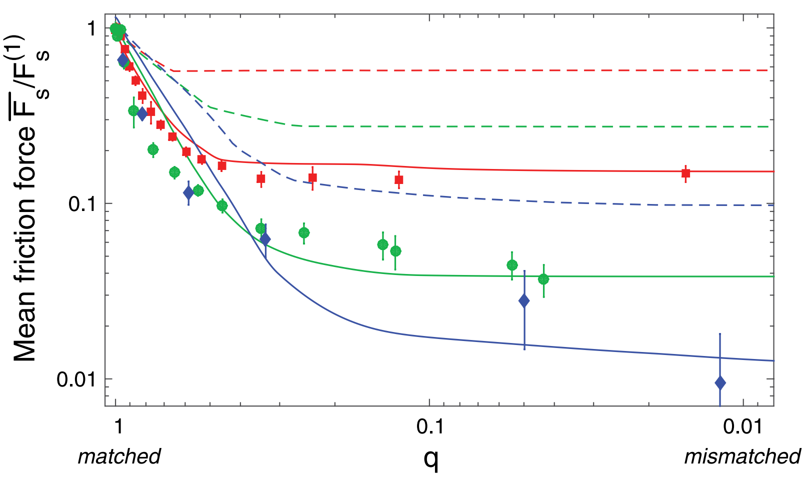

Fig. 4. The dependence of friction on object-substrate structural matching for different crystal sizes. Measured maximum static friction force F_s for $N = 2$, 3, and 6 ions (red squares, green circles, and blue diamonds, respectively), averaged over the ions and normalized to F_s as measured for a single trapped ion. Error bars represent 1 SD. Simulations for $N = 2$, 3, and 6 are shown for $T = 0$ (red, green, and blue dashed lines, respectively) and finite q-dependent temperature (red, green, and blue solid lines). Simulation parameters are chosen to match known experimental parameters: the measured temperature $k_BT(q = 1)/U \approx 0.05$ (corresponding to 48 μK); the optical-lattice depth $U/h = 20$ MHz (equivalent to $\eta = 4.6$); the driving velocity $v = 0.4$mm/s; and the recooling rate constant from laser cooling $r = 2\pi \times 3$ kHz. Only the $q = 0$ temperature is fitted, yielding $k_BT(q = 0)/U = 0.15$ (corresponding to 144 μK) for all the values of N shown [see (*28*)].

the structural suppression of friction is accompanied by a transition in the nature of transport from a simultaneous slipping regime reducible to an effective single-particle PT model, to a kink propagation regime characteristic of the infinite FK model.

In Fig. 4, we plot the measured maximum static friction force $\overline{F}_s$, averaged over the ions in the crystal, versus the matching q. (The dissipated energy $\overline{\Delta W}$ follows the same q dependence). As q is lowered from 1, the friction drops quickly, then slowly approaches a much reduced value at $q = 0$, which decreases with increasing crystal size. Notably, at $q = 0$ (mismatched limit) there is an almost 10-fold reduction in friction already for $N = 2$ ions, and a 100-fold reduction for $N = 6$ ions. Numerical simulations of this behavior at zero temperature (dashed lines in Fig. 4) show qualitative agreement but fail to account for the finite temperature of the ions in the experiment. For lower q values, the effective barrier separating two potential minima is reduced, and the friction becomes more sensitive to temperature (*28*). To take temperature-induced friction reduction (thermolubricity) (*1*) into account, we perform full dynamics simulations accounting for the finite crystal temperature (*28*) and find good agreement with the experiment (solid lines in Fig. 4). These simulations indicate that in the limit of low q, thermolubricity and superlubricity (mismatch-induced lubricity) reduce the observed friction by similar factors in our data.

Our results indicate that it may be possible to engineer nanofriction by structural control in finite-size systems. Intriguing future possibilities include the coupling to internal states of the ions (*30*) for the study of spin-dependent transport and friction (*22*) and the regime of weak periodic potentials, where quantum-mechanical tunneling may lead to new quantum phases (*19*, *22*).

REFERENCES AND NOTES

1. A. Vanossi, N. Manini, M. Urbakh, S. Zapperi, E. Tosatti, *Rev. Mod. Phys.* **85**, 529–552 (2013).
2. M. Urbakh, J. Klafter, D. Gourdon, J. Israelachvili, *Nature* **430**, 525–528 (2004).
3. V. Bormuth, V. Varga, J. Howard, E. Schäffer, *Science* **325**, 870–873 (2009).
4. C. H. Scholz, *Nature* **391**, 37–42 (1998).
5. K. Shinjo, M. Hirano, *Surf. Sci.* **283**, 473–478 (1993).
6. L. Prandtl, *Z. Angew. Math. Mech.* **8**, 85–106 (1928).
7. G. A. Tomlinson, *Philos. Mag.* **7**, 905–939 (1929).
8. O. M. Braun, Y. S. Kivshar, *The Frenkel-Kontorova Model: Concepts, Methods, and Applications* (Springer, New York, 2004).
9. Y. I. Frenkel, T. A. Kontorova, *Zh. Eksp. Teor. Fiz.* **8**, 1340 (1938).
10. S. Aubry, *Physica D* **7**, 240–258 (1983).
11. G. Binnig, C. F. Quate, C. Gerber, *Phys. Rev. Lett.* **56**, 930–933 (1986).
12. C. M. Mate, G. M. McClelland, R. Erlandsson, S. Chiang, *Phys. Rev. Lett.* **59**, 1942–1945 (1987).
13. R. W. Carpick, M. Salmeron, *Chem. Rev.* **97**, 1163–1194 (1997).
14. I. Szlufarska, M. Chandross, R. W. Carpick, *J. Phys. D* **41**, 123001 (2008).
15. A. Socoliuc, R. Bennewitz, E. Gnecco, E. Meyer, *Phys. Rev. Lett.* **92**, 134301 (2004).
16. M. Dienwiebel *et al.*, *Phys. Rev. Lett.* **92**, 126101 (2004).
17. M. Hirano, K. Shinjo, R. Kaneko, Y. Murata, *Phys. Rev. Lett.* **78**, 1448–1451 (1997).
18. T. Bohlein, J. Mikhael, C. Bechinger, *Nat. Mater.* **11**, 126–130 (2011).
19. I. García-Mata, O. V. Zhirov, D. L. Shepelyansky, *Eur. Phys. J. D* **41**, 325–330 (2007).
20. A. Benassi, A. Vanossi, E. Tosatti, *Nat. Commun.* **2**, 236 (2011).
21. D. Mandelli, A. Vanossi, E. Tosatti, *Phys. Rev. B* **87**, 195418 (2013).
22. T. Pruttivarasin, M. Ramm, I. Talukdar, A. Kreuter, H. Häffner, *New J. Phys.* **13**, 075012 (2011).
23. L. Karpa, A. Bylinskii, D. Gangloff, M. Cetina, V. Vuletić, *Phys. Rev. Lett.* **111**, 163002 (2013).
24. R. B. Linnet, I. D. Leroux, M. Marciante, A. Dantan, M. Drewsen, *Phys. Rev. Lett.* **109**, 233005 (2012).
25. M. Enderlein, T. Huber, C. Schneider, T. Schaetz, *Phys. Rev. Lett.* **109**, 233004 (2012).
26. D. Leibfried, R. Blatt, C. Monroe, D. Wineland, *Rev. Mod. Phys.* **75**, 281–324 (2003).
27. M. Cetina *et al.*, *New J. Phys.* **15**, 053001 (2013).
28. Materials and methods are available as supplementary material on *Science* Online.
29. S. N. Medyanik, W. K. Liu, I.-H. Sung, R. W. Carpick, *Phys. Rev. Lett.* **97**, 136106 (2006).
30. J. Mizrahi *et al.*, *Phys. Rev. Lett.* **110**, 203001 (2013).

ACKNOWLEDGMENTS

We thank W. Jhe and E. Demler for stimulating discussions and W. Jhe also for critical reading of the manuscript. This work was supported by the NSF-funded Center for Ultracold Atoms (grant PHY-0551153) and Canada's *Natural Sciences and Engineering Research Council* Postgraduate Scholarship program. All data presented here is in the supplementary materials.

SUPPLEMENTARY MATERIALS

www.sciencemag.org/content/348/6239/1115/suppl/DC1
Materials and Methods
Fig. S1
Database S1
Reference (*31*)

18 September 2014; accepted 1 May 2015
10.1126/science.1261422

FRICTION

Macroscale superlubricity enabled by graphene nanoscroll formation

Diana Berman,[1] Sanket A. Deshmukh,[1] Subramanian K. R. S. Sankaranarayanan,[1] Ali Erdemir,[2] Anirudha V. Sumant[1]*

Friction and wear remain as the primary modes of mechanical energy dissipation in moving mechanical assemblies; thus, it is desirable to minimize friction in a number of applications. We demonstrate that superlubricity can be realized at engineering scale when graphene is used in combination with nanodiamond particles and diamondlike carbon (DLC). Macroscopic superlubricity originates because graphene patches at a sliding interface wrap around nanodiamonds to form nanoscrolls with reduced contact area that slide against the DLC surface, achieving an incommensurate contact and substantially reduced coefficient of friction (~0.004). Atomistic simulations elucidate the overall mechanism and mesoscopic link bridging the nanoscale mechanics and macroscopic experimental observations.

Macroscopic friction and wear remain the primary modes of mechanical energy dissipation in moving mechanical assemblies such as pumps, compressors, and turbines, leading to unwanted material loss and wasted energy. It is estimated that nearly one third of the fuel used in automobiles is spent to overcome friction, while wear limits mechanical component life. Even a modest 20% reduction in friction can substantially affect cost economics in terms of energy savings and environmental benefits (*1*). In that context, superlubricity is desirable for various applications and therefore is an active area of research. To date, superlubricity has been primarily realized in a limited number of experiments involving atomically smooth and perfectly crystalline materials (*2*–*5*) and supported by theoretical studies (*6*, *7*). Superlubricity has been demonstrated for highly oriented pyrolytic graphite (HOPG) surfaces (*8*), as well as for multiwalled carbon nanotubes (MWCNTs), when the conditions for incommensurate contacts are met in a dry environment (*9*). Because these conditions are due to the incommensurability of lattice planes sliding against each other, they are referred to as structural lubricity and restricted to material interactions at the nanoscale. At the macroscale, this structural effect (hence, superlubricity) is lost because of the structural imperfections and disorder caused by many defects and deformations.

Low friction has recently been observed in centimeter-long double-walled carbon nanotubes with perfect atomic structures and long periodicity (*10*). Ultralow friction in disordered solid interfaces, such as self-mated DLC films (*11*–*14*) and in fullerenelike nanoparticles such as molybdenum disulfide (MoS_2) (*15*), has been observed under specific environmental and sliding conditions. However, the exact superlubricity mechanism in the above cases is still debatable and is not realized for industrial applications. In recent studies at the nano- and macroscale, graphene has shown a potential to substantially lower friction (*16*–*18*) and wear (*19*–*21*) under specific

[1]Center for Nanoscale Materials, 9700 South Cass Avenue, Argonne National Laboratory, Argonne, IL 60439, USA. [2]Energy Systems Division, 9700 South Cass Avenue, Argonne National Laboratory, Argonne, IL 60439, USA.
*Corresponding author. E-mail: sumant@anl.gov

conditions. However, sustained macroscale superlubricity, particularly at engineering scales, has yet to be demonstrated.

We demonstrate our observation of stable macroscale superlubricity while sliding a graphene-coated surface against a DLC-coated counterface. Our initial assumption was that the random network of mixed sp^3/sp^2 bonded carbon in DLC might provide the perfect incommensurate surface needed for the ordered graphene flakes to slide against DLC with least resistance. This was indeed proved to be true; however, the coefficient of friction (COF) values for graphene sliding against DLC in a dry environment were not in the superlubric regime (COF ~ 0.04, as shown in Fig. 1B). Initial observation of the wear debris revealed formation of graphene nanoscrolls in the wear track. This prompted us to use nanodiamond as an additive, which may act as nano ball bearings when covered by graphene, providing extra mechanical strength. We saw a dramatic reduction in friction, reaching the superlubric state [in Fig. 1B and inset, the COF dropped to near zero (0.004)] in a dry environment, when we introduced nanodiamond in combination with few-layer (three to four layers) graphene flakes on the silicon dioxide (SiO_2) substrate by means of a solution process method (figs. S1 and S2), providing a partial coverage on the SiO_2 surface (*22*). The observed wear marks on the flat (Fig. 1C) and ball sides were minimal and produced primarily by the contact pressure during sliding tests (fig. S3). Raman analysis of the wear track (Fig. 1C, inset) showed modification of graphene inside the wear track as observed in a decreased 2D peak (at ~2660 cm^{-1}) and an increased D peak (at ~1330 cm^{-1}) in comparison with the initial graphene's Raman signature, indicating a gradual loss of crystallinity of few-layer graphene and an increase in defects possibly due to tearing of graphene under constant sliding at high contact pressure (0.3 GPa). The Raman spectrum indicates no DLC transfer in the wear track during sliding, thus confirming that the superlubricity regime is not connected with the previously observed low-friction performance of DLC against DLC (fig. S14) (*12*).

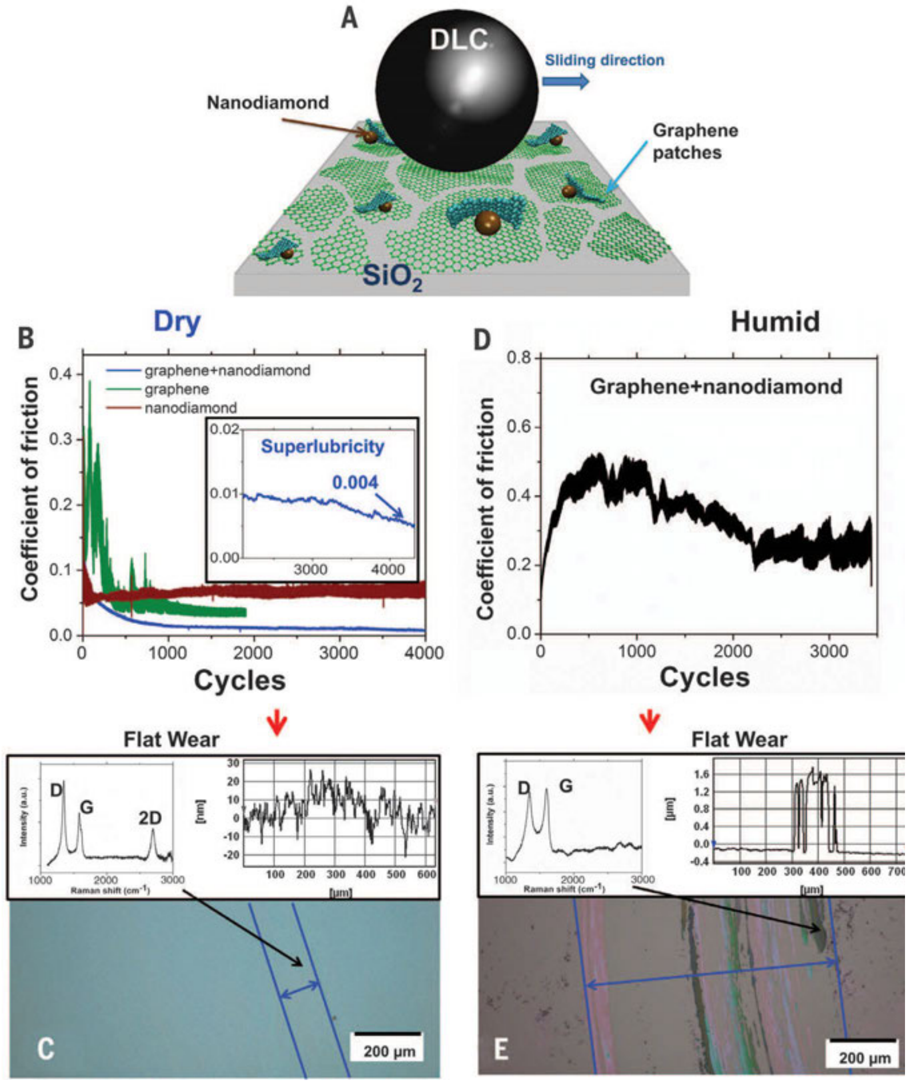

Fig. 1. Experimental demonstration of the superlubricity regime. (**A**) Not-to-scale schematic of the superlubricity test. (**B**) The COF for DLC ball sliding in a dry nitrogen environment against (i) graphene-plus-nanodiamonds (superlubricity state with COF ~ 0.004 ± 0.002), (ii) graphene alone (COF ~ 0.04 ± 0.01), and (iii) nanodiamond alone (COF ~ 0.07 ± 0.01). (Inset) A plot for superlubricity. (**C**) In the case of superlubricity, the wear tracks on the flat side and on the ball side (fig. S3) are almost invisible. (Inset) A typical Raman signature of defective graphene. (**D** and **E**) For graphene-plus-nanodiamond sliding against a DLC ball in a humid environment, (D) the COF reveals a high value of ~0.27 ± 0.04, (E) the corresponding wear track on the flat side is wide, and the inset shows a Raman signature corresponding to graphitized carbon debris. The tests were performed at room temperature under 1 N load and with 3 cm/s linear speed.

The necessity of using graphene-plus-nanodiamonds in establishing the superlubricity is demonstrated in Fig. 1B. In particular, graphene or nanodiamond when used alone on a SiO_2 substrate sliding against a DLC ball in a dry environment displays higher values of COF (0.04 and 0.07). Additionally, the erratic nature of COF indicates large wear debris formation.

Our experimental studies confirm that the stable superlubricity regime occurs over a wide range of test conditions; when the load was changed from 0.5 to 3 N, velocity was varied from 0.6 to 25 cm/s, temperature increased from 20°C to 50°C (fig. S15), and the substrate was changed to nickel or bare silicon (fig. S16). The temperature and velocity range for maintaining stable superlubricity is further backed by theoretical simulations (tables S2 and S3).

For graphene-plus-nanodiamonds in an ambient humid environment (relative humidity ~30%), both COF and wear were comparatively large (Fig. 1, D and E). A substantial amount of graphitized carbon debris was formed in the wear track, as shown by the optical images and Raman data (Fig. 1E and fig. S3), and the substrate itself suffered from substantial wear during sliding. The distinctiveness of the tribopair and dramatic dependence on the environmental conditions led us to further explore the underlyng mechanism for the observed superlubricity.

We carried out more detailed analysis of the wear track that formed during the superlubricity regime in dry nitrogen by sampling and examining the wear debris with transmission electron microscopy (TEM). As shown in the TEM images in Fig. 2, a large fraction of the nanodiamonds were wrapped by graphene nanoscrolls (more detailed scroll images are shown in fig. S4). Electron energy-loss spectra (EELS) confirmed the presence of diamond in the wear debris, as evident from the typical EELS signature for diamond. The π^* peak (at ~285 eV) in the carbon K-edge represents a small fraction of sp^2 bonded carbon owing to the presence of the few layers of graphene wrapped around the nanodiamond, which is similar to the disordered carbon shell observed previously in detonated nanodiamonds (*23*). For pure nanodiamonds,

this π^* peak should be absent (*23*, *24*), whereas in case of pure graphene scrolls, this π^* peak is higher (Fig. 2B, inset). Because of the random orientation of scrolls with diamond embedded inside, we had to focus the TEM differently in order to view clearly the diamond lattice and graphene layers; therefore, some of the scrolls in Fig. 2 do not show nanodiamonds inside.

To further explore the superlubricity mechanism, we performed molecular dynamics (MD) simulations (table S1) (*22*), and our simulations suggest that nanodiamonds can activate, guide, and stabilize the scrolling of initially planar graphene patches (fig. S5). During sliding in a dry environment, nanodiamonds facilitate scroll formation via two mechanisms: (i) Graphene platelets are highly reactive and easily attach to the dangling bonds present on the surface of nanodiamonds, initiating the scroll formation; and (ii) the sliding graphene patches encounter the three-dimensional (3D) structure of nanodiamonds, which act as obstructions (fig. S9). Additionally, the presence of topological defects (such as double vacancies or Stone-Wales) in graphene is expected to promote the scrolling behavior (fig. S12). On the basis of relative binding energetics between graphene-DLC and graphene-nanodiamond, we found that graphene prefers to wrap around the nanodiamond to promote higher surface contact (fig. S10). Once in a scrolled state, the final structures of graphene on diamond are well coordinated and stabilized by van der Waals forces.

Scroll formation and evolution of the COF are shown in Fig. 3, A and B, respectively, for a single graphene patch in a dry environment. At time $t < 1.0$ ns, COF values are high, ~0.2 to 0.4, because the graphene patch is in an extended or unscrolled state. The wrapping of a graphene sheet over the nanodiamonds begins at ~1.5 ns; this coincides with COF values dropping substantially, leading to a superlubric state that is maintained until the end of the simulation. Once formed, these scrolls slide against randomly arranged DLC atoms, which provide an incommensurate contact. This constant out-of-registry sliding translates into a superlubric regime. The COF also depends on the contact area between formed graphene scrolls and DLC. The superlubricity is thus attributed to (i) reduction in the interfacial contact area (>65%) and (ii) incommensurability between DLC and graphene scrolls.

At the molecular level, the observed superlubricity has its origin in graphene's nanoscopic anisotropic crystal structure, which consists of strong covalent intralayer bonding and weaker dispersive interlayer interactions. The structural contact between an incommensurate DLC ball and the graphene scrolls allows DLC to slide on top of the underlying graphene sheets by overcoming relatively small energetic barriers. In recent experiments, Dienwiebel *et al.* (*8*) observed friction reduction to vanishingly small values, depending on the degree of commensurability between the graphene flakes and the extended graphite surface. In an incommensurate state, the unit-cells in contact have to overcome much smaller barriers at any point in time, leading to considerably reduced resistance toward sliding. Consistent with the prediction of Mo *et al.* (*25*), we found that the friction force depends linearly on the number of atoms that chemically interact across the contact. The effective contact area between the graphene sheets and DLC decreases with time upon scrolling. Because friction is controlled by the short-range interactions even in the presence of dispersive

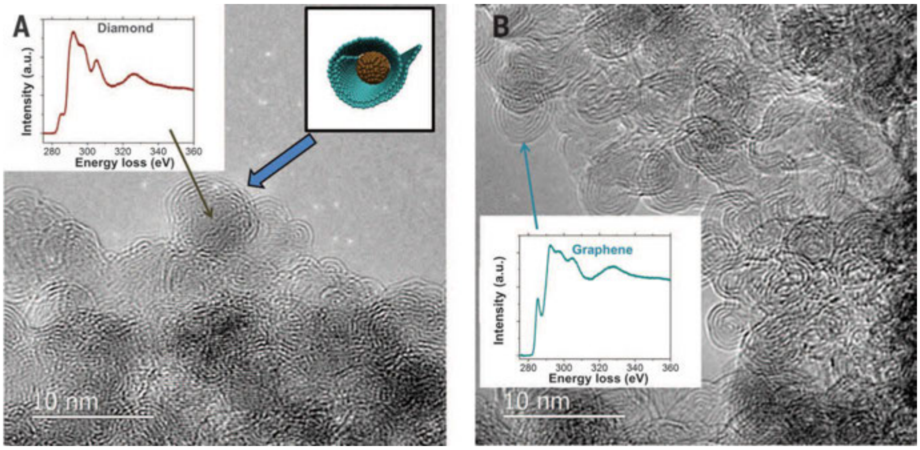

Fig. 2. Graphene nanoscrolls formation. (**A** and **B**) TEM images of the wear debris for DLC ball sliding against graphene-plus-nanodiamonds, demonstrating superlow friction in the dry environment. Graphene scroll formation is observed. (Insets) EELS for both diamond and graphene in the wear debris.

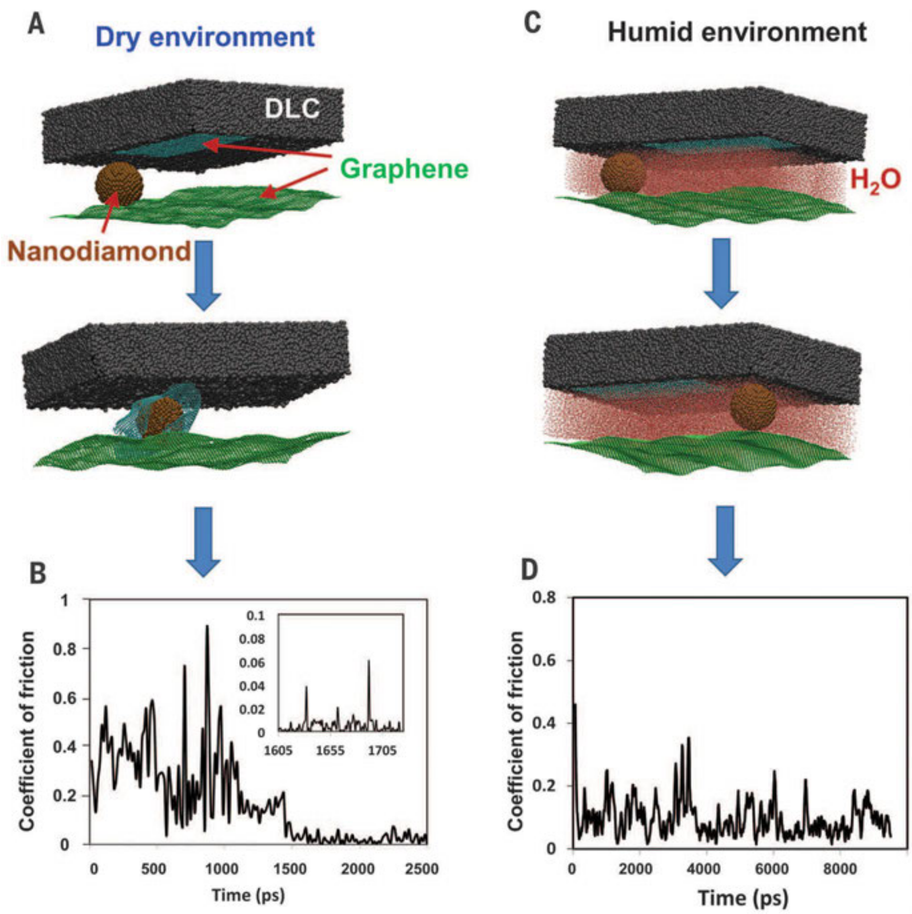

Fig. 3. Simulations of the single-scroll formation. (**A** to **D**) Temporal evolution of nanoscale friction for DLC ball sliding against graphene-plus-nanodiamonds in [(A) and (B)] dry and [(C) and (D)] humid environments extracted based on the MD simulation trajectories. Graphene scroll formation over nanodiamonds is observed in a dry environment (the steady-state COF is 0.005 ± 0.004), whereas ordered water layers above the graphene flakes prevent scroll formation in the humid environment (COF is 0.12 ± 0.04).

forces, scrolling-induced reduction in nanoscopic contact is substantial enough to lead to a superlubric state.

Our experiments suggest that the humid environment increases the friction and wear of the ball side because graphene layers remain strongly attached on the surface. We therefore performed MD simulations of the DLC-nanodiamond-graphene system in a humid environment (fig. S6). MD trajectories suggest formation of quasi-2D ordered water layers between the nanoscopic contacts, the DLC and graphene sheets (Fig. 3, C and D). These water layers prevent the scrolling of the graphene during sliding (fig. S7), and the ordered 2D water layers [based on calculated translational and tetrahedral orders (supplementary text) (*22*)] present a constant energy barrier for the DLC to overcome. These two effects result in little or no friction variation over time (Fig. 3D), and a nearly constant high-friction condition is maintained (COF ~ 0.1). We have simulated the effects of surface chemistry and considered the role of defects (supplementary text) (*22*). We found that the presence of defects greatly facilitates the adsorption of water from the ambient atmosphere (fig. S13). Water preferentially adsorbs and stabilizes defective sites, which further prevents the formation of scrolls.

To bridge the gap between the nanoscale mechanics and macroscopic contacts evident in our experiments, we performed a large-scale MD simulation for an ensemble of graphene-plus-nanodiamonds present between DLC and the underlying multilayered graphene substrate (fig. S8). The mesoscopic link is crucial to explain how the formation of nanoscrolls translates from a nanosystem with a single graphene patch (square-nanometer area of sliding interface) into the observed superlubricity at the macroscale (square-millimeter area). We evaluated the collective scrolling and tribological behavior of many individual graphene patches and created a density distribution of their tribological state in order to assess their contribution to the observed friction. During the initial sliding period at $t = 0$, the unscrolled graphene patches are in close contact with the interface. The contact area normalized with respect to the initial value at $t = 0$ is ~1 (*22*), as shown in Fig. 4C. The density distribution of COF values (Fig. 4B) shows a narrow distribution with a peak at ~0.6 to 0.7, suggesting that the system is in a high-friction state. With time (200 to 300 ps), the graphene patches increasingly scroll over nanodiamonds, and we observe a corresponding reduction in this peak intensity. The density profile shows a broader distribution and shifts prominently toward lower COFs (<0.2). The contact area, which is proportional to the number of interacting atoms, reduces by 40 to 50% during (*26*) this period. During the latter stages (~500 ps), most of the graphene patches are scrolled. The density profile shows a shift in the distribution to COF values <<0.01. The effective contact area in the present case is reduced significantly, by ~65 to 70%, and the mesoscopic system has reached a superlubric state.

The tribological evolution of a single graphene patch at the nanoscale resembles that of a single asperity contact, whereas the mesoscopic behavior resembles a multiple asperity contact. The friction mechanism at the mesoscale for an ensemble of graphene patches is not different from nanoscale (single patch). The initial tribological state of the patches, as well as the configuration of the patches versus nanodiamonds, dictates the dynamics of scroll formation, which in turn affects the dynamical evolution of COF for the mesoscopic system. The macroscopic contact in our experiments can be envisioned as comprising a much larger number of such smaller contacts or asperities, which explains the difference in time for the onset of the superlubric state in the experiments versus simulated systems.

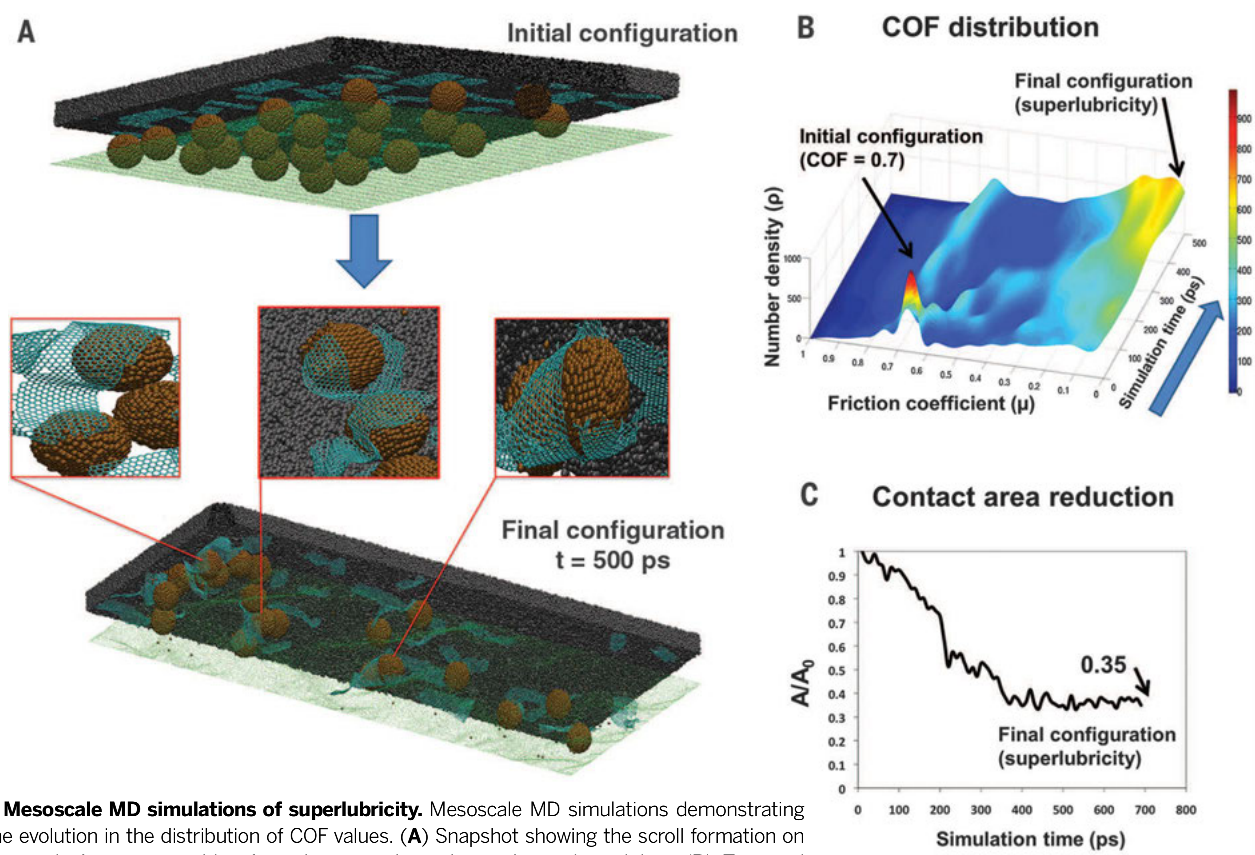

Fig. 4. Mesoscale MD simulations of superlubricity. Mesoscale MD simulations demonstrating the time evolution in the distribution of COF values. (**A**) Snapshot showing the scroll formation on nanodiamonds for an ensemble of graphene patches when subjected to sliding. (**B**) Temporal evolution of COF distribution averaged over an ensemble of graphene patches. (**C**) Evolution of the corresponding contact area. Initially at $t = 0$ ps, the patches are mostly sheetlike and in close contact with DLC, leading to an average COF of ~0.6 to 0.7. Sliding of DLC increases the probability of scroll formation by graphene patches, leading to a decrease in the average contact area, which manifests in the form of macroscopic superlubricity. The ensemble-averaged COF shifts to superlubric values at $t = 500$ ps, when most of the graphene patches are in a scrolled state.

REFERENCES AND NOTES

1. A. Z. Szeri, *Tribology: Friction, Lubrication, and Wear* (Hemisphere, Panama City, Panama, 1980).
2. M. Dienwiebel, N. Pradeep, G. S. Verhoeven, H. W. Zandbergen, J. W. M. Frenken, *Surf. Sci.* **576**, 197 (2005).
3. M. Hirano, K. Shinjo, R. Kaneko, Y. Murata, *Phys. Rev. Lett.* **78**, 1448–1451 (1997).
4. J. M. Martin, C. Donnet, T. Le Mogne, T. Epicier, *Phys. Rev. B Condens. Matter* **48**, 10583–10586 (1993).
5. X. Feng, S. Kwon, J. Y. Park, M. Salmeron, *ACS Nano* **7**, 1718–1724 (2013).
6. Y. Guo, W. Guo, C. Chen, *Phys. Rev. B* **76**, 155429 (2007).
7. M. Hirano, K. Shinjo, *Phys. Rev. B Condens. Matter* **41**, 11837–11851 (1990).
8. M. Dienwiebel *et al.*, *Phys. Rev. Lett.* **92**, 126101 (2004).
9. J. Cumings, A. Zettl, *Science* **289**, 602–604 (2000).
10. R. Zhang *et al.*, *Nat. Nanotechnol.* **8**, 912–916 (2013).
11. A. Erdemir, in *Handbook of Modern Tribology*, B. Bhushan, Ed. (CRC Press, Boca Raton, FL, 2001), pp. 787–818.
12. A. Erdemir, C. Donnet, *J. Phys. D Appl. Phys.* **39**, R311–R327 (2006).
13. J. A. Heimberg, K. J. Wahl, I. L. Singer, A. Erdemir, *Appl. Phys. Lett.* **78**, 2449 (2001).
14. C. Wang, S. Yang, Q. Wang, Z. Wang, J. Zhang, *Nanotechnology* **19**, 225709 (2008).
15. M. Chhowalla, G. A. J. Amaratunga, *Nature* **407**, 164–167 (2000).
16. Z. Deng, A. Smolyanitsky, Q. Li, X.-Q. Feng, R. J. Cannara, *Nat. Mater.* **11**, 1032–1037 (2012).
17. C. Lee *et al.*, *Science* **328**, 76–80 (2010).
18. L. Xu, T. B. Ma, Y. Z. Hu, H. Wang, *Nanotechnology* **22**, 285708 (2011).
19. D. Berman, A. Erdemir, A. V. Sumant, *Carbon* **54**, 454–459 (2013).
20. D. Berman, A. Erdemir, A. V. Sumant, *Carbon* **59**, 167–175 (2013).
21. S. S. Kandanur *et al.*, *Carbon* **50**, 3178–3183 (2012).
22. Materials and methods are available as supplementary materials on *Science* Online.
23. S. Turner *et al.*, *Adv. Funct. Mater.* **19**, 2116–2124 (2009).
24. V. N. Mochalin, O. Shenderova, D. Ho, Y. Gogotsi, *Nat. Nanotechnol.* **7**, 11–23 (2012).
25. Y. Mo, K. T. Turner, I. Szlufarska, *Nature* **457**, 1116–1119 (2009).
26. Z. Liu *et al.*, *Phys. Rev. Lett.* **108**, 205503 (2012).

ACKNOWLEDGMENTS

The help in the TEM data collection by Y. Liu is greatly appreciated. Use of the Center for Nanoscale Materials was supported by the U.S. Department of Energy, Office of Science, Office of Basic Energy Sciences, under contract DE-AC02-06CH11357. This research used resources of the National Energy Research Scientific Computing Center, which is supported by the Office of Science of the U.S. Department of Energy under contract DE-AC02-05CH11231. This research used tribological test facilities of the Energy Systems Division supported by the Vehicle Technologies Program of the Office of Energy Efficiency and Renewable Energy of the U.S. Department of Energy under contract DE-AC02-06CH11357. An award of computer time was provided by the Innovative and Novel Computational Impact on Theory and Experiment (INCITE) program. This research used resources of the Argonne Leadership Computing Facility at Argonne National Laboratory, which is supported by the Office of Science of the U.S. Department of Energy under contract DE-AC02-06CH11357. Experimental data and simulations are archived on servers at Argonne National Laboratory. Part of the experimental results are covered by a patent (US20140023864A1). Both D.B. and S.D. contributed equally in this work. D.B. performed the experiments and analyzed the data. S.D. and S.K.R.S. devised and performed the molecular dynamics simulations and performed all the related data analysis. A.V.S. conceived the idea, helped in the data analysis of experimental results, and directed the project. A.E. codirected the project and helped in the data analysis of tribological tests. S.K.R.S. guided the simulation effort. D.B., S.D., S.K.R.S., A.E., and A.V.S equally contributed to discussing the results and composing the manuscript.

SUPPLEMENTARY MATERIALS

www.sciencemag.org/content/348/6239/1118/suppl/DC1
Materials and Methods
Supplementary Text
Figs. S1 to S16
Tables S1 to S3
References (*27–45*)
Movie S1

2 October 2014; accepted 1 April 2015
Published online 14 May 2015;
10.1126/science.1262024

ORGANIC THIN FILMS

Rational synthesis of organic thin films with exceptional long-range structural integrity

Noriya Seiki,[1] Yoshiaki Shoji,[1*] Takashi Kajitani,[1,2] Fumitaka Ishiwari,[1] Atsuko Kosaka,[1,2] Takaaki Hikima,[3] Masaki Takata,[3] Takao Someya,[2] Takanori Fukushima[1,2*]

Highly oriented, domain-boundary–free organic thin films could find use in various high-performance organic materials and devices. However, even with state-of-the-art supramolecular chemistry, it is difficult to construct organic thin films with structural integrity in a size regime beyond the micrometer length scale. We show that a space-filling design, relying on the two-dimensional (2D) nested hexagonal packing of a particular type of triptycene, enables the formation of large-area molecular films with long-range 2D structural integrity up to the centimeter length scale by vacuum evaporation, spin-coating, and cooling from the isotropic liquid of the triptycene. X-ray diffraction analysis and microscopic observations reveal that triptycene molecules form a completely oriented 2D (hexagonal triptycene array) + 1D (layer stacking) structure, which is key for the long-range propagation of structural order.

Polymers with inherent flexibility and fluidity can be processed into macroscopic thin films with one-dimensional (1D) structural order with the assistance of shear stress and external fields (*1*, *2*). Such physical forces also allow the macroscopic alignment of 2D periodic structures formed by the microphase separation of block copolymers (*3*, *4*). Because polymer chains always fluctuate microscopically, polymeric systems may be advantageous in that the entropy loss associated with large-scale ordering does not seem to be so critical. However, the above situation does not hold true for small organic molecules. Given that self-assembly of small molecules generally proceeds via a nucleation-and-growth mechanism (*5*, *6*), it is difficult for the constituent molecules, once structured, to undergo large reordering. In principle, the construction of domain-boundary–free films from small organic molecules is considered to require single-site nucleation and subsequent propagation of the resulting structure throughout the entire film. This process poses a major obstacle to endowing organic films with structural integrity at macroscopic length scales, even beyond micrometer length scales.

To overcome this critical issue in the design of organic thin films, we developed a 2D + 1D assembly, inspired by the structure of highly oriented pyrolytic graphite. If a 2D molecular layer free of domain boundaries was constructed at macroscopic length scales, it could undergo 1D assembly to form a perfectly oriented molecular film with 3D structural integrity. The geometrical requirement for tessellation of regular polygons that can fill a Euclidean plane upon closest packing is limited to triangles, tetragons, and hexagons. However, the former two polygons have no geometrical constraints regarding vertex displacement, which can cause in-plane translational disorder (Fig. 1, A and B). Such disordering is not likely to occur with hexagons, although in-plane rotational disorder can occur (Fig. 1C); note that liquid crystalline films composed of a hexagonal columnar assembly exhibit scarcely any long-range lattice order (*7*, *8*). Nevertheless, if such rotational disorder can be suppressed, a hexagon could serve as an ideal structural element for uniform tessellation, and we anticipated that a three-bladed, propeller-shaped molecular motif could assemble into a 2D hexagonal structure by nested packing (Fig. 1D). Interpenetration of the propeller parts would not only suppress structural fluctuations at the molecular level but also correct locally occurring lattice mismatches, thus enabling a long-range propagation of the hexagonal structural order.

We used this space-filling design to construct a 2D layer with a particular type of triptycene, and we show that the resulting organic films possess extraordinary long-range 2D structural integrity up to the centimeter length scale. Triptycene, a propeller-shaped rigid molecule consisting of three 120°-oriented phenylene rings, offers a large free volume around the aromatic skeleton. A wide variety of triptycene derivatives have been synthesized as building blocks for macrocycles (*9*), polymer aligners (*10*), and porous solids (*11*, *12*) to exploit their

[1]Chemical Resources Laboratory, Tokyo Institute of Technology, 4259 Nagatsuta, Midori-ku, Yokohama 226-8503, Japan. [2]Bio-Harmonized Electronics Project, Exploratory Research for Advanced Technology (ERATO), Japan Science and Technology Agency (JST), 7-3-1 Hongo, Bunkyo-ku, Tokyo 113-8656, Japan. [3]RIKEN SPring-8 Center, 1-1-1 Kouto, Sayo, Hyogo 679-5148, Japan.
***Corresponding author. E-mail: yshoji@res.titech.ac.jp (Y.S.); fukushima@res.titech.ac.jp (T.F.)**

free volume for host-guest chemistry. Our space-filling design relies on mutual intrusion of the phenylene rings to create a highly dense, nested packing structure (Fig. 1D). Although nonsubstituted triptycene assembles in a different manner (*13*), our analysis of the Cambridge Structural Database (*14*, *15*) indicates that several triptycene derivatives adopt nested packing structures in crystals (*16–18*). However, this packing pattern has never received any special attention in the design of organic materials, except for one example of a liquid crystalline triptycene, which was reported to form a hexagonal lattice in its mesophase (*19*).

A tripodal functionalization of triptycene (Fig. 1E) could serve as a universal building block to achieve nested hexagonal packing, and we synthesized a series of tripodal paraffinic triptycenes (**Trip-C12**, **Trip-C18**, **Trip-C12-F**, and **Trip-C12′**) (Fig. 1E) by etherification of 1,8,13-trihydroxytriptycene with the corresponding alkyl halides [see supplementary materials (*20*)]. The incorporation of soft side chains endows the molecules with fluidity to facilitate the fabrication of film samples. The tripodal paraffinic triptycenes (Fig. 1E) in bulk formed a hexagonal lattice by nested packing. Differential scanning calorimetry of **Trip-C12**, upon cooling from its isotropic hot melt, displayed an exothermic crystallization peak at 207°C (fig. S1A). The powder x-ray diffraction (XRD) pattern of the bulk sample of **Trip-C12** in a glass capillary was obtained (*20*) after heating the crystalline sample above the melting point (210°C) and then cooling to 30°C. We assigned the multiple XRD peaks to a superposition of two sets of diffraction patterns (Fig. 2A). Four XRD peaks with *d*-spacings of 2.43, 1.21, 0.81, and 0.61 nm originated from a lamellar structure and were indexed, respectively, as diffractions from the (001), (002), (003), and (004) planes. The layer spacing (d = 2.43 nm) is comparable to the length of the long molecular axis of **Trip-C12** (2.1 nm). The XRD peaks observed at a wider-angle region (scattering vector $q > 9\ \mathrm{nm}^{-1}$) had *d*-spacings of 0.70, 0.40, 0.35, and 0.26 nm; the ratio of the *d*-spacings $(1 : \sqrt{3} : 2 : \sqrt{7})$ completely agrees with the values required for diffractions from the (100), (110), (200), and (210) planes of a hexagonal lattice. The lattice parameter, a = 0.81 nm, given by $2d_{100}/\sqrt{3}$, is consistent with the distance between centroids (0.80 nm) of in-plane triptycene moieties in single-crystalline **Trip-C12** and 1,8,13-trimethoxytriptycene (table S1 and fig. S2) (*20*).

The XRD profile of **Trip-C12** can be rationalized by considering that the nested hexagonal packing of the triptycene moieties gives 2D arrays that undergo 1D alignment through paraffinic domains of the dodecyl chains to form the lamellar structure (Fig. 2A, inset). We confirmed that all of the tripodal paraffinic triptycenes (Fig. 1E) similarly self-assemble to form a lamellar structure such that the hexagonal lattice parameters are almost identical, whereas the interlayer distances change depending on the length of the paraffinic side chains (table S2 and figs. S3 to S6). All of the structural features observed for the bulk samples indicate that the tripodal triptycene is an eligible motif for substantiating the 2D + 1D assembly.

When a powder sample of **Trip-C12**, sandwiched between 100-μm-thick sapphire substrates, was once heated (215°C) to an isotropic liquid and then cooled slowly (0.5°C/min) to 25°C (*21*), the resulting film showed an entirely dark image (fig. S7A) in polarized optical microscopy. A conoscope image of this nonbirefringent film showed an excellent symmetrical isogyre cross (fig. S7A, inset), indicating that a continuous layer structure is uniformly formed parallel to the substrate surface. The through-view XRD image of this film (Fig. 2, C and D) shows three sets of hexagonally arranged spots with *d*-spacings of 0.70, 0.40, and 0.35 nm arising from diffraction from the (100), (110), and (200) planes, respectively, of the hexagonal lattice formed by nested packing of the triptycene moiety. Diffraction from (00*n*) planes was not detected. From this XRD profile, together with the conoscopic image (fig. S7A, inset), we conclude that the 2D hexagonal arrays of the triptycene pile up parallel to the substrate surface. The domain of the **Trip-C12** assembly, featuring a 2D (hexagonal triptycene array) + 1D (layer stacking) structural order (*22*), is actually greater

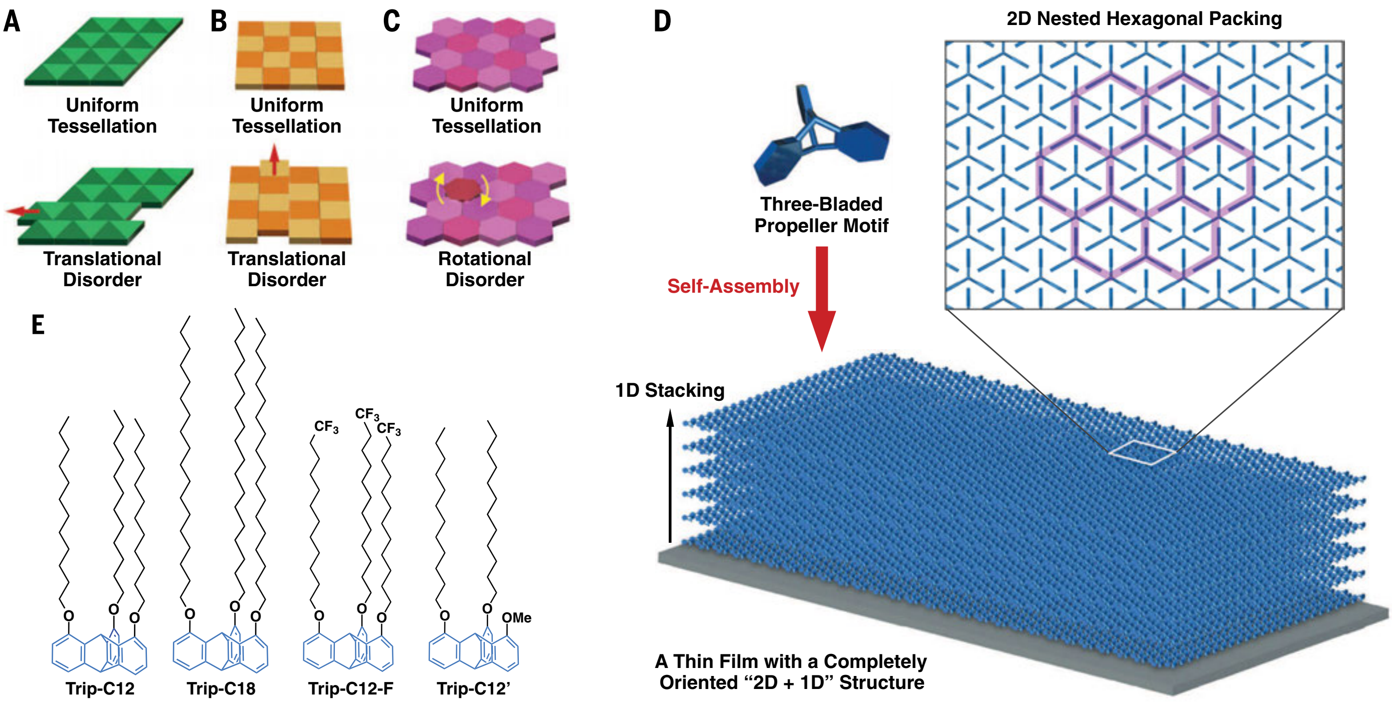

Fig. 1. Schematic representations of geometrical models and chemical compounds for the space-filling design. Uniform tessellation with regular polygons: triangles [(**A**), top], tetragons [(**B**), top], and hexagons [(**C**), top]. Translational and rotational disorder may occur for the former two polygons [(A and B), bottom] and hexagons [(C), bottom], respectively. (**D**) Space-filling model with a three-bladed, propeller-shaped motif, capable of forming a 2D hexagonal array by the interpenetration of its propeller parts (nested packing). The 2D hexagonal arrays stack one-dimensionally to form multilayers with long-range structural order. (**E**) Molecular structures of a series of tripodal paraffinic triptycenes (**Trip-C12**, **Trip-C18**, **Trip-C12-F**, and **Trip-C12′**) used for embodying the space-filling design. Me, methyl.

than the x-ray beam size (350 μm by 150 μm) used for the experiment. Even more surprising, through-view XRD images of the film, observed at more than 30 different points, displayed hexagonally arranged diffraction spots with identical orientation (Fig. 2D and figs. S8 and S9). This result means that the film of **Trip-C12** is domain-boundary–free at the centimeter length scale.

Although such a uniform assembly occurred only occasionally in a square-centimeter size regime, square-millimeter–sized films devoid of domain boundaries could be readily obtained by the slow cooling (≤0.5°C/min) of **Trip-C12** from its isotropic hot melt. We could not detect the occurrence of nucleation and growth by optical microscopy throughout the cooling process from the isotropic liquid (215°C) to solid (25°C). Instead, the system completely preserved a homogeneous appearance. Furthermore, **Trip-C12** hardly showed supercooling behavior (fig. S1A), which is generally associated with phase transitions between crystal and isotropic liquid. These observations are in sharp contrast to the case of usual crystallization in organic compounds. We presume that the uniform assembly of **Trip-C12** is not formed via direct growth from a locally occurring nucleus but rather via the fusion of dynamic domains, wherein triptycene molecules, capable of nested packing, fluctuate concertedly in such a way as to correct lattice mismatches. The dynamic behavior of the **Trip-C12** assembly is confirmed by the time-dependent 2D XRD images for a bulk sample, monitored at a temperature just below the isotropic liquid-to-crystal transition (fig. S11 and movie S1).

Spin-coating of a diluted toluene solution of **Trip-C12** on a silicon wafer produced a large-area monolayer film (fig. S12, A and B). Atomic force microscopy (AFM) of a spin-coated film shows that **Trip-C12** molecules were aligned vertical to the substrate surface with partial tilting (fig. S12, C to F), but AFM did not resolve the location of the triptycene moiety. To address this concern, we used a monolayer film of **Trip-C12-F** (Fig. 1E and fig. S13) with diagnostic CF_3 groups at the termini of the side chains and used time-of-flight low-energy atom scattering (TOFLAS) spectroscopy (fig. S14) to characterize the elemental composition of the topmost layer. The CF_3 groups are exclusively located at the outermost surface of the monolayer **Trip-C12-F** film, whereas the carbon-rich triptycene array was in contact with the substrate surface (fig. S14A). Judging from the order of the surface free energies (fluoroalkyl > alkyl > aryl groups) (*23*), **Trip-C12** most likely assembles on the substrate in a manner similar to **Trip-C12-F** (fig. S12C). Considering that the formation of conventional self-assembled monolayers requires polar functional groups that can bind to solid substrates (*24*), the assembling behavior of the fully paraffinic triptycenes, resulting in a uniform monolayer, is noteworthy.

The tripodal paraffinic triptycenes (Fig. 1E) could be vacuum-evaporated onto various substrates to give high-quality, uniform thin films to cover an area as large as a 2-inch (5-cm) silicon wafer (fig. S15). Even in assembly from the vapor phase, the triptycenes exerted their particular 2D structuring capability. Analysis by 2D grazing-incidence XRD (GI-XRD) (*20*) showed that evaporated films obtained from the present series of triptycenes had a completely oriented 2D + 1D structure. Typically, the GI-XRD image of a 50-nm-thick evaporated film of **Trip-C12** (Fig. 3, A and C) on a silicon wafer displays intense spots in the meridional direction with *d*-spacings of 2.21, 1.10, and 0.73 nm arising from the primary (001), secondary (002), and tertiary (003) diffraction planes, respectively, indicating that a 1D lamellar structure is formed vertical to the substrate. In the equatorial direction, there are two spots with *d*-spacings of 0.72 and 0.41 nm arising from the diffraction of the (100) and (110) planes of a 2D hexagonal lattice, respectively. Accordingly, the 2D triptycene arrays developed parallel to the substrate. When the evaporated film was thermally

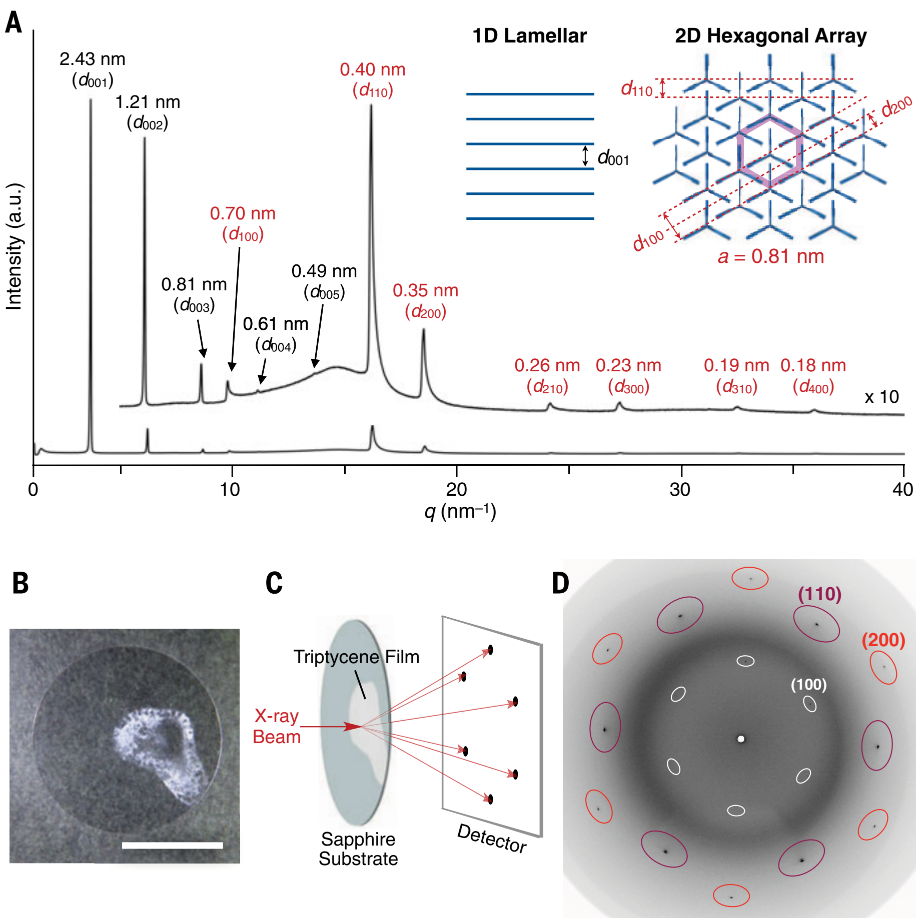

Fig. 2. Structural characterization of bulk and film samples of Trip-C12. (**A**) 1D XRD pattern (scattering vector q = 0 to 40 nm^{-1}) and schematic representation of the structural elements (inset) of a bulk sample of **Trip-C12** at 30°C upon cooling from its isotropic hot melt in a glass capillary (1.5 mm in diameter). a.u., arbitrary units. (**B**) Photograph of a macroscopic **Trip-C12** film sandwiched by sapphire substrates. Scale bar, 1.0 cm. The partial cloudiness of the film is caused by light scattering due to the surface roughness. (**C**) Schematic representation of the experimental setup for the through-view XRD measurement. (**D**) Through-view XRD image of the macroscopic **Trip-C12** film. Values in parentheses indicate Miller indices.

annealed (120°C for 1 hour), all of the diffraction peaks sharpened (Fig. 3B), and the lamellar layer spacing increased from 2.21 to 2.33 nm. Most likely, the paraffinic side chains of **Trip-C12** elongated upon thermal annealing to enhance the overall molecular order. AFM shows that the film surface after annealing becomes flat (fig. S16), and the observed height difference falls within 4.4 nm, corresponding to two molecular layers.

We evaluated the domain size by through-view XRD analysis of a 50-nm-thick evaporated film fabricated on a sapphire substrate (2.0 cm in diameter) (Fig. 3D). As shown in Fig. 3E, the diffraction from the (100), (110), and (200) planes of a hexagonal lattice was observed as short arcs, indicating that the 2D triptycene arrays in the film align to some extent within an area greater than the x-ray beam size (350 μm by 150 μm). This result is in contrast to the case with the aforementioned sandwich film (Fig. 2B), which displayed hexagonally arranged diffraction spots (Fig. 2D). Nevertheless, when through-view XRD images (Fig. 3, E to H) were taken at different points of the film at least 1 cm apart, hexagonally arranged diffraction arcs appeared at identical positions. This trend was clearer in the angular dependence of the corresponding 1D XRD profiles (Fig. 3, I and J). Thus, the evaporated film was devoid of detectable domain boundaries, at least in the centimeter size regime, although the orientational order among the 2D triptycene arrays within the 1D lamellar structure should not be perfect.

By virtue of the complete molecular orientation (Fig. 4A), the evaporated film of **Trip-C12** exhibited a very large optical anisotropy. Thus, electronic absorption spectra of the 50-nm-thick evaporated film of **Trip-C12** on a quartz substrate show the largest absorbance (λ_{max} = 229 nm) when the angle θ of incident ultraviolet (UV) light is perpendicular to the film (Fig. 4). The absorbance dramatically decreased when θ becomes shallower (90° → 15°). These observations are consistent with a theoretical prediction (*20*) in which the transition dipole moment of a model compound (1,8,13-trimeoxytriptycene) of **Trip-C12** faces in a direction virtually perpendicular to its longer molecular axis (fig. S17). Complete molecular orientation can be achieved regardless of the type of substrates. The GI-XRD

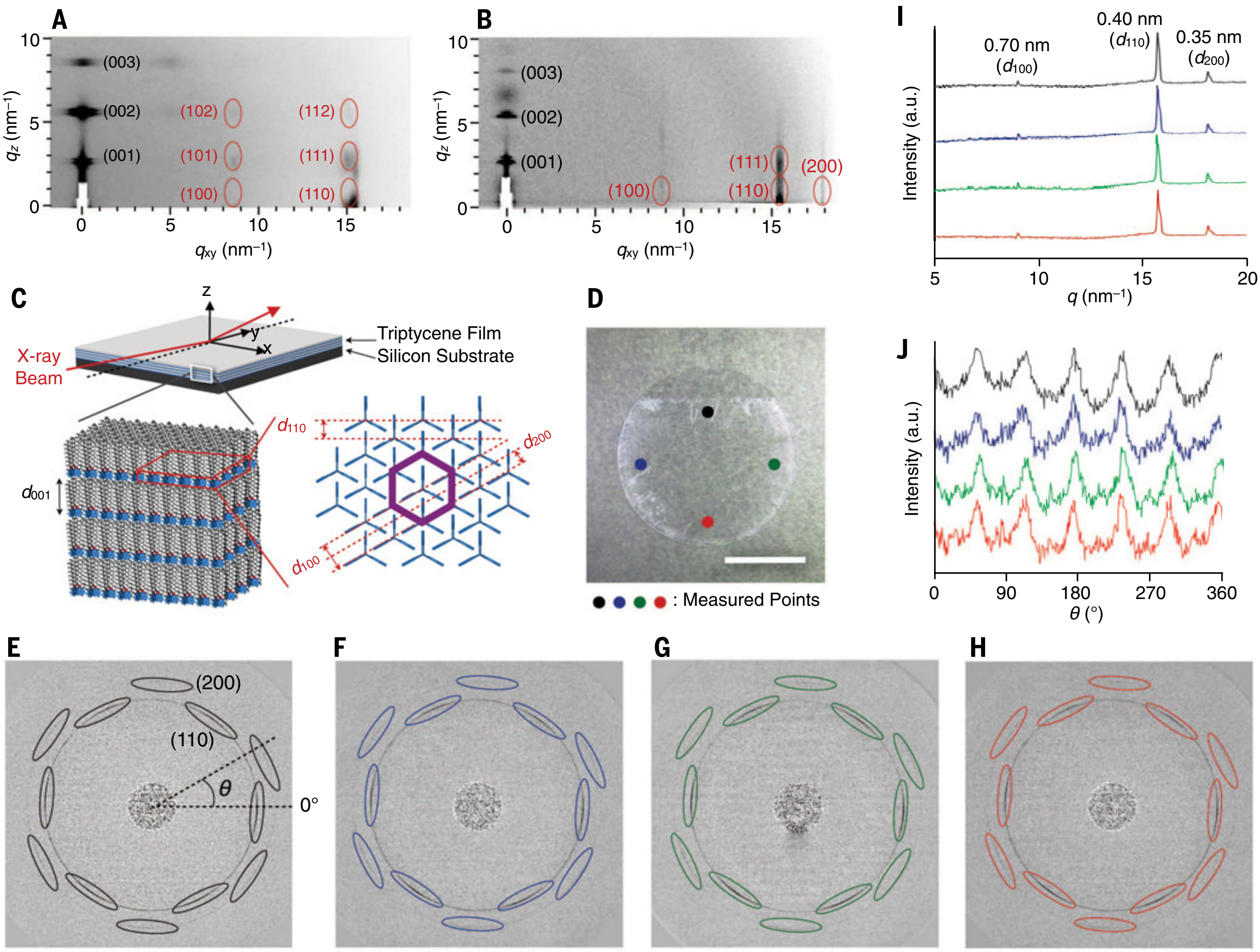

Fig. 3. Structural characterization of the evaporated films of Trip-C12. 2D GI-XRD images of a 50-nm-thick evaporated film of **Trip-C12** on a silicon wafer before (**A**) and after (**B**) thermal annealing at 120°C for 1 hour. Values in parentheses indicate Miller indices. (**C**) Schematic representations of the experimental setup for GI-XRD and the assembly structure of a **Trip-C12** film on a substrate. (**D**) Photograph of a 50-nm-thick evaporated film of **Trip-C12** on a sapphire substrate. Black, blue, green, and red circles indicate the measured points in the through-view XRD analysis. Scale bar, 1.0 cm. (**E** to **H**) Through-view XRD images of the **Trip-C12** film measured at the black (E), blue (F), green (G), and red (H) circles in (D). The images were corrected by subtracting the background diffractions from the sapphire substrate. Values in parentheses indicate Miller indices. 1D XRD profile (**I**) and angular dependency (**J**) of the peak intensity of the diffraction from the (110) plane converted from the through-view XRD images. The black, blue, green, and red profiles were obtained from the data of (E), (F), (G), and (H), respectively. The θ value corresponds to the value denoted in (E).

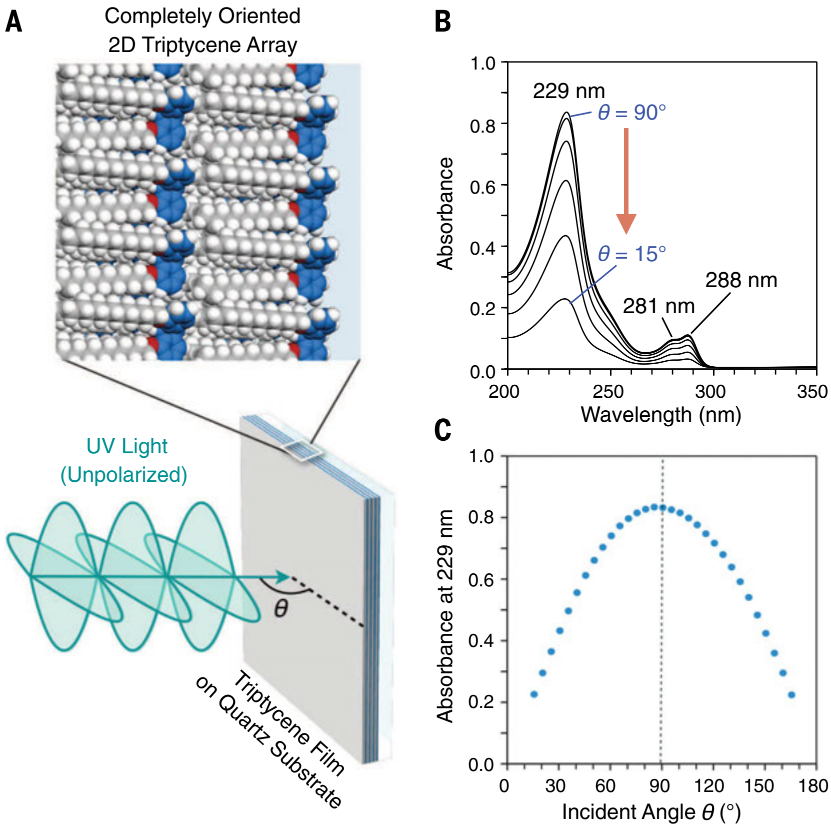

Fig. 4. Anisotropic absorption properties of the evaporated film of Trip-C12. (**A**) Schematic illustration of the experimental setup for the electronic absorption spectroscopy of a **Trip-C12** film on a quartz substrate. The angle of incident unpolarized UV light is represented by θ. Substrate and beam sizes are 20.0 mm by 20.0 mm by 1.0 mm and 3.0 mm by 11.0 mm, respectively. (**B**) Electronic absorption spectra of the 50-nm-thick evaporated film of **Trip-C12** on a quartz substrate, measured upon exposure to unpolarized UV light with various incident angles (θ = 90°, 75°, 60°, 45°, 30°, and 15°). The spectra were corrected for both the irradiated area and the contribution of the absorption of the substrate. (**C**) Incident angle dependence of the absorbance at 229 nm of the evaporated film of **Trip-C12**.

images observed for evaporated films of **Trip-C12** (50 nm in thickness)—fabricated on polyimide, polyethylene terephthalate, quartz, and mica—are essentially identical to one another (fig. S18) and also to those observed for the evaporated film on a silicon wafer (Fig. 3, A and B).

Analogous to **Trip-C12**, **Trip-C18** and **Trip-C12′** (Fig. 1E) afford completely oriented films upon vacuum evaporation. Based on GI-XRD analysis, the lattice parameter (a = 0.82 nm) of the hexagonal triptycene array for the **Trip-C18** film is virtually identical to that for **Trip-C12** (a = 0.81 nm), whereas the layer spacing is increased (2.96 nm) because of the longer paraffinic side chains (fig. S19) (*25*). Meanwhile, the 2D hexagonal lattice parameters for the **Trip-C12′** and **Trip-C12** assemblies are identical to one another (fig. S20), though the 1D layer spacing for **Trip-C12′** (1.93 nm) is shorter than that for **Trip-C12** (2.33 nm). The evaporated film of **Trip-C12′** shows no detectable change in its GI-XRD profile before and after thermal annealing, indicating that **Trip-C12′**, with only two dodecyl groups, can achieve a thermodynamically stable packing structure through simple evaporation (fig. S20). The triptycene films display excellent thermal stability. For example, an evaporated film of **Trip-C12** shows no detectable change in the GI-XRD profiles before and after heating at 200°C for 1 hour. The nested packing is sufficiently thermally robust to preserve the 2D hexagonal triptycene array up to a temperature close to the melting point of the constituent molecule (210°C).

Without dedicated anchoring to solid substrates, appropriately designed triptycene molecules can form completely oriented films regardless of the type of substrates. The tripodal triptycenes may serve as useful scaffolds for integrating functional molecular units and, in turn, for the development of high-performance thin-film materials.

REFERENCES AND NOTES

1. S. L. Kwolek, P. W. Morgan, J. R. Schaefgen, L. W. Gulrich, *Macromolecules* **10**, 1390–1396 (1977).
2. J. C. Wittmann, P. Smith, *Nature* **352**, 414–417 (1991).
3. H. Jinnai, R. J. Spontak, T. Nishi, *Macromolecules* **43**, 1675–1688 (2010).
4. T. Asari, S. Arai, A. Takano, Y. Matsushita, *Macromolecules* **39**, 2232–2237 (2006).
5. J. J. De Yoreo, P. G. Vekilov, *Rev. Mineral. Geochem.* **54**, 57–93 (2003).
6. T. F. A. De Greef *et al.*, *Chem. Rev.* **109**, 5687–5754 (2009).
7. S. Zamir *et al.*, *J. Am. Chem. Soc.* **116**, 1973–1980 (1994).
8. T. Osawa *et al.*, *Angew. Chem. Int. Ed.* **51**, 7990–7993 (2012).
9. C.-F. Chen, *Chem. Commun.* **47**, 1674–1688 (2011).
10. T. M. Swager, *Acc. Chem. Res.* **41**, 1181–1189 (2008).
11. M. Mastalerz, I. M. Oppel, *Angew. Chem. Int. Ed.* **51**, 5252–5255 (2012).
12. P. Kissel, D. J. Murray, W. J. Wulftange, V. J. Catalano, B. T. King, *Nat. Chem.* **6**, 774–778 (2014).
13. R. G. Hazell, G. S. Pawley, C. E. Lund Petersen, *J. Cryst. Mol. Struct.* **1**, 319–324 (1971).
14. Cambridge Structural Database, version 5.31 (2014), www.ccdc.cam.ac.uk/Solutions/CSDSystem/Pages/CSD.aspx.
15. F. H. Allen, *Acta Crystallogr. B* **58**, 380–388 (2002).
16. M. H. P. Ardebili, D. A. Dougherty, K. Mislow, L. H. Schwartz, J. G. White, *J. Am. Chem. Soc.* **100**, 7994–7997 (1978).
17. K. Yamamura, T. Kawashima, K. Eda, F. Tajima, M. Hashimoto, *J. Mol. Struct.* **737**, 1–6 (2005).
18. J. Chmiel *et al.*, *Eur. J. Org. Chem.* **2010**, 3897–3907 (2010).
19. S. Norvez, *J. Org. Chem.* **58**, 2414–2418 (1993).
20. Materials and methods are available as supplementary materials on *Science* Online.
21. Rapid cooling (e.g., 5°C/min) of the isotropic liquid of **Trip-C12** results in the formation of multidomain films (fig. S7B).
22. Atomic force microscopy of a thin film fabricated by spin-coating a diluted toluene solution of **Trip-C12** allows the visualization of the 2D (hexagonal triptycene array) + 1D (layer stacking) structure (fig. S10).
23. D. Janssen, R. De Palma, S. Verlaak, P. Heremans, W. Dehaen, *Thin Solid Films* **515**, 1433–1438 (2006).
24. A. Ulman, *Chem. Rev.* **96**, 1533–1554 (1996).
25. **Trip-C12** and **Trip-C18** are miscible with each other in the molar ratios of **Trip-C12**:**Trip-C18** = 2:1, 1:1, and 1:2 and coassemble into a well-defined 2D + 1D structure (fig. S21).

ACKNOWLEDGMENTS

This work was supported by KAKENHI (no. 24350055); a Grant-in-Aid for Scientific Research on Innovative Areas "π-Figuration" (no. 26102001) of The Ministry of Education, Culture, Sports, Science, and Technology, Japan; and a grant from the NAGASE Science Technology Foundation (2012). The synchrotron XRD experiments were performed at the BL44B2 and BL45XU in the SPring-8 with the approval of the RIKEN SPring-8 Center (proposal nos. 20130025 and 20140056). We thank H. Sato (Rigaku Corporation) for the single-crystal x-ray crystallography of **Trip-C12** and T. Tada (Tokyo Institute of Technology) for the density functional theory calculations. We acknowledge Pascal Co. for the measurement of TOFLAS spectroscopy. Crystal data for **Trip-C12** and **Trip-C1** are available from the Cambridge Crystallographic Data Center under reference numbers CCDC-1031109 and CCDC-1031110, respectively, via www.ccdc.cam.ac.uk/data_request/cif.

SUPPLEMENTARY MATERIALS

www.sciencemag.org/content/348/6239/1122/suppl/DC1
Materials and Methods
Figs. S1 to S21
Tables S1 to S3
References (*26*–*43*)
Movie S1

17 March 2015; accepted 6 May 2015
10.1126/science.aab1391

NITROGEN CYCLING

Rapid nitrous oxide cycling in the suboxic ocean

Andrew R. Babbin,[1,2*] Daniele Bianchi,[3] Amal Jayakumar,[1] Bess B. Ward[1]

Nitrous oxide (N_2O) is a powerful greenhouse gas and a major cause of stratospheric ozone depletion, yet its sources and sinks remain poorly quantified in the oceans. We used isotope tracers to directly measure N_2O reduction rates in the eastern tropical North Pacific. Because of incomplete denitrification, N_2O cycling rates are an order of magnitude higher than predicted by current models in suboxic regions, and the spatial distribution suggests strong dependence on both organic carbon and dissolved oxygen concentrations. Furthermore, N_2O turnover is 20 times higher than the net atmospheric efflux. The rapid rate of this cycling coupled to an expected expansion of suboxic ocean waters implies future increases in N_2O emissions.

Anthropogenically derived atmospheric N_2O concentrations increased over the past century (*1–3*), but the natural marine sources and sinks of N_2O have been difficult to quantify. Because of the paucity of direct measurements of N_2O production and consumption in the ocean, current rate estimates and predictions of how the N_2O budget will respond to a changing climate remain uncertain (*4*). The most concentrated oceanic sources of N_2O to the atmosphere are the suboxic (0 to 20 μmol l^{-1}) waters overlying the oxygen minimum zones (OMZs), based on measurements and models of supersaturated N_2O concentrations (*5*, *6*). Furthermore, N_2O is produced by both nitrification and denitrification, but the overall importance of each process is uncertain. Nitrification, the oxidation of ammonium to nitrite and further to nitrate, exhibits maximum rates just below the well-lit surface layer, where remineralization rates supplying ammonium are highest. Nitrification generates an N_2O by-product (*7*) whose yield is enhanced by suboxic concentrations—the yield of N_2O, as a fraction of nitrite production, can be as high as 10% in culture (*8*, *9*) and 0.4% in the environment (*10*, *11*). However, at very low (less than a few micromolar) oxygen concentrations, nitrification ceases (*12*), and no N_2O can be produced via this pathway.

Denitrification, the stepwise reductions of nitrate and nitrite through NO and N_2O to nitrogen gas, occurs in the ocean only when molecular oxygen is sufficiently low (less than 3 μmol l^{-1}) (*13*). This anaerobic process results in local N_2O minima within the OMZ core but has the potential to be a major N_2O source at the suboxic-anoxic interface (the oxycline) at the top of the OMZ. Over this narrow depth interval, N_2O consumption by the nitrous oxide reductase enzyme is inhibited by O_2 at an extent greater than its production in the denitrification sequence (*14*). Further, because the denitrification steps are predominantly heterotrophic, the rates are enhanced at shallow depths, where the supply of newly produced labile organic matter from the surface (*13*) is greater. Incomplete denitrification (reduction of NO_3^- to N_2O rather than to N_2) may account for a flux that is ignored or not explicitly represented in most biogeochemical ocean and climate models. Indeed, in culture experiments (*14*, *15*) and sediment incubations (*16*) at suboxic but nonzero O_2 concentrations, denitrification activity decreased as expected with increasing O_2 concentrations, but the N_2O yield (i.e., the proportion of denitrification halting at N_2O) increased to ~50% (*15*).

We directly measured the reduction of N_2O to dinitrogen gas by using labeled isotopic $(^{15}N)_2O$ tracer incubation experiments at three stations in the eastern tropical North Pacific (ETNP), the largest suboxic zone (*17*) and a major site of N_2O production (*18*, *19*). N_2O reduction is the only major biological N_2O consumption process; because production occurs via multiple pathways, in situ production rates via isotopic tracer techniques cannot be directly constrained (*20*).

The transect across the ETNP (fig. S1) showed the characteristic features associated with OMZs, namely a N_2O concentration peak (~100 nmol l^{-1}) at the base of a steep oxygen gradient and an N_2O concentration minimum in the core of the OMZ. All three sites displayed similar alignments of oxygen, N_2O, and nitrite maxima and minima (Fig. 1A), indicating similar mechanisms affecting the biogeochemistry across the region. The similarity between the N_2O profile at the offshore station 2 and data from a nearby site measured 12 years prior (*19*) (Fig. 1B) indicates long-term stability in the shape and peak magnitudes of the N_2O profiles.

N_2O consumption rates (Fig. 2) measured across all three profiles were up to 35 nmol l^{-1} day^{-1}, indicating residence times as low as 1 day (calculated from the concentration divided by the biological rate). This fast turnover was observed throughout the OMZ core, presumably because of tight coupling of sequential denitrification steps. Within the oxycline, the N_2O residence times increased and the reduction rates decreased sharply as O_2 increased. This synchronism is consistent with oxygen poisoning of the nitrous oxide reductase enzyme above the OMZ. Moreover, and of greater consequence to atmospheric N_2O emissions, an estimate of the rate of production based on a one-dimensional (1D) transport-reaction balance (fig. S3) was systematically larger than that of consumption near the base of the oxycline. This 1D estimate is likely to be conservative, because the inclusion of horizontal transport terms, which act to erode the N_2O peak, would require an increase in the N_2O source to maintain the balance (table S2 and supplementary text). The observed near-shore (station 1) rates of N_2O reduction and production decreased with depth (Fig. 2), resembling the depth-dependent power law decay of organic carbon supply (*13*). This organic carbon dependence of N_2O cycling was also apparent from the occurrence of the highest rates near shore, where the greatest primary production occurs. These measurements highlight the large spatial heterogeneity of N_2O cycling dependent on organic carbon export in the ETNP.

We investigated the broader implications of such rapid N_2O cycling with a mechanistic, 1D model of OMZ biogeochemistry (supplementary materials) built on parameterizations widely adopted in ocean biogeochemical models, including biological N_2O production via nitrification, enhanced at suboxic concentrations (*4*, *6*, *21*, *22*), and consumption via denitrification (*19*). Following previous parameterizations (*21*), we defined an oxygen threshold of 2 μmol l^{-1}, above which N_2O was produced and below which, consumed. However, this 1D model with N_2O production from nitrification alone generated a production rate (maximum of 0.3 nmol l^{-1} day^{-1}) that was a fraction of the net production rate calculated from the measured consumption (Fig. 3A). The observed N_2O concentration peaks measured here at >100 nmol l^{-1} (Fig. 1) are likely not reproduced in models (*21*), including our 1D version (which only achieves a maximum of 70 nmol l^{-1}), because they do not include explicit production by incomplete denitrification. The importance of denitrification to N_2O production has been implicated by measurements across all three major OMZs: the ETNP (*18*, *23*), the eastern tropical South Pacific (ETSP) (*24*), and the Arabian Sea (*20*, *25*).

We expanded the 1D model to separate the N_2O production and consumption terms of denitrification and allow for O_2-dependent decoupling (*26*). With this change, denitrification became a major N_2O source in the low-O_2 waters directly overlying the OMZ (9.3 μmol m^{-2} day^{-1}) and was comparable in size to the source from nitrification (9.1 μmol m^{-2} day^{-1}). Furthermore, the maximum modeled net N_2O production rate of 0.6 nmol l^{-1} day^{-1} is consistent with our observations (Fig. 3B), with a peak concentration of >110 nmol l^{-1}. Such agreement could not be achieved with production via nitrification alone and suggests that denitrification constitutes a major and largely overlooked source of N_2O. This conclusion also holds for a range of model parameters and formulations, including a simple

[1]Department of Geosciences, Princeton University, Princeton, NJ 08544, USA. [2]Department of Civil and Environmental Engineering, Massachusetts Institute of Technology, Cambridge, MA 02139, USA. [3]School of Oceanography, University of Washington, Seattle, WA 98105, USA.
*Corresponding author. E-mail: babbin@mit.edu

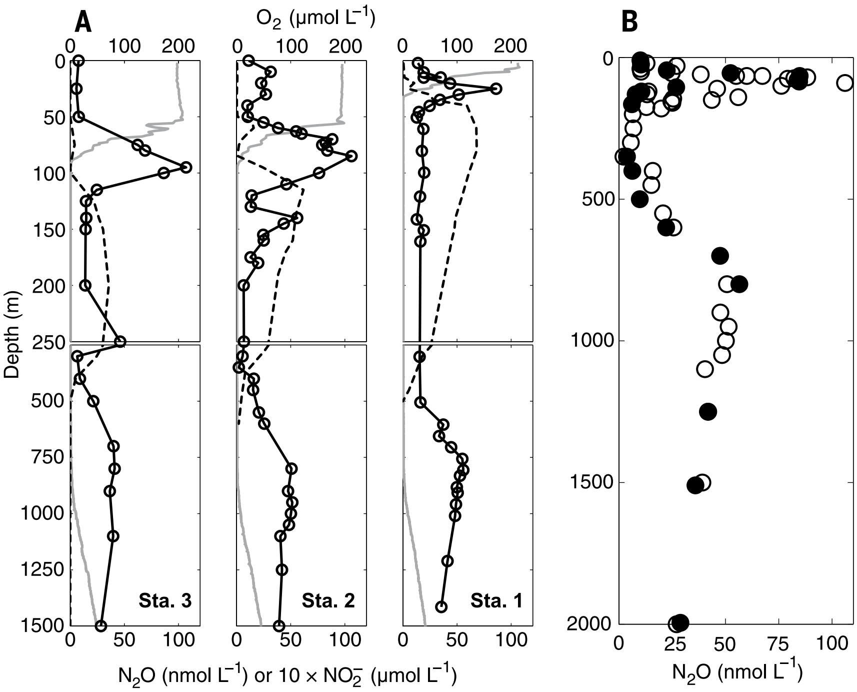

Fig. 1. Biogeochemical measurements. (**A**) Depth profiles of N_2O (open circles), O_2 (solid gray line), and NO_2^- (dashed line) concentrations at the three stations included in this study. (**B**) Comparison of N_2O concentration data (open circles) from station 2 collected in April 2012 with those from a previous study (*19*) (solid circles) of a nearby location (16°N 107°W) in spring 2000.

representation of lateral transports, as shown by a series of sensitivity studies (fig. S2, table S2, and supplementary text).

Similar to the model results, a conservative average from offshore measurements at the base of the oxycline indicated a net production rate on order of ~1 nmol l^{-1} day^{-1}. Based on the measured rates and the observed extent of the suboxic layer at the base of the oxycline of the three profiles, production exceeds consumption across a thickness of ~10 ± 4 m (SD) immediately overlying the anoxic layer. A 1 nmol l^{-1} day^{-1} imbalance integrated over 10 m equates to an air-sea N_2O flux of 10 μmol m^{-2} day^{-1}, which is comparable (30 to 100%) to the fluxes estimated in the analogous suboxic ETSP (*24*). Our model including a denitrification N_2O source produced a similar atmospheric efflux of 13 μmol m^{-2} day^{-1}. As an order-of-magnitude estimate, integrating a 10 μmol m^{-2} day^{-1} flux horizontally over the extent of the suboxic ETNP ($25.7 \times 10^{12} \pm 1.5 \times 10^{12}$ m^2) yields a net atmospheric N_2O flux out of the ETNP OMZ of 1.3 ± 0.1 Tg of N $year^{-1}$. Furthermore, if we conservatively estimate the average reduction rate based on our measurements within the ETNP OMZ (2 nmol l^{-1} day^{-1}) and integrate over the full volume of the anoxic ETNP OMZ ($1.2 \times 10^{15} \pm 0.5 \times 10^{15}$ m^3), the total cycling rate through N_2O is 25 ± 10 Tg of N $year^{-1}$, or 20 times higher than the net efflux. This gross rate of N_2O generation is comparable to previous estimates of denitrification rates from the ETNP (*27*–*30*). Because the net outgassing of N_2O to the atmosphere results from the residual between large production and reduction rates, it could change greatly in response to even a small decoupling of production and consumption, caused, for example, by more frequent O_2 injections (*31*) or changes in the volume and geometry of suboxic zones (*32*, *33*).

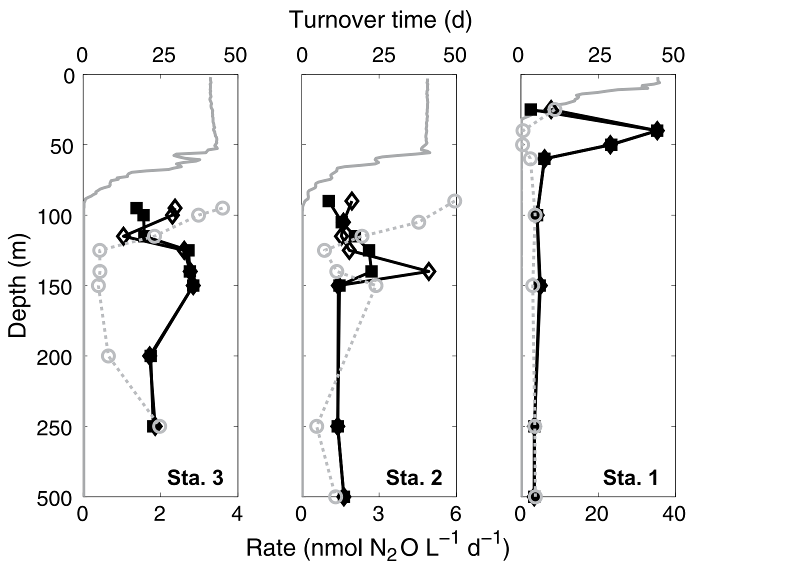

Fig. 2. N_2O cycling rates. Rates of measured N_2O consumption (solid squares) and calculated production (open diamonds) are shown at the three stations. Turnover times are indicated by open circles. Scaled (0 to 100% saturation) O_2 concentration profiles (solid gray line) are included for reference (see Fig. 1 for concentrations). Note the broken vertical axis between 250 and 500 m. N_2O production was calculated by using the measured consumption rates and concentration profiles and assuming a vertical balance between advection, diffusion, consumption, and production. Lateral transport processes, which would tend to erode the N_2O peak and thus require more production, were ignored here, making these production rates likely lower estimates (supplementary text).

Our results show that the net accumulation of N_2O in the OMZs on the multiyear time scales dictated by ocean circulation hides the delicate balance between production and consumption that proceeds on time scales at least one order of magnitude faster. Over long time scales into the future, expanding and shoaling OMZs resulting from changes in physical circulation, widespread ocean deoxygenation (*34*), and increased fertilizer runoff stimulating phytoplankton blooms could exacerbate marine N_2O accumulation and outgassing (*4*, *31*). This increase would be especially important given the rapid biological rates measured in the ETNP. The rapid turnover of N_2O in OMZs also implies that shorter time scale variations influence N_2O

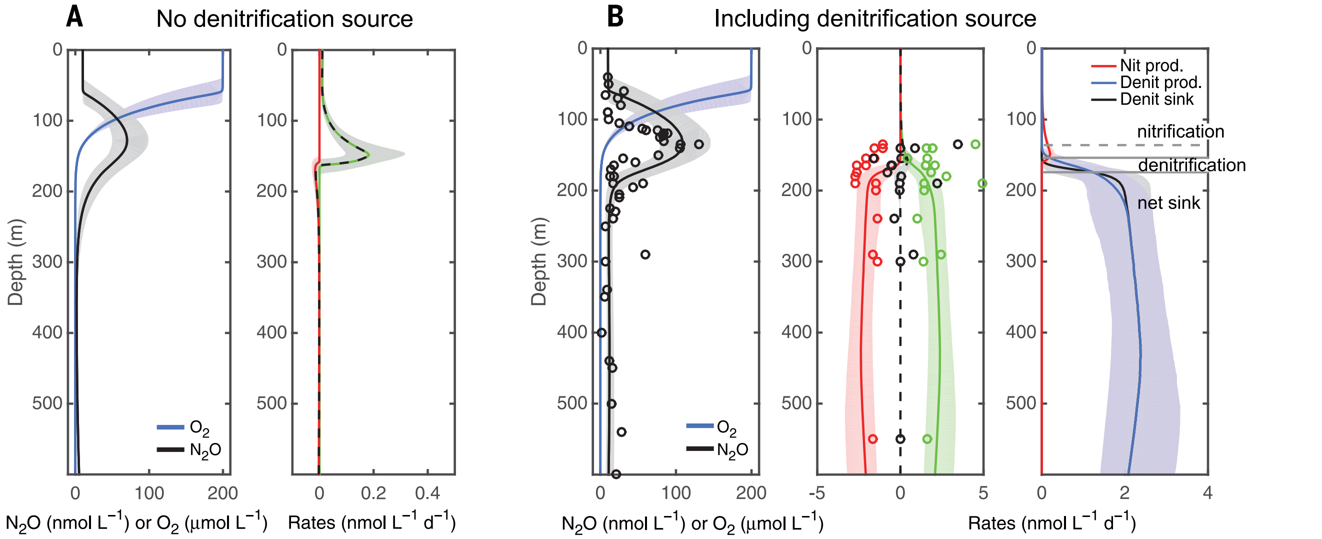

Fig. 3. One-dimensional model of N_2O cycling in the OMZ. (**A**) Modeled N_2O and O_2 concentrations using a mechanistic 1D model of OMZ biogeochemistry, with rates of production from nitrification (green) and consumption from denitrification (red). The net rate is given by the dashed black curve. (**B**) As in (A) but with an additional N_2O source from denitrification included. The third graph separates the different production and consumption terms. Points show measurements at stations 2 and 3. Model and data profiles have been shifted vertically to align the N_2O peaks to the mean model N_2O peak depth. Solid horizontal gray lines separate the layers of nitrification-dominated production, denitrification-dominated production, and net denitrification consumption. The dashed gray line shows where denitrification begins to act as a major N_2O source in the model. Envelopes in all graphs show the standard deviation from an ensemble of Monte Carlo runs (N = 5000) simultaneously varying all of the parameterizations.

flux, as reported for the Arabian Sea's annual monsoons (*35*). El Niño–Southern Oscillation strongly affects the mixed layer and thermocline depths and surface productivity in the eastern tropical Pacific. Via this natural variability, the OMZs of the ETNP and the ETSP should expand and shoal during a La Niña and contract during an El Niño (*36*).

Current estimates of the marine N_2O sources to the atmosphere that do not mechanistically account for incomplete denitrification, including the Intergovernmental Panel on Climate Change (IPCC) estimate of ~4 Tg of N year^{-1}, are low considering the overall denitrification rates to N_2 in the OMZs (*33*, *35*, *37*). If we assume that the three major OMZs are approximately equivalent, the N_2O production rates predicted here would account for 4 Tg of N year^{-1} from the OMZs alone. This is a conservative analysis, limited to the offshore sites and ignoring the coastal region with higher rates and imbalances (Fig. 2). Inclusion of coastal sites could substantially increase this estimate. Further, models parameterizing N_2O production via only nitrification require tuning by some additional suboxic process to produce N_2O in the OMZs and better simulate concentration distributions (*4*, *22*, *38*). The directly measured rates and simple model presented in this paper show that these tunings do not capture the dynamics necessary to represent accurately marine N_2O cycling.

REFERENCES AND NOTES

1. J. Flückiger *et al.*, *Science* **285**, 227–230 (1999).
2. A. R. Ravishankara, J. S. Daniel, R. W. Portmann, *Science* **326**, 123–125 (2009).
3. G. Myhre *et al.*, in *Climate Change 2013: The Physical Science Basis. Contribution of Working Group I to the Fifth Assessment Report of the Intergovernmental Panel on Climate Change*, T. F. Stocker *et al.*, Eds. (Cambridge Univ. Press, Cambridge, 2013), pp. 659–740.
4. J. Martinez-Rey, L. Bopp, M. Gehlen, A. Tagliabue, N. Gruber, *Biogeosciences Discuss.* **11**, 16703–16742 (2014).
5. Y. Cohen, L. I. Gordon, *J. Geophys. Res. Oceans* **84**, 347–353 (1979).
6. P. Suntharalingam, J. L. Sarmiento, *Global Biogeochem. Cycles* **14**, 429–454 (2000).
7. A. E. Santoro, C. Buchwald, M. R. McIlvin, K. L. Casciotti, *Science* **333**, 1282–1285 (2011).
8. T. J. Goreau *et al.*, *Appl. Environ. Microbiol.* **40**, 526–532 (1980).
9. F. Lipschultz *et al.*, *Nature* **294**, 641–643 (1981).
10. J. W. Elkins, S. C. Wofsy, M. B. McElroy, C. E. Kolb, W. A. Kaplan, *Nature* **275**, 602–606 (1978).
11. H. P. J. de Wilde, M. J. M. de Bie, *Mar. Chem.* **69**, 203–216 (2000).
12. W. Martens-Habbena, P. M. Berube, H. Urakawa, J. R. de la Torre, D. A. Stahl, *Nature* **461**, 976–979 (2009).
13. A. R. Babbin, R. G. Keil, A. H. Devol, B. B. Ward, *Science* **344**, 406–408 (2014).
14. H. Körner, W. G. Zumft, *Appl. Environ. Microbiol.* **55**, 1670–1676 (1989).
15. M. R. Betlach, J. M. Tiedje, *Appl. Environ. Microbiol.* **42**, 1074–1084 (1981).
16. K. S. Jørgensen, H. B. Jensen, J. Sørensen, *Can. J. Microbiol.* **30**, 1073–1078 (1984).
17. A. Paulmier, D. Ruiz-Pino, *Prog. Oceanogr.* **80**, 113–128 (2009).
18. N. Yoshida, A. Hattori, T. Saino, S. Matsuo, E. Wada, *Nature* **307**, 442–444 (1984).
19. H. Yamagishi *et al.*, *J. Geophys. Res. Biogeosciences* **112**, G02015 (2007).
20. J. C. Nicholls, C. A. Davies, M. Trimmer, *Limnol. Oceanogr.* **52**, 156–168 (2007).
21. C. Nevison, J. H. Butler, J. W. Elkins, *Global Biogeochem. Cycles* **17**, 1119 (2003).
22. X. Jin, N. Gruber, *Geophys. Res. Lett.* **30**, 2249 (2003).
23. T. Yoshinari *et al.*, *Mar. Chem.* **56**, 253–264 (1997).
24. L. Farías *et al.*, *Limnol. Oceanogr.* **54**, 132–144 (2009).
25. S. W. A. Naqvi *et al.*, *Proc. Indian Acad. Sci. Earth Planet. Sci.* **107**, 367–378 (1998).
26. T. Dalsgaard *et al.*, *MBio* **5**, e01966-e14 (2014).
27. C. Deutsch, N. Gruber, R. M. Key, J. L. Sarmiento, A. Ganachaud, *Global Biogeochem. Cycles* **15**, 483–506 (2001).
28. D. Bianchi, J. P. Dunne, J. L. Sarmiento, E. D. Galbraith, *Global Biogeochem. Cycles* **26**, GB2009 (2012).
29. T. DeVries, C. Deutsch, F. Primeau, B. Chang, A. Devol, *Nat. Geosci.* **5**, 547–550 (2012).
30. T. DeVries, C. Deutsch, P. A. Rafter, F. Primeau, *Biogeosciences* **10**, 2481–2496 (2013).
31. L. A. Codispoti, *Science* **327**, 1339–1340 (2010).
32. L. Stramma, G. C. Johnson, J. Sprintall, V. Mohrholz, *Science* **320**, 655–658 (2008).
33. S. W. A. Naqvi *et al.*, *Nature* **408**, 346–349 (2000).
34. R. F. Keeling, A. Körtzinger, N. Gruber, *Annu. Rev. Mar. Sci.* **2**, 199–229 (2010).
35. H. W. Bange *et al.*, *Atmos. Chem. Phys.* **1**, 61–71 (2001).
36. T. Ito, C. Deutsch, *Global Biogeochem. Cycles* **27**, 1119–1128 (2013).
37. H. W. Bange, *Atmos. Environ.* **40**, 198–199 (2006).
38. P. Suntharalingam *et al.*, *Geophys. Res. Lett.* **39**, L07605 (2012).

ACKNOWLEDGMENTS

We thank the captain and crew of the R/V *Thomas G. Thompson* and chief scientist A. H. Devol for assistance in sampling and A. Morello and X. Peng for help with nitrite and N_2O measurements, respectively. J. L. Sarmiento provided valuable inputs in the development of the oxygen minimum zone model. This work was funded by a National Defense Science and Engineering Graduate Fellowship to A.R.B., NSF grant no. 1029951 to B.B.W. and A.J., and University of Washington funding to D.B. A.R.B. was additionally supported by a NSF Postdoctoral Research Fellowship in Biology (no. 1402109) while preparing the paper. All data measurements presented in this paper are included in table S3. The 1D MATLAB model code and output are available in the supplementary materials. A.R.B. and B.B.W. designed and conducted the shipboard experiments and analysis, D.B. designed and implemented the 1D model, and A.J. measured N_2O concentrations. All authors analyzed the data and model results and wrote the paper.

SUPPLEMENTARY MATERIALS

www.sciencemag.org/content/348/6239/1127/suppl/DC1
Materials and Methods
Supplementary Text
Figs. S1 to S3
Tables S1 to S3
References (*39*–*53*)
Supplementary Data

12 February 2015; accepted 28 April 2015
10.1126/science.aaa8380

POLITICAL SCIENCE

Exposure to ideologically diverse news and opinion on Facebook

Eytan Bakshy,[1*†] Solomon Messing,[1†] Lada A. Adamic[1,2]

Exposure to news, opinion, and civic information increasingly occurs through social media. How do these online networks influence exposure to perspectives that cut across ideological lines? Using deidentified data, we examined how 10.1 million U.S. Facebook users interact with socially shared news. We directly measured ideological homophily in friend networks and examined the extent to which heterogeneous friends could potentially expose individuals to cross-cutting content. We then quantified the extent to which individuals encounter comparatively more or less diverse content while interacting via Facebook's algorithmically ranked News Feed and further studied users' choices to click through to ideologically discordant content. Compared with algorithmic ranking, individuals' choices played a stronger role in limiting exposure to cross-cutting content.

Exposure to news and civic information is increasingly mediated through online social networks and personalization (*1*). Information abundance provides individuals with an unprecedented number of options, shifting the function of curating content from newsroom editorial boards to individuals, their social networks, and manual or algorithmic information sorting (*2*–*4*). Although these technologies have the potential to expose individuals to more diverse viewpoints (*4*, *5*), they also have the potential to limit exposure to attitude-challenging information (*2*, *3*, *6*), which is associated with the adoption of more extreme attitudes over time (*7*) and misperception of facts about current events (*8*). This changing environment has led to speculation around the creation of "echo chambers" (in which individuals are exposed only to information from like-minded individuals) and "filter bubbles" (in which content is selected by algorithms according to a viewer's previous behaviors), which are devoid of attitude-challenging content (*3*, *9*). Empirical attempts to examine these questions have been limited by difficulties in measuring news stories' ideological leanings (*10*) and measuring exposure—relying on either error-laden, retrospective self-reports or behavioral data with limited generalizability—and have yielded mixed results (*4*, *9*, *11*–*15*).

We used a large, comprehensive data set from Facebook that allows us to (i) compare the ideological diversity of the broad set of news and opinion shared on Facebook with that shared by individuals' friend networks, (ii) compare this with the subset of stories that appear in individuals' algorithmically ranked News Feeds, and (iii) observe what information individuals choose to consume, given exposure on News Feed. We constructed a deidentified data set that includes 10.1 million active U.S. users who self-report their ideological affiliation and 7 million distinct Web links (URLs) shared by U.S. users over a 6-month period between 7 July 2014 and 7 January 2015. We classified stories as either "hard" (such as national news, politics, or world affairs) or "soft" content (such as sports, entertainment, or travel) by training a support vector machine on unigram, bigram, and trigram text features (details are available in the supplementary materials, section S1.4.1). Approximately 13% of these URLs were classified as hard content. We further limited the set of hard news URLs to the 226,000 distinct hard-content URLs shared by at least 20 users who volunteered their ideological affiliation in their profile, so that we could accurately measure ideological alignment. This data set included ~3.8 billion potential exposures (cases in which an individual's friend shared hard content, regardless of whether it appeared in her News Feed), 903 million exposures (cases in which a link to the content appears on screen in an individual's News Feed), and 59 million clicks, among users in our study.

We then obtained a measure of content alignment (A) for each hard story by averaging the ideological affiliation of each user who shared the article. Alignment is not a measure of media slant; rather, it captures differences in the kind of content shared among a set of partisans, which can include topic matter, framing, and slant. These scores, averaged over websites, capture key differences in well-known ideologically aligned media sources: FoxNews.com is aligned with conservatives ($A_s = +.80$), whereas the HuffingtonPost.com is aligned with liberals ($A_s = -0.65$) (additional detail and validation are provided in the supplementary materials, section S1.4.2). We observed substantial polarization among hard content shared by users, with the most frequently shared links clearly aligned with largely liberal or conservative populations (Fig. 1).

The flow of information on Facebook is structured by how individuals are connected in the network. The interpersonal networks on Facebook are different from the segregated structure of political blogs (*16*); although there is clustering according to political affiliation on Facebook, there are also many friendships that cut across ideological affiliations. Among friendships with individuals who report their ideological affiliation in their profile, the median proportion of friendships that liberals maintain with conservatives is 0.20, interquartile range (IQR) [0.09, 0.36]. Similarly, the median proportion of friendships that conservatives maintain with liberals is 0.18, IQR [0.09, 0.30] (Fig. 2).

How much cross-cutting content individuals encounter depends on who their friends are and what information those friends share. If individuals acquired information from random others, ~45% of the hard content that liberals would be exposed to would be cross-cutting, compared with 40% for conservatives (Fig. 3B). Of course, individuals do not encounter information at random in offline environments (*14*) nor on the Internet (*9*). Despite the slightly higher volume of conservatively aligned articles shared (Fig. 1), liberals tend to be connected to fewer friends who share information from the other side, compared with their conservative counterparts: Of the hard news stories shared by liberals' friends, 24% are cross-cutting, compared with 35% for conservatives (Fig. 3B).

The media that individuals consume on Facebook depends not only on what their friends share but also on how the News Feed ranking

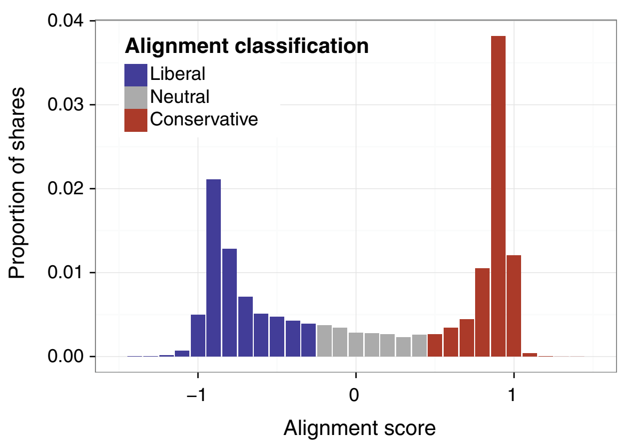

Fig. 1. Distribution of ideological alignment of content shared on Facebook measured as the average affiliation of sharers weighted by the total number of shares. Content was delineated as liberal, conservative, or neutral on the basis of the distribution of alignment scores (details are available in the supplementary materials).

[1]Facebook, Menlo Park, CA 94025, USA. [2]School of Information, University of Michigan, Ann Arbor, MI, USA.
*Corresponding author. E-mail: ebakshy@fb.com †These authors contributed equally to this work.

algorithm sorts these articles and what individuals choose to read (Fig. 3A). The order in which users see stories in the News Feed depends on many factors, including how often the viewer visits Facebook, how much they interact with certain friends, and how often users have clicked on links to certain websites in News Feed in the past. We found that after ranking, there is on average slightly less cross-cutting content: The risk ratio comparing the probability of seeing cross-cutting content relative to ideologically consistent content is 5% for conservatives and 8% for liberals (supplementary materials, section S1.7).

Individual choice futher limits exposure to ideologically cross-cutting content. After adjusting for the effect of position [the click rate on a link is negatively correlated with its position in the News Feed (fig. S5)], we estimated the risk ratio comparing the likelihood that an individual clicks on a cross-cutting content relative to a consistent content to be 17% for conservatives and 6% for liberals, a pattern that is consistent with prior research (*4*, *17*). Despite these tendencies, there is substantial room for individuals to consume more media from the other side; on average, viewers clicked on 7% of hard content available in their feeds.

Our analysis has limitations. Although the vast majority of U.S. social media users are on Facebook (*18*), our study is limited to active users who volunteer an ideological affiliation on this social media platform. Facebook's users tend to be younger, more educated, and more often female as compared with the U.S. population as a whole (*18*). Other forms of social media, such as blogs or Twitter, have been shown to exhibit different patterns of homophily among politically interested users, largely because ties tend primarily to form based on common topical interests and/or specific content (*16*, *19*), whereas Facebook ties primarily reflect many different offline social contexts: school, family, social activities, and work, which have been found to be fertile ground for fostering cross-cutting social ties (*20*). In addition, our distinction between exposure and consumption is imperfect; individuals may read the summaries of articles that appear in the News Feed and therefore be exposed to some of the articles' content without clicking through.

This work informs long-standing questions about how media exposure is shaped by our social networks. Although partisans tend to maintain relationships with like-minded contacts [which is consistent with (*21*)], on average more than 20% of an individual's Facebook friends who report an ideological affiliation are from the opposing party, leaving substantial room for exposure to opposing viewpoints (*22*, *23*). Furthermore, in contrast to concerns that people might "listen and speak only to the like-minded" while online (*6*), we found exposure to cross-cutting content (Fig. 3B) along a hypothesized route: traditional media shared in social media (*4*, *24*). Perhaps unsurprisingly, we show that the composition of our friend networks is the most important factor limiting the mix of content encountered in social media. The way that sharing occurs within these networks is not symmetric: Liberals tend to be connected to fewer friends who share conservative content than are conservatives (who tend to be linked to more friends who share liberal content).

Within the population under study here, individual choices (*2*, *13*, *15*, *17*) more than algorithms (*3*, *9*) limit exposure to attitude-challenging content in the context of Facebook. Despite the differences in what individuals consume across ideological lines, our work suggests that individuals are exposed to more cross-cutting discourse in social media than they would be under the digital reality envisioned by some (*2*, *6*). Rather than people browsing only ideologically aligned news sources or opting out of hard news altogether, our work shows that social media expose

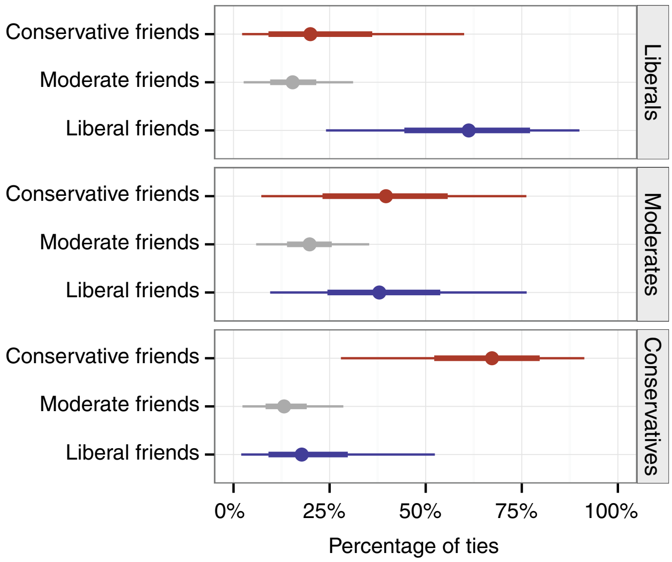

Fig. 2. Homophily in self-reported ideological affiliation. Proportion of links to friends of different ideological affiliations for liberal, moderate, and conservative users. Points indicate medians, thick lines indicate interquartile ranges, and thin lines represent 10th to 90th percentile ranges.

A

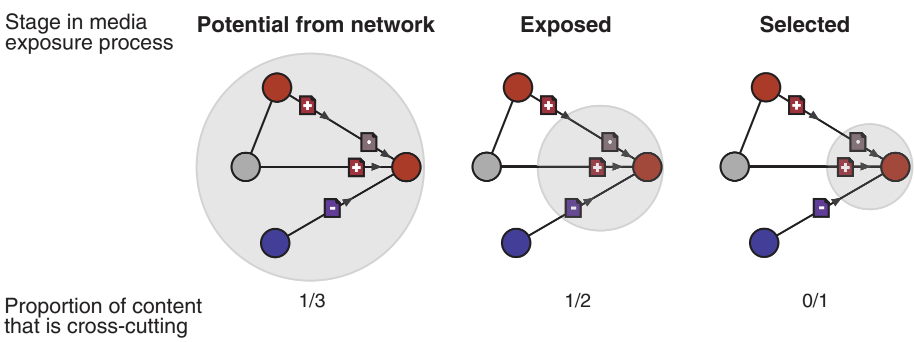

B

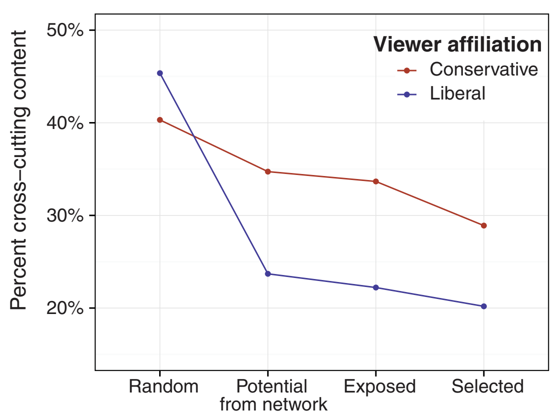

Fig. 3. Cross-cutting content at each stage in the diffusion process. (**A**) Illustration of how algorithmic ranking and individual choice affect the proportion of ideologically cross-cutting content that individuals encounter. Gray circles illustrate the content present at each stage in the media exposure process. Red circles indicate conservatives, and blue circles indicate liberals. (**B**) Average ideological diversity of content (i) shared by random others (random), (ii) shared by friends (potential from network), (iii) actually appeared in users' News Feeds (exposed), and (iv) users clicked on (selected).

individuals to at least some ideologically cross-cutting viewpoints (4). Of course, we do not pass judgment on the normative value of cross-cutting exposure. Although normative scholars often argue that exposure to a diverse "marketplace of ideas" is key to a healthy democracy (25), a number of studies have found that exposure to cross-cutting viewpoints is associated with lower levels of political participation (22, 26, 27). Regardless, our work suggests that the power to expose oneself to perspectives from the other side in social media lies first and foremost with individuals.

REFERENCES AND NOTES

1. K. Olmstead, A. Mitchell, T. Rosenstiel, *Navigating news online*. Pew Research Center (2011); available at www.journalism.org/analysis_report/navigating_news_online.
2. W. L. Bennett, S. Iyengar, *J. Commun.* **58**, 707–731 (2008).
3. E. Pariser, *The Filter Bubble: What the Internet Is Hiding from You* (Penguin Press, London, 2011).
4. S. Messing, S. J. Westwood, *Communic. Res.* **41**, 1042–1063 (2012).
5. E. Bakshy, I. Rosenn, C. Marlow, L. Adamic, *Proc. 21st Int. Conf. World Wide Web Pages* **1201.4145** (2012).
6. C. R. Sunstein, *Republic.com 2.0* (Princeton Univ. Press, Princeton, NJ, 2007).
7. N. Stroud, *Polit. Behav.* **30**, 341–366 (2008).
8. S. Kull, C. Ramsay, E. Lewis, *Polit. Sci. Q.* **118**, 569–598 (2003).
9. S. Flaxman, S. Goel, J. M. Rao, "Ideological segregation and the effects of social media on news consumption," SSRN Scholarly Paper ID 2363701, Social Science Research Network, Rochester, NY (2013).
10. T. Groeling, *Annu. Rev. Polit. Sci.* **16**, 129–151 (2013).
11. M. Gentzkow, J. M. Shapiro, *Q. J. Econ.* **126**, 1799–1839 (2011).
12. M. J. LaCour, "A balanced information diet, not echo chambers: Evidence from a direct measure of media exposure," SSRN Scholarly Paper ID 2303138, Social Science Research Network, Rochester, NY (2013).
13. E. Lawrence, J. Sides, H. Farrell, *Perspect. Polit.* **8**, 141 (2010).
14. D. O. Sears, J. L. Freedman, *Public Opin. Q.* **31**, 194 (1967).
15. N. A. Valentino, A. J. Banks, V. L. Hutchings, A. K. Davis, *Polit. Psychol.* **30**, 591–613 (2009).
16. L. A. Adamic, N. Glance, in *Proceedings of the 3rd International Workshop on Link Discovery* (ACM, New York, 2005), pp. 36–43.
17. S. Iyengar, K. S. Hahn, *J. Commun.* **59**, 19–39 (2009).
18. M. Duggan, A. Smith, "Social media update 2013," Pew Research Center (2013); available at www.pewinternet.org/2013/12/30/social-media-update-2013.
19. M. D. Conover, J. Ratkiewicz, M. Francisco, B. Gonçalves, A. Flammini, F. Menczer, Political polarization on Twitter. *Fifth International AAAI Conference on Weblogs and Social Media* (2011).
20. D. C. Mutz, J. J. Mondak, *J. Polit.* **68**, 140 (2006).
21. S. Goel, W. Mason, D. J. Watts, *J. Pers. Soc. Psychol.* **99**, 611–621 (2010).
22. D. C. Mutz, *Am. J. Polit. Sci.* **46**, 838–855 (2002).
23. B. Bishop, *The Big Sort: Why the Clustering of Like-Minded America Is Tearing Us Apart* (Houghton Mifflin Harcourt, New York, 2008).
24. D. C. Mutz, P. S. Martin, *Am. Polit. Sci. Rev.* **95**, 97 (2001).
25. T. Mendelberg, *Deliber. Particip.* **6**, 151–193 (2002).
26. R. Huckfeldt, J. M. Mendez, T. Osborn, *Polit. Psychol.* **25**, 65–95 (2004).
27. R. Bond, S. Messing, *Am. Polit. Sci. Rev.* **109**, 62–78 (2015).

ACKNOWLEDGMENTS

We thank J. Bailenson, D. Eckles, A. Franco, K. Garrett, J. Grimmer, S. Iyengar, B. Karrer, C. Nass, A. Peysakhovich, S. Taylor, R. Weiss, S. Westwood, J. M. White, and anonymous reviewers for their valuable feedback. The following code and data are archived in the Harvard Dataverse Network, http://dx.doi.org/10.7910/DVN/LDJ7MS: "Replication Data for: Exposure to Ideologically Diverse News and Opinion on Facebook"; R analysis code and aggregate data for deriving the main results (tables S5 and S6); Python code and dictionaries for training and testing the hard-soft news classifier; aggregate summary statistics of the distribution of ideological homophily in networks; and aggregate summary statistics of the distribution of ideological alignment for hard content shared by the top 500 most shared websites. The authors of this work are employed and funded by Facebook. Facebook did not place any restrictions on the design and publication of this observational study, beyond the requirement that this work was to be done in compliance with Facebook's Data Policy and research ethics review process (www.facebook.com/policy.php).

SUPPLEMENTARY MATERIALS

www.sciencemag.org/content/348/6239/1130/suppl/DC1
Materials and Methods
Supplementary Text
Figs. S1 to S10
Tables S1 to S6
References (28–35)

20 October 2014; accepted 27 April 2015
Published online 7 May 2015;
10.1126/science.aaa1160

ECOPHYSIOLOGY

Climate change tightens a metabolic constraint on marine habitats

Curtis Deutsch,[1]* Aaron Ferrel,[2]† Brad Seibel,[3] Hans-Otto Pörtner,[4] Raymond B. Huey[5]

Warming of the oceans and consequent loss of dissolved oxygen (O_2) will alter marine ecosystems, but a mechanistic framework to predict the impact of multiple stressors on viable habitat is lacking. Here, we integrate physiological, climatic, and biogeographic data to calibrate and then map a key metabolic index—the ratio of O_2 supply to resting metabolic O_2 demand—across geographic ranges of several marine ectotherms. These species differ in thermal and hypoxic tolerances, but their contemporary distributions are all bounded at the equatorward edge by a minimum metabolic index of ~2 to 5, indicative of a critical energetic requirement for organismal activity. The combined effects of warming and O_2 loss this century are projected to reduce the upper ocean's metabolic index by ~20% globally and by ~50% in northern high-latitude regions, forcing poleward and vertical contraction of metabolically viable habitats and species ranges.

Climate change is altering ecosystems by shifting distributions, phenologies, and interactions among species, but understanding how these changes are caused by climatic influences on physiology and fitness remains a challenge (1). In the ocean, increased metabolic rates due to rising temperatures will be accompanied by declines in dissolved O_2, potentially restricting organismal aerobic capacities (2–4). The physiology of hypoxic and thermal tolerance of marine species is well understood (3, 5–7). Lacking, however, is a general mechanistic model that quantifies how O_2 and temperature jointly restrict large-scale biogeographic distributions now and in the future. Here, we combine laboratory and field data to demonstrate that temperature and O_2 together limit the contemporary ranges of marine ectotherms and to derive empirically based estimates of habitat loss in the warmer and less oxygenated oceans projected by this century's end.

For marine habitats to be metabolically viable, the environmental O_2 supply rate (S) must exceed an animal's resting metabolic demand (D). The rate of O_2 supply increases with ambient O_2 pressure (PO_2) and with respiratory efficacy (8). Thus, $S = \alpha_S B^{\delta} PO_2$, where respiratory efficacy is the product of α_s, a per-mass rate of gas transfer between water and animal and its scaling with body mass, B^{δ}. Resting metabolic demand also scales with B and with absolute temperature (T), according to $D = \alpha_D B^{\varepsilon} \exp(-E_o/k_B T)$, where α_D is a taxon-specific baseline metabolic rate, ε is its allometric scaling, E_o is its temperature dependence, and k_B is Boltzmann's constant (9).

We define a metabolic index, denoted Φ, as the ratio of O_2 supply to an organism's resting O_2 demand

$$\Phi = A_o B^n \frac{PO_2}{\exp(-E_o/k_B T)} \qquad (1)$$

where $A_o = \alpha_s/\alpha_d$ is the ratio of rate coefficients for O_2 supply and metabolic rate, and n is the difference between the respective allometric scalings ($n = \delta - \varepsilon$). If Φ falls below a critical threshold value of 1, organisms must either suppress aerobic activity (5) or initiate anaerobic metabolism, conditions that are physiologically unsustainable. Conversely, values above 1 enable organismal metabolic rates to increase by a factor of Φ above resting levels, permitting critical activities such as feeding, defense, growth, and reproduction. Thus, for a given environment, Φ estimates the ratio of maximum sustainable metabolic rate to the minimum rate necessary for maintenance for a given species.

We analyzed data from published studies in which hypoxia tolerance was determined at

[1]School of Oceanography, University of Washington, Seattle, WA 98195, USA. [2]Department of Atmospheric and Oceanic Sciences, University of California, Los Angeles, CA 90095, USA. [3]Biological Sciences Department, University of Rhode Island, Kingston, RI 02881, USA. [4]Alfred Wegener Institute, D-27570 Bremerhaven, Germany. [5]Department of Biology, University of Washington, Seattle, WA 98195, USA.
***Corresponding author. E-mail: cdeutsch@uw.edu** †Present address: Los Angeles Unified School District, Los Angeles, CA 90085, USA.

multiple temperatures (Fig. 1). Hypoxia tolerance was measured as the O_2 level below which the resting rate of metabolism cannot be maintained, anaerobic metabolic end products accumulate, or mortality increases. Such conditions correspond to the threshold value of $\Phi = 1$, allowing the parameters in Eq. 1 (n, E_o, and A_o) to be estimated (*10*). These parameters vary among species (table S1) due to differences in resting metabolic rates and oxygen uptake capacity (*11*–*14*). Within species, body mass weakly affected critical PO_2, PO_2^{crit} (n = –0.3 to 0) (fig. S1), suggesting that size-associated increases in O_2 uptake capacity (δ) largely compensate for increases in metabolic rate with size (ε) (*15*, *16*). Temperature on average accounted for 87% of the intraspecies variation in PO_2^{crit} (table S1), with slopes (E_o) for most of the species between 0.36 to 1.06 eV, similar to estimates for diverse physiological rates (*17*).

To evaluate whether the metabolic index limits the geographic range of species, we compared the spatial distributions of the index in the ocean with distributions of several marine species. Physiological and biogeographic data were available for four Atlantic species that live in diverse habitats (cod in open waters, rock crab in benthic zones, seabream in subtropics, eelpout in subpolar oceans) and differ widely in thermal and hypoxic tolerance (table S2). Using climatological temperature and O_2 data (*10*), we computed the seasonally varying three-dimensional distributions of the metabolic index. The global patterns of Φ are nearly identical among species because the patterns derive from environmental gradients of temperature and PO_2. Species differences in A_o scale the absolute values of Φ but not its spatial pattern, and variations in E_o only weakly alter the relative influence of temperature and O_2 gradients. The geographical distribution of Φ is also insensitive to whether O_2 uptake depends on the concentration, partial pressure, or diffusivity of O_2 in seawater (*10*, *18*) (fig. S2). Thus, when mapped relative to an arbitrary reference location, the spatial distribution and temporal variations in Φ are qualitatively independent of species.

For all studied species, the metabolic index in the upper ocean varies by more than 10-fold across latitude (Fig. 2A, values normalized to the tropical average), reflecting low subsurface PO_2 and high metabolic rates in tropical waters (low Φ) but generally high PO_2 and low metabolic rates in cooler, higher-latitude waters (high Φ). In contrast, vertical variation in Φ (Fig. 2B) is relatively small, because both temperature and O_2 decrease with depth and their individual effects on metabolic index are partly offsetting. In strong oxygen minimum zones (OMZs), however, O_2 declines more rapidly with depth than does metabolism, such that Φ decreases sharply with depth. Seasonal variability of Φ is generally small, except near OMZs, and in marginal seas and western boundary currents (fig. S3). Because the largest variations in Φ occur across latitude, we focus on whether latitudinal ranges of species are limited by the metabolic index.

From maps of the geographic distribution and metabolic index for the four focal species, we identified the occupied site where Φ was lowest: This was invariably at the southern (equatorward) range limit (Fig. 3). Across all species, seasons, and body masses, the minimum Φ varied only between 2 and 5 (table S3). Thus, marine environments appear viable only if they support metabolic rates at least 2 to 5 times resting rates. This critical metabolic index (Φ_{crit}) reflects not only the minimal physiological requirements for survival ($\Phi > 1$) but also additional energy required for key ecological activities ($\geq \Phi_{crit}$). Interestingly, sustained field metabolic rates of diverse terrestrial species are typically 1.5 to 5 times resting rates (*19*). This factorial increase is similar to values of Φ_{crit} of marine ectotherms, which suggests that it represents a fundamental metabolic requirement both on land and in the ocean but restricts the equatorial range limit only in the ocean.

Populations that migrate seasonally provide further support that the metabolic index restricts viable habitats. Western and eastern Atlantic cod share a common Φ_{crit} at their southern range border. Western cod migrate along the North

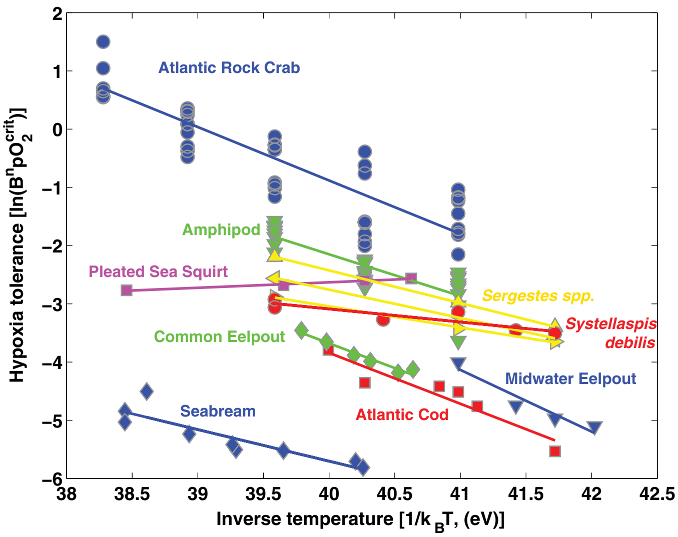

Fig. 1. Hypoxia tolerance versus inverse temperature. Laboratory data were compiled from published literature (see the supplementary materials) for 16 species in which hypoxic thresholds (PO_2^{crit}) were experimentally determined at three or more different temperatures. Of these species, 11 showed statistically significant relationships to temperature. Hypoxic thresholds are measured as the O_2 level below which the rate of metabolism cannot be maintained or an increase in mortality is observed. The parameters of the metabolic index are obtained from the slope (E_o) and intercept (A_o) of the linear regressions (table S1) (*10*).

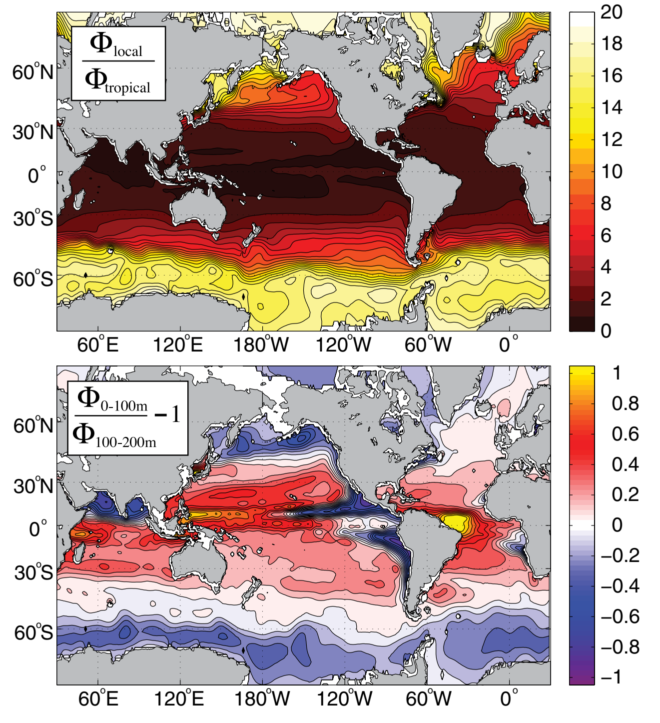

Fig. 2. Global relative distribution of metabolic index. The metabolic index is computed from climatological temperature and O_2 and normalized to depict large-scale patterns but not absolute values. Variation across latitude (**top**) is shown for the depth-averaged metabolic index of the upper ocean (0 to 200 m), divided by the mean value throughout the tropics (15°S to 15°N, 0 to 200 m). The metabolic index increases by >10-fold from the tropics to high latitudes due to the tendency for warm waters to have low O_2. Variation with depth (**bottom**) is computed as the relative difference between the average value in the upper 100 m and the average from 100 to 200 m. Negative values correspond to a decrease in Φ with depth. Vertical variations of Φ are reduced by the compensating decreases in both temperature and O_2 with depth but can be strongly negative in the presence of sharp OMZs. Both maps are computed with E_o = 0.7 eV, but the patterns depend only slightly on this parameter.

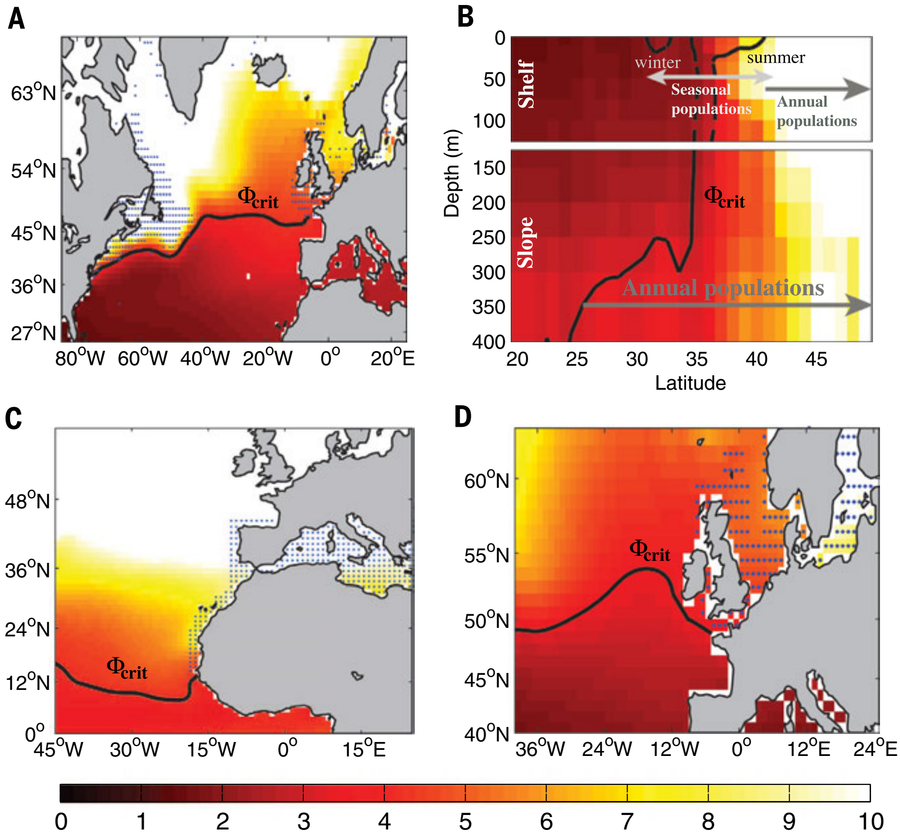

Fig. 3. Distribution of the metabolic index (Φ) in the Atlantic Ocean for all four species in Fig. 1 with documented marine population distributions. (**A**) Atlantic cod, (**B**) Atlantic rock crab, (**C**) sharpsnout seabream, and (**D**) common eelpout. For each species, Φ is averaged over its observed depth range (cod, 0 to 400 m; eelpout, 0 to 40 m; seabream, 0 to 60 m) except for rock crab, where values have been averaged over longitude in bottom grid cells along the North American margin. The minimum value found within the species distribution (Φ_{crit}) is contoured (black lines; values in table S3). For rock crabs, the contour of Φ includes both monthly maximum (winter) and minimum (summer) values above 100 m; below 100 m, it is cumulatively averaged downward along the slope at each latitude, to approximate the effect of seasonal movement of these crabs up and down the continental shelf. Occurrence data for each species are plotted (blue dots, interpolated to climate grid) for all species except crabs, whose latitudinal range of seasonal and year-round (annual) habitat in shelf and slope waters is indicated by gray arrows (see the supplementary materials).

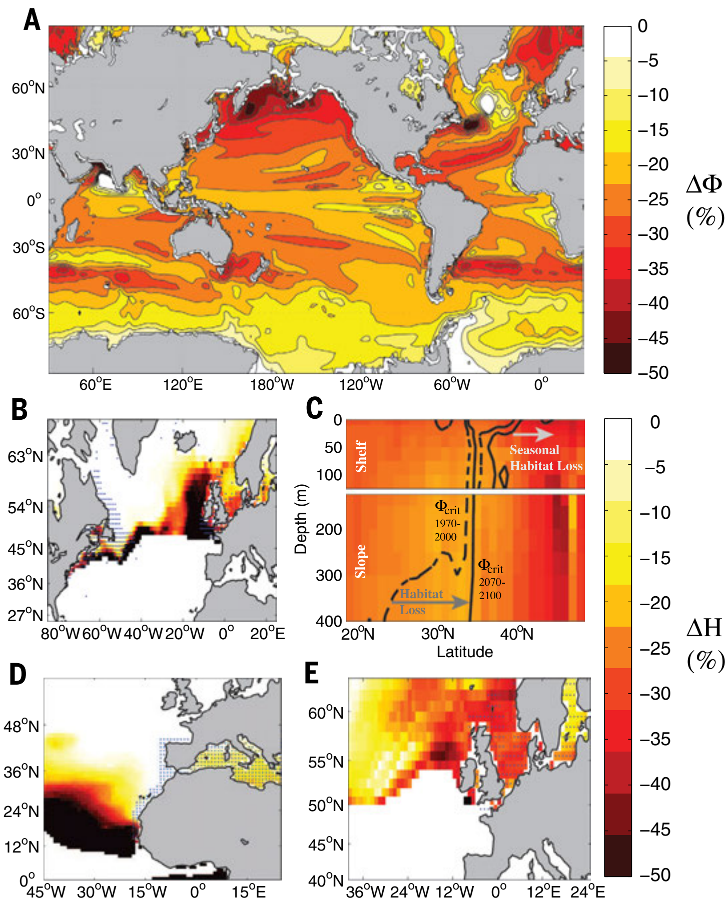

Fig. 4. Change in metabolic index and associated habitat compression from 1971–2000 to 2071–2100. (**A**) Global fractional change in Φ averaged over the upper 200 m, as projected by multiple Earth system model simulations under an 8.5 W/m^2 greenhouse gas emissions scenario (Representative Concentration Pathway 8.5), averaged across species. White areas indicate an increase in metabolic index, in all cases attributable to an increase in subsurface O_2. The individual contributions of changes in temperature and O_2 are shown in fig. S6. (**B** to **E**) Projected loss of metabolic habitat (denoted ΔH) for species with calibrated metabolic index values. Metabolic habitat is defined as any grid cell with $\Phi > \Phi_{crit}$ on a monthly basis. For cod (B), seabream (D), and eelpout (E), habitat changes are mapped as the percentage of change in annual mean thickness of the habitable water column between 1971–2000 and 2071–2100. For Atlantic rock crab (C), the background color map shows relative changes in Φ (%), and contours indicate the migration of Φ_{crit}. For all species, the relative change is an average over all months, so that the loss of habitat includes both vertical compression and a shortening of the habitable season.

American coast between 37°N in winter and 41°N in summer, paralleling seasonal shifts of Φ_{crit} (fig. S4A). Eastern cod migrate vertically, moving from cool temperatures in surface waters in winter to deeper waters in summer, in parallel with Φ_{crit} (fig. S4B). Seasonal migrations of benthic Atlantic rock crab also coincide with variations in Φ_{crit} in bottom waters (Fig. 3B). On the continental shelf, the latitudinal limits of seasonal crab populations in the mid-Atlantic Bight and of year-round populations north of 40°N are both delineated by a common Φ_{crit}. Deeper waters of the continental slope (100 to 400 m) have a metabolic index above Φ_{crit}, thus providing refugia for populations migrating from shallower shelf environments during summer (*10*).

Projected climate changes by this century's end (2071 to 2100) will affect the distribution of the metabolic index and thus of marine animals (Fig. 4). Climate models predict substantial warming and deoxygenation throughout most of the upper ocean (fig. S5 and table S4) (*10*). This implies global reductions in the metabolic index (Fig. 4A) throughout the upper water column (0 to 400 m), with a model-average decline of 21% (intermodel range 17 to 25%). Only ~1/3 of this reduction is attributable to O_2 loss, indicating that future marine hypoxia will be driven primarily by rising temperature, not by declining O_2 (*3*). The decline in Φ, and the relative contribution of temperature versus O_2, vary geographically (fig. S6). In mid-latitude Northern Hemisphere oceans—where fisheries are often highly productive—the metabolic index, and thus habitat suitability, should decline dramatically (~50%). The Pacific is prone to some of the largest reductions in Φ, driven by its larger projected fractional decrease in O_2 (figs. S5 and S6).

The focal species studied here illustrate how projected warming plus O_2 loss should shift metabolically viable habitats by century's end (Fig. 4, B to E). Habitable zones will often be vertically compressed and habitable seasons shortened throughout geographic ranges, but overall habitat losses are projected to be greatest near the equatorward edge of ranges, where Φ is low. For example, in the western subtropical Atlantic, where a wide swath of benthic habitat of rock crab is already close to Φ_{crit}, a 30% reduction in Φ would force a poleward retreat of slope populations from ~25°N to ~35°N. For other focal species, the average cumulative loss of habitat, measured as the reduction in currently occupied water volume with $\Phi > \Phi_{crit}$, ranges from 14 to 26% (table S5) (intermodel range 9 to 42%). These losses in aerobic habitat may be partially offset by habitat expansions where species ranges are now limited by cold tolerance.

Our results suggest that climate constraints on aerobic energy provision are the primary factors governing the equatorward range limit for diverse marine ectotherms. Thus, the metabolic index provides a simple but powerful metric linking physiology and biogeography with current and future environmental conditions. Even so, climate-forced ecosystem shifts will be complex, because changes in the metabolic index may be exacerbated by declines in net primary productivity (*20*), ocean acidification, and pollution (*1*), or ameliorated by acclimation and genetic adaptation (*21*). Biotic interactions will be altered because currently interacting species—if they have different metabolic sensitivities—will show noncoincident range contractions. Polar species may face increased competition caused by the invasion by lower-latitude species. Shallow-water predators may benefit from upwelling migrations of deeper water prey (*22*), and prey may benefit if their predators move away (*23*). Thus, climate shifts in the metabolic index may alter species ecologies even where metabolic indices exceed critical limits. Predictions of differential responses of ecologically interacting species to future shifts in metabolic indices will require more studies of temperature-dependent hypoxic tolerances, especially those of interacting and potentially interacting species.

REFERENCES AND NOTES

1. C. B. Field *et al.*, in *Climate Change 2014: Impacts, Adaptation, and Vulnerability. Part A: Global and Sectoral Aspects. Contribution of Working Group II to the Fifth Assessment Report of the Intergovernmental Panel on Climate Change*, C. B. Field *et al.*, Eds. (Cambridge University Press, Cambridge, UK and New York, NY, USA, 2014), pp. 35–94.
2. F. E. J. Fry, *Effect of the Environment on Animal Activity, University of Toronto Studies Biological Series No. 55* (Univ. of Toronto Press, Toronto, 1947).
3. H.-O. Pörtner, R. Knust, *Science* **315**, 95–97 (2007).
4. B. A. Seibel, *J. Exp. Biol.* **214**, 326–336 (2011).
5. P. W. Hochachka, *Trans. Am. Fish. Soc.* **119**, 622–628 (1990).
6. J. J. Childress, B. A. Seibel, *J. Exp. Biol.* **201**, 1223–1232 (1998).
7. H.-O. Pörtner, *J. Exp. Biol.* **213**, 881–893 (2010).
8. J. Piiper, P. Dejours, P. Haab, H. Rahn, *Respir. Physiol.* **13**, 292–304 (1971).
9. J. F. Gillooly, J. H. Brown, G. B. West, V. M. Savage, E. L. Charnov, *Science* **293**, 2248–2251 (2001).
10. See supplementary materials on *Science* Online.
11. B. A. Hills, G. M. Hughes, *Respir. Physiol.* **9**, 126–140 (1970).
12. B. A. Seibel, J. C. Drazen, *Philos. Trans. R. Soc. Lond. B Biol. Sci.* **362**, 2061–2078 (2007).
13. S. S. Killen, D. Atkinson, D. S. Glazier, *Ecol. Lett.* **13**, 184–193 (2010).
14. J. R. Friedman, N. E. Condon, J. C. Drazen, *Limnol. Oceanogr.* **57**, 1701–1710 (2012).
15. H. A. Woods, *Am. Zool.* **39**, 244 (1999).
16. G. E. Nilsson, S. Östlund-Nilsson, *Biol. Rev. Camb. Philos. Soc.* **83**, 173–189 (2008).
17. A. I. Dell, S. Pawar, V. M. Savage, *Proc. Natl. Acad. Sci. U.S.A.* **108**, 10591–10596 (2011).
18. W. C. E. P. Verberk, D. T. Bilton, P. Calosi, J. I. Spicer, *Ecology* **92**, 1565–1572 (2011).
19. J. R. Speakman, *Adv. Ecol. Res* **36**, 177 (2000).
20. L. Bopp *et al.*, *Biogeosciences* **10**, 6225–6245 (2013).
21. G. N. Somero, *J. Exp. Biol.* **213**, 912–920 (2010).
22. J. A. Koslow, R. Goericke, A. Lara-Lopez, W. Watson, *Mar. Ecol. Prog. Ser.* **436**, 207–218 (2011).
23. J. S. Stewart, J. C. Field, U. Markaida, W. F. Gilly, *Deep Sea Res. Part II Top. Stud. Oceanogr.* **95**, 197–208 (2013).

ACKNOWLEDGMENTS

Research was supported by the National Science Foundation (grants OCE-1419323, OCE-1458967, OCE-1459243, and ID 1038016), the Gordon and Betty Moore Foundation (grant GBMF3775 to C.D.), and the Polar regions and Coasts in a changing Earth System program (Alfred Wegener Institute). We thank the originators of the laboratory physiological data used here (available in the supplementary materials) and the individual climate modeling groups (table S4) and the World Climate Research Programme for producing and making available the CMIP5 model output. The technical support of H. Frenzel and the suggestions of K. Nagy, D. Jacobs, and two anonymous reviewers are gratefully acknowledged.

SUPPLEMENTARY MATERIALS

www.sciencemag.org/content/348/6239/1132/suppl/DC1
Materials and Methods
Supplementary Text
Figs. S1 to S6
Tables S1 to S5
References (*24–51*)

24 October 2014; accepted 5 May 2015
10.1126/science.aaa1605

CORAL REEFS

Limited scope for latitudinal extension of reef corals

Paul R. Muir,[1]* Carden C. Wallace,[1] Terence Done,[1,2] J. David Aguirre[3,4]

An analysis of present-day global depth distributions of reef-building corals and underlying environmental drivers contradicts a commonly held belief that ocean warming will promote tropical coral expansion into temperate latitudes. Using a global data set of a major group of reef corals, we found that corals were confined to shallower depths at higher latitudes (up to 0.6 meters of predicted shallowing per additional degree of latitude). Latitudinal attenuation of the most important driver of this phenomenon—the dose of photosynthetically available radiation over winter—would severely constrain latitudinal coral range extension in response to ocean warming. Latitudinal gradients in species richness for the group also suggest that higher winter irradiance at depth in low latitudes allowed a deep-water fauna that was not viable at higher latitudes.

The growth of phototrophic corals, those that rely on energy from endosymbiotic algae or "zooxanthellae," is determined by three primary latitude-correlated environmental factors (solar radiation, temperature, aragonite saturation) and by a number of factors not related to latitude (e.g., nature and depth of the substratum, wave climate, salinity, water quality, siltation regime) (*1*, *2*). Among the primary drivers of coral growth, only one—the amount of

Fig. 1. Sampling sites used in the study. The global database (*16*) comprises 14,235 records of latitude, longitude, and depth of 104 staghorn coral specimens collected at 1397 sites. For inclusion at a site, a species is recorded only if at least one specimen was collected for taxonomic verification.

solar radiation that penetrates into the ocean and fuels photosynthesis—is unlikely to change substantially with climate change. Solar radiation at the sea surface diminishes with increasing latitude as winter day length and solar elevation decrease (*3*); solar radiation further attenuates through the water column, thereby limiting the depth at which phototrophic corals can survive (*4*, *5*).

These findings have led to the hypothesis that phototrophic corals should be restricted to shallower depths at higher latitudes (*2*, *6*, *7*). Here, we tested this hypothesis using an extensive specimen-based global data set of the depth and latitudinal distributions of 104 species of reef corals of the genera *Acropora* and *Isopora* (the "staghorn" corals; Fig. 1). High diversity of growth forms in these genera provides by far the greatest variety among corals of microhabitats for fishes (*8*) and invertebrates (*9*). However, staghorn corals, which make up a large proportion of coral species richness and cover of the world's richest coral reefs (*2*, *10*), are under threat (*11*), particularly from increasing sea surface temperatures, which cause corals to bleach, succumb to disease, and die en masse (*12*). Nonetheless, there is contemporary (*13*, *14*) and fossil (*15*) evidence for poleward range expansions of staghorn corals associated with increasing sea temperatures. We show here that local daily winter insolation will ultimately limit any such poleward expansion made possible by contemporary ocean warming, and hence will limit the expansion of associated biota.

In the global data set (Fig. 2), the maximum depth limit (0.975 quantile) of staghorn corals was deepest (26 m) at the equator (5°S to 5°N) and shallowest at their latitudinal extremes (11 m ≥ 30°N; 9 m ≥ 30°S). A polynomial quantile regression mixed model (*16*) revealed a strong latitudinal gradient in depth limits, both for all species combined and for latitudinally widespread species only (Fig. 2 and table S1). This suggests that the latitudinal gradient in maximum depth was driven not by changes in species composition but by an environmental driver that affects all species. Using species distribution models (MaxEnt), we showed (*16*) that temperature, aragonite saturation, and salinity in well-mixed reef waters were relatively poor predictors of the maximum depth of occurrence of staghorn corals: None of these three factors was limiting at any depth at the poleward limit of staghorn coral distribution (Fig. 3, A to C, and table S3). In contrast, photosynthetically available radiation (PAR; wavelengths 400 to 700 nm), modeled for clear reef waters (*16*) and specifically winter PAR (*17*, *18*), was a strong predictor of the limits to depth across the latitudinal distribution (Fig. 3 and table S4). Daily PAR decreases gradually with latitude (*3*), and the greatest differential between low and high latitudes occurs during winter. Declines in winter irradiance are further amplified underwater by additional surface reflection and long subsurface path length, both associated with low winter Sun angles. Our modeling (*16*) showed that during local midwinter (*17*) at latitude 0°, daily PAR at 20 m depth is 43% of surface PAR, whereas at 34°N it is only 35%. We found that winter PAR constrains the depth of occurrence of staghorn corals, accounting for the latitudinal gradient in depth distribution, and that it could in principle exclude staghorn corals from shallow substrata otherwise deemed suitable for corals on the basis of temperature and aragonite saturation alone (*19*).

Fig. 2. Latitudinal gradient in the maximum depth limits of staghorn corals. Polynomial quantile regression mixed model (0.975 quantile) is indicated by solid line, with 95% confidence intervals shaded. Accurate depth data were available for 104 species and 14,235 specimens. Analysis of latitudinally widespread species only (22 species) produced an almost identical model, indicating that the latitudinal gradient was not driven by changes in species composition (tables S1 and S5).

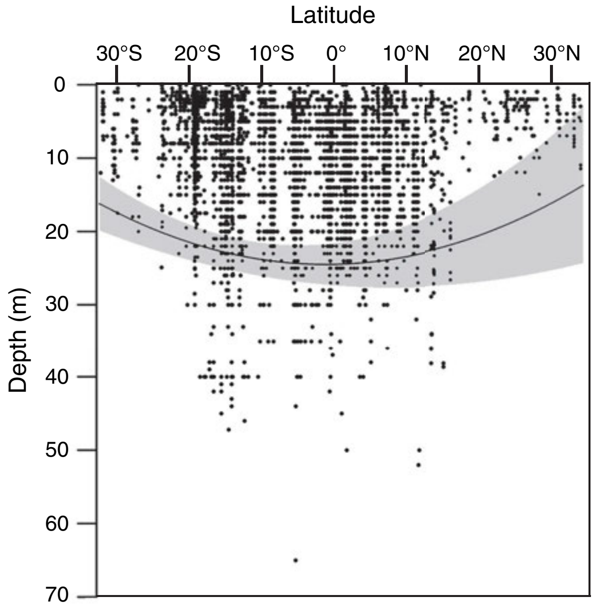

The geographic or depth limit beyond which coral growth is vigorous enough for reef building or growth of carbonate platforms, termed the "Darwin point," has been shown to be determined by aragonite saturation, temperature, and light (*1*, *4*, *6*, *19*–*21*). Modeling indicates that reef building mainly occurs for aragonite saturation greater than 3.4, annual minimum temperature greater than 18°C, and on substrata where PAR is greater than 250 $\mu E\ m^{-2}\ s^{-1}$ (equivalent to 7 to 8 mol photons $m^{-2}\ day^{-1}$), (*6*, *19*–*21*). However, reef corals commonly occupy non-reef habitats such as rocky shores or shallow embayments well beyond the latitudinal limits of reef building (*2*, *10*); the determinants of their distributional limits have not been quantified, although it is commonly held that they are constrained latitudinally mainly by temperature [reviewed in (*2*)] and vertically mainly by light (*3*, *4*, *20*). We found that winter PAR of 5.2 mol photons $m^{-2}\ day^{-1}$ is a strong predictor of the depth and latitudinal limits of distribution of staghorn corals (*16*), which have a high dependence on a steady supply of photosynthate produced by their zooxanthellae (*22*). We posit that the 5.2 mol photons $m^{-2}\ day^{-1}$ isolume represents a key threshold for coral physiology below which their zooxanthellae's photosynthetic production does not meet their basal metabolic needs. In this respect, staghorn corals are like some marine plants, whose limits of depth and latitude are also determined by daily hours of irradiance above a threshold basal compensation point (*20*), and they are unlike other growth forms of corals

[1]Museum of Tropical Queensland, Townsville, Queensland 4810, Australia. [2]Australian Institute of Marine Science, PMB #3, Townsville MC, Queensland 4810, Australia. [3]Institute of Natural and Mathematical Sciences, Massey University, Albany, New Zealand. [4]School of Biological Sciences, University of Queensland, Brisbane, Queensland 4072, Australia.
*Corresponding author. E-mail: paul.muir@qm.qld.gov.au

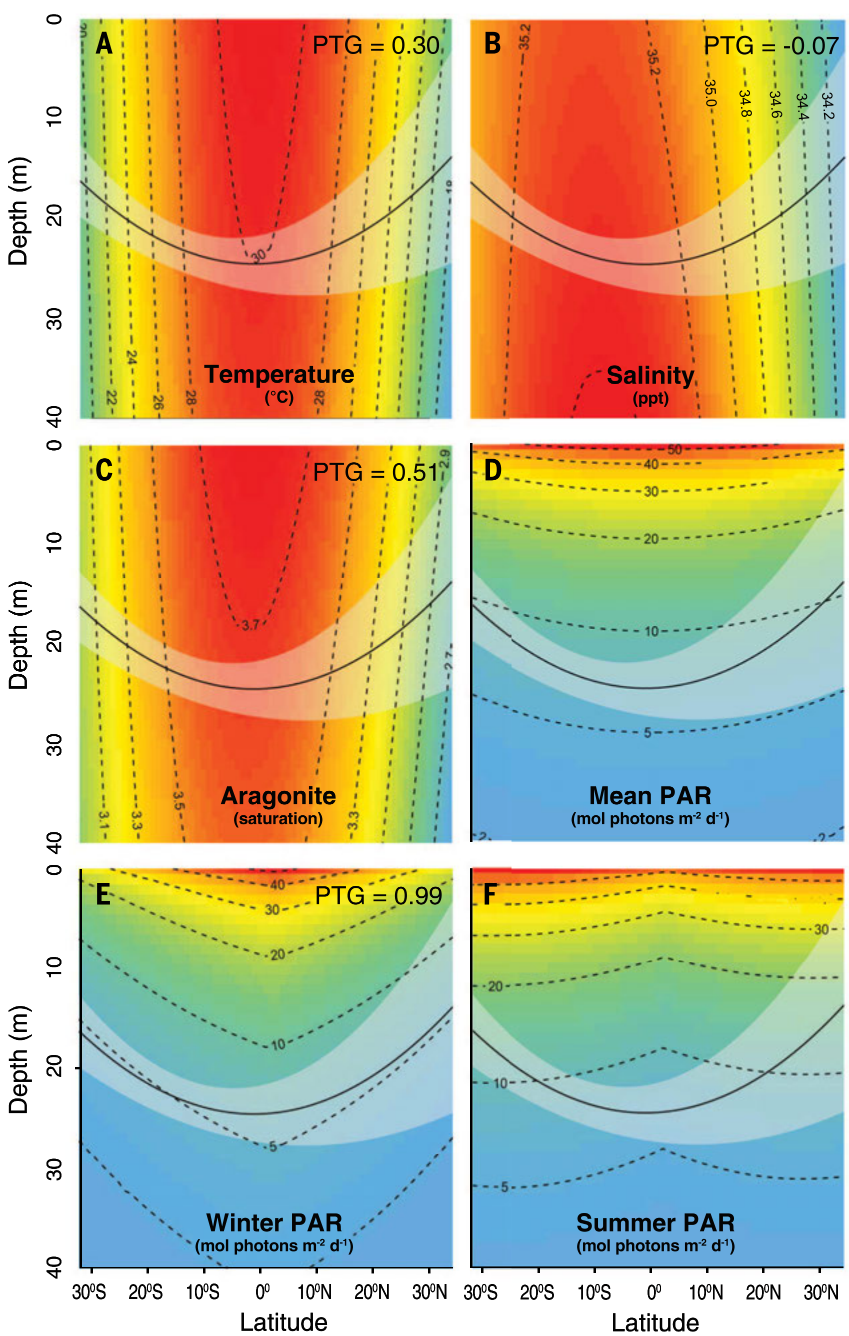

Fig. 3. Analysis of environmental predictors of maximum depth limits. (**A** to **C**) Mean annual temperature (A), salinity (B), and aragonite saturation (C). (**D** to **F**) Mean daily dose of photosynthetically available radiation (PAR) over an entire year (D), winter (*17*) (E), and summer (*16*, *17*) (F). Solid line in each panel indicates maximum staghorn coral depth limits (0.975 quantile regression), with 95% confidence interval shaded. PTG (proportion of total gain) values represent the proportional contribution of each factor, in isolation, to the predictive power of the full species distribution model; that is, PTG = [gain (single predictor)]/[gain (full model)]. The strongest predictor of the depth and latitudinal distribution of staghorn corals was winter PAR (PTG = 0.99). A threshold of 5.2 mol photons m^{-2} day^{-1} best accounted for the predicted maximum depth limits (*16*).

that can substantially supplement winter nutritional shortfalls through stored energy reserves and/or heterotrophy (*22*). We showed that there is a factor of 4 variation in winter PAR requirement among the 104 staghorn coral species reported on here (*16*), likely reflecting species-specific adaptations, including a number of attributes associated with reduced light at depth: flattened branch morphologies to maximize interception of light (*2*, *10*), changes in the density and type of zooxanthellae (*23*), and some capacity for heterotrophic nutrition (*24*). However, their efficacy as specific adaptations to seasonally low light at high latitudes has not been reported.

The depth-limiting effects of winter PAR also appear to contribute to a strong latitudinal gradient in species richness in staghorn corals (Fig. 4A). This pattern is consistent with reef corals overall (*2*, *25*) and many other marine and terrestrial taxa (*26*–*28*). Categorizing species by their maximum depth limits, we found that the richness gradient was largely driven by a deep-water fauna restricted to low latitudes (Fig. 4A). By contrast, mid-water species richness remained relatively constant to mid-latitudes, whereas shallow water species richness was retained until latitudes 27° to 28°. We contend that the low-latitude combination of high winter irradiance and suitable substrata at depth constitutes a niche for staghorn corals that does not exist at higher latitudes. This niche is occupied by a central Indonesia–west Pacific fauna typically with fragile and laterally flattened skeletal morphology that limits its members to deep, calm waters well below the influence of waves and swell (*29*); suitable substrata in deep calm waters at higher latitudes receive insufficient winter irradiance to support this fauna. This mechanism, and the emergent latitudinal patterns of richness of staghorn corals, are aspects of the topography-environment relationships that are not addressed in biogeophysical models of reefs and carbonate platforms (*1*, *19*, *20*). Moreover, although factors

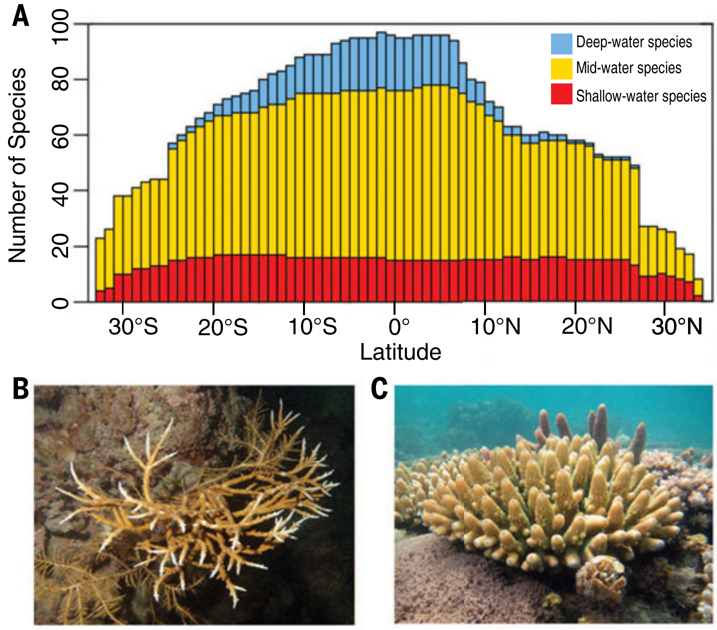

Fig. 4. Latitudinal trends in staghorn coral species richness. (**A**) Categorization of species according to their maximum depth limits (0.975 quantile) (*16*) (table S5). The deep-water species account for much of the latitudinal gradient in species richness. Species richness was calculated for 1° latitude bins. (**B**) Example of a deep-water species (*Acropora pichoni*) restricted to low-latitude habitats. (**C**) A widely distributed shallow-water species (*A. gemmifera*).

such as habitat availability, evolutionary history, vicariance events, and sea surface temperature undoubtedly contribute to patterns of species richness in reef corals overall (*2*, *25*, *28*–*30*), this study makes a compelling case for the overriding importance of light in controlling the poleward attenuation of species richness in a major coral group.

Recent observations of poleward range extensions in corals suggest there is potential for corals to colonize higher latitudes as sea surface temperatures increase (*13*–*15*, *31*). However, to meet their current winter light requirements, staghorn corals would need to decrease their maximum depth by a predicted (*16*) 0.6 m for each degree of latitude that their range extended beyond their present northern and southern limits. Species currently at their poleward limits of distribution, their depth range already restricted (Fig. 2), have little scope for further shallowing, or consequently, latitudinal extension. For tropical shallow and mid-water fauna (Fig. 4), contraction into shallower depths would bring into play potentially range-limiting parameters of shallow microenvironments such as damage from waves and swells, extremes of temperature and salinity, competition with shallow corals and macroalgae (*2*), and ultimately, subaerial exposure at low tide (*7*). Deep-water species currently restricted to depth at low latitudes (Fig. 4) are also unlikely to colonize shallow waters for the same reasons and would therefore remain latitudinally constrained by winter PAR requirements. In addition, constraints on staghorn coral depth distribution and potential for latitudinal extension may be exacerbated by factors that increase the attenuation of light in the water column and thus reduce winter PAR, such as increased phytoplankton and sediment associated with agricultural runoff, urban development, and dredging (*32*, *33*). Until now, two climate-sensitive environmental variables, aragonite saturation and temperature, have been emphasized as the main contemporary drivers of latitudinal limits to the growth of coral reefs (*1*, *20*, *21*). Here, we have shown how winter irradiance regime—a climatic constant—may be the ultimate limiter of any potential latitudinal extension of the range of staghorn corals made possible by anthropogenic warming of temperate seas.

REFERENCES AND NOTES

1. J. A. Kleypas, J. W. McManus, L. A. B. Meñez, *Am. Zool.* **39**, 146–159 (1999).
2. J. E. N. Veron, *Corals of the World* (Australian Institute of Marine Science, Townsville, 2000).
3. J. W. Campbell, T. Aarup, *Limnol. Oceanogr.* **34**, 1490–1499 (1989).
4. R. W. Grigg, *Coral Reefs* **25**, 77–84 (2006).
5. K. R. Anthony, M. O. Hoogenboom, S. R. Connolly, *Funct. Ecol.* **19**, 17–26 (2005).
6. R. W. Grigg, *Coral Reefs* **1**, 29–34 (1982).
7. T. J. Done, in *Encyclopedia of Modern Coral Reefs*, D. Hopley, Ed. (Springer, Dordrecht, Netherlands, 2011), pp. 281–293.
8. S. K. Wilson *et al.*, *Glob. Change Biol.* **14**, 2796–2809 (2008).
9. J. S. Stella, G. P. Jones, M. S. Pratchett, *Coral Reefs* **29**, 957–973 (2010).
10. C. C. Wallace, *Staghorn Corals of the World* (CSIRO, Melbourne, 1999).
11. K. E. Carpenter *et al.*, *Science* **321**, 560–563 (2008).
12. O. Hoegh-Guldberg *et al.*, *Science* **318**, 1737–1742 (2007).
13. W. F. Precht, R. B. Aronson, *Front. Ecol. Environ* **2**, 307–314 (2004).
14. H. Yamano, K. Sugihara, K. Nomura, *Geophys. Res. Lett.* **38**, L04601 (2011).
15. B. J. Greenstein, J. M. Pandolfi, *Glob. Change Biol.* **14**, 513–528 (2008).
16. See supplementary materials on *Science* Online.
17. Local midwinter was defined for each degree of latitude as the day of minimum daily PAR and the four seasons defined around this day (*16*). Midsummer PAR was relatively consistent with latitude; therefore, seasonal variation in PAR was inversely correlated with winter PAR and our analyses could not disentangle these terms. Large seasonal changes in daily irradiance could produce photosystem overload in summer and/or energy deficits in winter; however, the dynamics of photoacclimation of corals (*18*) are such that this would be an unlikely limiting factor.
18. K. R. Anthony, O. Hoegh-Guldberg, *Oecologia* **134**, 23–31 (2003).
19. J. M. Guinotte, R. W. Buddemeier, J. A. Kleypas, *Coral Reefs* **22**, 551–558 (2003).
20. J.-P. Gattuso *et al.*, *Biogeosciences* **3**, 489–513 (2006).
21. E. Couce, A. Ridgwell, E. J. Hendy, *J. Biogeogr.* **39**, 1508–1523 (2012).
22. Y. Loya *et al.*, *Ecol. Lett.* **4**, 122–131 (2001).
23. P. R. Frade, P. Bongaerts, A. J. S. Winkelhagen, L. Tonk, R. P. M. Bak, *Limnol. Oceanogr.* **53**, 2711–2723 (2008).
24. F. Houlbrèque, C. Ferrier-Pagès, *Biol. Rev. Camb. Philos. Soc.* **84**, 1–17 (2009).
25. D. R. Bellwood, T. P. Hughes, *Science* **292**, 1532–1535 (2001).
26. D. Jablonski, K. Roy, J. W. Valentine, *Science* **314**, 102–106 (2006).
27. H. Hillebrand, *Mar. Ecol. Prog. Ser.* **273**, 251–267 (2004).
28. D. P. Tittensor *et al.*, *Nature* **466**, 1098–1101 (2010).
29. C. C. Wallace, in *Where Worlds Collide*, I. Metcalf, Ed. (Balkema, Rotterdam, 2001), pp. 168–178.
30. S. A. Keith, A. H. Baird, T. P. Hughes, J. S. Madin, S. R. Connolly, *Proc. R. Soc. B* **280**, 20130818 (2013).
31. O. Hoegh-Guldberg *et al.*, *Science* **321**, 345–346 (2008).
32. C. S. Yentsch *et al.*, *J. Exp. Mar. Biol.* **268**, 171–183 (2002).
33. Our modeling indicates that an increase in chlorophyll of 0.5 μg $liter^{-1}$ in clear reef waters produced a 60% reduction in winter PAR at 10 m depth, latitude 34°N.

ACKNOWLEDGMENTS

We thank the many colleagues who assisted with collection of data and specimens, W. Gregg for providing source code and advice for PAR modeling, S. Connolly and R. Dunne for assistance early in this study, M. Geraci for advice regarding analyses, and J. Doyle, M. Beger, P. Bongaerts, S. Blomberg, J. Dwyer, J. Bennett, M. Sams, N. Bruce, J. Pandolfi, R. Berkelmans, R. Kelley, L. Liggins, A. Smith, M. Pawley, and A. Kozyr for critical comments and advice. J.D.A. is supported by a Rutherford Foundation of New Zealand postdoctoral fellowship. Data access: Species occurrence records for each depth and latitude as well as the environmental surfaces are available on Dryad (https://datadryad.org/resource/doi:10.5061/dryad.3b568).

SUPPLEMENTARY MATERIALS

www.sciencemag.org/content/348/6239/1135/suppl/DC1
Materials and Methods
Figs. S1 to S5
Tables S1 to S5
References (*34*–*45*)

12 August 2014; accepted 24 April 2015
10.1126/science.1259911

SOCIAL EVOLUTION

Genomic signatures of evolutionary transitions from solitary to group living

Karen M. Kapheim,[1,2,3*†] Hailin Pan,[4*] Cai Li,[4,5] Steven L. Salzberg,[6,7] Daniela Puiu,[7] Tanja Magoc,[7] Hugh M. Robertson,[1,2] Matthew E. Hudson,[1,8] Aarti Venkat,[1,8,9] Brielle J. Fischman,[1,10,11] Alvaro Hernandez,[12] Mark Yandell,[13,14] Daniel Ence,[13] Carson Holt,[13,14] George D. Yocum,[15] William P. Kemp,[15] Jordi Bosch,[16] Robert M. Waterhouse,[17,18,19,20] Evgeny M. Zdobnov,[17,18] Eckart Stolle,[21,22] F. Bernhard Kraus,[21,23] Sophie Helbing,[21] Robin F. A. Moritz,[21,24] Karl M. Glastad,[25] Brendan G. Hunt,[26] Michael A. D. Goodisman,[25] Frank Hauser,[27] Cornelis J. P. Grimmelikhuijzen,[27] Daniel Guariz Pinheiro,[28,29] Francis Morais Franco Nunes,[30] Michelle Prioli Miranda Soares,[28] Érica Donato Tanaka,[31] Zilá Luz Paulino Simões,[28] Klaus Hartfelder,[32] Jay D. Evans,[33] Seth M. Barribeau,[34] Reed M. Johnson,[35] Jonathan H. Massey,[2,36] Bruce R. Southey,[37] Martin Hasselmann,[38] Daniel Hamacher,[38] Matthias Biewer,[38] Clement F. Kent,[39,40] Amro Zayed,[39] Charles Blatti III,[1,41] Saurabh Sinha,[1,41] J. Spencer Johnston,[42] Shawn J. Hanrahan,[42] Sarah D. Kocher,[43] Jun Wang,[4,44,45,46,47†] Gene E. Robinson,[1,48†] Guojie Zhang[4,49†]

The evolution of eusociality is one of the major transitions in evolution, but the underlying genomic changes are unknown. We compared the genomes of 10 bee species that vary in social complexity, representing multiple independent transitions in social evolution, and report three major findings. First, many important genes show evidence of neutral evolution as a consequence of relaxed selection with increasing social complexity. Second, there is no single road map to eusociality; independent evolutionary transitions in sociality have independent genetic underpinnings. Third, though clearly independent in detail, these transitions do have similar general features, including an increase in constrained protein evolution accompanied by increases in the potential for gene regulation and decreases in diversity and abundance of transposable elements. Eusociality may arise through different mechanisms each time, but would likely always involve an increase in the complexity of gene networks.

The evolution of eusociality involves changes in the unit of natural selection, from the individual to a group (*1*). Bees evolved eusociality multiple times and are extremely socially diverse (*2*) (Fig. 1), but all pollinate angiosperms, including many crops essential to the human diet (*3*). Simple eusociality may be facultative or obligate, and both forms are characterized by small colonies with a reproductive queen and one or more workers that, due to social and nutritional cues, forego reproduction to cooperatively care for their siblings (*2*). Further evolutionary elaborations have led to complex eusociality, "superorganisms" with colonies of several thousand individuals, sophisticated modes of communication, and morphological specializations for division of labor (*4*).

Theory predicts that the evolution of simple eusociality involves increased regulatory flexibility of ancestral gene networks to create specialized reproductive and nonreproductive individuals, and the evolution of complex eusociality requires genetic novelty to coordinate emergent properties of group dynamics (*5*). To test these predictions, we analyzed five de novo and five publicly available draft genome sequences of 10 bee species from three families, representing two independent origins of eusociality in Apidae and Halictidae and two independent elaborations of simple to complex eusociality in two apid tribes [Apini (honeybees) and Meliponini (stingless bees); Fig. 1]. The draft genomes were of comparable, high quality (supplementary materials).

We found that the transition from solitary to group life is associated with an increased capacity for gene regulation. We scanned the promoter regions of 5865 single-copy orthologs among the 10 species to calculate a motif score [representing the number and binding strength of experimentally characterized transcription factor binding sites (TFBSs)] for 188 *Drosophila melanogaster* TFs (*6*) with at least one ortholog in each of the 10 bees, and correlated motif score with social complexity, using phylogenetically independent contrasts (*7*). Of 2101 significantly correlated motif-gene pairs, 89% were positive and 11% negative, showing that TFs tend to have increased capacity to regulate genes in eusocial species of bees, relative to solitary species (Fig. 2A, supplementary materials).

Further evidence for increased capacity for gene regulation throughout social evolution is a positive ranked correlation between social complexity and the number of genes predicted to be methylated (*7*) (Spearman's rho = 0.76, P = 0.01; phylogenetically corrected Spearman's rho = 0.64, P = 0.06; Fig. 2B; bioinformatics predictions validated with bisulfite sequencing data for three invertebrate species; supplementary materials). DNA methylation affects gene expression in a variety of ways (*8*). Thus, this result suggests an expansion in regulatory capacity with increasingly sophisticated sociality.

The potential for increased regulatory capacity was further revealed at the protein-coding level. Increased social complexity also is associated with rapid evolution of genes involved in coordinating gene regulation. A Bayesian phylogenetic covariance analysis (*9*) of 5865 single-copy orthologs identified 162 genes with accelerated evolution in species with increased social complexity (*7*) (additional data table S3). These rapidly evolving genes were significantly enriched ($P < 0.05$) for Gene Ontology (GO) terms related to regulation of transcription, RNA splicing, ribosomal structure, and regulation of translation (supplementary text and tables S11 and S12). Similar results have been reported for bee and ant species (*10*–*13*); our findings reveal the underlying causes. Approximately two-thirds of these genes are under stronger directional selection in species with increasingly complex eusociality, but we also detected nonadaptive evolution. One-third of the rapidly evolving genes are under relaxed purifying selection in species with complex eusociality, possibly due to reduced effective population sizes (*14*).

We also found an additional 109 genes, significantly enriched ($P < 0.05$) for functions related to protein transport and neurogenesis, which evolve slower with increased social complexity (supplementary text, table S13, and additional data table S3). This includes orthologs of *derailed 2* and *frizzled*, which function as Wnt signaling receptors in *Drosophila* synaptogenesis (*15*), and *rigor mortis*, a nuclear receptor involved in hormone signaling (*16*). A similar pattern of reduced evolutionary rate has been described for genes expressed in human and honey bee brains, potentially due to increasing pleiotropic constraint in complex gene networks (*17*, *18*). Constrained protein evolution of neural and endocrine-related genes seems at odds with the evolution of complexity, but this constraint appears to be compensated for, or perhaps driven by, increased capacity for gene regulation.

We next investigated whether these molecular evolution patterns involve similar sets of genes and cis-regulatory elements among the early (facultative and obligate simple eusociality) and advanced (complex eusociality) stages of independent social transitions. We identified lineage-specific differences in coding sequences and promoter regions of 1526 "social genes" for which evolutionary rate (dN/dS) is faster or slower with increased social complexity in two independent origins and two independent elaborations of eusociality (*7*)

(Fig. 1). Among these lineage-specific social genes, we found common patterns of cis-regulatory evolution: gains of TFBSs in the promoters of genes that evolve slower with increasing social complexity (Fig. 2C and supplementary text). This suggests that a shared feature of both independent origins and elaborations of eusociality is increasingly constrained protein evolution with increasing potential for novel gene expression patterns. The TFs responsible for this pattern were different for each social transition, even though our analysis was limited to highly conserved TFs (Table 1). Several function in neurogenesis or neural plasticity, or are prominent regulators of endocrine-mediated brain gene expression in honeybees (*19*, *20*).

We found further lineage-specific differences among the rapidly evolving "social genes" themselves. Genes undergoing accelerated evolution at the origins of eusociality were significantly enriched for GO terms related to signal transduction in both Apidae and Halictidae, but they shared only six genes (6 out of 354 and 167 genes, respectively; hypergeometric test, $P = 0.82$; Fig. 2D and additional data tables S5 and S6). Rapid evolution of signal transduction pathways may be a necessary step in all origins of eusociality to mediate intracellular responses to novel social and environmental stimuli (*10*), but selection appears to have targeted different parts of these pathways in each independent transition. Caste-specific expression and other analyses of these genes are needed to determine their function in eusociality.

Genes showing signatures of rapid evolution with the elaborations of complex eusociality were also highly disparate between honeybees and stingless bees, with only 43 shared genes and no shared enriched GO terms (43 out of 625 and 512 genes, respectively; hypergeometric test, $P = 0.70$; Fig. 2D and additional data tables S5 and S6). In addition, only 2 out of 5865 single-copy orthologs showed a signature of convergent evolution by fitting a dendrogram based on social complexity significantly better than the accepted molecular phylogeny (*7*) (supplementary text and fig. S21). Similarly, families of major royal jelly protein genes, sex-determining genes, odorant receptors, and genes involved in lipid metabolism expanded in some, but not all, lineages of complex eusocial bees (*7*) (Table 2 and supplementary text). These results suggest that gene family expansion is associated with complex eusociality as predicted (*5*), but involves different genes in each case. Despite striking convergence of social traits among the superorganisms (*4*), the final stages of transformation to this level of biological organization do not necessarily involve common molecular pathways.

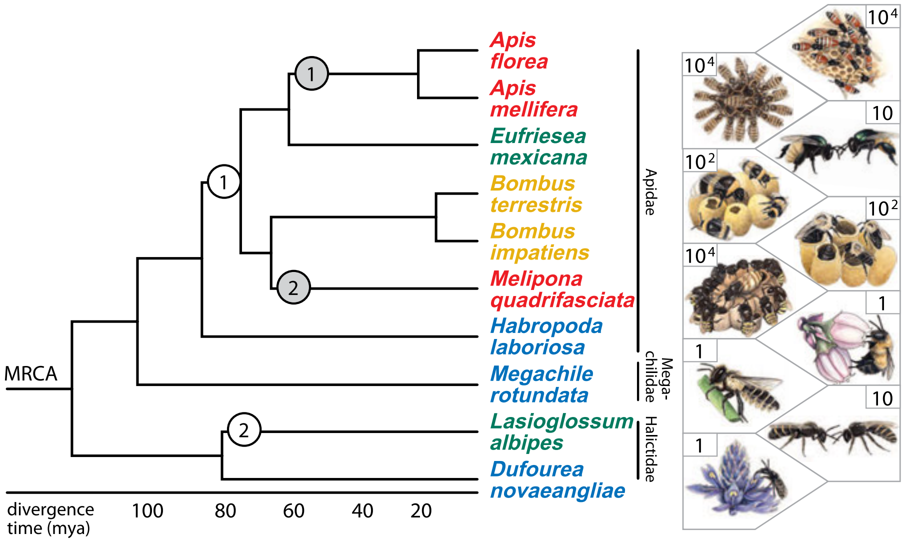

Fig. 1. Phylogeny and divergence times (*28*) of bees selected for genome analysis. We analyzed two independent origins of simple eusociality from a solitary ancestor, one each in Apidae (white circle 1) and Halictidae (white circle 2), and two independent elaborations of complex eusociality in honeybees (gray circle 1) and stingless bees (gray circle 2). Most bees mate once, but honeybees mate with multiple males. All bees eat pollen and nectar from flowering plants. Species names are colored according to degree of social complexity: blue: ancestrally solitary; green: facultative simple eusociality; orange: obligate simple eusociality; red: obligate complex eusociality. The social biology of *E. mexicana* is unknown, but is representative of the facultative simple eusocial life history (*29*). Numbers in each box are approximate colony size on a log scale. MRCA, most recent common ancestor; mya, millions of years ago.

[1]Carl R. Woese Institute for Genomic Biology, University of Illinois at Urbana-Champaign, Urbana, IL 61801, USA. [2]Department of Entomology, University of Illinois at Urbana-Champaign, Urbana, IL 61801, USA. [3]Department of Biology, Utah State University, Logan, UT 84322, USA. [4]China National GeneBank, BGI-Shenzhen, Shenzhen, 518083, China. [5]Centre for GeoGenetics, Natural History Museum of Denmark, University of Copenhagen, Copenhagen, 1350, Denmark. [6]Departments of Biomedical Engineering, Computer Science, and Biostatistics, Johns Hopkins University, Baltimore, MD 21218, USA. [7]Center for Computational Biology, McKusick-Nathans Institute of Genetic Medicine, Johns Hopkins University School of Medicine, Baltimore, MD 21205, USA. [8]Department of Crop Sciences, University of Illinois at Urbana-Champaign, Urbana, IL 61801, USA. [9]Department of Human Genetics, University of Chicago, Chicago, IL 60637, USA. [10]Program in Ecology and Evolutionary Biology, University of Illinois at Urbana-Champaign, Urbana, IL 61801, USA. [11]Department of Biology, Hobart and William Smith Colleges, Geneva, NY 14456, USA. [12]Roy J. Carver Biotechnology Center, University of Illinois at Urbana-Champaign, Urbana, IL 61801, USA. [13]Department of Human Genetics, Eccles Institute of Human Genetics, University of Utah, Salt Lake City, UT 84112, USA. [14]USTAR Center for Genetic Discovery, University of Utah, Salt Lake City, UT 84112, USA. [15]U.S. Department of Agriculture–Agricultural Research Service (USDA-ARS) Red River Valley Agricultural Research Center, Biosciences Research Laboratory, Fargo, ND 58102, USA. [16]Center for Ecological Research and Forestry Applications (CREAF), Universitat Autonoma de Barcelona, 08193 Bellaterra, Spain. [17]Department of Genetic Medicine and Development, University of Geneva Medical School, 1211 Geneva, Switzerland. [18]Swiss Institute of Bioinformatics, 1211 Geneva, Switzerland. [19]Computer Science and Artificial Intelligence Laboratory, Massachusetts Institute of Technology (MIT), Cambridge, MA 02139, USA. [20]The Broad Institute of MIT and Harvard, Cambridge, MA 02142, USA. [21]Institute of Biology, Department Zoology, Martin-Luther-University Halle-Wittenberg, Hoher Weg 4, D-06099 Halle (Saale), Germany. [22]Queen Mary University of London, School of Biological and Chemical Sciences Organismal Biology Research Group, London E1 4NS, UK. [23]Department of Laboratory Medicine, University Hospital Halle, Ernst Grube Strasse 40, D-06120 Halle (Saale), Germany. [24]German Centre for Integrative Biodiversity Research (iDiv), Halle-Jena-Leipzig, 04103 Leipzig, Germany. [25]School of Biology, Georgia Institute of Technology, Atlanta, GA 30332, USA. [26]Department of Entomology, University of Georgia, Griffin, GA 30223, USA. [27]Center for Functional and Comparative Insect Genomics, Department of Biology, University of Copenhagen, Copenhagen, Denmark. [28]Departamento de Biologia, Faculdade de Filosofia, Ciências e Letras de Ribeirão Preto, Universidade de São Paulo, 14040-901 Ribeirão Preto, SP, Brazil. [29]Departamento de Tecnologia, Faculdade de Ciências Agrárias e Veterinárias, Universidade Estadual Paulista (UNESP), 14884-900 Jaboticabal, SP, Brazil. [30]Departamento de Genética e Evolução, Centro de Ciências Biológicas e da Saúde, Universidade Federal de São Carlos, 13565-905 São Carlos, SP, Brazil. [31]Departamento de Genética, Faculdade de Medicina de Ribeirão Preto, Universidade de São Paulo, 14049-900 Ribeirão Preto, SP, Brazil. [32]Departamento de Biologia Celular e Molecular e Bioagentes Patogênicos, Faculdade de Medicina de Ribeirão Preto, Universidade de São Paulo, 14049-900 Ribeirão Preto, SP, Brazil. [33]USDA-ARS Bee Research Lab, Beltsville, MD 20705 USA. [34]Department of Biology, East Carolina University, Greenville, NC 27858, USA. [35]Department of Entomology, Ohio Agricultural Research and Development Center, Ohio State University, Wooster, OH 44691, USA. [36]Department of Ecology and Evolutionary Biology, University of Michigan, Ann Arbor, MI 48109, USA. [37]Department of Animal Sciences, University of Illinois, Urbana, IL 61801, USA. [38]Department of Population Genomics, Institute of Animal Husbandry and Animal Breeding, University of Hohenheim, Germany. [39]Department of Biology, York University, Toronto, ON M3J 1P3, Canada. [40]Janelia Farm Research Campus, Howard Hughes Medical Institue, Ashburn, VA 20147, USA. [41]Department of Computer Science, University of Illinois at Urbana-Champaign, Urbana, IL 61801, USA. [42]Department of Entomology, Texas A&M University, College Station, TX 77843, USA. [43]Department of Organismic and Evolutionary Biology, Museum of Comparative Zoology, Harvard University, Cambridge, MA 02138, USA. [44]Department of Biology, University of Copenhagen, 2200 Copenhagen, Denmark. [45]Princess Al Jawhara Center of Excellence in the Research of Hereditary Disorders, King Abdulaziz University, Jeddah 21589, Saudi Arabia. [46]Macau University of Science and Technology, Avenida Wai long, Taipa, Macau 999078, China. [47]Department of Medicine, University of Hong Kong, Hong Kong. [48]Center for Advanced Study Professor in Entomology and Neuroscience, University of Illinois at Urbana-Champaign, Urbana, IL 61801, USA. [49]Centre for Social Evolution, Department of Biology, Universitetsparken 15, University of Copenhagen, DK-2100 Copenhagen, Denmark.
*These authors contributed equally to this work. †**Corresponding author. E-mail: karen.kapheim@usu.edu (K.M.K.); wangj@genomics.org.cn (J.W.); generobi@illinois.edu (G.E.R.); zhanggj@genomics.org.cn (G.Z.)**

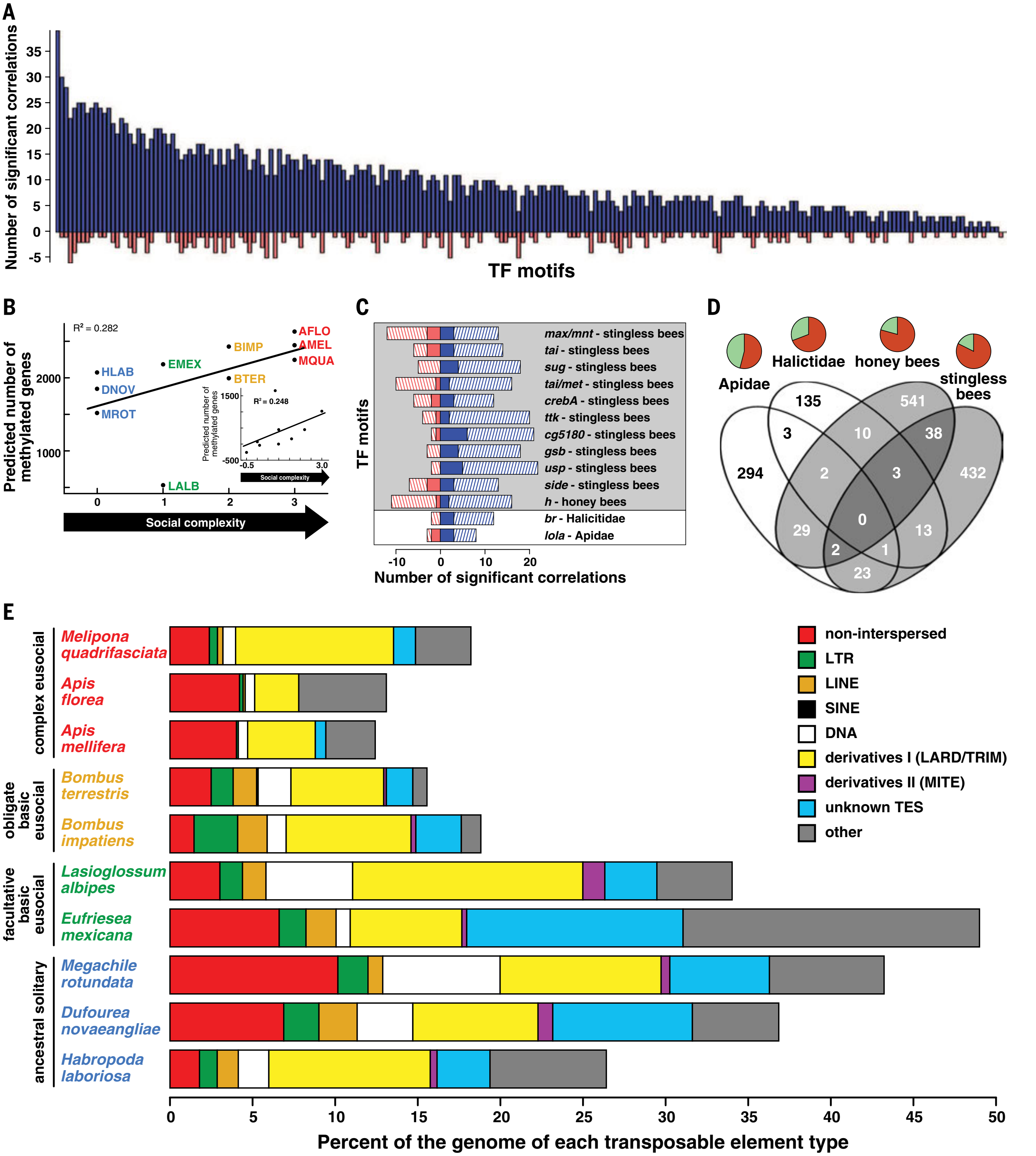

Fig. 2. Genomic signatures of evolutionary transitions from solitary to group life. (**A**) Increasing social complexity is associated with increasing presence of cis-regulatory TFBSs in promoter regions. Each bar represents a TFBS for which presence correlates significantly with social complexity (blue: positive; red: negative). (**B**) Relationship between predicted number of methylated genes and social complexity before and after (inset) phylogenetic correction (see text for statistics). (**C**) TFBS motifs showing a relationship between social complexity and evolutionary rate of coding and noncoding sequences in different lineages. Bar length indicates the number of significant correlations (blue: positive; red: negative) between each motif score and social complexity (from Table 1) among genes evolving faster (solid) or slower (hatched) in lineages with different levels of social complexity [from (D)]. Background shading follows circle shading in Fig. 1. (**D**) Number of genes for which evolutionary rate is faster or slower in lineages with higher compared to lower social complexity. Pie charts represent the proportion of genes evolving slower (light green) or faster (dark orange) with increased social complexity. Venn diagram shading follows circle shading in Fig. 1. (**E**) Complex eusocial species have a reduced proportion of repetitive DNA compared to other bees (see text for statistics). LTR, long terminal repeat; LINE, long interspersed element; SINE, short interspersed element; DNA, DNA transposon; LARD, large retrotransposon derivative; TRIM, terminal repeat retrotransposon in miniature; MITE, miniature inverted-repeat transposable element; TES, transposable elements.

The major transitions in evolution involve a reduction in conflict as the level of natural selection rises from the individual to the group (*1*). Extending this to intragenomic conflict may explain our finding of decreased diversity and abundance of transposable elements (TEs) with increasing social complexity (*7*) (regression after phylogenetic correction, $F = 8.99$, adjusted $R^2 = 0.47$, $P = 0.017$; Fig. 2E, figs. S42 to S44, and supplementary text). This may be a consequence of increased recombination rates among highly eusocial insects (*21*, *22*) or because key features of complex eusociality lead to decreased exposure to parasites and pathogens that horizontally transmit TEs (*4*, *23*). Eusociality in bees may thus provide natural immunity against certain types of intragenomic conflict.

Our results and those in (*10*–*13*) support the prediction that changes in gene regulation are key features of evolutionary transitions in biological organization (*5*). Our results further reveal the convergent adaptive and nonadaptive evolutionary processes common to both the early and advanced stages of multiple independent transitions from solitary to group living. It is now clear that there are lineage-specific genetic changes associated with independent origins of eusociality in bees, and independent elaborations of eusociality in both bees and ants. This includes different sets of genes showing caste-biased expression across species (*24*–*26*) and, as we have shown, evolutionary modifications of TEs, gene methylation, and cis-regulatory patterns associated with the suite of life-history traits that define eusociality. This suggests that if it were possible to "replay life's tape" (*27*), eusociality may arise through different mechanisms each time, but would likely always involve an increase in the complexity of gene networks.

Table 1. Transcription factors (TFs) and corresponding motifs associated with origins and elaborations of eusociality in bees. [Motif names: Fly Factor Survey (6); supplementary text.]

Motif	*D. melanogaster* TFs	Hypergeometric test *P*-value
	Solitary to simple eusociality–Apidae	
lola_PQ_SOLEXA	*Lola*	0.0047
	Solitary to simple eusociality–Halictidae	
br_PL_SOLEXA_5	*Br*	0.0016
	Simple eusociality to complex eusociality–honeybees	
h_SOLEXA_5	*dpn,h*	0.0027
	Simple eusociality to complex eusociality–stingless bees	
Side_SOLEXA_5	*E_spl, HLHm3, HLHm5, HLHm7, HLHmbeta, HLHmdelta, HLHmgamma, Side*	0.0008
usp_SOLEXA	*EcR,svp,usp*	0.0013
CrebA_SOLEXA	*CrebA*	0.0040
CG5180_SOLEXA	CG5180	0.0044
tai_Met_SOLEXA_5	*Mio_bigmax,tai_Met*	0.0045
ttk_PA_SOLEXA_5	*Ttk*	0.0078
gsb_SOLEXA	*gsb,Poxn,prd*	0.0083
tai_SOLEXA_5	*Tai*	0.0100

Table 2. Relative size of select gene families as related to social complexity in bees.

Family	Function	Eusocial bees compared to solitary bees
	Differences among bees	
Major royal jelly	Brood feeding	Expanded only in *Apis*
Sex determination pathway genes	Sex-specific development	Expanded in some eusocial lineages
Odorant receptors	Olfaction	Expanded in complex eusocial lineages
Lipid metabolism genes	Metabolic processing of lipids	Expanded in complex eusocial lineages
	Similarities across bees	
Biogenic amines receptors, neuropeptides, GPCRs*	Neural plasticity	Similar
Insulin-signaling and ecdysone pathway genes	Insect development, caste determination in honeybees, behavioral plasticity as adults	Similar
Immunity	Infectious disease protection	Similar
Cytochrome P450 monooxygenase genes	Detoxification	Similar

*GPCRs, G protein–coupled receptors.

REFERENCES AND NOTES

1. J. Maynard Smith, E. Szathmáry, *The Major Transitions in Evolution* (Oxford Univ. Press, Oxford, UK, 1995).
2. C. D. Michener, *The Social Behavior of the Bees* (Harvard Univ. Press, Cambridge, MA, 1974).
3. A.-M. Klein *et al.*, *Proc. Biol. Sci. B* **274**, 303–313 (2007).
4. H. Hölldobler, E. O. Wilson, *The Superorganism: The Beauty, Elegance and Strangeness of Insect Societies* (Norton, New York, 2009).
5. B. R. Johnson, T. A. Linksvayer, *Q. Rev. Biol.* **85**, 57–79 (2010).
6. L. J. Zhu *et al.*, *Nucleic Acids Res.* **39**, D111–D117 (2011).
7. Materials and methods are available as supplementary materials on *Science* Online.
8. H. Yan *et al.*, *Annu. Rev. Entomol.* **60**, 435–452 (2015).
9. N. Lartillot, R. Poujol, *Mol. Biol. Evol.* **28**, 729–744 (2011).
10. S. H. Woodard *et al.*, *Proc. Natl. Acad. Sci. U.S.A.* **108**, 7472–7477 (2011).
11. B. A. Harpur *et al.*, *Proc. Natl. Acad. Sci. U.S.A.* **111**, 2614–2619 (2014).
12. J. Roux *et al.*, *Mol. Biol. Evol.* **31**, 1661–1685 (2014).
13. D. F. Simola *et al.*, *Genome Res.* **23**, 1235–1247 (2013).
14. J. Romiguier *et al.*, *J. Evol. Biol.* **27**, 593–603 (2014).
15. M. Park, K. Shen, *EMBO J.* **31**, 2697–2704 (2012).
16. J. Gates, G. Lam, J. A. Ortiz, R. Losson, C. S. Thummel, *Development* **131**, 25–36 (2004).
17. D. Brawand *et al.*, *Nature* **478**, 343–348 (2011).
18. D. Molodtsova, B. A. Harpur, C. F. Kent, K. Seevananthan, A. Zayed, *Front. Genet.* **5**, 431 (2014).
19. D. W. Pfaff, A. P. Arnold, A. M. Etgen, R. T. Rubin, S. E. Fahrbach, Eds., *Hormones, Brain and Behavior* (Elsevier, New York, 2009).
20. S. Chandrasekaran *et al.*, *Proc. Natl. Acad. Sci. U.S.A.* **108**, 18020–18025 (2011).
21. L. Wilfert, J. Gadau, P. Schmid-Hempel, *Heredity* **98**, 189–197 (2007).
22. E. S. Dolgin, B. Charlesworth, *Genetics* **178**, 2169–2177 (2008).
23. S. Schaack, C. Gilbert, C. Feschotte, *Trends Ecol. Evol.* **25**, 537–546 (2010).
24. B. Feldmeyer, D. Elsner, S. Foitzik, *Mol. Ecol.* **23**, 151–161 (2014).
25. P. G. Ferreira *et al.*, *Genome Biol.* **14**, R20 (2013).
26. B. G. Hunt *et al.*, *Proc. Natl. Acad. Sci. U.S.A.* **108**, 15936–15941 (2011).
27. S. J. Gould, *Wonderful Life: The Burgess Shale and the Nature of History* (Norton, New York, 1989).
28. S. Cardinal, B. N. Danforth, *Proc. Biol. Sci.* **280**, 20122686 (2013).
29. S. Cardinal, B. N. Danforth, *PLOS ONE* **6**, e21086 (2011).

ACKNOWLEDGMENTS

Data deposition at National Center for Biotechnology Information: *H. laboriosa*, *D. novaeangliae*, *E. mexicana*, *M. quadrifasciata*, and *M. rotundata* genome assemblies accession numbers PRJNA279436, PRJNA279825, PRJNA279814, PRJNA279820, and PRJNA66515. Funding for genome sequencing and analysis: BGI, a U.S. National Institutes of Health Pioneer Award (DP1 OD006416) to G.E.R., and European Union Marie Curie International Incoming Fellowship (300837) to G.Z. Additional

funding: U.S. National Science Foundation grant DEB-0640690 (M.A.D.G.) and DEB-0743154 (G.E.R. and M.E.H); Danish Council for Independent Research grants 10-081390 (C.L.) and 0602-01170B (C.J.P.G.); Lundbeck Foundation (C.J.P.G); Georgia Tech–Elizabeth Smithgall Watts endowment (M.A.D.G.); Marie Curie International Outgoing Fellowship PIOF-GA-2011-303312 (R.M.W.); Swiss National Science Foundation award 31003A-125350, Commission Informatique of the University of Geneva, Schmidheiny Foundation, and Swiss Institute of Bioinformatics (E.M.Z.); and Natural Sciences and Engineering Research Council of Canada Discovery Grant and Early Research Award (A.Z.). This project was conducted under the auspices of the i5K Initiative. We thank the Roy J. Carver Biotechnology Center (sequencing services); N. Lartillot (advice on Coevol); T. Newman (assistance with DNA extractions); and E. Hadley (assistance with figures). Computational support: D. Davidson, N. Band, D. Slater (University of Illinois), J. H. Kidner and H. Scharpenberg (Martin-Luther-University Halle-Wittenberg); Compute Canada; and Center for High Performance Computing at the University of Utah. J. Himes created the illustrations in Fig. 1. We are grateful to T. Pitts-Singer, H. G. Hall, B. N. Danforth, J. Gibbs, and S. Cardinal for providing bee specimens; R. Ayala for identification of *E. mexicana*; J. Vega and the staff at Estación de Biología Chamela, Universidad Nacional Autónoma de México (UNAM), for support during collecting trips; and S. A. Cameron for insightful discussion.

SUPPLEMENTARY MATERIALS

www.sciencemag.org/content/348/6239/1139/suppl/DC1
Materials and Methods
Supplementary Text
Figs. S1 to S44
Tables S1 to S32
Additional Data Tables S1 to S12
References (*30–151*)
Author Contributions

19 December 2014; accepted 6 May 2015
Published online 14 May 2015;
10.1126/science.aaa4788

HUMAN OOCYTES

Error-prone chromosome-mediated spindle assembly favors chromosome segregation defects in human oocytes

Zuzana Holubcová,[1] Martyn Blayney,[2] Kay Elder,[2] Melina Schuh[1]*

Aneuploidy in human eggs is the leading cause of pregnancy loss and several genetic disorders such as Down syndrome. Most aneuploidy results from chromosome segregation errors during the meiotic divisions of an oocyte, the egg's progenitor cell. The basis for particularly error-prone chromosome segregation in human oocytes is not known. We analyzed meiosis in more than 100 live human oocytes and identified an error-prone chromosome-mediated spindle assembly mechanism as a major contributor to chromosome segregation defects. Human oocytes assembled a meiotic spindle independently of either centrosomes or other microtubule organizing centers. Instead, spindle assembly was mediated by chromosomes and the small guanosine triphosphatase Ran in a process requiring ~16 hours. This unusually long spindle assembly period was marked by intrinsic spindle instability and abnormal kinetochore-microtubule attachments, which favor chromosome segregation errors and provide a possible explanation for high rates of aneuploidy in human eggs.

Meiosis in human oocytes is more prone to chromosome segregation errors than mitosis (*1*, *2*), meiosis during spermatogenesis (*3*, *4*), and female meiosis in other organisms (*3*, *5*). Despite its importance for fertility and human development, meiosis in human eggs has hardly been studied. Human oocytes are only available in small numbers, warranting single-cell assays capable of extracting maximal information. Although high-resolution live-cell microscopy is an ideal method, oocyte development in the ovary poses challenges to direct imaging. We therefore established an experimental system (*6*) for ex vivo high-resolution fluorescence microscopy of human oocytes freshly harvested from women undergoing gonadotropin-stimulated in vitro fertilization cycles. To establish the major stages of meiosis in this system, we simultaneously monitored microtubules and chromosomes for ~24 to 48 hours (Fig. 1 and movie S1). Similar to the situation in situ (*7*), human oocytes matured into fertilizable eggs over this time course, as judged by the formation of a polar body. The morphologically identifiable stages (Fig. 1A) at characteristic times after nuclear envelope breakdown [(NEBD), set to 0 hours] provided a time-resolved framework for human oocyte meiosis (Fig. 1B). This reference timeline post-NEBD is used throughout this paper.

Before NEBD, chromosomes were highly condensed and clustered around the nucleolus. Instead of rapidly nucleating microtubules upon NEBD, human oocytes first formed a chromosome aggregate that was largely devoid of microtubules (Fig. 1A; movie S1; and fig. S1, A and B). Microtubules were first observed at ~5 hours, when they started to form a small aster within the chromosome aggregate. As the microtubule aster grew, the chromosomes became individualized and oriented on the surface of the aster with their kinetochores facing inwards. The microtubule aster then extended into an early bipolar spindle that carried the chromosomes on its surface (Fig. 1A; movie S1; and fig. S1, C to E). The chromosomes then entered the spindle but remained distributed throughout the entire spindle volume. Chromosomes first congressed in the spindle center at ~13 hours but continued to oscillate around the spindle equator. Stable chromosome alignment was typically only achieved close to anaphase onset (Fig. 1, A and B, and movie S1). Unexpectedly, the spindle volume increased over the entire course of meiosis, up until anaphase onset (Fig. 1, C and D). The barrel-shaped spindle formed in this process consisted of loosely clustered bundles of microtubules and lacked astral microtubules (movie S2 and fig. S2). At ~17 hours, the oocytes progressed into anaphase and eliminated half of the homologous chromosomes in a polar body. Nearly a day after NEBD, the oocytes had formed a bipolar metaphase II spindle and matured into a fertilizable egg. The stages and timing of meiosis were highly reproducible among oocytes (Fig. 1, A and B) and could also be observed in fixed oocytes (fig. S1, A to I). Importantly, 79.0% of imaged human oocytes extruded a polar body. This indicates that the imaging assays, as well as the methods by which the oocytes were obtained and processed, did not have a prominent effect on meiotic progression.

The surprisingly slow and gradual build-up of the spindle over 16 hours (Fig. 1, C and D) is in stark contrast to mitosis, where spindle assembly takes only ~30 min (*8*), or meiosis in mouse oocytes, where it takes 3 to 5 hours (*9–11*). During mitosis, two centrosomes ensure the rapid assembly of a spindle. In oocytes of many species, centrosomes are absent but functionally replaced by microtubule organizing centers (MTOCs) that lack centrioles (*9*, *12*). Human oocytes also lack centrosomes (*13–15*), but whether acentriolar MTOCs participate in spindle assembly is unclear (*16–19*). We consistently detected pericentrin- and γ-tubulin–positive MTOCs at the spindle poles of mitotic cells and metaphase I and II (MI and MII) mouse oocytes, but never at MI or MII spindles in human oocytes (Fig. 2, A and B, and fig. S3). Thus, our data suggest that meiotic spindles in human oocytes lack detectable MTOCs.

In *Xenopus* egg extracts, chromosomes can serve as sites of microtubule nucleation if centrosomes are absent (*20*). The human oocytes we imaged also initiated microtubule nucleation in the region of the chromosome aggregate (78 of 78 live human oocytes). High-resolution imaging of fixed human oocytes confirmed that microtubules were first nucleated on chromosomes, emanating primarily from kinetochores (Fig. 2C, movie S3, and fig. S4). MTOC-nucleated cytoplasmic asters, such as those seen in chromosomal proximity upon NEBD in mouse oocytes (*9*), could not be detected. Thus, chromosomes, not MTOCs, serve as major sites of microtubule nucleation in human oocytes.

[1]Medical Research Council, Laboratory of Molecular Biology, Francis Crick Avenue, Cambridge Biomedical Campus, Cambridge CB2 0QH, UK. [2]Bourn Hall Clinic, Bourn, Cambridge CB23 2TN, UK.
***Corresponding author. E-mail: mschuh@mrc-lmb.cam.ac.uk**

Chromatin-mediated spindle assembly is driven by the small guanosine triphosphatase Ran. Guanosine triphosphate (GTP)–bound Ran is replenished around chromosomes by its chromatin-bound GTP exchange factor RCC1 and locally releases spindle assembly factors from inhibitory binding to importins (*21*–*23*). To test whether Ran-GTP is required for spindle assembly in human oocytes, we blocked its function with the guanosine diphosphate–locked mutant Ran T24N, which acts as a dominant-negative variant of Ran (*24*, *25*). Ran T24N severely delayed the onset of microtubule nucleation and impaired spindle assembly (Fig. 2, D to F, and movie S4). In mouse and *Drosophila* oocytes, spindles have defects but still assemble if Ran is inhibited (*9*, *26*, *27*). Thus, our data suggest that spindle assembly in human oocytes is independent of MTOCs but mediated by chromosomes and dependent on Ran-GTP.

The period between chromosome-mediated microtubule nucleation (~5 hours) and establishment of a bipolar spindle with aligned chromosomes (~16 hours) displayed considerable spindle instability. Although the microtubule aster transformed into a bipolar spindle at ~7 hours, this spindle often failed to maintain bipolarity (Fig. 3A and movie S5). In 44% of oocytes, the spindles rounded up and became apolar, which we classified as moderate spindle instability. In 38% of oocytes, the spindles even progressed through a prolonged multipolar stage, which we classified as severe spindle instability (Fig. 3, A and B). Multipolar and apolar spindles were also observed in fixed oocytes that had not been imaged (fig. S6). Although spindle instability lasted for an average of 7.5 ± 3.1 hours (Fig. 3C), the vast majority of oocytes progressed into anaphase with bipolar spindles and extruded a polar body (fig. S5). The apparent instability of the spindle in human oocytes is in stark contrast to mitotic spindles and meiotic spindles in other species such as mouse oocytes, which rarely become unstable upon establishment of a bipolar spindle (Fig. 3D).

Next, we investigated whether spindle instability correlates with chromosome segregation errors. Normal chromosome segregation is characterized by simultaneous separation of all homologous chromosomes. Chromosomes that lag behind during anaphase increase the possibility of aneuploidy due to inappropriate partitioning of chromosomes upon cytokinesis. We thus scored our imaging data set for the presence and degree of lagging chromosomes and spindle instability. Oocytes with prominent chromosome bridges or chromosomes that remained in the center of the spindle during anaphase were classified as having persistent lagging chromosomes. Oocytes with a few chromosomes that segregated more slowly than the rest of the chromosomes but did not remain in the center of the spindle were classified as having transiently lagging chromosomes (Fig. 3E). Notably, 72% of oocytes with severe spindle instability went on to have persistent lagging chromosomes during anaphase (Fig. 3F). In contrast, oocytes with a stable spindle were never observed to have persistent lagging chromosomes. Oocytes with unstable spindles were also significantly more likely to have chromosome alignment defects (fig. S7).

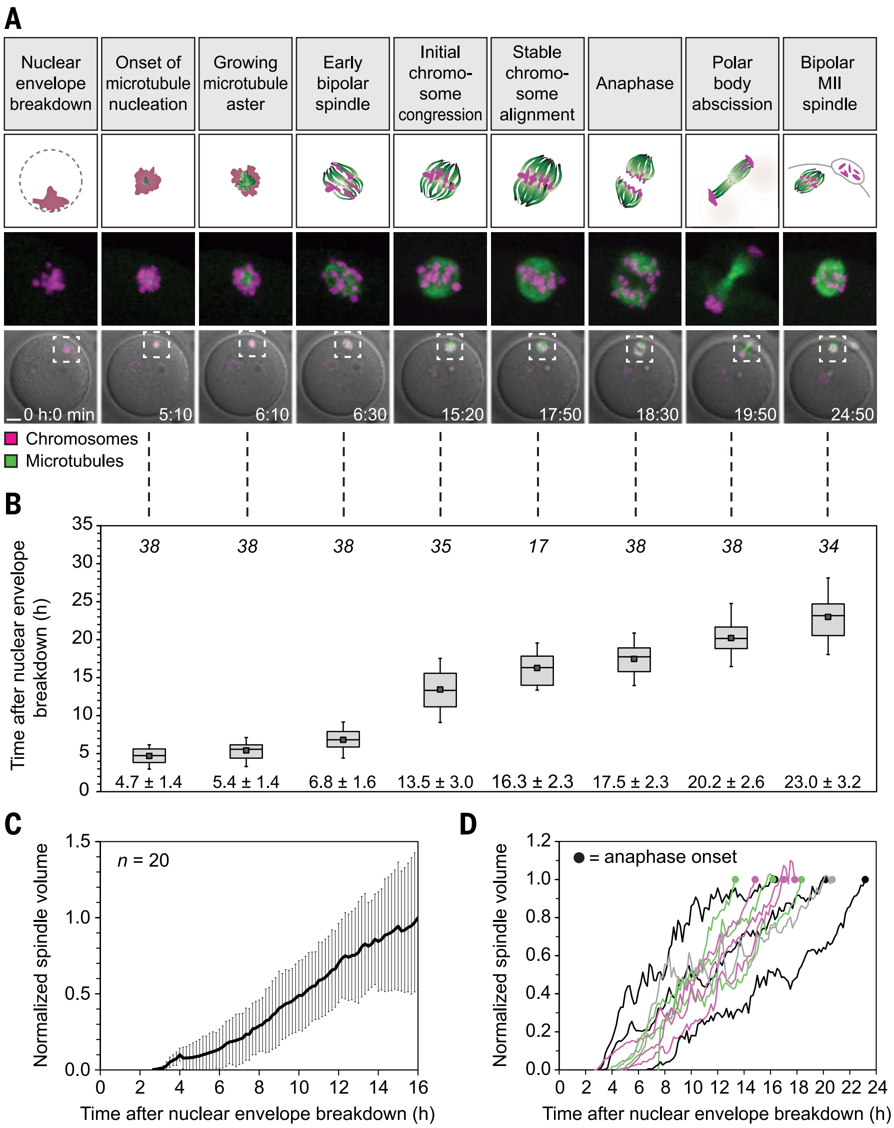

Fig. 1. Stages of meiosis in live human oocytes. (**A**) Stages of meiosis in human oocytes determined from live human oocytes expressing enhanced green fluorescent protein–microtubule-associated protein 4 (EGFP-MAP4) (microtubules) and histone 2B–monomeric red fluorescent protein 1 (H2B-mRFP1) (chromosomes). A schematic representation of each stage (scheme; microtubules in green, chromosomes in magenta) and stage-specific time-lapse images (*z* projections, four sections, every 5 μm) merged with differential interference contrast are shown (bottom row). Outlined regions are magnified above (middle row). Scale bar, 20 μm. Time is displayed in hours: minutes. (**B**) Quantification of timing of meiotic progression from live oocytes expressing EGFP-MAP4 (microtubules) and H2B-mRFP1 (chromosomes), as shown in (A). The box plot shows median (horizontal lines), mean (small squares), 25th and 75th percentiles (boxes), and 5th and 95th percentiles (whiskers) of time after NEBD. The number of oocytes is specified in italics. Only oocytes in which the whole maturation process was recorded (from before NEBD to bipolar MII spindle formation) were included. h, hours. (**C** and **D**) The spindle volume was quantified in live human oocytes expressing EGFP-MAP4 (microtubules), as shown in (A). Averaged data from 20 oocytes (C) and examples of individual curves up until anaphase onset (D) are shown.

The chromosome segregation defects could be due to progression into anaphase with abnormal kinetochore-microtubule attachments. To test this hypothesis, we fixed oocytes using a cold treatment assay that preferentially preserves kinetochore-associated microtubules. During early spindle assembly, the kinetochores were already associated with microtubules, but a prominent spindle axis was absent. The kinetochore fibers were instead randomly oriented relative to each other and only partially focused into several small poles distributed throughout the chromosome-microtubule assembly. Oocytes fixed close to anaphase onset had formed a bipolar spindle, in which most bivalent chromosomes were bioriented (Fig. 4A and movie S6). But unexpectedly, only ~80% of kinetochores were correctly attached to microtubules, being linked to a single spindle pole (amphitelic attachment). In contrast, 20% of kinetochores remained attached to both spindle poles (merotelic attachment) (Fig. 4, B and C, and fig. S8). These data suggest that human oocytes are less efficient in correcting kinetochore-microtubule attachments than mitotic cells (*28*) and mouse oocytes (*29*). Our observation that persistent lagging chromosomes are most likely to occur in oocytes with severe spindle instability suggests that these oocytes are particularly likely to progress into anaphase with abnormal kinetochore-microtubule attachments.

This study allows us to draw several conclusions with implications for the causes of egg aneuploidy. The single most notable feature of human oocyte meiosis is an unusually dynamic and slowly assembling meiotic spindle. This feature could be the consequence of absent centrosomes or other MTOCs, either of which could more rapidly generate a bipolar spindle. Instead, chromosomes and Ran-GTP are employed for spindle assembly. The spindles assembled by this mechanism display a high proportion of abnormal kinetochore-microtubule attachments. The spindles are also intrinsically unstable, and the degree of spindle instability correlates with the degree of chromosome segregation errors. Spindle instability could hinder the establishment of accurate kinetochore-microtubule attachments and thereby promote chromosome segregation errors. Alternatively, spindle instability may reflect attempts of the chromosomes to establish stable bipolar microtubule attachments, which could be more challenging in human oocytes, possibly due to structural features of their chromosomes. Progression into anaphase with these

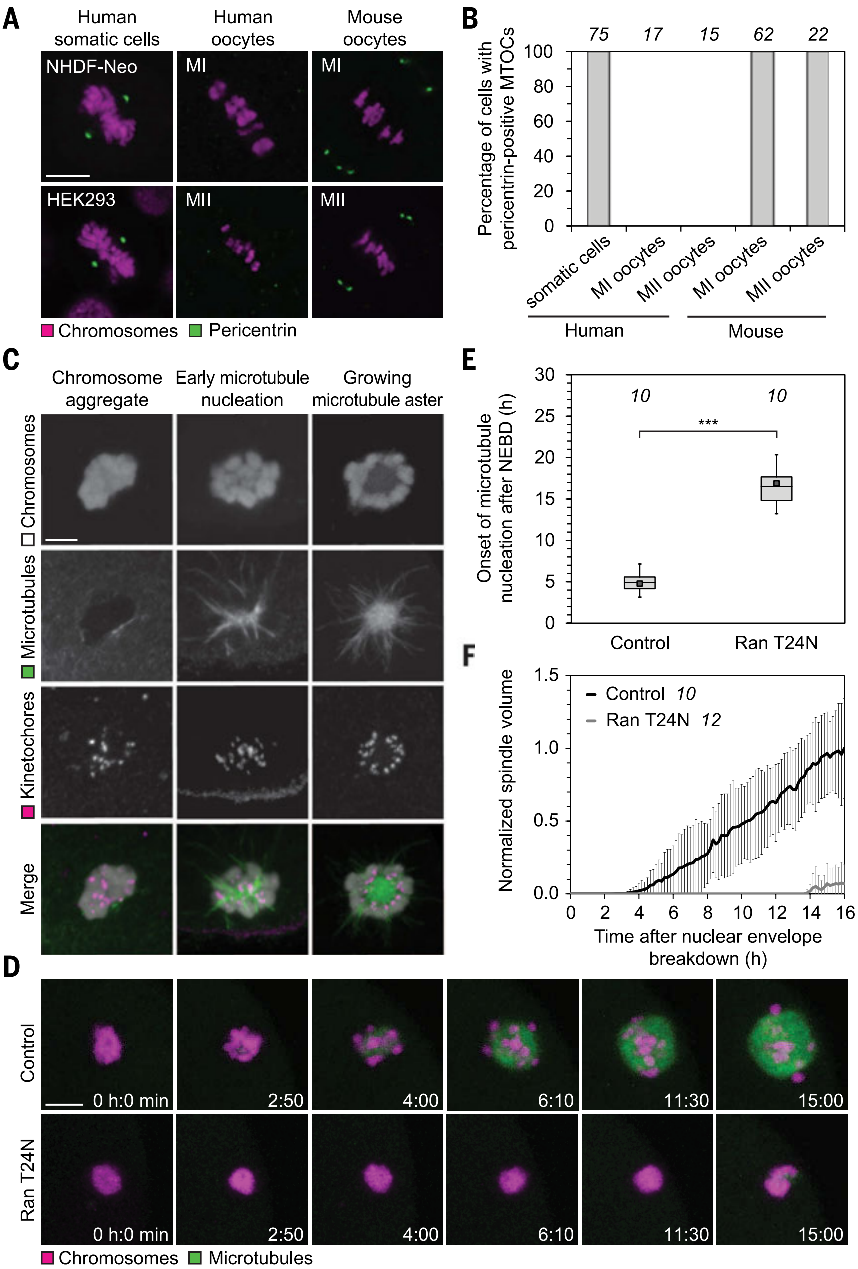

Fig. 2. Chromosomes mediate spindle assembly in human oocytes. (**A**) Immunofluorescence staining of pericentrin and chromosomes (Hoechst) in somatic cells, as well as mouse and human MI and MII oocytes. Scale bar, 10 μm. NHDF-Neo, normal human dermal fibroblasts derived from neonatal foreskin; HEK293, human embryonic kidney 293 cells. (**B**) Spindles of somatic cells, as well as MI and MII spindles in mouse and human oocytes [as shown in (A)] were scored for the presence of pericentrin-positive MTOCs. The number of cells is specified in italics. (**C**) Immunofluorescence staining (z projections of six sections, every 0.3 μm) of kinetochores (CREST), microtubules (α-tubulin), and chromosomes (Hoechst) in human oocytes fixed at different times shortly after NEBD. Scale bar, 10 μm. (**D**) Live human oocytes expressing H2B-mRFP1 (chromosomes) and EGFP-MAP4 (microtubules) upon microinjection with Ran T24N (lower panel) or bovine serum albumin (BSA) (top panel) (z projections of four sections, every 5 μm). Scale bar, 10 μm. (**E**) Onset of microtubule nucleation in live human oocytes expressing EGFP-MAP4 upon microinjection with either Ran T24N or BSA. The box plot is as in Fig. 1B. The number of oocytes is specified in italics. ***$P < 10^{-14}$ (t test). Two oocytes injected with Ran T24N never nucleated microtubules. (**F**) The spindle volume was quantified in live human oocytes expressing EGFP-MAP4 upon microinjection with either Ran T24N or BSA. The number of oocytes is specified in italics.

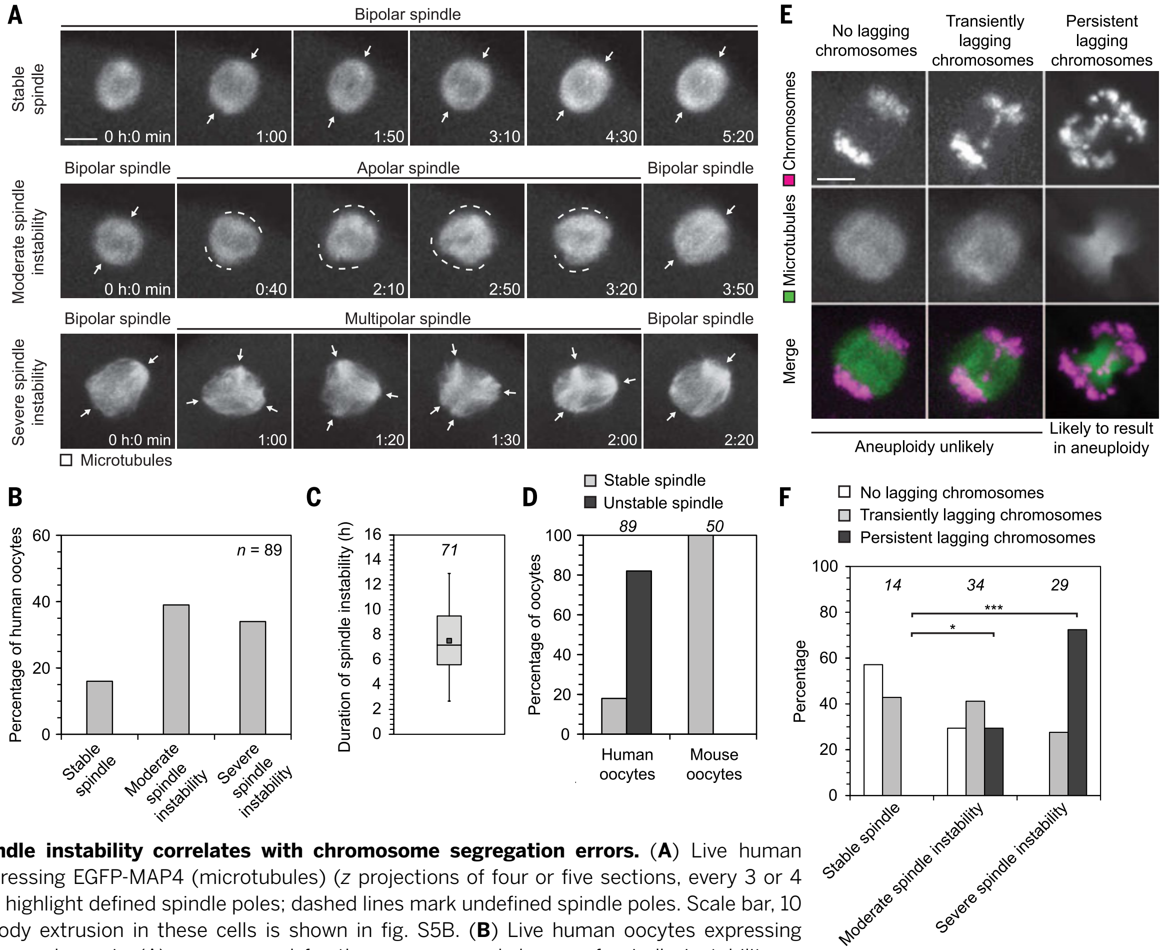

Fig. 3. Spindle instability correlates with chromosome segregation errors. (**A**) Live human oocytes expressing EGFP-MAP4 (microtubules) (*z* projections of four or five sections, every 3 or 4 μm). Arrows highlight defined spindle poles; dashed lines mark undefined spindle poles. Scale bar, 10 μm. Polar body extrusion in these cells is shown in fig. S5B. (**B**) Live human oocytes expressing EGFP-MAP4, as shown in (A), were scored for the presence and degree of spindle instability. *n*, number of oocytes. (**C**) The duration of spindle instability was measured in live human oocytes expressing EGFP-MAP4, as shown in (A). The box plot is as in Fig. 1B. The number of oocytes is specified in italics. (**D**) Live human and mouse oocytes expressing EGFP-MAP4 (microtubules) were scored for the presence of spindle instability. The number of oocytes is specified in italics. (**E**) Illustration of classes of lagging chromosomes in live human oocytes expressing H2B-mRFP1 (chromosomes) and EGFP-MAP4 (microtubules) (*z* projections of three or five sections, every 3 or 5 μm). Scale bar, 10 μm. (**F**) Live human oocytes expressing H2B-mRFP1 (chromosomes) and EGFP-MAP4 (microtubules), as shown in (E), were scored for the presence of transiently lagging or persistent lagging chromosomes. The number of oocytes is specified in italics. $^*P < 0.05$; $^{***}P < 10^{-6}$ (Fisher's exact test).

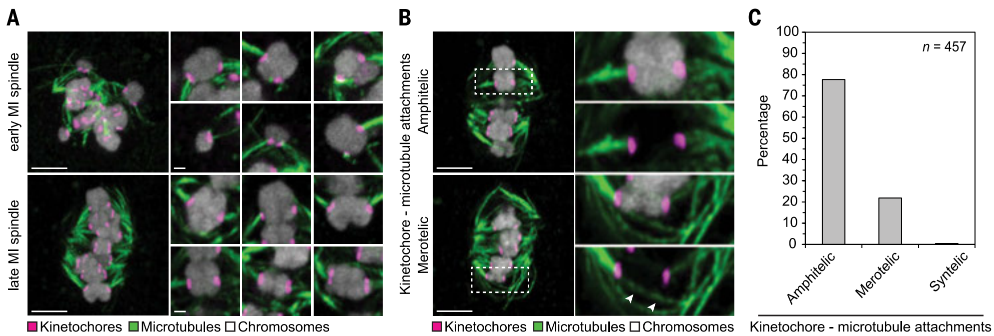

Fig. 4. Correction of kinetochore-microtubule attachments is incomplete close to anaphase. (**A**) Immunofluorescence staining (*z* projections of 13 sections, every 0.3 μm) of kinetochores (CREST) and microtubules (α-tubulin) in cold-treated human oocytes fixed during early or late spindle assembly. Chromosomes were labeled with Hoechst. Scale bars in overview panels (left), 5 μm. High-resolution images of six individual chromosome bivalents from the overview are shown on the right (*z* projections of two sections, every 0.3 μm). Scale bars (right), 1 μm. (**B**) Illustration of amphitelic and merotelic kinetochore-microtubule attachments. Immunofluorescence staining (*z* projections of three sections, every 0.3 μm) of kinetochores (CREST) and microtubules (α-tubulin) in cold-treated human oocytes fixed close to anaphase onset. Chromosomes were labeled with Hoechst. The outlined regions are magnified on the right. Arrowheads denote merotelically attached microtubules. Scale bars, 5 μm. (A and B) All images were deconvolved. Background signal outside of the spindle area was masked in a kinetochore channel (magenta). (**C**) Ten cold-treated oocytes fixed close to anaphase onset [as shown in (B)] were scored for amphitelic, merotelic, or syntelic kinetochore-microtubule attachments. In one case, the bivalent's kinetochores were attached to the same, instead of opposite, poles (syntelic attachment). *n*, number of kinetochore-microtubule attachments.

abnormal attachments would put the oocyte at risk of chromosome segregation errors (fig. S9), providing at least one mechanism for the relatively frequent aneuploidy of eggs, even in young women (*3*, *30*). Our findings may also explain why human oocytes are more prone to aneuploidy than oocytes from mice or other organisms, where the presence of MTOCs may render spindle assembly and chromosome segregation more efficient.

REFERENCES AND NOTES

1. S. I. Nagaoka, T. J. Hassold, P. A. Hunt, *Nat. Rev. Genet.* **13**, 493–504 (2012).
2. K. A. Knouse, J. Wu, C. A. Whittaker, A. Amon, *Proc. Natl. Acad. Sci. U.S.A.* **111**, 13409–13414 (2014).
3. F. Pacchierotti, I. D. Adler, U. Eichenlaub-Ritter, J. B. Mailhes, *Environ. Res.* **104**, 46–69 (2007).
4. C. Templado, F. Vidal, A. Estop, *Cytogenet. Genome Res.* **133**, 91–99 (2011).
5. A. Danylevska, K. Kovacovicova, T. Awadova, M. Anger, *Chromosome Res.* **22**, 365–373 (2014).
6. Materials and methods are available as supplementary materials on *Science* Online.
7. C. A. Gemzell, *Fertil. Steril.* **13**, 153–168 (1962).
8. M. Held *et al*., *Nat. Methods* **7**, 747–754 (2010).
9. M. Schuh, J. Ellenberg, *Cell* **130**, 484–498 (2007).
10. Z. Holubcová, G. Howard, M. Schuh, *Nat. Cell Biol.* **15**, 937–947 (2013).
11. A. Kolano, S. Brunet, A. D. Silk, D. W. Cleveland, M. H. Verlhac, *Proc. Natl. Acad. Sci. U.S.A.* **109**, E1858–E1867 (2012).
12. G. Manandhar, H. Schatten, P. Sutovsky, *Biol. Reprod.* **72**, 2–13 (2005).
13. D. Szöllösi, J. Mandelbaum, M. Plachot, J. Salat-Baroux, J. Cohen, *J. In Vitro Fert. Embryo Transfer* **3**, 232–242 (1986).
14. A. H. Sathananthan *et al*., *Microsc. Res. Tech.* **69**, 396–407 (2006).
15. A. H. Sathananthan, *Micron* **44**, 1–20 (2013).
16. S. J. Pickering, M. H. Johnson, P. R. Braude, E. Houliston, *Hum. Reprod.* **3**, 978–989 (1988).
17. D. E. Battaglia, P. Goodwin, N. A. Klein, M. R. Soules, *Hum. Reprod.* **11**, 2217–2222 (1996).
18. D. E. Battaglia, N. A. Klein, M. R. Soules, *Mol. Hum. Reprod.* **2**, 845–851 (1996).
19. M. A. George, S. J. Pickering, P. R. Braude, M. H. Johnson, *Mol. Hum. Reprod.* **2**, 445–456 (1996).
20. R. Heald *et al*., *Nature* **382**, 420–425 (1996).
21. R. E. Carazo-Salas *et al*., *Nature* **400**, 178–181 (1999).
22. O. J. Gruss *et al*., *Cell* **104**, 83–93 (2001).
23. E. Karsenti, I. Vernos, *Science* **294**, 543–547 (2001).
24. R. E. Carazo-Salas, O. J. Gruss, I. W. Mattaj, E. Karsenti, *Nat. Cell Biol.* **3**, 228–234 (2001).
25. C. Klebe, F. R. Bischoff, H. Ponstingl, A. Wittinghofer, *Biochemistry* **34**, 639–647 (1995).
26. J. Dumont *et al*., *J. Cell Biol.* **176**, 295–305 (2007).
27. J. Cesario, K. S. McKim, *J. Cell Sci.* **124**, 3797–3810 (2011).
28. D. Cimini, B. Moree, J. C. Canman, E. D. Salmon, *J. Cell Sci.* **116**, 4213–4225 (2003).
29. T. S. Kitajima, M. Ohsugi, J. Ellenberg, *Cell* **146**, 568–581 (2011).
30. A. Obradors *et al*., *Cytogenet. Genome Res.* **133**, 119–126 (2011).

ACKNOWLEDGMENTS

We are grateful to the clinicians at Bourn Hall Clinic for their support of this study, the nursing team that was instrumental in recruiting patients and obtaining their informed consent, and the embryology team for identifying and preparing the test oocytes and for their enthusiastic support of this project from the outset. We thank T. Izzard for help in obtaining approval of this study by the UK's National Research Ethics Service, as well as S. Munro, R. Hegde, and D. Clift for comments on the manuscript. The research leading to these results has received financial support from the European Research Council under grant agreement no. 337415 and from the Lister Institute of Preventive Medicine. The data are contained in the manuscript and the supplementary materials.

SUPPLEMENTARY MATERIALS

www.sciencemag.org/content/348/6239/1143/suppl/DC1
Materials and Methods
Figs. S1 to S9
References (*31*–*35*)
Movies S1 to S6

19 February 2015; accepted 30 April 2015
10.1126/science.aaa9529

ELECTRON MICROSCOPY

2.2 Å resolution cryo-EM structure of β-galactosidase in complex with a cell-permeant inhibitor

Alberto Bartesaghi,[1*] Alan Merk,[1*] Soojay Banerjee,[1] Doreen Matthies,[1] Xiongwu Wu,[2] Jacqueline L. S. Milne,[1] Sriram Subramaniam[1†]

Cryo–electron microscopy (cryo-EM) is rapidly emerging as a powerful tool for protein structure determination at high resolution. Here we report the structure of a complex between *Escherichia coli* β-galactosidase and the cell-permeant inhibitor phenylethyl β-D-thiogalactopyranoside (PETG), determined by cryo-EM at an average resolution of ~2.2 angstroms (Å). Besides the PETG ligand, we identified densities in the map for ~800 water molecules and for magnesium and sodium ions. Although it is likely that continued advances in detector technology may further enhance resolution, our findings demonstrate that preparation of specimens of adequate quality and intrinsic protein flexibility, rather than imaging or image-processing technologies, now represent the major bottlenecks to routinely achieving resolutions close to 2 Å using single-particle cryo-EM.

Icosahedral viruses were the first biological assemblies whose structures were determined at near-atomic resolution using cryo–electron microscopy (cryo-EM) combined with methods for image averaging (*1*–*10*). Over the past 2 years, structures for a variety of nonviral assemblies have been reported using cryo-EM at resolutions between ~2.8 and ~4.5 Å (*11*–*20*). Four of these instances have been of complexes with sizes below 1 MD: the 700-kD proteasome at 3.3 Å (*16*) and 2.8 Å resolution (*17*), the 465-kD *Escherichia coli* β-galactosidase (β-Gal) at 3.2 Å resolution (*18*), the 440-kD anthrax protective antigen pore at 2.9 Å (*19*), and the 300-kD TrpV1 ion channel at 3.4 Å resolution (*20*). Because these structures are of complexes that are dispersed in the aqueous phase, the peripheral regions of the proteins are less ordered and are at lower resolution than the more central regions; nevertheless, most side-chain densities are clearly delineated in the well-ordered regions of the maps. In crystallographically determined structures of proteins at resolutions of 2.3 Å or better, features such as protein-ligand hydrogen bonding, salt bridges, and location of key structured water molecules can be ascertained with a high degree of confidence (*21*). There is great potential for the use of cryo-EM methods in applications such as drug discovery and development if similar resolutions could be achieved without crystallization. Whether there are fundamental limitations with currently available methods for specimen preparation, microscope hardware, inelastic scattering from the ice layer, inaccuracies in microscope alignment, detector technology, data collection procedures, or image processing software to achieve resolutions approaching 2 Å is a question that remains unanswered in the current context of rapid advances in the cryo-EM field (*22*). This is especially relevant for smaller protein complexes (<1 MD) with low symmetry, where the errors in alignment of the projection images make the analysis more challenging than for larger or more symmetric complexes such as ribosomes and ordered viruses (*23*).

We recently reported the structure of *E. coli* β-Gal at 3.2 Å resolution (*18*). Comparing the cryo-EM–derived structure with that derived from x-ray crystallography, we identified regions such as the periphery of the protein and crystal contact zones where there were measurable deviations between crystal and solution structures. To test whether we could further improve map resolution, we explored a range of experimental conditions including variations in specimen preparation, imaging, and steps in data processing (see supplementary materials and methods). We analyzed the structure of β-Gal bound to phenylethyl β-D-thiogalactopyranoside (PETG), a potent inhibitor that blocks enzyme activity by replacing the oxygen in the O-glycosidic bond with a sulfur atom. Although no crystal structure is available for the complex formed between *E. coli* β-Gal and PETG, a crystal structure is available for PETG bound to *Trichoderma reesei* β-Gal (*24*). There is, however, very little sequence similarity (sequence identity of 12.8% determined by Clustal 12.1) between the two variants, with the *T. reesei* variant displaying a completely different fold and crystallizing as a monomer instead of a tetramer (fig. S1).

Cryo-EM images recorded from plunge-frozen specimens of the β-Gal–PETG complex and the corresponding radially averaged power spectra were analyzed to select images displaying signal at high resolution (fig. S2, A to C). For each recorded image, we also assessed the extent of movement during the course of the ~8-s exposure

[1]Laboratory of Cell Biology, Center for Cancer Research, National Cancer Institute, National Institutes of Health, Bethesda, MD 20892, USA. [2]Laboratory of Computational Biology, National Heart, Lung, and Blood Institute, National Institutes of Health, Bethesda, MD 20892, USA.
*These authors contributed equally to this work. **†Corresponding author. E-mail: ss1@nih.gov**

(fig. S2D). From a data set of 1487 images that displayed detectable signal in the power spectra extending beyond 3 Å and that had low amounts of beam-induced movement during the exposure, we extracted 93,686 molecular images using automated particle-selection procedures using a Gaussian disk as a template. We used various combinations and subsets of the frames collected from each region and iteratively evaluated their contribution to map quality (fig. S3A). The final map, which we assessed as having the highest overall map quality, was obtained using the information in the images collected from ~12 electrons (e^-)/Å^2 of each exposure (Fig. 1A). We estimate the overall average resolution of the map to be ~2.2 Å, using both the 0.143 Fourier shell correlation (FSC) criterion, as well as the resolution at which an FSC obtained between the experimental cryo-EM map and the map computed from the map-derived cryo-EM atomic model has a value of 0.5 (fig. S3B). This was further supported by visual inspection of map quality (movie S1). The 2.2 Å mean resolution of our map indicates that some regions, such as at the periphery, are at lower resolution than 2.2 Å, whereas other regions closer to the center are at higher resolution, displaying features consistent with electron density maps from x-ray structures determined at resolutions of ~2 Å (fig. S4).

An overview of the density map for one of the four equivalent chains in the β-Gal complex and densities for regions from different portions of the molecule are shown in Fig. 1. The path of the polypeptide chain is well delineated, enabling placement of the sequence into the density map (Fig. 1, B to D). Examination of the map also shows clear densities for several backbone carbonyl groups and several ordered water molecules in the structure. We identified 194 densities in each protomer where we could place water molecules with confidence based on the shape of the local density, map value, and location at the right distance range for hydrogen bonding to polar groups in the vicinity. In the majority of instances, these water molecules are at locations also identified in the 1.7 Å crystal structure of β-Gal (Protein Data Bank ID 1DP0), providing independent validation of their assignment. Selected examples of tightly bound water molecules in the structure are shown in Fig. 2, illustrating instances where they are present in connected chains, coordinated to multiple polar residues, coordinated to the polypeptide backbone, or coordinated to the Mg^{2+} ion in the active site. The fact that water molecules can be placed with confidence in a structure of a 465-kD complex determined by single-particle cryo-EM is an exciting advance that bodes well for the use of cryo-EM in drug-discovery applications.

The cryo-EM map includes density for PETG in the active site (Fig. 3A). The key catalytic residues Glu^{461} (general base for acid catalysis), coordinating to the Mg^{2+} ion, and Glu^{537} (nucleophile) are in close proximity to the ligand, with density for a structured water molecule visible in the binding pocket. In addition, other residues that stabilize the binding of the inhibitor (Asn^{102}, Asp^{201}, Met^{502}, Tyr^{503}, His^{540}, Asp^{598}, Phe^{601}, Val^{795}, and Trp^{999}) also show appropriate steric dispositions, as displayed in Fig. 3B. There are substantial differences in the orientation and location of the PETG molecule in the *T. reesei* enzyme (Fig. 3C), with rotation of the benzyl moiety around the S–C-7 single bond by almost 180°. This is perhaps not unexpected, given that there is very little overall structural similarity between the enzymes from these two species (fig. S1) and the pattern of residues that are involved in H-bonding to the ligand are also different (Fig. 3, B and D). Stereochemical parameters of the key conserved catalytic residues (Glu^{200} and Glu^{298}) in the *T. reesei* complex are different from those in the *E. coli* complex, as are the general distribution of nonpolar residues that stabilize the inhibitor in the pocket, establishing the value of direct determination of the actual structure of the ligand in a protein complex, even when a related structure is available.

In Fig. 4, we show examples of the densities observed for each of the 20 standard amino acids, where the level of detail at which individual C, N, and O atoms are observed is consistent with maps derived from x-ray crystallography at nominal resolutions of ~2 Å (fig. S4). However, in contrast to a $2F_{obs} - F_{calc}$ map obtained by x-ray crystallography, both phases and amplitudes of cryo-EM density maps are derived experimentally from the images, eliminating the need to assign phases derived from the atomic model, as is customarily done in x-ray crystallography. As a consequence, density contours in cryo-EM maps are subject to inaccuracies from

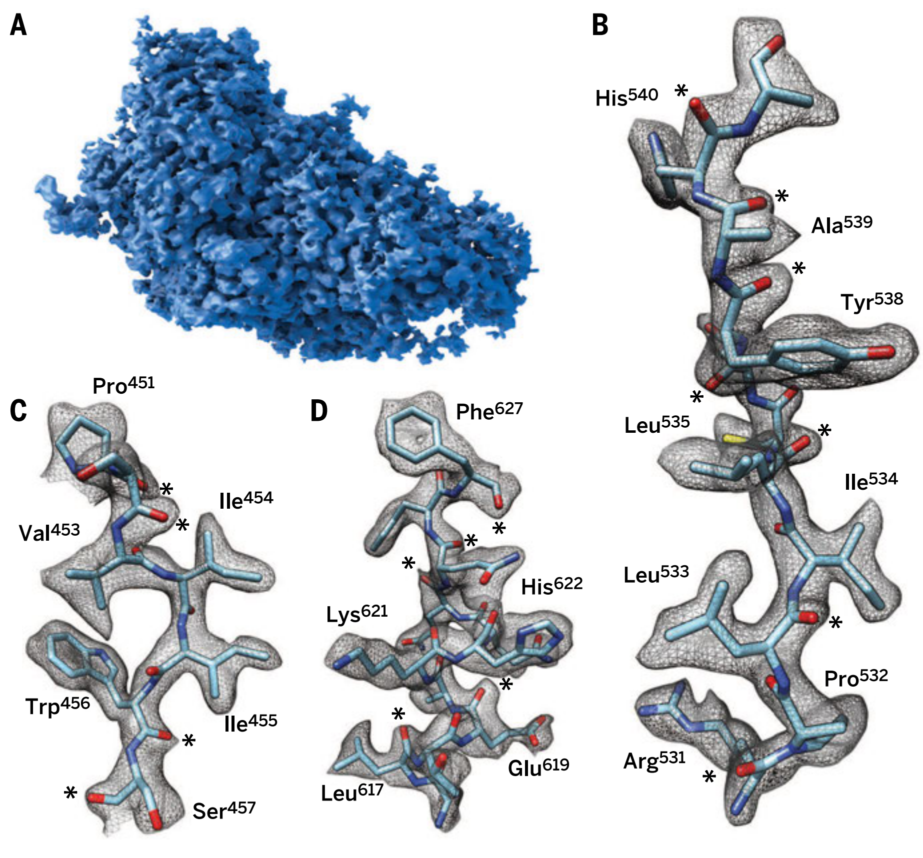

Fig. 1. Cryo-EM density map of the β-Gal–PETG complex at 2.2 Å resolution. (**A**) Surface representation of the density map of one of the four protomers in the tetrameric complex. (**B** to **D**) Visualization of selected map regions showing delineation of secondary structural elements, amino acid densities, and carbonyl moieties (indicated by asterisks). The density for Phe^{627} is thinned out in the center of the aromatic ring, revealing the presence of a "hole" in the ring, a feature typically observed in structures determined by x-ray crystallography at resolutions of ~2 Å.

a number of resolution-lowering distortions (instances of which are visible in Fig. 4A) that can arise at various stages of data collection and processing. Factors that can contribute to distortions include inaccuracies in determination of the contrast transfer function for each image, errors in orientation determination during refinement, distinct patterns of radiation damage in each of the molecular images used for reconstruction, and the changes introduced from applying a uniform temperature factor correction to scale the map. Despite these distortions, which appear to be random, the overall shape of the residues can nevertheless be distinguished clearly. As more structures are determined at these higher resolutions, it is possible that there may be enough statistical basis to study these distortions quantitatively, and perhaps exploit patterns that may emerge from this analysis to improve refinement strategies to achieve even higher resolution.

The data collection schemes currently used in cryo-EM with direct electron detectors enable the use of numerous combinations in which the dose can be fractionated during the exposure, as well as a number of ways in which different subsets of the frames collected for each exposure can be combined to generate a three-dimensional (3D) reconstruction. The map we present in Figs. 1 to 4 was obtained from a subset that excludes the very early portion of the exposure, uses the next 12 $e^{-}/Å^{2}$, and excludes the latter part of the exposure. In the course of our studies, we analyzed many different maps constructed by using different subsets of the exposure. The highest-resolution features, such as holes in the rings of the aromatic residues (Fig. 4 and fig. S4), were better resolved in maps constructed using the interval of the exposure containing the highest-resolution information (fig. S3A).

Based on our present analysis and its comparison with our earlier cryo-EM structure of β-Gal at 3.2 Å resolution, we can now articulate our best understanding of all of the changes that we introduced that enabled us to improve the resolution to ~2.2 Å. Perhaps the most important is the much more careful selection of regions where the ice was thin enough to obtain the highest detectable signals yet thick enough to allow a spread of orientations (as judged by the distribution of orientations assigned to each molecular image used to construct the final map). Second, the use of a lower dose rate to minimize the effects of coincidence loss of the detector and the use of a finer pixel size resulted in improved image contrast and maximization of amplitudes at low resolution (*25*), which allowed us to go to closer to focus and still be able to correctly pick and align particles. Third, we carried out 3D classification throughout the iterative refinement cycle, which we did not do in the case of the structure at 3.2 Å resolution. Finally, we believe that the use of nearest-neighbor interpolation during motion correction, coupled with better-quality data, allowed improved recovery of higher-resolution information in the final reconstruction.

X-ray crystallographic methods have led to the deposition of almost 95,000 atomic-resolution protein and protein-nucleic acid structures over the past few decades. There have been impressive advances in speed and resolution, as well as in the development of highly automated workflows over the years. Relative to those of the x-ray field, cryo-EM methods are still in an early phase of development, with only ~30 deposited models for coordinates derived from electron microscopic analysis at near-atomic resolution. The recent progress by many groups worldwide suggests that this number will increase rapidly and will extend to specimens that may not be easily amenable to crystallization. Our demonstration here that the structure of a ligand-protein complex can be determined in the solution phase at resolutions close to 2 Å suggests that cryo-EM is positioned to become an indispensable tool in structural biology and for drug-discovery applications.

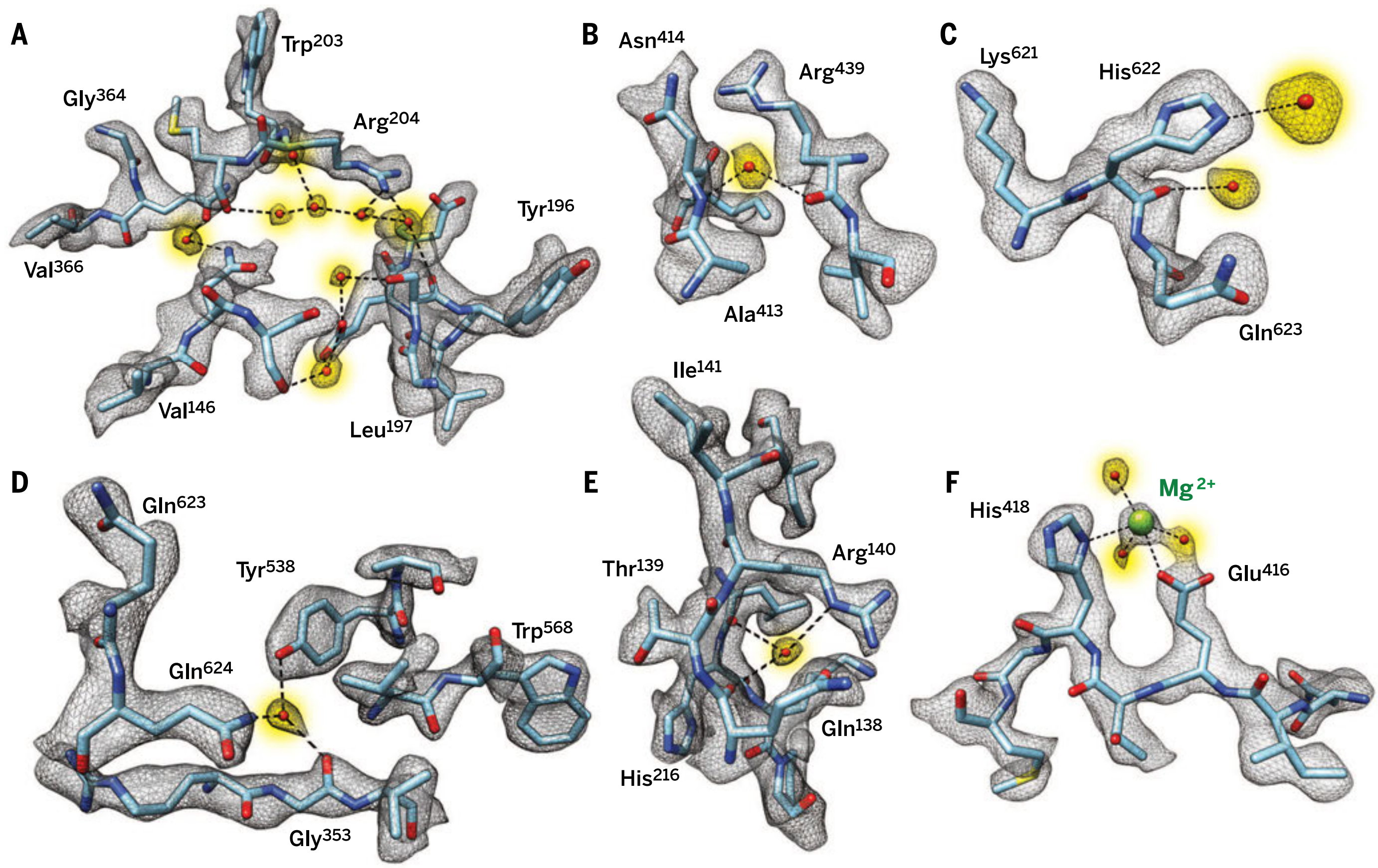

Fig. 2. Visualization of tightly bound water molecules in the structure of the β-Gal–PETG complex. (**A** to **F**) Selected examples of densities for water molecules (highlighted in yellow) hydrogen bonded in pearl-string–like chains (A), connected to the polypeptide backbone and multiple amino acid side chains [(B) to (E)], or interacting with the Mg^{2+} ion in the active site (F).

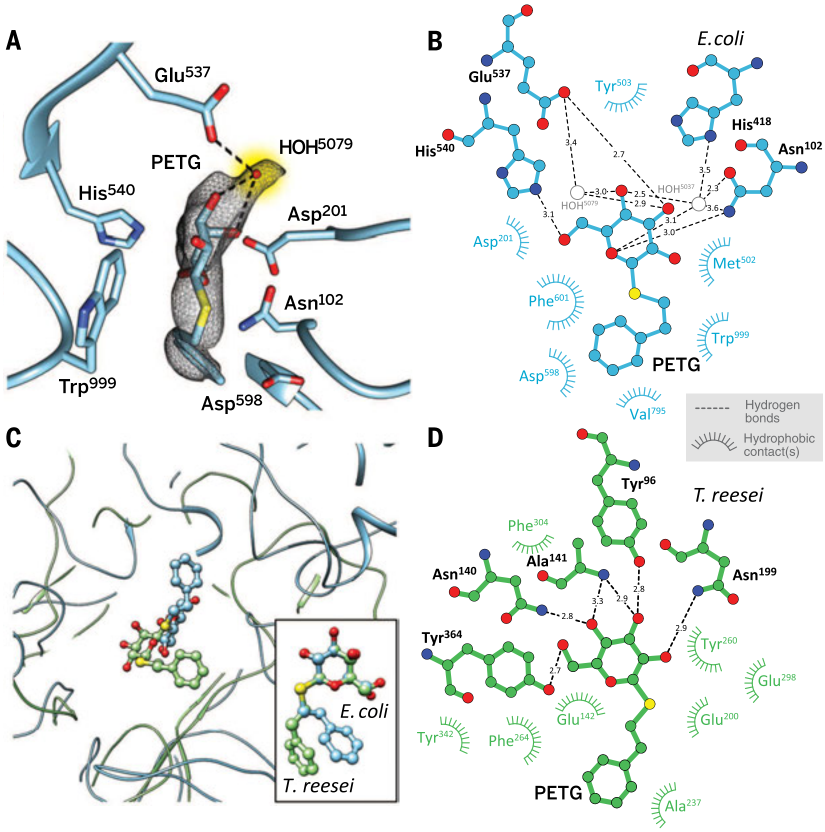

Fig. 3. Active-site structure in PETG-liganded *E. coli* β-Gal. (**A**) Uncorrected cryo-EM density map showing density for PETG, an associated water molecule, and six of the amino acids that line the binding pocket. (**B**) Plot of distances of various parts of PETG to residues in the vicinity of β-Gal from *E. coli*, determined using LIGPLOT (www.ebi.ac.uk/thornton-srv/software/LIGPLOT/). (**C**) Superposition of the ligand binding pocket structures in β-Gal from *E. coli* (light blue, determined by cryo-EM at 2.2 Å resolution) and *T. reesei* (green, determined by x-ray crystallography at 1.4 Å resolution), illustrating the differences in protein and ligand structures. (Inset) Comparison between the corresponding configurations of PETG. (**D**) Plot of distances of various parts of PETG to amino acids in the vicinity of β-Gal from *T. reesei*, determined using LIGPLOT.

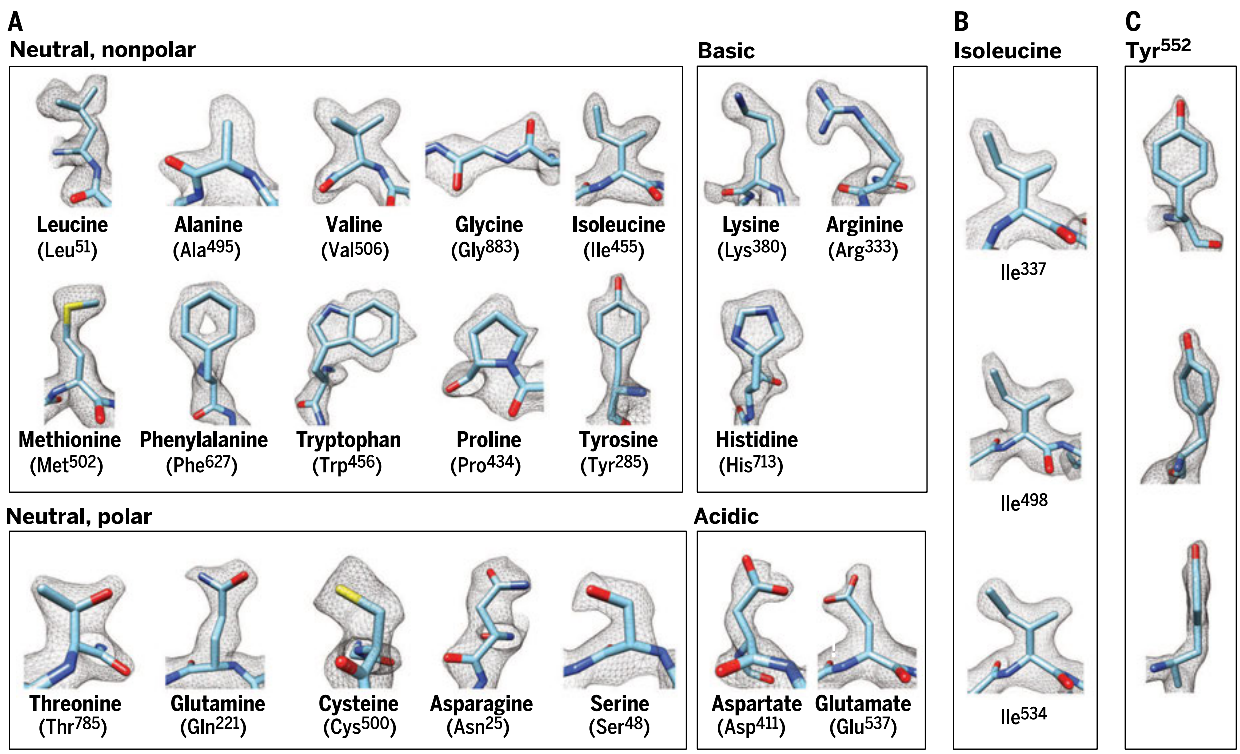

Fig. 4. Illustration of map quality at the level of amino acids. (**A**) Visualization of map density for examples of each of the 20 standard amino acids, which are grouped into neutral (nonpolar and polar), basic, and acidic categories. (**B** and **C**) Illustration of contours of densities for multiple Ile residues (B) and front, tilted, and edge views for Tyr^{552} (C). In each case, the density contours are consistent with the 2.2 Å resolution we report.

REFERENCES AND NOTES

1. N. Grigorieff, S. C. Harrison, *Curr. Opin. Struct. Biol.* **21**, 265–273 (2011).
2. F. Guo *et al.*, *Proc. Natl. Acad. Sci. U.S.A.* **111**, E4606–E4614 (2014).
3. H. Liu *et al.*, *Science* **329**, 1038–1043 (2010).
4. X. Liu *et al.*, *Nat. Struct. Mol. Biol.* **17**, 830–836 (2010).
5. E. C. Settembre, J. Z. Chen, P. R. Dormitzer, N. Grigorieff, S. C. Harrison, *EMBO J.* **30**, 408–416 (2011).
6. Z. Wang *et al.*, *Nat. Commun.* **5**, 4808 (2014).
7. M. Wolf, R. L. Garcea, N. Grigorieff, S. C. Harrison, *Proc. Natl. Acad. Sci. U.S.A.* **107**, 6298–6303 (2010).
8. X. Yu, P. Ge, J. Jiang, I. Atanasov, Z. H. Zhou, *Structure* **19**, 652–661 (2011).
9. X. Zhang *et al.*, *Nat. Struct. Mol. Biol.* **20**, 105–110 (2013).
10. X. Zhang, L. Jin, Q. Fang, W. H. Hui, Z. H. Zhou, *Cell* **141**, 472–482 (2010).
11. X. C. Bai, I. S. Fernandez, G. McMullan, S. H. Scheres, *eLife* **2**, e00461 (2013).
12. A. Amunts *et al.*, *Science* **343**, 1485–1489 (2014).
13. B. J. Greber *et al.*, *Nature* **515**, 283–286 (2014).
14. P. Lu *et al.*, *Nature* **512**, 166–170 (2014).
15. N. Fischer *et al.*, *Nature* **520**, 567–570 (2015).
16. X. Li *et al.*, *Nat. Methods* **10**, 584–590 (2013).
17. M. G. Campbell, D. Veesler, A. Cheng, C. S. Potter, B. Carragher, *eLife* **4**, e06380 (2015).
18. A. Bartesaghi, D. Matthies, S. Banerjee, A. Merk, S. Subramaniam, *Proc. Natl. Acad. Sci. U.S.A.* **111**, 11709–11714 (2014).
19. J. Jiang, B. L. Pentelute, R. J. Collier, Z. H. Zhou, *Nature* 10.1038/nature14247 (2015).
20. M. Liao, E. Cao, D. Julius, Y. Cheng, *Nature* **504**, 107–112 (2013).
21. T. L. Blundell, H. Jhoti, C. Abell, *Nat. Rev. Drug Discov.* **1**, 45–54 (2002).
22. D. Agard, Y. Cheng, R. M. Glaeser, S. Subramaniam, in *Advances in Imaging and Electron Physics*, P. W. Hawkes, Ed. (Elsevier, Amsterdam, 2014), chap. 2, pp. 113–137.
23. R. Henderson, *Q. Rev. Biophys.* **28**, 171–193 (1995).
24. M. Maksimainen *et al.*, *J. Struct. Biol.* **174**, 156–163 (2011).
25. X. Li *et al*, *J. Struct. Biol.* **184**, 251–260 (2013).

ACKNOWLEDGMENTS

This research was supported by funds from the Intramural Research Program of the NIH, Center for Cancer Research, National Cancer Institute, and the Intramural AIDS Targeted Antiviral Program. We thank R. Mueller and J. Cometa for technical assistance with electron microscopy, P. Mooney and F. Ulmer for advice and assistance with optimizing detector performance, K. Podolsky for assistance with data collection, J.-J. Fernandez for providing the code to run the TOMOCTFFIND program, and V. Falconieri for assistance in preparation of the figures and the supplementary movie. This study used the high-performance computational capabilities of the Biowulf Linux cluster at NIH (http://biowulf.nih.gov). The density map and refined atomic model have been deposited with the Electron Microscopy Data Bank (accession number EMD-2984) and the Protein Data Bank (entry code 5a1a), respectively.

SUPPLEMENTARY MATERIALS

www.sciencemag.org/content/348/6239/1147/suppl/DC1
Materials and Methods
Figs. S1 to S4
References (*26–34*)
Movie S1

20 March 2015; accepted 29 April 2015
Published online 7 May 2015;
10.1126/science.aab1576

NEURODEGENERATION

C9ORF72 repeat expansions in mice cause TDP-43 pathology, neuronal loss, and behavioral deficits

Jeannie Chew,[1,2] Tania F. Gendron,[1] Mercedes Prudencio,[1] Hiroki Sasaguri,[1] Yong-Jie Zhang,[1] Monica Castanedes-Casey,[1] Chris W. Lee,[1] Karen Jansen-West,[1] Aishe Kurti,[1] Melissa E. Murray,[1] Kevin F. Bieniek,[1,2] Peter O. Bauer,[1] Ena C. Whitelaw,[1] Linda Rousseau,[1] Jeannette N. Stankowski,[1] Caroline Stetler,[1] Lillian M. Daughrity,[1] Emilie A. Perkerson,[1] Pamela Desaro,[3] Amelia Johnston,[3] Karen Overstreet,[3] Dieter Edbauer,[4,5,6] Rosa Rademakers,[1,2] Kevin B. Boylan,[3] Dennis W. Dickson,[1,2] John D. Fryer,[1,2] Leonard Petrucelli[1,2]*

The major genetic cause of frontotemporal dementia and amyotrophic lateral sclerosis is a G_4C_2 repeat expansion in *C9ORF72*. Efforts to combat neurodegeneration associated with "c9FTD/ALS" are hindered by a lack of animal models recapitulating disease features. We developed a mouse model to mimic both neuropathological and clinical c9FTD/ALS phenotypes. We expressed $(G_4C_2)_{66}$ throughout the murine central nervous system by means of somatic brain transgenesis mediated by adeno-associated virus. Brains of 6-month-old mice contained nuclear RNA foci, inclusions of poly(Gly-Pro), poly(Gly-Ala), and poly(Gly-Arg) dipeptide repeat proteins, as well as TDP-43 pathology. These mouse brains also exhibited cortical neuron and cerebellar Purkinje cell loss, astrogliosis, and decreased weight. $(G_4C_2)_{66}$ mice also developed behavioral abnormalities similar to clinical symptoms of c9FTD/ALS patients, including hyperactivity, anxiety, antisocial behavior, and motor deficits.

An intronic G_4C_2 repeat expansion in the chromosome 9 open reading frame 72 (*C9ORF72*) gene is the major genetic cause of frontotemporal dementia (FTD) and amyotrophic lateral sclerosis (ALS) (*1*, *2*). Although FTD and ALS are characterized, respectively, by cognitive and behavioral symptoms and by motor symptoms, there is clinical and neuropathological overlap between the two diseases. The precise mechanisms by which the *C9ORF72* mutation contributes to "c9FTD/ALS" remain elusive, but toxicity mediated by RNA bidirectionally transcribed from the expansion [$r(G_4C_2)_{exp}$ and $r(G_2C_4)_{exp}$] is thought to play an important role (*3–12*). Repeat-containing transcripts form intranuclear RNA foci believed to sequester various RNA-binding proteins (*8*, *9*, *11*, *13–17*), and they are also susceptible to repeat-associated non-ATG (RAN) translation resulting in the synthesis of "c9RAN proteins" of repeating dipeptides (*18–21*). Despite advances made toward elucidating c9FTD/ALS pathogenesis, many questions remain because of the lack of mouse models recapitulating key disease features.

To investigate the neurotoxic effects linked to the expanded G_4C_2 repeat and to create a model for testing new therapies in vivo, we sought to generate mice that develop clinical and pathological features of c9FTD/ALS. We used an adeno-associated viral vector to mediate robust expression of either 2 or 66 G_4C_2 repeats, lacking an ATG start codon, in the central nervous system (CNS) of mice. Six months after intracerebroventricular (ICV) administration of AAV2/9-$(G_4C_2)_{66}$ (n = 11) or AAV2/9-$(G_4C_2)_2$ (n = 12) to postnatal day 0 mice, which results in predominantly neuronal transduction (*22*), a thorough characterization of the mice was undertaken.

To assess whether RNA foci are formed in $(G_4C_2)_{66}$ mice, we performed RNA fluorescence in situ hybridization using a probe against $r(G_4C_2)$. As anticipated, no foci were detected in control $(G_4C_2)_2$ mice (Fig. 1A), but nuclear foci were detected throughout the CNS of $(G_4C_2)_{66}$ mice (Fig. 1, B to E), reminiscent of those observed in c9FTD/ALS patients (Fig. 1, F and G). Foci were present across all layers of the cortex (Fig. 1B), in Purkinje cells of the cerebellum (Fig. 1C), in the CA1 to CA3 fields of the hippocampus (Fig. 1D), and in the thalamus (table S1). Foci were also observed, albeit to a lesser extent, in the ventral horn of the spinal cord (Fig. 1E), as well as in the hippocampal dentate gyrus, cerebellar granular and molecular layers, and the amygdala (table S1). The number of foci-positive cells ranged from 40 to 54% in the cortex, motor cortex, hippocampus, and cerebellar Purkinje layer (Fig. 1H).

To investigate RAN translation in $(G_4C_2)_{66}$ mice, we first used a poly(Gly-Pro) [poly(GP)]

[1]Department of Neuroscience, Mayo Clinic, 4500 San Pablo Road, Jacksonville, FL 32224, USA. [2]Neurobiology of Disease Graduate Program, Mayo Graduate School, Mayo Clinic College of Medicine, Rochester, MN 55905, USA. [3]Department of Neurology, Mayo Clinic, 4500 San Pablo Road, Jacksonville, FL 32224, USA. [4]German Center for Neurodegenerative Diseases (DZNE) Munich, Feodor-Lynen-Strasse 17, 81337 Munich, Germany. [5]Institute for Metabolic Biochemistry, Ludwig-Maximilians University Munich, Feodor-Lynen-Strasse 17, 81337 Munich, Germany. [6]Munich Cluster of Systems Neurology (SyNergy), Munich, Germany.
***Corresponding author. E-mail: petrucelli.leonard@mayo.edu**

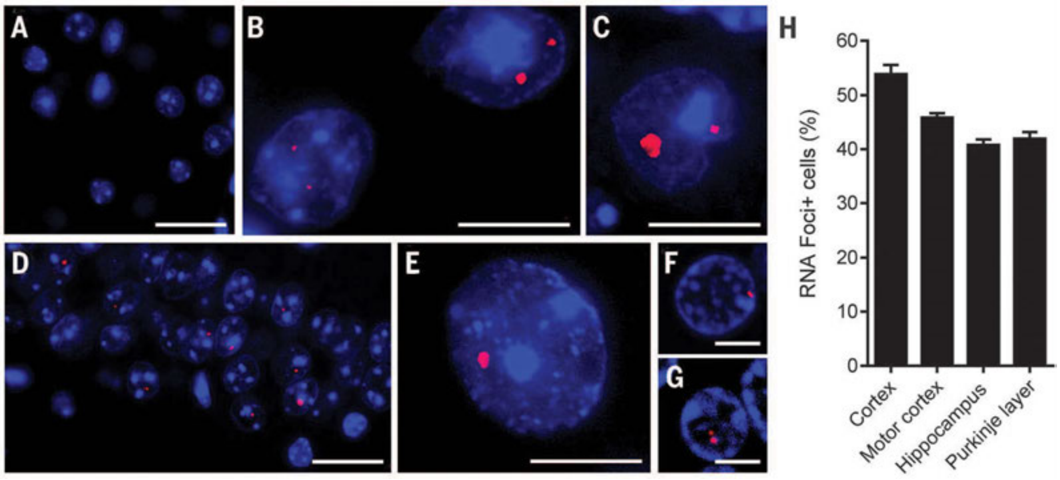

Fig. 1. Intranuclear RNA foci were detected in the CNS of $(G_4C_2)_{66}$ mice. The presence of $r(G_4C_2)$ RNA foci in brain and spinal cord of 6-month-old $(G_4C_2)_2$ and $(G_4C_2)_{66}$ mice was evaluated by RNA fluorescence in situ hybridization. (**A**) Foci were not detected in $(G_4C_2)_2$ mice; shown is a representative image of the cortex. (**B** to **G**) In $(G_4C_2)_{66}$ mice, RNA foci were detected in various regions—including the cortex (B), cerebellum (C), hippocampus (D), and spinal cord (E)—and were similar to foci observed in the cortex (F) and cerebellum (G) of c9FTD/ALS patients. (**H**) The average percentage of cells containing nuclear RNA foci in the indicated brain regions of $(G_4C_2)_{66}$ mice (n = 11) was calculated. The total number of cells counted per region was 500 for cortex, motor cortex, and hippocampus (CA1 to CA3) and 100 for Purkinje cells. Scale bars: (A), (D), (F), and (G), 25 μm; (B), (C), and (E), 10 μm.

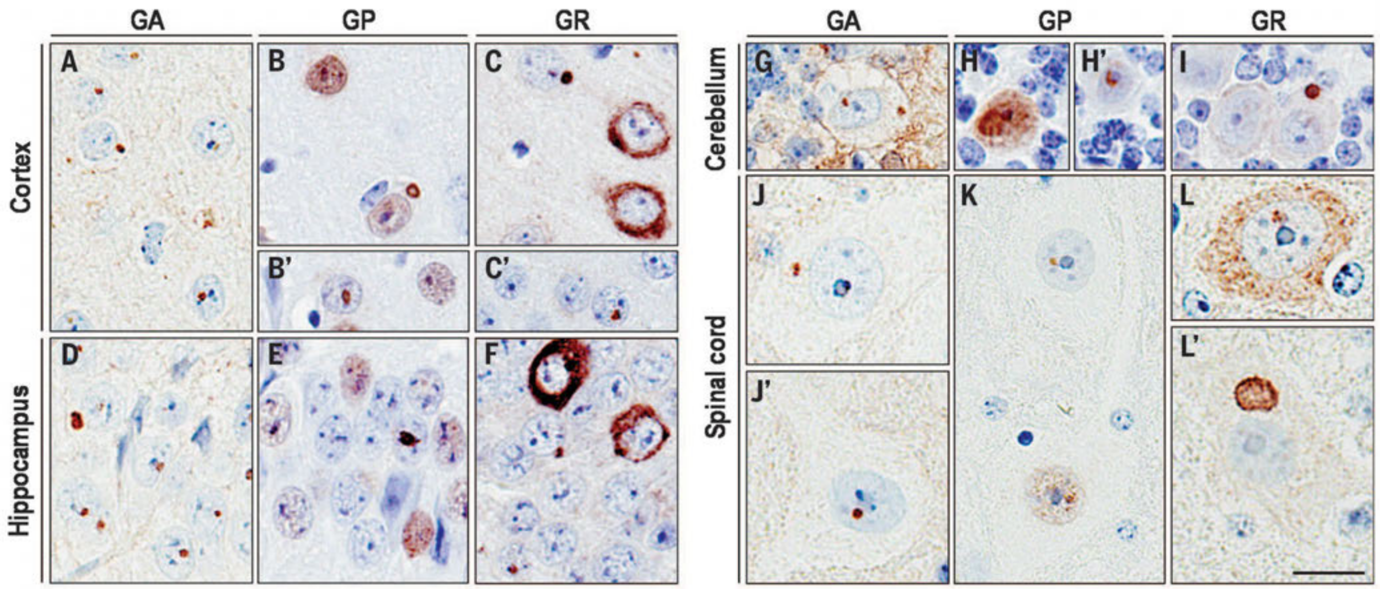

Fig. 2. c9RAN protein pathology was detected throughout the CNS of $(G_4C_2)_{66}$ mice. Intranuclear and cytoplasmic inclusions immunopositive for poly(GA), poly(GP), or poly(GR) were observed in various regions of the CNS of 6-month-old $(G_4C_2)_{66}$ mice, including the cortex (**A** to **C′**), hippocampus (**D** to **F**), cerebellum (**G** to **I**), and spinal cord (**J** to **L′**). Note also the diffuse nuclear poly(GP) staining [(B), (B′), (E), (H), and (K)] and diffuse cytoplasmic poly(GR) staining [(C), (F), and (L)]. Semiquantitative analysis of c9RAN protein staining in different neuroanatomical regions is provided in table S1. No c9RAN proteins were detected in 6-month-old control $(G_4C_2)_2$ mice (fig. S3). Scale bar, 20 μm.

immunoassay and observed robust poly(GP) expression in brain homogenates of $(G_4C_2)_{66}$ mice but not $(G_4C_2)_2$ mice (fig. S1). In addition, c9RAN protein inclusions were specifically expressed in the CNS of $(G_4C_2)_{66}$ mice (Fig. 2 and fig. S2), as seen in c9FTD/ALS patients (fig. S3). Indeed, $r(G_4C_2)_{66}$ was RAN translated in all frames. In the cortex and hippocampus of $(G_4C_2)_{66}$ mice, and less frequently in the cerebellum and spinal cord, globular poly(Gly-Ala) [poly(GA)], poly(GP), or poly(Gly-Arg) [poly(GR)] inclusions were detected most frequently in the nucleus, but cytoplasmic inclusions were also present. We also observed cells with diffuse nuclear poly(GP) staining and diffuse cytoplasmic poly(GR) staining. On the basis of semiquantitative analysis, cells immunopositive for poly(GA) or poly(GP) were more frequent than those immunopositive for poly(GR) (table S1), consistent with c9FTD/ALS c9RAN protein pathology (*23*). The majority of c9RAN protein inclusions in $(G_4C_2)_{66}$ mice were ubiquitin-positive (fig. S4), as in c9FTD/ALS (*24*), and localized to microtubule-associated protein 2–positive neurons but rarely to glial fibrillary acidic protein (GFAP)–positive cells (fig. S5). About 70% of cortical cells immunopositive for poly(GP) inclusions also contained at least one RNA focus (fig. S6).

Inclusions of phosphorylated TDP-43 (pTDP-43) are yet another neuropathological feature of c9FTD/ALS (Fig. 3, A and A′) (*23*). Remarkably, nuclear, and occasionally cytoplasmic, inclusions of endogenous pTDP-43 were observed in the cortex (Fig. 3, B and B′) and hippocampus (Fig. 3C) of $(G_4C_2)_{66}$ mice that were present in about 7 to 8% of cells (Fig. 3E) but were not observed in $(G_4C_2)_2$ mice (Fig. 3D). Immunoblot analysis of hemibrain urea fractions confirmed the presence of insoluble pTDP-43 in $(G_4C_2)_{66}$ mice (Fig. 3F). Insoluble pTDP-43 was predominantly monomeric, but oligomers of ~80 kD were also observed. The high-molecular-

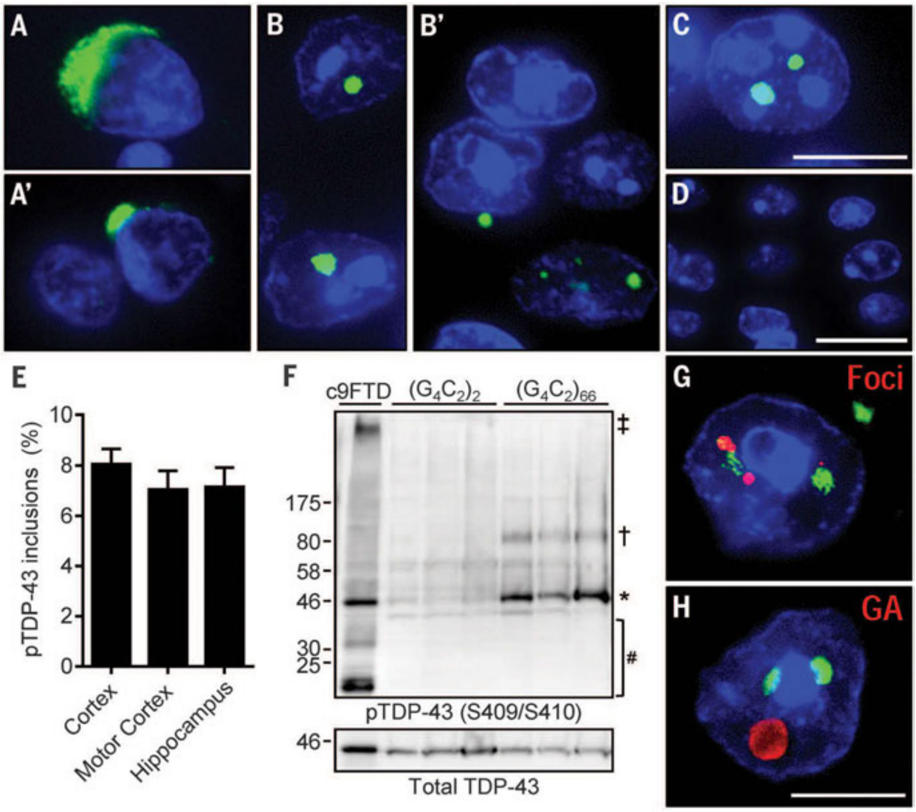

Fig. 3. $(G_4C_2)_{66}$ mice developed inclusions composed of pTDP-43. (**A** and **A′**) Representative pTDP-43 inclusions in postmortem c9FTD/ALS frontal cortex sections. (**B** to **D**) Similarly, multiple cells with nuclear, and occasionally cytoplasmic pTDP-43, inclusions were observed in the cortex (B and B′) and hippocampus (C) of 6-month-old $(G_4C_2)_{66}$ mice. No pTDP-43 immunoreactivity was detected in control $(G_4C_2)_2$ mice; shown is a representative image of the cortex (D). (**E**) The average percentage of cells with pTDP-43 inclusions in the indicated regions was calculated on the basis of evaluations of 500 cells per mouse (n = 6 mice). (**F**) pTDP-43 was detected in brain urea fractions from $(G_4C_2)_{66}$ mice and a c9FTD patient but not from $(G_4C_2)_2$ mice. Symbols: ‡high molecular weight species; †oligomers; *full-length protein; #cleavage products. (**G**) Of 250 cells containing pTDP-43 inclusions examined among five $(G_4C_2)_{66}$ mice, all were found to contain nuclear foci. (**H**) Of 250 cells containing pTDP-43 inclusions examined among five $(G_4C_2)_{66}$ mice, ~75% were found to be positive for poly(GA) inclusions. Nuclei are stained blue in (A) to (D), (G), and (H). Scale bars: (A) to (C), (G), and (H), 10 μm; (D), 20 μm.

weight or truncated pTDP-43 species seen in c9FTD were not detected in $(G_4C_2)_{66}$ mice under these conditions. Of the 250 cortical cells with pTDP-43 pathology examined among five $(G_4C_2)_{66}$ mice, all harbored at least one nuclear RNA focus (Fig. 3G). Similarly, ~75% of cells with pTDP-43 pathology also contained poly(GA) inclusions. Despite the coexistence of both proteins in a given cell, they did not localize to the same inclusions (Fig. 3H).

Next, we evaluated whether expression of the expanded repeat caused neurodegeneration and gliosis. In $(G_4C_2)_{66}$ mice, the number of NeuN-positive neurons in the whole cortex and motor cortex was significantly reduced by 17% and 23%, respectively (Fig. 4, A to F), and 11% fewer Purkinje cells were present in the cerebellum (fig. S7, A to C). No such cell loss was observed in the hippocampus, thalamus, or spinal cord. Immunoreactivity for GFAP, a marker of reactive gliosis, was increased in the cortex of $(G_4C_2)_{66}$ mice (fig. S7, D to F).

To determine whether the combination of pathological features described above affected behavior, 6-month-old $(G_4C_2)_2$ and $(G_4C_2)_{66}$ mice were subjected to a battery of behavioral tasks. At this time point, no significant difference in body weight was detected between male mice expressing 2 or 66 repeats, but female $(G_4C_2)_{66}$ mice exhibited an 11% decrease in body weight compared with female $(G_4C_2)_2$ mice (fig. S8A). A modest, but statistically significant, decrease in brain weight in $(G_4C_2)_{66}$ mice was evident (fig. S8B), which again suggested that the expanded repeat caused brain atrophy. The open-field assay can be used to evaluate general locomotor activity, exploration, and anxiety-like behavior in a novel environment. $(G_4C_2)_{66}$ mice showed a decreased tendency to explore the center of the open field (Fig. 4, G and H), which is suggestive of anxiety-like behavior. $(G_4C_2)_{66}$ mice also traveled a longer distance in comparison with $(G_4C_2)_2$-expressing mice (Fig. 4I) and at a greater speed (fig. S8C), indicative of hyperactivity. Such hyperactivity has been linked to behavioral disinhibition in a mouse model of Alzheimer's disease (*25*).

To examine whether the behavioral phenotype of $(G_4C_2)_{66}$ mice includes a social component, we used a three-chamber social interaction test. This test assesses the active interaction time of the test mouse, with a novel probe mouse housed in a cylinder within one of the chambers and an empty cylinder in the opposite chamber. Compared with $(G_4C_2)_2$ mice, $(G_4C_2)_{66}$ mice spent more time in the chamber with the empty cylinder than in the chamber containing the probe mouse (Fig. 4J), which suggested social abnormalities.

Finally, motor coordination and balance of mice were evaluated using the Rota-Rod test in which mice have to keep their balance on a rotating rod. Although no significant difference in time spent on the rod before falling off was seen between $(G_4C_2)_{66}$ and $(G_4C_2)_2$ mice on the first day of testing, from the second day onward $(G_4C_2)_{66}$ mice fell significantly faster, which is indicative of motor impairments (Fig. 4K).

Here, we found that mice expressing $(G_4C_2)_{66}$ throughout the CNS developed RNA foci, ubiquitin-positive inclusions of c9RAN proteins, and pTDP-43 inclusions, as well as cortical neuron and cerebellar Purkinje cell loss. These abnormalities likely contributed to the behavioral phenotype of $(G_4C_2)_{66}$ mice that suggested the disinhibition, anxiety, impaired social cognition, and motor skill deficits observed in c9FTD/ALS patients (*26*). These data demonstrate that the expression of expanded sense G_4C_2 repeats is sufficient to cause neuropathological changes and neurodegeneration; however, additional studies are required to determine the contribution of antisense repeats to disease.

$(G_4C_2)_{66}$ mice should prove valuable in deciphering pathomechanisms associated with the *C9ORF72* repeat expansion. Indeed, the observation of pTDP-43 inclusions in $(G_4C_2)_{66}$ mice suggests that the repeat expansion is an initiator of TDP-43 pathology. Because all examined cells with TDP-43 pathology were found to contain foci, repeat-containing RNA or the foci themselves may be responsible for instigating TDP-43 abnormalities. As $(G_4C_2)_{66}$ mice recapitulate neuropathological and clinical phenotypes of c9FTD/ALS, they also offer an attractive model for testing potential therapeutics targeting $r(G_4C_2)_{exp}$, such as antisense oligonucleotides (*8*, *11*, *12*) and small molecules (*27*). In fact, our findings suggest that such approaches may not only mitigate foci formation and RAN translation, they may also alleviate TDP-43–mediated toxicity.

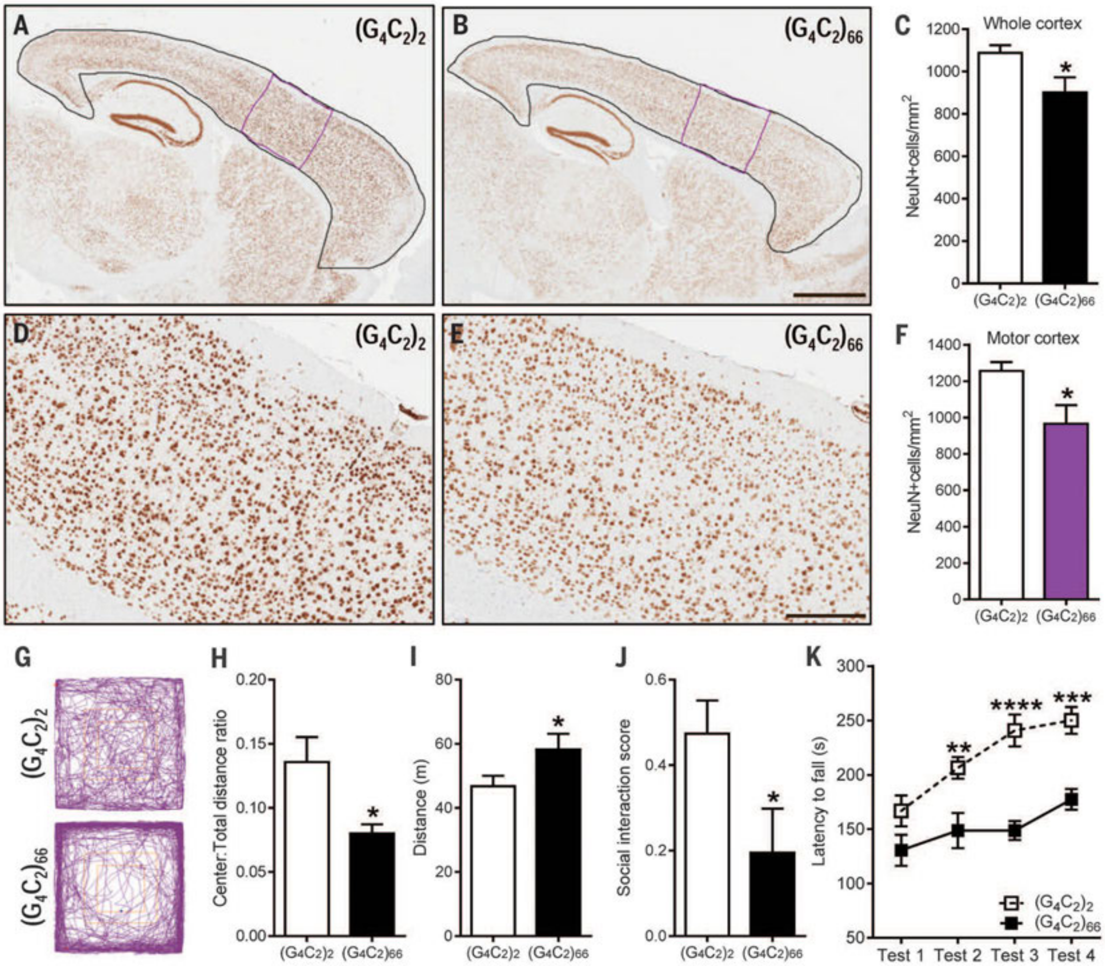

Fig. 4. $(G_4C_2)_{66}$ mice developed cortical neuron loss and exhibited behavior and motor deficits at 6 months of age. (**A** and **B**) Representative images of NeuN-labeled cells in the cortex of $(G_4C_2)_2$ mice (n = 6) and $(G_4C_2)_{66}$ mice (n = 6). (**C**) Quantification of NeuN-positive cells in the whole cortex [area delineated in black in (A) and (B)]. (**D** and **E**) Enhanced magnification of the motor cortex [area delineated in purple in (A) and (B)]. (**F**) Quantification of NeuN-positive cells in the motor cortex. (**G** to **I**) In the open-field test, $(G_4C_2)_{66}$ mice (n = 11) displayed signs of increased anxiety-like behavior compared with $(G_4C_2)_2$ mice (n = 12), as evidenced by representative traces (G) and a significant decrease in distance traveled in the center area normalized to total distance traveled (H). $(G_4C_2)_{66}$ mice traveled a greater distance overall (I), which is indicative of hyperactivity. (**J**) In the social interaction test, $(G_4C_2)_{66}$ mice had a decreased interaction score, which is indicative of social deficits. (**K**) Motor deficits, manifesting as a decreased latency to fall from a rotating rod, were observed in $(G_4C_2)_{66}$ mice on test day 2 to 4 of the Rota-Rod test. Scale bars: (A) and (B), 1 mm; (D) and (E), 300 μm. Data are presented as means ± SEM; *P < 0.05, unpaired, two-tailed Student's t-test. ****P < 0.0001, ***P < 0.001, **P < 0.01, two-way analysis of variance followed by Sidak's multiple comparisons test. Abbreviated units: m, meters; s, seconds.

REFERENCES AND NOTES

1. M. DeJesus-Hernandez *et al.*, *Neuron* **72**, 245–256 (2011).
2. A. E. Renton *et al.*, *Neuron* **72**, 257–268 (2011).
3. S. Mizielinska *et al.*, *Science* **345**, 1192–1194 (2014).
4. Y. J. Zhang *et al.*, *Acta Neuropathol.* **128**, 505–524 (2014).
5. S. May *et al.*, *Acta Neuropathol.* **128**, 485–503 (2014).
6. I. Kwon *et al.*, *Science* **345**, 1139–1145 (2014).
7. X. Wen *et al.*, *Neuron* **84**, 1213–1225 (2014).
8. C. J. Donnelly *et al.*, *Neuron* **80**, 415–428 (2013).
9. S. Almeida *et al.*, *Acta Neuropathol.* **126**, 385–399 (2013).
10. Y. B. Lee *et al.*, *Cell Reports* **5**, 1178–1186 (2013).
11. D. Sareen *et al.*, *Sci. Transl. Med.* **5**, 208ra149 (2013).
12. C. Lagier-Tourenne *et al.*, *Proc. Natl. Acad. Sci. U.S.A.* **110**, E4530–E4539 (2013).
13. K. Mori *et al.*, *Acta Neuropathol.* **125**, 413–423 (2013).
14. K. Reddy, B. Zamiri, S. Y. Stanley, R. B. Macgregor Jr., C. E. Pearson, *J. Biol. Chem.* **288**, 9860–9866 (2013).
15. Z. Xu *et al.*, *Proc. Natl. Acad. Sci. U.S.A.* **110**, 7778–7783 (2013).
16. J. Cooper-Knock *et al.*, *Brain* **137**, 2040–2051 (2014).
17. A. R. Haeusler *et al.*, *Nature* **507**, 195–200 (2014).
18. P. E. Ash *et al.*, *Neuron* **77**, 639–646 (2013).
19. K. Mori *et al.*, *Acta Neuropathol.* **126**, 881–893 (2013).
20. K. Mori *et al.*, *Science* **339**, 1335–1338 (2013).
21. T. F. Gendron *et al.*, *Acta Neuropathol.* **126**, 829–844 (2013).
22. P. Chakrabarty *et al.*, *PLOS ONE* **8**, e67680 (2013).
23. I. R. Mackenzie, P. Frick, M. Neumann, *Acta Neuropathol.* **127**, 347–357 (2014).
24. D. M. Mann *et al.*, *Acta Neuropathol. Commun.* **1**, 68 (2013).
25. F. J. Gil-Bea, B. Aisa, R. Schliebs, M. J. Ramírez, *Behav. Neurosci.* **121**, 340–344 (2007).
26. B. F. Boeve, N. R. Graff-Radford, *Alzheimers Res. Ther.* **4**, 29 (2012).
27. Z. Su *et al.*, *Neuron* **83**, 1043–1050 (2014).

ACKNOWLEDGMENTS

This work was supported by the National Institute on Aging, NIH [P50AG016574 (L.P.)]; National Institute of Neurological Disorders and Stroke, NIH [R21NS089979 (T.F.G. and K.B.B.), R21NS084528 (L.P.), R21NS079807 (Y.-J.Z.), R01NS088689 (L.P.), R01NS063964 (L.P.), R01NS077402 (L.P.), and P01NS084974 (L.P., D.W.D., R.R., and K.B.B.)]; National Institute of Environmental Health Services, NIH [R01ES20395 (L.P.)]; U.S. Department of Defense [ALS Research Program AL130125 (L.P.)]; Mayo Clinic Foundation (L.P.); Mayo Clinic Center for Regenerative Medicine (P.O.B.); Mayo Graduate School (J.C. and K.F.B.); ALS Association (T.F.G., Y.-J.Z., P.O.B., K.B.B., and L.P.); Robert Packard Center for ALS Research at Johns Hopkins (L.P.); Target ALS (L.P.); Alzheimer's Association [NIRP-14-304425 (Y.-J.Z.) and NIRP-12-259289 (J.D.F.)]; and European Research Council under European Union's Seventh Framework Programme [FP7/2014-2019 no. 617198 [DPR-MODELS] (D.E.)]. L.P. and T.F.G. have filed a patent (no. 14/162,570) in the United States regarding the use of poly(GP) immunoassays as a diagnostic for *C9ORF72* repeat expansion–related diseases. The data are tabulated in the manuscript and the supplementary materials.

SUPPLEMENTARY MATERIALS

www.sciencemag.org/content/348/6239/1151/suppl/DC1
Materials and Methods
Figs. S1 to S8
Tables S1
References (*28*–*35*)

16 February 2015; accepted 6 May 2015
Published online 14 May 2015;
10.1126/science.aaa9344

CELL BIOLOGY

Reversible centriole depletion with an inhibitor of Polo-like kinase 4

Yao Liang Wong,[1*] John V. Anzola,[2*] Robert L. Davis,[2*] Michelle Yoon,[2] Amir Motamedi,[2] Ashley Kroll,[1] Chanmee P. Seo,[2] Judy E. Hsia,[2] Sun K. Kim,[3] Jennifer W. Mitchell,[3] Brian J. Mitchell,[3] Arshad Desai,[1] Timothy C. Gahman,[2] Andrew K. Shiau,[2†‡] Karen Oegema[1†‡]

Centrioles are ancient organelles that build centrosomes, the major microtubule-organizing centers of animal cells. Extra centrosomes are a common feature of cancer cells. To investigate the importance of centrosomes in the proliferation of normal and cancer cells, we developed centrinone, a reversible inhibitor of Polo-like kinase 4 (Plk4), a serine-threonine protein kinase that initiates centriole assembly. Centrinone treatment caused centrosome depletion in human and other vertebrate cells. Centrosome loss irreversibly arrested normal cells in a senescence-like G_1 state by a p53-dependent mechanism that was independent of DNA damage, stress, Hippo signaling, extended mitotic duration, or segregation errors. In contrast, cancer cell lines with normal or amplified centrosome numbers could proliferate indefinitely after centrosome loss. Upon centrinone washout, each cancer cell line returned to an intrinsic centrosome number "set point." Thus, cells with cancer-associated mutations fundamentally differ from normal cells in their response to centrosome loss.

Centrioles template assembly of cilia and recruit pericentriolar material to form centrosomes (*1*, *2*). Centriole duplication is tightly controlled, so that mitotic cells have precisely two centrosomes (*3*, *4*). Supernumerary centrosomes are prevalent in cancer and have been postulated to contribute to tumorigenesis (*5*–*7*), perhaps by promoting chromosomal instability (*8*, *9*) or increasing cellular invasiveness (*10*). However, whether cancer cells become dependent upon extra centrosomes for proliferation is unknown.

Centriole assembly is controlled by the serine-threonine protein kinase Polo-like kinase 4 (Plk4) (*11*–*15*). Of all the compounds previously reported to bind Plk4, only CFI-400945 and related analogs exhibit any in vitro Plk4 selectivity (*16*–*20*), and none prevent centrosome assembly in cells. CFI-400945 also induces centrosome amplification and phenotypes associated with Aurora B inhibition (fig. S1) (*18*). Therefore, to develop a selective Plk4 inhibitor with in vivo efficacy, we chose the pan-Aurora kinase inhibitor VX-680, which also inhibits Plk4 (*16*, *17*, *20*), as a template (fig. S2, A and B). Guided by modeling, we introduced a methoxy substituent at the VX-680 C5 position (magenta shading in Fig. 1A) to target the rare hinge-region methionine in Plk4 (Met^{91}) (fig. S2B) and generated a compound with ~15-fold in vitro preference for Plk4 over Aurora A. Out of an additional 390 analogs synthesized and characterized, 133 (34%) had half-maximal inhibitory concentration (IC_{50}) values ≤100 nM for Plk4 in vitro, but only one, LCR-015 (in which the VX-680 cyclopropylamide was replaced with a benzyl sulfone) (orange shading in Fig. 1A), depleted centrosomes in NIH/3T3 mouse embryonic fibroblasts and HCT-116 human colon carcinoma cells at concentrations <10 μM (fig. S2A). Optimization of LCR-015 produced two highly selective Plk4 inhibitors with robust cellular activity: centrinone [LCR-263; inhibition constant (K_i) = 0.16 nM in vitro; centrosome depletion at 100 nM] and centrinone-B (LCR-323; K_i = 0.6 nM in vitro; centrosome depletion at 500 nM) (Fig. 1A). A 2.65 Å centrinone-Plk4 kinase domain cocrystal structure (Fig. 1, B and C, and table S1) revealed that the benzyl sulfone moiety required for cellular activity (orange in Fig. 1, A and C) wraps around the catalytic lysine (Lys^{41}) and forms hydrophobic contacts with Asp^{154} of the Asp-Phe-Gly (DFG) motif (Fig. 1C and fig. S2C), which should disfavor transition to the active state. Both centrinones exhibited >1000-fold selectivity for Plk4 over Aurora A/B (Fig. 1A and table S2) in vitro and did not affect cellular Aurora A or B substrate phosphorylation at concentrations that deplete centrosomes (fig. S2D). In vitro screening against 442 human kinases (*16*) at ~500 × K_i and subsequent dose-response analysis indicated high selectivity (tables S3 and S4), particularly against mitotic kinases. Although we report data obtained with centrinone, key results were replicated with centrinone-B.

Plk4 inhibition prevents new centriole assembly without disassembling preexisting centrioles (*11*, *12*, *14*). Consistent with this, centrinone treatment of HeLa human cervical carcinoma cells led to a progressive reduction in foci containing centriolar and pericentriolar material markers at each round of cell division, until most cells lacked centrioles and centrosomes (Fig. 1D and fig. S2E). Centriole loss prevented formation of primary cilia and resulted in the absence of focal microtubule organization during recovery from nocodazole treatment (fig. S3, A and B). Golgi organization was unaffected (fig. S3C), consistent with its ability to nucleate microtubules independently of centrosomes (*21*). Centriole loss was fully reversible; 10 days after centrinone washout, all cells exhibited normal centrosome numbers (Fig. 1D). Treatment with centrinone reduced centriole number in multiciliated *Xenopus* epithelial cells, which indicated that Plk4 also controls centriole amplification in differentiated cells (fig. S4). To confirm that these effects were due to Plk4 inhibition, we generated a Plk4 mutant [in which Gly^{95} is replaced by Leu (G95L)] with wild-type biochemical activity that sterically hindered centrinone binding [K_i (mutant)/K_i (wild type) > 400] (table S2 and fig. S2C). Treatment with centrinone blocked centriole amplification in cells overexpressing wild-type but not G95L Plk4 (Fig. 1E), which confirmed that centrinone prevents centriole assembly by inhibiting Plk4.

For the first 2 days after centrinone addition, when cells retained two or one centrosomes, the proliferation of HeLa and NIH/3T3 cells was identical to controls; this was followed by a decrease in proliferation rate coincident with the appearance of centrosome-less cells (Fig. 2A, Fig. 1D, and fig. S5). Cells treated long-term continued to proliferate at the slower rate and returned to the control rate after washout-mediated centrosome recovery (Fig. 2B). Measurement by single-cell imaging in cells coexpressing green fluorescent protein–proliferating cell nuclear antigen (GFP-PCNA) and histone 2B–red fluorescent protein (H2B-RFP) revealed that G_1+S and G_2 durations were not substantially different in centrosome-less cells compared with controls (Fig. 2D and fig. S6). Imaging of cells coexpressing centrin-GFP and H2B-RFP revealed that mitotic duration was increased by ~20 min in centrosome-less NIH/3T3 cells and by ~1 hour in HeLa cells (fig. S7). Consistent with prior work (*22*, *23*), centrosome loss increased the frequency of mitotic errors (Fig. 2E and fig. S7), which resulted in cell death (Fig. 2F and fig. S6C) that quantitatively explained the reduced proliferation after centrosome removal (fig. S6D). Centrosome-less NIH/3T3 and HeLa cells arrested in response to DNA damage and also retained the ability to bypass this arrest when treated with caffeine (fig. S8).

To determine whether centriole depletion is preferentially deleterious to cell lines with supernumerary centrosomes, we analyzed the basal level of centrosome amplification across a panel of 21 cell lines that continued to proliferate after centrinone treatment (table S5). Nine lines spanning a range of amplification levels (HeLa, 4%; NIH/3T3, 6%; U2OS, 7%; HCT116, 9%; Calu-6, 11%; MDA-MB-231, 16%; BT-549, 19%; and N1E-115-1, 81%) were depleted of centrosomes, and their proliferation rate was compared with dimethyl sulfoxide (DMSO)–treated controls (Fig. 2, A and

[1]Department of Cellular and Molecular Medicine, Ludwig Institute for Cancer Research, University of California, San Diego, La Jolla, CA 92093, USA. [2]Small Molecule Discovery Program, Ludwig Institute for Cancer Research, La Jolla, CA 92093, USA. [3]Department of Cell and Molecular Biology, Northwestern University, Feinberg School of Medicine, Chicago, IL 60611, USA.
*These authors contributed equally to this work. †These authors contributed equally to this work. **‡Corresponding author. E-mail: koegema@ucsd.edu (K.O.); ashiau@ucsd.edu (A.K.S.)**

C). We observed no correlation between basal centrosome amplification state and proliferation after centrosome depletion, which indicated that cells with multiple centrosomes are not addicted to them.

To study the origins of centrosome amplification within cancer cell lines, we depleted centrosomes from three cell lines that normally exhibit low (HeLa, 4%); medium (BT-549, 19%); or high (N1E-115-1, 81%) amplification (Fig. 2G). We then washed out centrinone and counted centrosomes at regular intervals. In all three lines, centrinone washout triggered an initial wave of centrosome overduplication (Fig. 2G and fig. S9, A and C), owing to the lack of copy number control during de novo assembly and elevated Plk4 levels that resulted from inhibition of autophosphorylation-mediated degradation (figs. S1C and S9D). This wave of overduplication was followed by a gradual return to a centrosome number distribution similar to that before depletion (Fig. 2G). Live imaging of HeLa cells revealed that recovery of the original distribution occurred by removal of cells with supernumerary centrosomes via multipolar mitoses with death of the resulting progeny (fig. S9B). Thus, each cancer cell line has an intrinsic centrosome number distribution, or "set point," that is independent of preexisting centrosomes and reflects a dynamic equilibrium between ongoing overduplication and selection against cells with extra centrosomes.

To determine whether centrosomes are required for the proliferation of normal human cells, we analyzed the effect of centrosome depletion in three cell lines and three primary cell cultures. Prior work with RPE1 human retinal pigment epithelial cells showed that transient centrosome removal did not block passage through the subsequent G_1-S transition (*24*), but the effect of multigenerational centrosome removal could not be analyzed because S-phase entry triggered de novo centriole assembly. Using centrinone to persistently block centriole assembly in RPE1 cells, we found that centrosome loss coincided with a plateau in cell number (Fig. 3A). A 12-day passaging assay and flow cytometry showed that centrosome depletion led to cell cycle arrest in G_1 (Fig. 3E and fig. S10A); an identical arrest was observed after centrosome depletion in three primary cell cultures and two other lines lacking cancer-associated mutations (table S6 and fig. S10, B and D). Centrinone treatment did not lead to centrosome loss or proliferation arrest in RPE1 cells where both endogenous *PLK4* alleles were engineered to express the centrinone-resistant G95L mutant (Fig. 3B and fig. S11), which indicated that the arrest is triggered by centrosome loss due to Plk4 inhibition.

The potent G_1 arrest in the absence of centrosomes was in contrast to the normal progression through G_1-S observed after transient centrosome removal (*24*). To address this difference, we used live-cell imaging to establish the lineage of RPE1 cells coexpressing centrin-GFP and H2B-RFP after acute centrinone treatment (Fig. 3C). Pioneer one-centrosome mothers divided at normal frequency, but a significant fraction of their one- and zero-centrosome progeny arrested (25.5% and 33.0%, respectively). The majority (70%) of

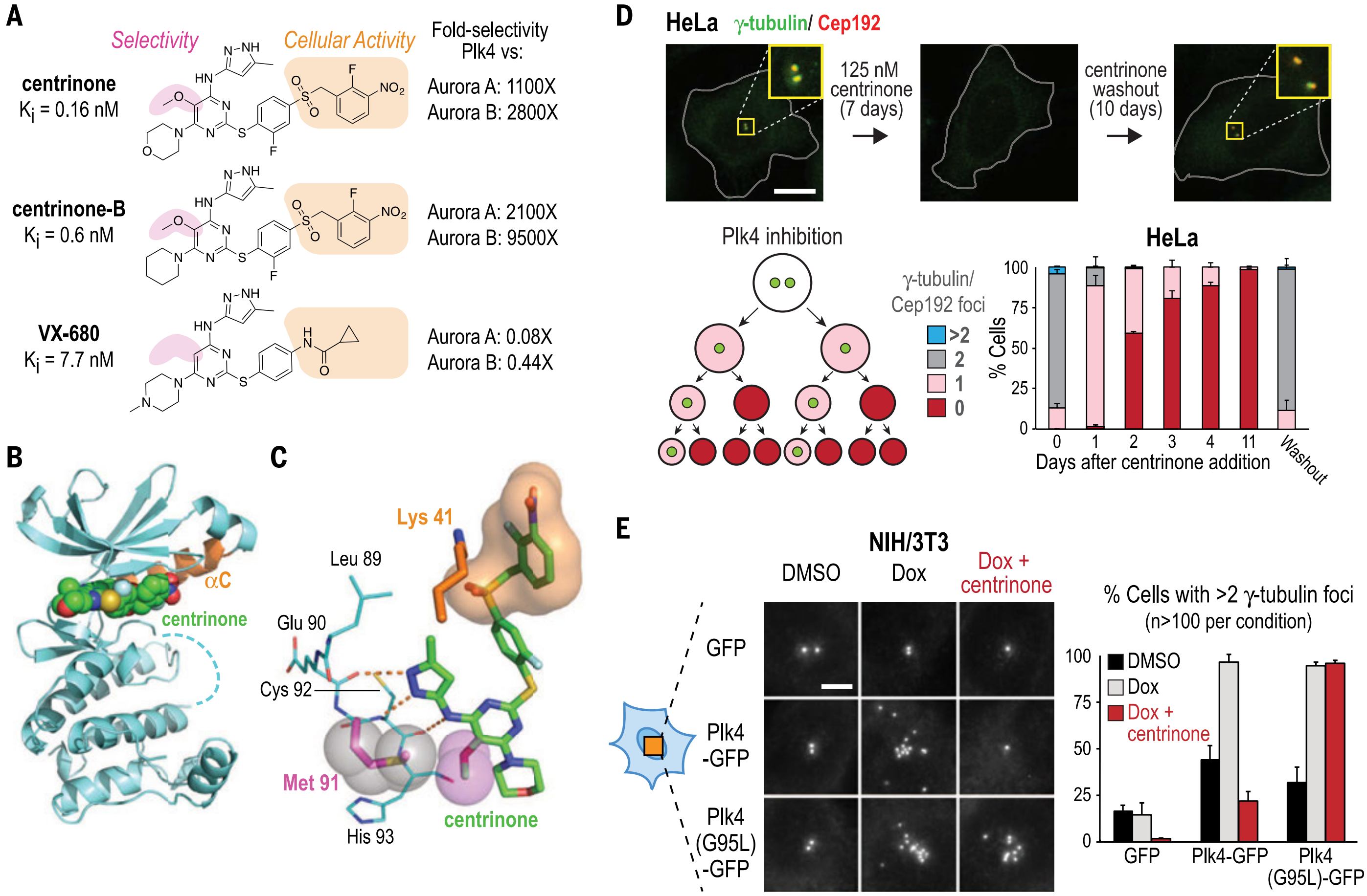

Fig. 1. Centrinone is a selective Plk4 inhibitor that reversibly depletes centrioles from cells. (**A**) Chemical structures, K_i values, and selectivities [Plk4 versus Aurora A/B; K_i (kinase)/K_i (Plk4)] of the centrinones and VX-680. (**B**) Crystal structure of the centrinone-Plk4 kinase domain complex (orange αC helix). (**C**) Close-up of centrinone in the Plk4 active site. The aminopyrazole moiety of centrinone hydrogen bonds (orange dashes) with the main chain carbonyl of Glu[90] and the carbonyl and amide nitrogen of Cys[92]. The 5-methoxy substituent (magenta spheres) packs against the Met[91] side chain (magenta stick and gray spheres). The benzyl sulfone moiety (orange surface) wraps around Lys[41] (orange). (**D**) HeLa cells 7 days after centrinone addition and 10 days after centrinone washout. (Insets: 3.3× magnified). Scale bar, 10 μm. Schematic shows progressive centrosome depletion after Plk4 inhibition. Bar graph shows the centrosome number distribution after centrinone addition and washout. (**E**) γ-Tubulin foci in NIH/3T3 cells induced to overexpress wild-type or centrinone-resistant (G95L) Plk4-GFP. Scale bar, 5 μm. Data in (D) and (E) are means ± SD; number of experiments (*N*) = 3.

the progeny of pioneer zero-centrosome mothers arrested. That one-centrosome progeny of one-centrosome mothers arrested indicates that cells detect loss of even a single centrosome. Thus, penetrant G_1 arrest requires one to two cell cycles after centrosome removal, which explains why it was not observed after transient centrosome ablation. We speculate that progressive arrest, rather than an immediate block when one or both centrosomes are absent, allows for rescue by the de novo centriole assembly pathway.

Of the cell lines we identified that continue to proliferate in the absence of centrosomes, 12 have mutations in or suppress expression of p53 (table S5), which suggests that the arrest is p53-dependent. Consistent with this, immunoblot analysis showed increased levels of p53 and its downstream effector p21 after centrosome depletion (Fig. 3D and fig. S10C). Fixed analysis in RPE1 cells and primary fibroblasts revealed that this p53 increase paralleled the arrest observed in the lineage analysis (fig. S10, E and F), and small hairpin RNA (shRNA)–mediated p53 depletion in RPE1 cells allowed indefinite proliferation in the absence of centrosomes (Fig. 3E). Three lines of evidence indicate that the p53-dependent arrest was not a consequence of DNA

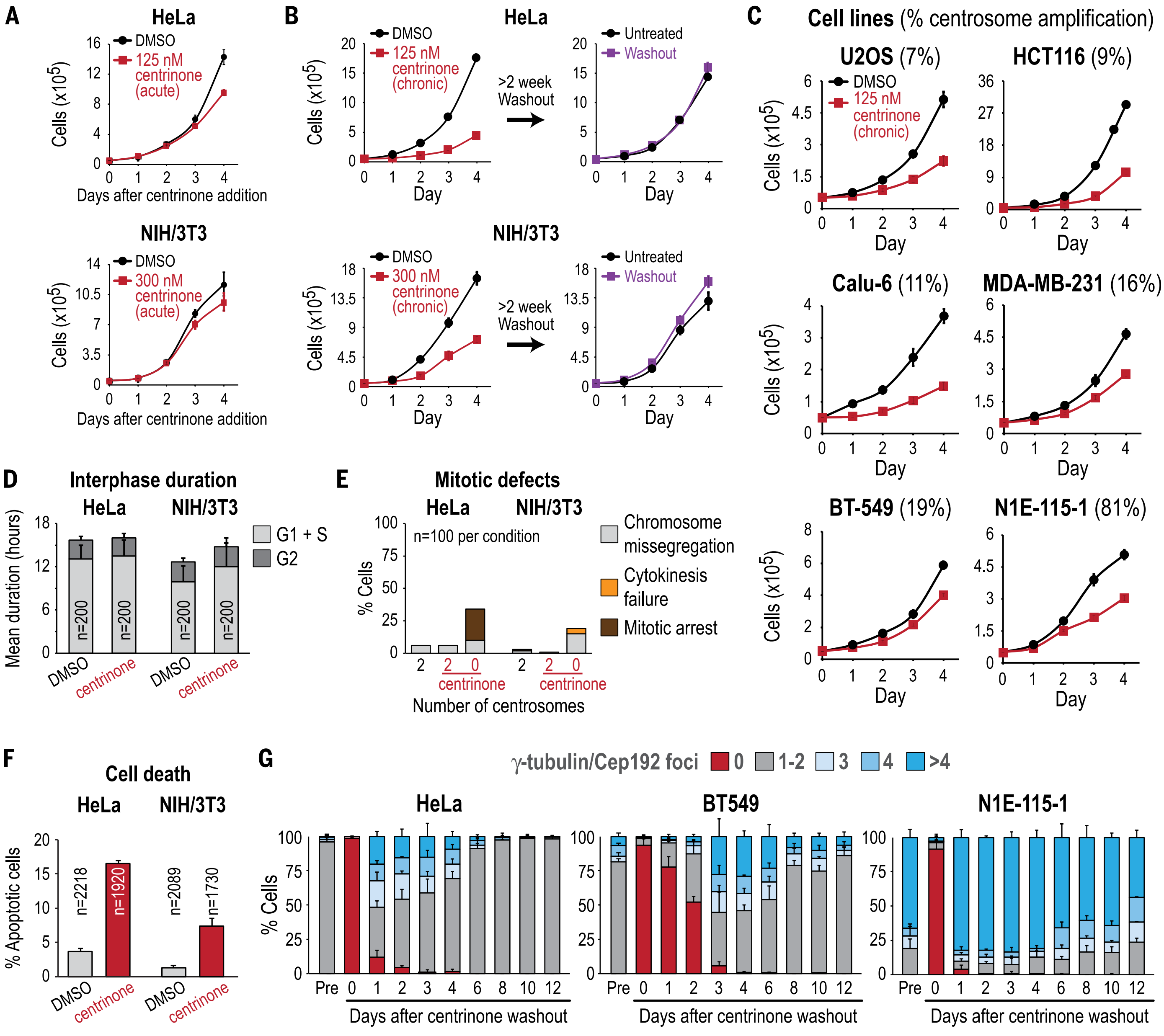

Fig. 2. Transformed cells proliferate indefinitely in the absence of centrosomes. (**A**) Proliferation curves of HeLa and NIH/3T3 cells immediately after addition of centrinone or DMSO (control). (**B**) Proliferation curves after chronic (>2 weeks) centrinone treatment (left), or after chronic centrinone treatment followed by drug washout for >2 weeks (right). (**C**) Proliferation curves after chronic (>2 weeks) centrinone treatment in cell lines with varying degrees of centrosome amplification. Numbers in parentheses are percentages of cells exhibiting centrosome amplification in untreated population. Data in (A) to (C) are means ± SEM (*N* = 3). (**D**) G_1+S and G_2 durations measured in HeLa and NIH/3T3 cells coexpressing GFP-PCNA and H2B-RFP (see fig. S6). Data are means ± SD. (**E**) Percentage of cells exhibiting mitotic defects measured in HeLa and NIH/3T3 cells coexpressing centrin-GFP and H2B-RFP (see fig. S7). (**F**) Percentage of cells undergoing cell death in HeLa and NIH/3T3 cells, measured by using a fluorescent caspase substrate. Data are means ± SD (*N* = 2). (**G**) Graphs showing centrosome number distribution over time after centrinone washout from HeLa, BT-549, and N1E-115-1 cells treated long-term (>2 weeks). The centrosome number distribution in untreated cells ("Pre" bars) is also shown for each cell line. Data are means ± SD (*N* = 3).

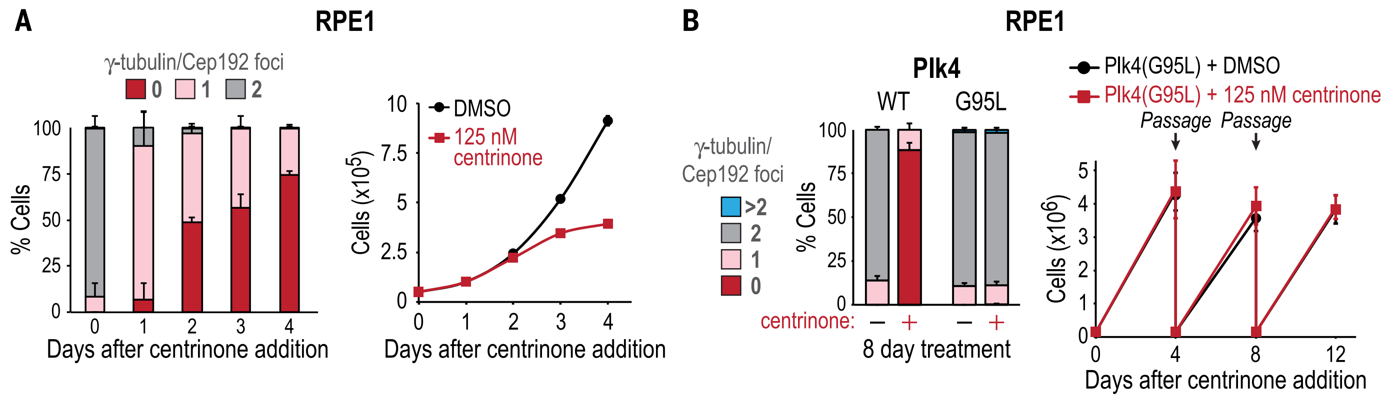

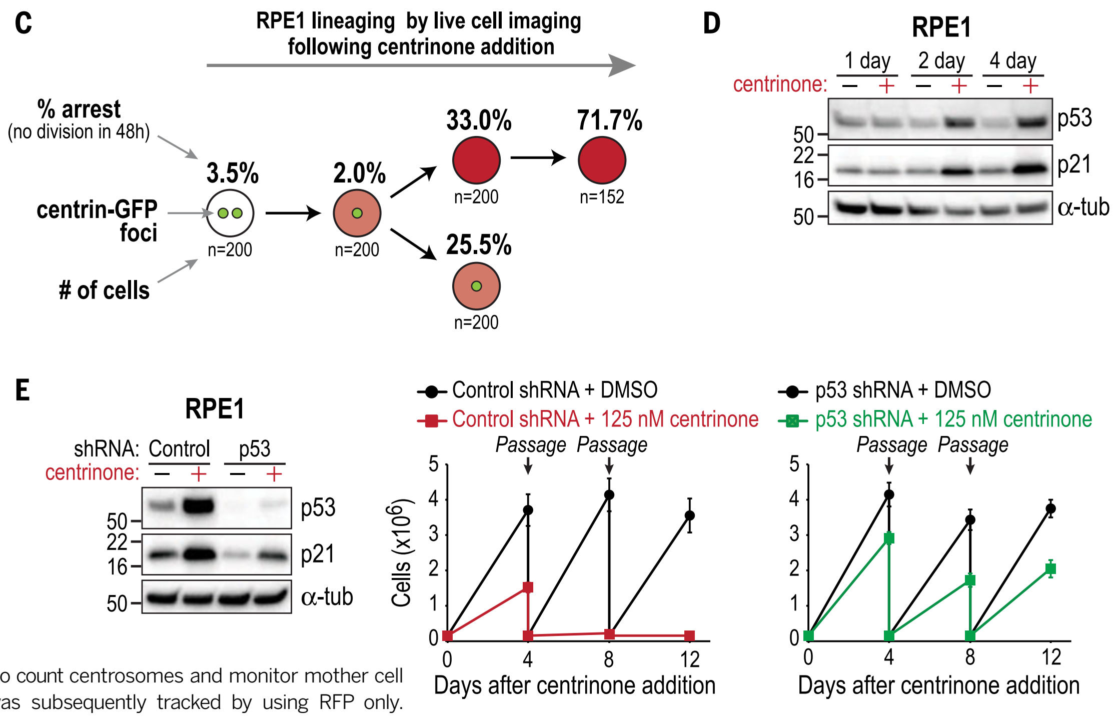

Fig. 3. Centrosome loss triggers a p53-dependent arrest in normal cells. (**A**) Centrosome number distribution (left; data are means ± SD; *N* = 3) and proliferation (right, data are means ± SEM; *N* = 3) of RPE1 cells after centrinone addition. (**B**) (left) Centrosome number distribution in RPE1 cells expressing WT or centrinone-resistant G95L (homozygous knock-in at the endogenous locus) Plk4. (Right) Passaging assay on RPE1 Plk4 G95L cells. Data are means ± SD (*N* = 2). (**C**) Lineage analysis showing the percentage of RPE1 cells with the indicated number of centrosomes arresting in each generation after centrinone addition (*N* = 2). Cells coexpressing centrin-GFP and H2B-RFP were initially filmed in both GFP and RFP channels to count centrosomes and monitor mother cell mitosis. Daughter cell fate was subsequently tracked by using RFP only. Arrest was the inability to enter mitosis within 48 hours of cell birth. (**D**) Western blot of p53 and p21 in RPE1 cells. α-tub, α-tubulin. (**E**) Western blot of RPE1 cells expressing control or p53 shRNA, and passaging assay of RPE1 cells expressing control or p53 shRNA after centrinone addition. Data are means ± SD (*N* = 2).

damage. First, no posttranslational modifications were observed at eight p53 residues associated with DNA damage signaling (Ser^{9}, Ser^{15}, Ser^{20}, Ser^{33}, Ser^{37}, Ser^{315}, and Ser^{392} phosphorylation and Lys^{382} acetylation) (Fig. 4A and fig. S12A) (*25*, *26*). Second, γ-H2A.X foci, which mark sites of double-stranded DNA breaks, were not more abundant in centrinone-treated cells (Fig. 4B and fig. S12B). Third, chemical inhibition of the DNA damage–response kinases ATM, ATR, Chk1, and DNA-PK had no effect on the proliferation arrest induced by centrosome loss (fig. S12C). The G_1 arrest induced by centrosome loss was also not due to stress signaling; p38 stress kinase, activated by both doxorubicin-induced DNA damage and chromosome missegregation (induced by Mps1 inhibition), was not activated by centrosome loss (Fig. 4C), and a p38 inhibitor had no effect on the G_1 arrest (fig. S12, D and E). Knockdown of LATS2 or expression of constitutively active YAP—both recently shown to bypass a Hippo pathway–mediated arrest resulting from cytokinesis failure (*27*)—also did not bypass the arrest caused by centrosome loss (Fig. 4D and fig. S13).

When mitosis is artificially prolonged beyond ~90 min in RPE1 cells (unperturbed duration is ~20 min), a mitotic duration sensor arrests the resulting progeny in G_1 in a p53-dependent manner (*28*) (Fig. 4E, left). In a study of Sas4$^{-/-}$ mouse embryos, it was proposed that centriole loss delays mitosis and activates the sensor, which triggers p53-dependent apoptosis (*29*, *30*). To test this idea, we correlated the mitotic duration of mother cells with daughter cell fate during the course of centrosome depletion (Fig. 4E and fig. S14A). All one-centrosome mothers and 87% of zero-centrosome mothers spent less time in mitosis than the duration sensor timing cutoff (dashed black line in Fig. 4E), with most completing this step in significantly less time. There was no correlation between mitotic duration in the mother cell and daughter cell fate. Thus, the G_1 arrest triggered by centrosome loss is not a result of extended mitotic duration. In addition, chromosome missegregation was observed only in a minority of cells (asterisks in Fig. 4E), which suggested that aneuploidy resulting from centrosome loss was not the cause of the arrest. Consistent with this, after deliberate induction of chromosome missegregation via Mps1 inhibition, only 11% of the progeny of mothers with visible missegregation arrested in G_1 (fig. S14B).

Our results indicate that the p53-mediated G_1 arrest after centrosome loss is not due to any previously described signaling mechanism. Instead, centrosome loss resembles the effect of chemically blocking the interaction between p53 and MDM2, the E3 ubiquitin ligase that targets p53 for degradation (*31*). Both centrosome loss and treatment with the Mdm2 inhibitor R7112 raised p53 levels without genotoxic stress and led to increased MDM2 and decreased MDM4 levels (Fig. 4F). However, whereas R7112 washout led

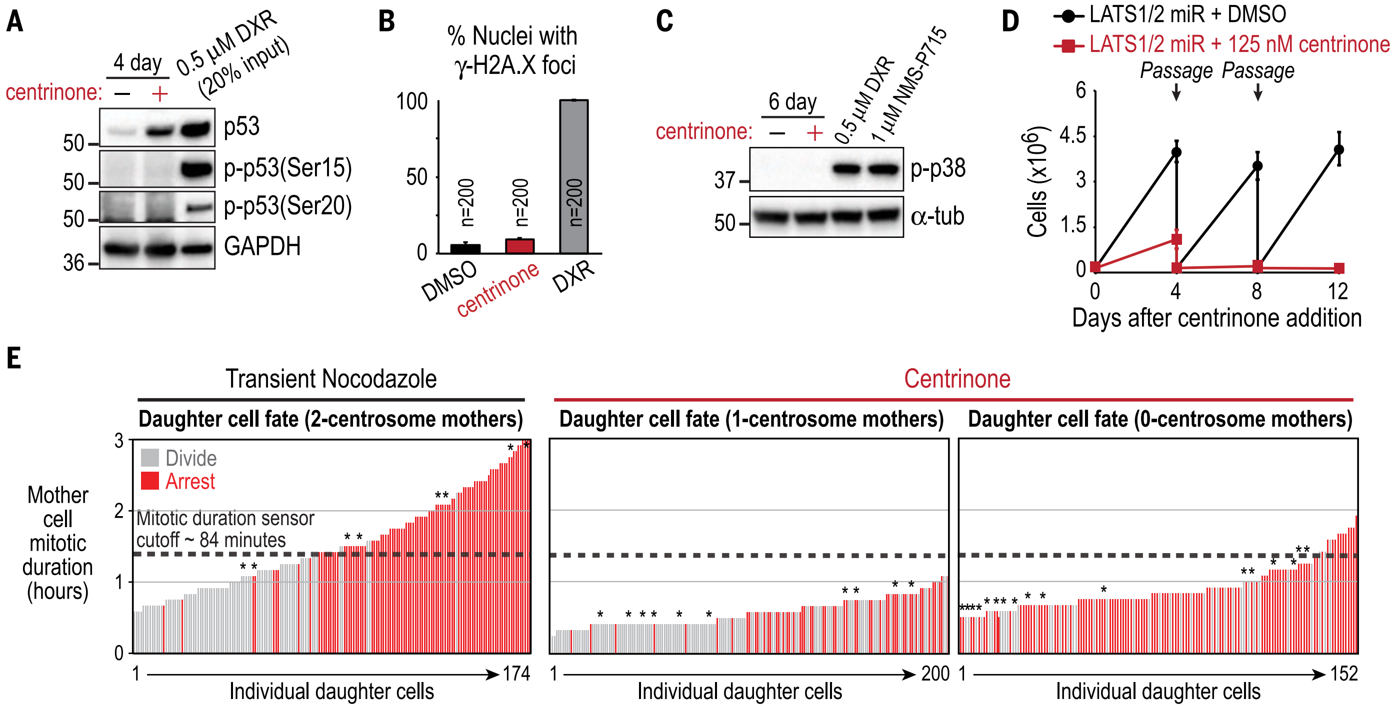

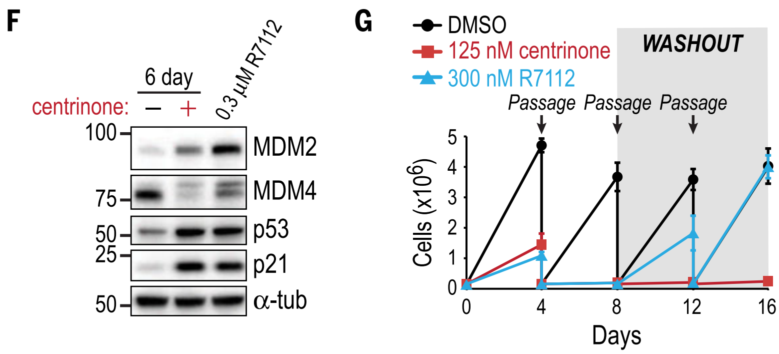

Fig. 4. The irreversible G_1 arrest after centrosome loss occurs via an unidentified mechanism. (**A**) Western blot for p53 phosphoepitopes associated with DNA damage in RPE1 cells treated with centrinone or doxorubicin as a positive control. (**B**) Quantification of γ-H2A.X foci in RPE1 nuclei. Data are means ± SD ($N = 3$). (**C**) Western blot of activated p38 in RPE1 cells. (**D**) Passaging assay of RPE1 cells expressing LATS1/2 microRNA, after addition of centrinone. (**E**) Daughter cell fate in RPE1 cells coexpressing centrin-GFP and H2B-RFP. Vertical bars represent measurements from individual daughter cells. Bar height is the time their mother spent in mitosis, and color indicates arrest (red) or division (gray). Asterisks indicate chromosome missegregation in the mother cell. Daughter cell fate after nocodazole treatment of mother cells with a normal two-centrosome complement (left) confirms the existence of a mitotic duration sensor that arrests daughter cells if the mother cell spends more than ~84 min (black dashed lines on all plots) in mitosis. (**F**) Western blot of RPE1 cells treated with centrinone or R7112. (**G**) Passaging assay of RPE1 cells after addition (day 0) and washout (day 8) of centrinone or R7112. Data in (D) and (G) are means ± SD ($N = 2$).

to resumption of proliferation, centrinone washout did not (Fig. 4G), even though arrested cells remained viable for >3 weeks. This difference could result from centrosomes being necessary to suppress p53 levels and new centriole assembly requiring S-phase entry. Effectively, this would trap centrosome-less G_1-arrested cells in a "Catch-22" situation—unable to reduce p53 levels and enter S-phase because they lack centrosomes and, at the same time, unable to form new centrosomes because they cannot enter S-phase.

In summary, the Plk4 inhibitor centrinone permits reversible knockout of centrioles and centrosomes and may prove broadly useful for analysis of these organelles. Centrinone treatment revealed that centrosomes are essential for the proliferation of normal human cells, settling a long debate and highlighting an important difference from *Drosophila* (*32*). In their absence, a centrosome loss sensor arrests cells in G_1 in a p53-dependent manner distinct from previously described signaling mechanisms. In addition to preventing the proliferation of centrosome-less cells, the centrosome loss sensor may also serve a physiological function. As centrosome inactivation is coincident with differentiation in many contexts (*33*–*35*), we speculate that it may not only be important to form specialized microtubule arrays, but may also function as a barrier restricting cell cycle reentry. Cancer-derived cell lines, irrespective of their basal amplification state, continue to proliferate without centrosomes, albeit with substantially reduced mitotic fidelity. The differential effect of centrosome removal on normal cells and cells with cancer-associated mutations suggests the possibility of combining centrosome depletion with other perturbations to selectively target dividing cancer cells.

REFERENCES AND NOTES

1. I. A. Drummond, *Curr. Opin. Cell Biol.* **24**, 24–30 (2012).
2. H. Schatten, *Histochem. Cell Biol.* **129**, 667–686 (2008).
3. D. A. Brito, S. M. Gouveia, M. Bettencourt-Dias, *Curr. Opin. Cell Biol.* **24**, 4–13 (2012).
4. E. N. Fîrat-Karalar, T. Stearns, *Philos. Trans. R. Soc. Lond. B Biol. Sci.* **369**, 20130460 (2014).
5. T. Boveri, *Zur Frage der Entstehung maligner Tumoren* (Gustav Fischer Verlag, Jena, Germany, 1914).
6. S. A. Godinho, D. Pellman, *Philos. Trans. R. Soc. Lond. B Biol. Sci.* **369**, 20130467 (2014).
7. E. A. Nigg, L. Čajánek, C. Arquint, *FEBS Lett.* **588**, 2366–2372 (2014).
8. N. J. Ganem, S. A. Godinho, D. Pellman, *Nature* **460**, 278–282 (2009).
9. W. T. Silkworth, I. K. Nardi, L. M. Scholl, D. Cimini, *PLOS ONE* **4**, e6564 (2009).
10. S. A. Godinho *et al.*, *Nature* **510**, 167–171 (2014).
11. M. Bettencourt-Dias *et al.*, *Curr. Biol.* **15**, 2199–2207 (2005).
12. R. Habedanck, Y. D. Stierhof, C. J. Wilkinson, E. A. Nigg, *Nat. Cell Biol.* **7**, 1140–1146 (2005).
13. J. Kleylein-Sohn *et al.*, *Dev. Cell* **13**, 190–202 (2007).
14. K. F. O'Connell *et al.*, *Cell* **105**, 547–558 (2001).
15. N. Peel, N. R. Stevens, R. Basto, J. W. Raff, *Curr. Biol.* **17**, 834–843 (2007).
16. M. I. Davis *et al.*, *Nat. Biotechnol.* **29**, 1046–1051 (2011).
17. E. F. Johnson, K. D. Stewart, K. W. Woods, V. L. Giranda, Y. Luo, *Biochemistry* **46**, 9551–9563 (2007).

18. J. M. Mason et al., Cancer Cell 26, 163–176 (2014).
19. P. B. Sampson et al., J. Med. Chem. 58, 147–169 (2015).
20. D. A. Sloane et al., ACS Chem. Biol. 5, 563–576 (2010).
21. R. M. Rios, Philos. Trans. R. Soc. Lond. B Biol. Sci. 369, 20130462 (2014).
22. A. Khodjakov, C. L. Rieder, J. Cell Biol. 153, 237–242 (2001).
23. J. H. Sir et al., J. Cell Biol. 203, 747–756 (2013).
24. Y. Uetake et al., J. Cell Biol. 176, 173–182 (2007).
25. L. M. Jenkins, S. R. Durell, S. J. Mazur, E. Appella, Carcinogenesis 33, 1441–1449 (2012).
26. N. D. Lakin, S. P. Jackson, Oncogene 18, 7644–7655 (1999).
27. N. J. Ganem et al., Cell 158, 833–848 (2014).
28. Y. Uetake, G. Sluder, Curr. Biol. 20, 1666–1671 (2010).
29. H. Bazzi, K. V. Anderson, Proc. Natl. Acad. Sci. U.S.A. 111, E1491–E1500 (2014).
30. D. Izquierdo, W. J. Wang, K. Uryu, M. F. Tsou, Cell Reports 8, 957–965 (2014).
31. H. Shen, C. G. Maki, Curr. Pharm. Des. 17, 560–568 (2011).
32. R. Basto et al., Cell 125, 1375–1386 (2006).
33. F. Bartolini, G. G. Gundersen, J. Cell Sci. 119, 4155–4163 (2006).
34. M. Stiess et al., Science 327, 704–707 (2010).
35. K. D. Sumigray, T. Lechler, BioArchitecture 1, 221–224 (2011).

ACKNOWLEDGMENTS

We thank Z. Li for leading the Sundia Meditech chemistry team, Advanced Photon Source NE-CAT (supported by NIH GM103403) for assistance with x-ray data collection, Q. Zhu and I. Verma for the p53 and Glu4 shRNA lentiviruses, A. Holland and D. Cleveland for the Plk4-YFP DLD-1 cell line, R. Gassmann for help with initial cell-based assays, M. Kaulich for technical advice on CRISPR/Cas9, and A. Dammermann for generation of the Sas6 and Cep192 antibodies. J.V.A, R.L.D., M.Y., A.M., C.P.S., J.E.H., A.D., T.C.G., A.K.S., and K.O. receive salary and other support from the Ludwig Institute for Cancer Research. This work was supported by NIH grants to K.O. (GM074207) and B.J.M. (GM089970), and with funds from the Hilton Ludwig Cancer Prevention Initiative to A.K.S. and T.C.G. The data described here are tabulated in the main paper and Supplementary Materials. The structure of the centrinone-bound Plk4 kinase domain complex has been deposited in the Protein Data Bank (4YUR). The Ludwig Institute for Cancer Research has filed a patent application (62/149,292) related to the structures, syntheses, and uses of centrinone, centrinone B, and chemically related Plk4 inhibitors. Requests for the centrinones should be directed to A.K.S. (ashiau@ucsd.edu).

SUPPLEMENTARY MATERIALS

www.sciencemag.org/content/348/6239/1155/suppl/DC1
Materials and Methods
Figs. S1 to S14
Tables S1 to S6
References (36–63)

17 December 2014; accepted 17 April 2015
Published online 30 April 2015;
10.1126/science.aaa5111

AGING STEM CELLS

A Werner syndrome stem cell model unveils heterochromatin alterations as a driver of human aging

Weiqi Zhang,[1*] Jingyi Li,[2*] Keiichiro Suzuki,[3*] Jing Qu,[4*] Ping Wang,[1] Junzhi Zhou,[1] Xiaomeng Liu,[2] Ruotong Ren,[1] Xiuling Xu,[1] Alejandro Ocampo,[3] Tingting Yuan,[1] Jiping Yang,[1] Ying Li,[1] Liang Shi,[5] Dee Guan,[1] Huize Pan,[1] Shunlei Duan,[1] Zhichao Ding,[1] Mo Li,[3] Fei Yi,[6] Ruijun Bai,[4] Yayu Wang,[5] Chang Chen,[1] Fuquan Yang,[1] Xiaoyu Li,[7] Zimei Wang,[8] Emi Aizawa,[3] April Goebl,[3,9] Rupa Devi Soligalla,[3] Pradeep Reddy,[3] Concepcion Rodriguez Esteban,[3] Fuchou Tang,[2,10,11,12]† Guang-Hui Liu,[1,8,11,13]† Juan Carlos Izpisua Belmonte[3]†

Werner syndrome (WS) is a premature aging disorder caused by WRN protein deficiency. Here, we report on the generation of a human WS model in human embryonic stem cells (ESCs). Differentiation of WRN-null ESCs to mesenchymal stem cells (MSCs) recapitulates features of premature cellular aging, a global loss of H3K9me3, and changes in heterochromatin architecture. We show that WRN associates with heterochromatin proteins SUV39H1 and HP1α and nuclear lamina–heterochromatin anchoring protein LAP2β. Targeted knock-in of catalytically inactive *SUV39H1* in wild-type MSCs recapitulates accelerated cellular senescence, resembling WRN-deficient MSCs. Moreover, decrease in WRN and heterochromatin marks are detected in MSCs from older individuals. Our observations uncover a role for WRN in maintaining heterochromatin stability and highlight heterochromatin disorganization as a potential determinant of human aging.

Werner syndrome (WS), also known as adult progeria, recapitulates certain aspects of human physiological aging (*1*). WS is caused by mutations in the *WRN* gene, resulting in loss of WRN expression or function (*1*). WRN protein plays roles in DNA replication, transcription, repair, and recombination, as well as telomere maintenance, indicating that one of the major causes for WS pathogenesis relates to genomic instability (*1*, *2*). Epigenetic alterations have been associated with cellular aging in diverse model organisms (*2*–*4*). In humans, somatic cells derived from patients with premature aging syndromes are characterized by loss of heterochromatin marks (*5*–*7*). However, it is unclear whether epigenetic dysregulation is involved in WS pathogenesis.

Generation of patient-specific induced pluripotent stem cells (iPSCs) represents a promising avenue to model and study human aging and aging-associated disorders (*8*). WS-specific iPSC lines may constitute an ideal source for in vitro modeling of WS. However, we found that WS patient fibroblast lines deposited in different cell banks presented severe karyotypic abnormalities and secondary DNA mutations associated with advanced stages of WS pathology. To create an unbiased human WS cellular model, we sought to generate an isogenic WS embryonic stem cell (ESC) line by knocking out exons 15 and 16 of the *WRN* gene encoding the conserved DNA helicase domain (*9*). After two rounds of homologous recombination using helper-dependent adenoviral vector (HDAdV) (*10*, *11*), we successfully generated homozygous *WRN*-null ESC lines (ESCs-$WRN^{-/-}$) (Fig. 1, A and B, and fig. S1, A to D). ESCs-$WRN^{-/-}$ expressed pluripotency markers, maintained normal karyotype, and could differentiate into all three germ layers (Fig. 1A and fig. S2, A to E). ESCs-$WRN^{-/-}$ lacked detectable WRN protein, as determined by Western blot using antibodies specific to the N or C terminus of WRN (Fig. 1B). No difference in cell cycle kinetics and cell growth rate between wild-type and WRN-null ESCs was observed (fig. S2, F to H).

WS patients are mainly characterized by premature aging pathologies associated with degeneration of mesodermal tissues, i.e., osteoporosis, atherosclerosis, and gray hair (*1*). We hypothesized that WS patients may suffer from an accelerated exhaustion of the mesenchymal stem cell (MSC) pool. This was tested by differentiating ESCs-$WRN^{-/-}$ into MSCs. MSCs-$WRN^{-/-}$ expressed MSC-specific cell surface markers CD73, CD90, CD105; lacked expression of MSC-irrelevant antigens, including CD45, CD34, and CD43 (fig. S3A); and

[1]National Laboratory of Biomacromolecules, Institute of Biophysics, Chinese Academy of Sciences, Beijing 100101, China. [2]Biodynamic Optical Imaging Center, College of Life Sciences, Peking University, Beijing 100871, China. [3]Gene Expression Laboratory, Salk Institute for Biological Studies, 10010 North Torrey Pines Road, La Jolla, CA 92037, USA. [4]State Key Laboratory of Reproductive Biology, Institute of Zoology, Chinese Academy of Sciences, Beijing 100101, China. [5]Diagnosis and Treatment Center for Oral Disease, the 306th Hospital of the PLA, Beijing, China. [6]Department of Molecular and Cellular Physiology, Stanford University School of Medicine, Stanford, CA 94305, USA. [7]College of Life Sciences, Peking University, Beijing 100871, China. [8]The Center for Anti-aging and Regenerative Medicine, Shenzhen University, Shenzhen 518060, China. [9]Universidad Católica San Antonio de Murcia, Campus de los Jerónimos s/n, 30107 Guadalupe, Murcia, Spain. [10]Ministry of Education Key Laboratory of Cell Proliferation and Differentiation, Beijing 100871, China. [11]Center for Molecular and Translational Medicine (CMTM), Beijing 100101, China. [12]Peking-Tsinghua Center for Life Sciences, Peking University, Beijing 100871, China. [13]Beijing Institute for Brain Disorders, Beijing 100069, China.
*These authors contributed equally to this work. **†Corresponding author. E-mail: ghliu@ibp.ac.cn (G.-H.L.); tangfuchou@pku.edu.cn (F.T.); belmonte@salk.edu (J.C.I.B.)**

could differentiate into osteoblasts, chondrocytes, and adipocytes (fig. S3, B and C) (*12*).

Upon serial passaging, WRN-deficient MSCs recapitulated major phenotypes of premature aging, including premature loss of proliferative potential, increased number of senescence-associated–β-galactosidase (SA-β-gal)–positive cells, up-regulated expression of aging-associated genes p16^{Ink4a} and p21^{Waf1}, and activation of senescence-associated secretory phenotype (SASP) (Fig. 1, C to E, and fig. S3, D to G) (*13*). Moreover, when WRN-deficient MSCs expressing luciferase were transplanted into the muscle of nonobese diabetic/severe combined immunodeficiency (NOD/SCID) mice, they underwent an accelerated attrition compared to wild-type MSCs (Fig. 1F and fig. S3H). These results demonstrated that the loss of WRN promotes premature senescence in MSCs.

WRN deficiency in MSCs resulted in elevated DNA damage response (DDR), indicated by increased nuclear foci for 53BP1, γ-H2AX, and phosphorylated ATM/ATR substrates (fig. S4, A to C). Restoration of WRN activity by lentivirus-mediated expression in MSCs-*WRN*$^{-/-}$ resulted in partial alleviation of DDR and cellular senescence (fig. S4, D and E). To investigate potential chromosomal abnormalities resulting from the loss of WRN protein, we performed genome-wide copy number variation (CNV) analysis by deep sequencing. In the time frame examined, genomic integrity was minimally affected in MSCs-*WRN*$^{-/-}$ (fig. S4F).

Epigenetic alteration has been considered as a hallmark of aging (*2*). MSCs-*WRN*$^{-/-}$ showed a distinct nuclear Hoechst 33342 staining pattern with markedly enlarged nuclei and a high pixel-to-pixel coefficient of variation (CV) value, indicating possible changes in chromatin structure (Fig. 2A and fig. S5A). Moreover, WRN-deficient MSCs exhibited accelerated diminishment of heterochromatin-associated inner nuclear membrane (INM) proteins LAP2β and LBR and reduced heterochromatin structure underneath the nuclear envelope, as indicated by immunostaining and electron microscopy (Fig. 2B and fig. S5, B and C) (*14*). These results suggest a progressive disorganization of heterochromatin in WRN-deficient MSCs.

Further investigation of heterochromatin reorganization at histone and DNA levels revealed marked down-regulation of the constitutive heterochromatin mark H3K9me3 (trimethylated histone H3 at lysine-9) in MSC-*WRN*$^{-/-}$ (Fig. 2C and fig. S5, D and E). In contrast, H3K27me3 showed slight down-regulation, whereas H3K4me3, a mark for euchromatin fiber, exhibited comparable levels between WRN-deficient and wild-type MSCs (Fig. 2C and fig. S5, D and E). We did not observe obvious genome-wide alteration of 5-methylcytosine (5mC) in WRN-deficient MSCs (Fig. 2C). Bioinformatic analysis identified 73 H3K9me3-enriched "mountains" throughout the genome in MSCs-*WRN*$^{+/+}$, which are characterized by >20 kb of consecutive peaks of H3K9me3 (Fig. 2D). Of these H3K9me3 mountains, 28 (38%) were lost in MSCs-*WRN*$^{-/-}$ (Fig. 2D). Interestingly, 24 (86%) of these impaired H3K9me3 mountains resided in subtelomeric or subcentromeric regions (Fig. 2, D and E, and table S1).

RNA sequencing (RNA-seq) identified 1047 RefSeq genes that showed differential expression in MSCs-*WRN*$^{-/-}$ (fig. S6, A and B, and table S2). The most obviously down-regulated genes were centromere-packaging proteins and components of the nuclear membrane (fig. S6, A to E, and table S3). These results indicate alterations in nuclear structure and epigenomic organization, potentially leading to a progressive loss of heterochromatin structure in MSCs as a consequence of WRN depletion.

In agreement with previous reports describing WRN as a telomere-associated protein required for telomere maintenance (*15*), compromised telomerase activity and shorter telomere length were detected in MSC-*WRN*$^{-/-}$ (fig. S7, A and B). In addition, chromatin immunoprecipitation–quantitative polymerase chain reaction (ChIP-QPCR) showed binding of WRN to the H3K9me3-enriched centromeric loci α-Satellite (α-Sat) and Satellite 2 (Sat2) (Fig. 3A) (*16*). Depletion of WRN resulted in an increase in centromeric γ-H2AX signal and a loss of H3K9me3 from α-Sat and Sat2 loci accompanied by up-regulation of transcripts from these sequences (Fig. 3, A and B, and fig. S7C). Coimmunoprecipitation (Co-IP) analysis revealed WRN as part of a complex containing the major histone methyltransferase for H3K9me3—SUV39H1, HP1α, and LAP2β, a nuclear envelope component that recruits heterochromatin via anchoring to HP1α (Fig. 3C and fig. S7D) (*17*). These observations suggest a role for WRN, together with SUV39H1 and HP1α, in the stabilization of heterochromatin.

We next tested whether disorganization of heterochromatin could contribute to accelerated cellular senescence. Knockdown of SUV39H1 or HP1α in wild-type MSCs led to a reduction of overall H3K9me3 and induction of cellular senescence, as assayed by Western blot, SA-β-gal staining, and p16 expression (Fig. 3D and fig. S8, A to D). On the contrary, overexpression of HP1α up-regulated H3K9me3 levels and repressed cellular senescence in WRN-deficient MSCs (fig. S8, E to H). To confirm these observations, we

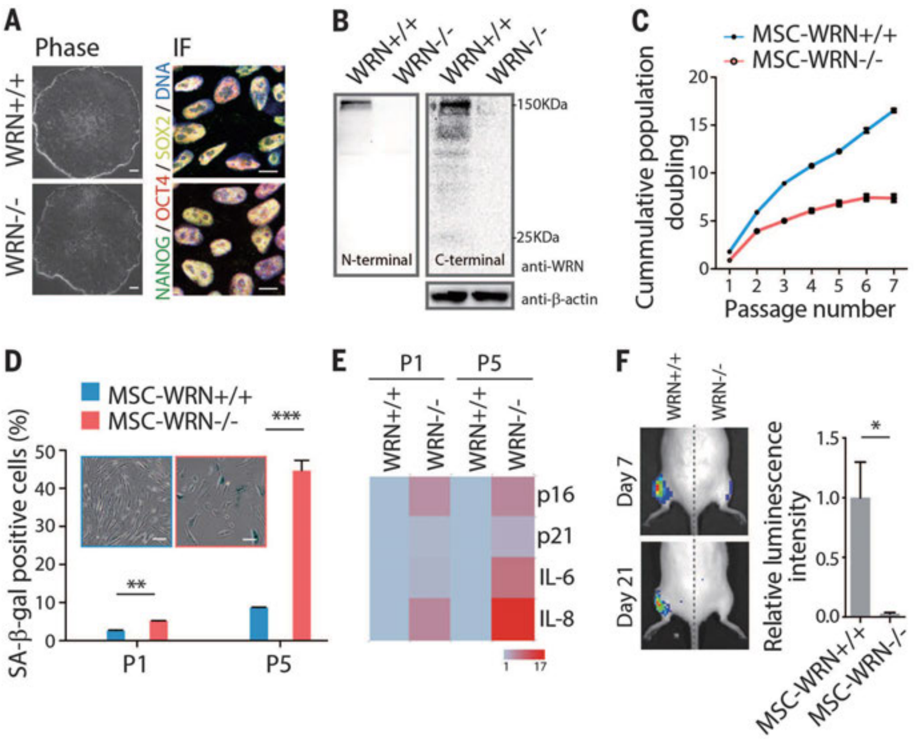

Fig. 1. WRN-deficient MSCs exhibit phenotypes associated with premature cellular senescence. (**A**) Morphology and immunofluorescence (IF) analyses of pluripotency markers in ESCs. Scale bar, 100 μm and 10 μm, respectively. (**B**) Western blot analysis of WRN expression in ESCs using anti-WRN N-terminal (ab200) and C-terminal (SC-5629) antibodies. (**C**) Growth curve analyzing the cumulative population doubling of MSCs. (**D**) Senescence-associated (SA)–β-gal staining in passage 1 (P1) and P5 MSCs. Scale bar, 50 μm. (**E**) Quantitative RT-PCR analysis of the indicated genes in P1 and P5 MSCs. Transcript levels were normalized to MSCs-*WRN*$^{+/+}$ group. Genes with greater mean value are color coded toward red. (**F**) Photon flux from muscle of a NOD-SCID mouse transplanted with MSCs-*WRN*$^{+/+}$ (left) and MSCs-*WRN*$^{-/-}$ (right) expressing luciferase. All data are represented as mean + SEM. *$P < 0.05$, **$P < 0.01$, ***$P < 0.001$ by Student's *t* test; $n = 3$ independent experiments.

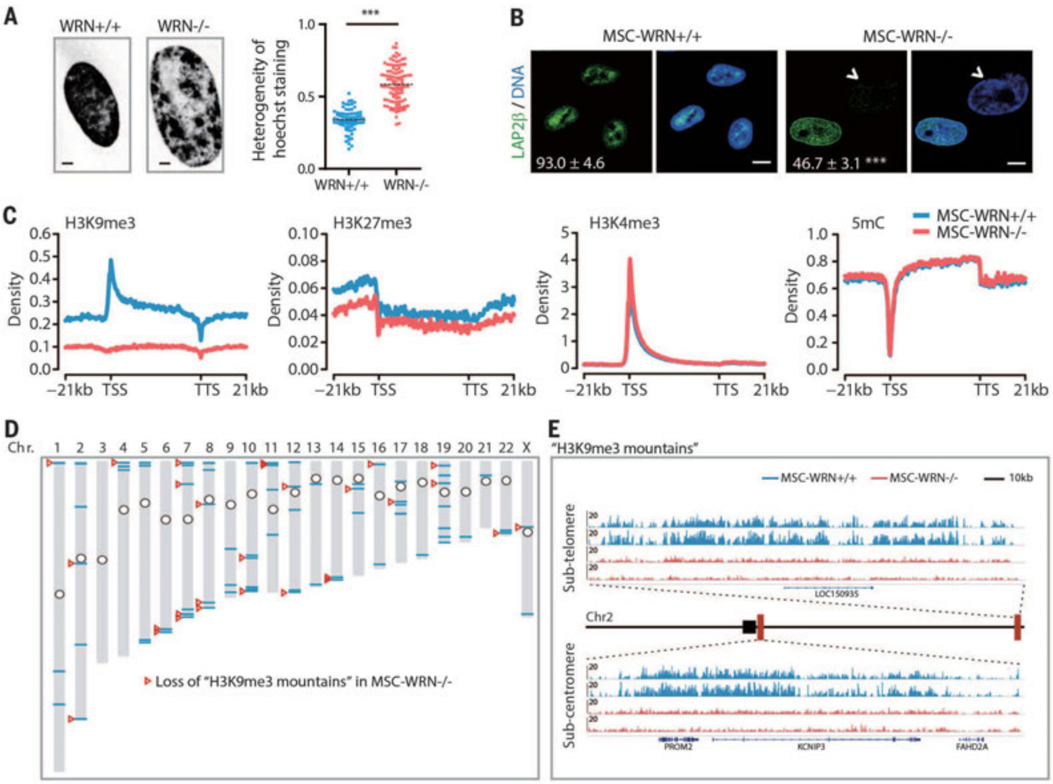

Fig. 2. Epigenomic analyses of WRN-deficient MSCs. (**A**) Left: Chromatin structure of MSCs shown by Hoechst 33342 staining of the nucleus. Scale bar, 5 μm. Right: CV value of nuclear Hoechst staining intensity used to evaluate the heterogeneity (pixel-to-pixel variation) of Hoechst intensity. (**B**) Immunofluorescence analyses of LAP2β expression in MSC-*WRN*$^{+/+}$ and MSC-*WRN*$^{-/-}$ at P5. Arrowheads denote abnormal nuclei with decreased LAP2β expression (percentage of LAP2β–positive nuclei in corner). Scale bar, 10 μm. n = 3 independent experiments. (**C**) Enrichment of H3K9me3, H3K27me3, H3K4me3, and 5mC on the gene bodies and 21 kb upstream of TSS (transcription start site) and 21 kb downstream of TTS (transcription terminal site) regions in the human genome. (**D**) Sketch map of "H3K9me3 mountain" distribution over 23 chromosomes. The blue lines indicate 73 "H3K9me3 mountains" present in MSCs-*WRN*$^{+/+}$, whereas 48 (65.8%) of them are localized within 5 Mb regions around the telomeres or centromeres. The red arrowheads indicate 28 "H3K9me3 mountains," which are lost in MSCs-*WRN*$^{-/-}$. The circles indicate the centromeres of chromosomes. (**E**) Representative images showing two "H3K9me3 mountains" on chromosome 2 in the subtelomere or subcentromere regions in P5 MSCs-*WRN*$^{-/-}$ and MSCs-*WRN*$^{+/+}$. Two biological replicates of each sample are presented. Black square denotes the centromere; red rectangles denote the position of the presented subtelomere and subcentromere regions, respectively. All data are represented as mean + SEM. ***P < 0.001 by Student's t test.

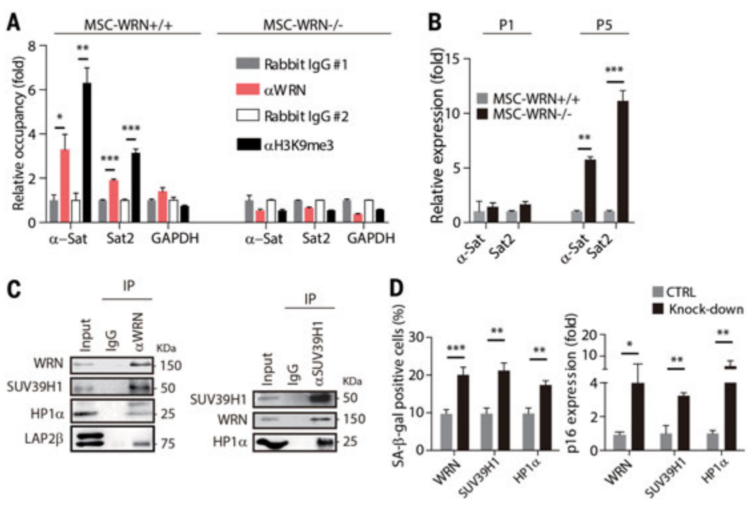

Fig. 3. WRN associates with centromeric heterochromatin and forms a molecular complex with SUV39H1 and HP1α. (**A**) Enrichment of WRN and H3K9me3 within the region of α-Sat or Sat2 as measured by ChIP-qPCR. (**B**) Quantitative RT-PCR analysis of centromeric repetitive element transcripts in MSCs at the indicated passages. (**C**) Left, coimmunoprecipitation of SUV39H1, HP1α, and LAP2β protein with endogenous WRN protein; Right, co-immunoprecipitation of WRN and HP1α with endogenous SUV39H1 in wild-type MSCs. (**D**) SA-β-gal staining (left) and p16 transcript (right) analyses in wild-type MSCs transduced with control lentiviral vector (CTRL) or lentiviral vector encoding for the indicated short hairpin RNA (Knock-down). All data are represented as mean + SEM. *P < 0.05, **P < 0.01, and ***P < 0.001 by Student's t test; n = 3 independent experiments.

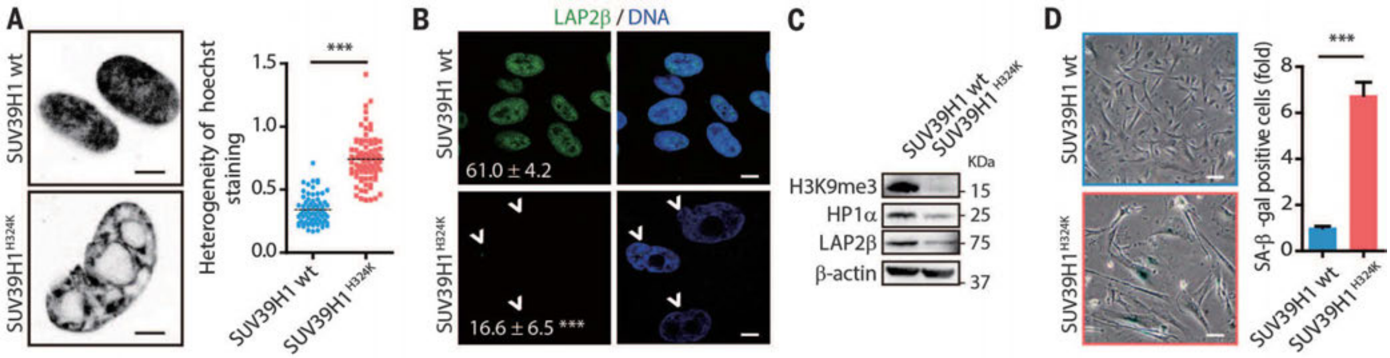

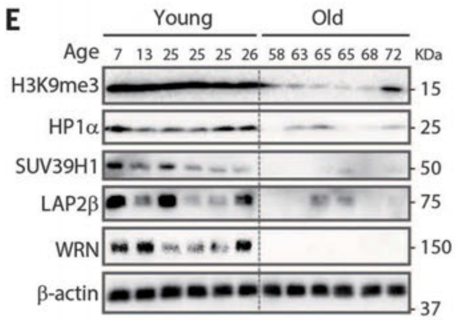

Fig. 4. *SUV39H1*^{H324K} mutant MSCs exhibit defective nuclear envelope and heterochromatin, as well as phenotypes of premature cellular senescence. (**A**) As described in Fig. 2A (left), Hoechst staining images of the nucleus; right, CV value of nuclear Hoechst staining intensity used to evaluate the heterogeneity (pixel-to-pixel variation) of Hoechst intensity. (**B**) Immunofluorescence analyses of LAP2β expression in MSCs. Arrowheads denote the abnormal nuclei with decreased LAP2β (percentages of normal nuclei presented at corner). Scale bar, 20 μm. $n = 3$ independent experiments. (**C**) Western blot analysis of the indicated proteins in MSCs. (**D**) SA-β-gal staining in MSCs at P5. Scale bar, 50 μm. $n = 3$ independent experiments. (**E**) Western blot analysis of the indicated proteins in human primary MSCs derived from old and young healthy individuals at P4 (see table S4). All data are represented as mean + SEM. $^{***}P < 0.001$ by Student's *t* test.

generated pluripotent ESCs-*SUV39H1*^{H324K} lines harboring catalytically inactivated endogenous SUV39H1 (fig. S9, A to D). Upon differentiation, MSCs-*SUV39H1*^{H324K} displayed drastic nuclear structural and chromosomal changes, loss of INM proteins LAP2β and LBR, decreased levels of H3K9me3 and HP1α, up-regulation of centromeric repetitive sequence transcription, and coordinated transcriptional down-regulation of centromere-packaging components (Fig. 4, A to C, and fig. S10, A and B). MSCs-*SUV39H1*^{H324K} recapitulated premature aging phenotypes observed in WRN-deficient MSCs, including retarded cell growth and accelerated cellular senescence determined by SA-β-gal staining (Fig. 4D and fig. S10, C to E). High expression of SUV39H2, a germline-specific histone methyltransferase, and/or other factors may functionally compensate for SUV39H1 deficiency in ESCs (fig. S10F) (*18*, *19*), where upon inactivation of the WRN-SUV39H1 axis, no discernible heterochromatin change was observed (figs. S10G and S8A). It should be noted that MSCs-*SUV39H1*^{H324K} exhibit neither increased γ-H2AX ($P = 0.773$) and phosphorylated ATM/ATR substrates ($P = 0.279$), nor telomere attrition (figs. S10H and S7, A and B). These results indicate that heterochromatin destabilization promotes premature aging in MSCs.

Finally, we asked whether heterochromatin disorganization could be a common hallmark for physiological human stem cell aging. For this purpose, we compared the levels of heterochromatin marks in primary dental pulp MSCs derived from six young (7- to 26-year-old) and six old (58- to 72-year-old) individuals (fig. S10I and table S4) (*20*). A marked down-regulation of WRN protein associated with a decrease in H3K9me3, HP1α, SUV39H1, and LAP2β levels in MSCs derived from old individuals (Fig. 4E). Therefore, specific heterochromatin changes may underlie both pathological and physiological MSC aging.

In summary, we have found that WRN protein, besides its role in DNA repair, functions to safeguard heterochromatin stability (fig. S11). Our results reveal that the progressive heterochromatin disorganization observed in WRN-deficient MSCs underlies cellular aging, but more extensive studies are needed to examine its role during physiological aging. The methodologies and observations introduced here may be used and extended toward the systematic study of other age-associated molecular events with relevance to human aging and age-related disorders.

REFERENCES AND NOTES

1. B. A. Kudlow, B. K. Kennedy, R. J. Monnat Jr., *Nat. Rev. Mol. Cell Biol.* **8**, 394–404 (2007).
2. C. López-Otín, M. A. Blasco, L. Partridge, M. Serrano, G. Kroemer, *Cell* **153**, 1194–1217 (2013).
3. G. Pegoraro *et al.*, *Nat. Cell Biol.* **11**, 1261–1267 (2009).
4. E. L. Greer *et al.*, *Nature* **466**, 383–387 (2010).
5. G.-H. Liu *et al.*, *Nature* **472**, 221–225 (2011).
6. D. K. Shumaker *et al.*, *Proc. Natl. Acad. Sci. U.S.A.* **103**, 8703–8708 (2006).
7. J. D. Miller *et al.*, *Cell Stem Cell* **13**, 691–705 (2013).
8. G. H. Liu, Z. Ding, J. C. Izpisua Belmonte, *Curr. Opin. Cell Biol.* **24**, 765–774 (2012).
9. D. B. Lombard *et al.*, *Mol. Cell. Biol.* **20**, 3286–3291 (2000).
10. G.-H. Liu *et al.*, *Nature* **491**, 603–607 (2012).
11. K. Suzuki *et al.*, *Cell Stem Cell* **15**, 31–36 (2014).
12. G. H. Liu *et al.*, *Nat. Commun.* **5**, 4330 (2014).
13. F. Rodier, J. Campisi, *J. Cell Biol.* **192**, 547–556 (2011).
14. T. Dechat, S. A. Adam, P. Taimen, T. Shimi, R. D. Goldman, *Cold Spring Harb. Perspect. Biol.* **2**, a000547 (2010).
15. A. S. Multani, S. Chang, *J. Cell Sci.* **120**, 713–721 (2007).
16. D. Wang *et al.*, *Proc. Natl. Acad. Sci. U.S.A.* **110**, 5516–5521 (2013).
17. N. Kourmouli *et al.*, *EMBO J.* **19**, 6558–6568 (2000).
18. D. O'Carroll *et al.*, *Mol. Cell. Biol.* **20**, 9423–9433 (2000).
19. W. Zhang, J. Qu, K. Suzuki, G.-H. Liu, J. C. Izpisua Belmonte, *Trends Cell Biol.* **23**, 587–592 (2013).
20. G. B. Tomar *et al.*, *Biochem. Biophys. Res. Commun.* **393**, 377–383 (2010).

ACKNOWLEDGMENTS

We are grateful to W. G. Zhu, L. Comai, K. Mitani, P. Ng, and A. Lieber for sharing experimental materials; L. Sun, W. Ding, G. Yuan, and X. Zhu from Center for Biological Imaging for technical assistance; and M. Schwarz and L. Zhao for administrative help. This work was supported by National Natural Science Foundation of China (NSFC: 81330008), National Basic Research Program of China (973 Program, 2015CB964800; 2014CB910500; 2014CB964600; 2012CB966704), the Strategic Priority Research Program of the Chinese Academy of Sciences (XDA01020312), NSFC (31222039; 31201111; 81371342; 81300261; 81300677; 81271266; 81471414; 81422017; 81401159; 31322037; 81471407), National High Technology Research and Development Program of China (863 program: 2015AA020307), Beijing Natural Science Foundation (7141005; 5142016), Key Research Program of the Chinese Academy of Sciences (KJZDEW-TZ-L05), the Thousand Young Talents program of China, National Laboratory of Biomacromolecules (012kf02;2013kf05;2013kf11;2014kf02;2015kf10) and State Key Laboratory of Drug Research (SIMM1302KF-17), and China Postdoctoral Science Foundation Grant (2013M530751). K.S and M.L. are supported by a California Institute for Regenerative Medicine Training Grant. A.O. was partially supported by an NIH Ruth L. Kirschstein National Research Service Award Individual Postdoctoral Fellowship. The physiological human cell aging studies were supported by UCAM. The J.C.I.B. laboratory was supported by The Glenn Foundation, The G. Harold and Leila Y. Mathers Charitable Foundation, and The Leona M. and Harry B. Helmsley Charitable Trust (2012-PG-MED002). All materials are available from the G.-H.L., F.T., and J.C.I.B. laboratories under a material transfer agreement with Institute of Biophysics (CAS), Peking University, or The Salk Institute for Biological Studies. Myc-HP1α plasmid can be obtained from W. G. Zhu under a material transfer agreement with Peking University.

SUPPLEMENTARY MATERIALS

www.sciencemag.org/content/348/6239/1160/suppl/DC1
Material and Methods
Figs. S1 to S11
Table S1 to S5
References (*21*–*47*)

21 October 2014; accepted 15 April 2015
Published online 30 April 2015;
10.1126/science.aaa1356

Methotrexate ELISA Kit
Methotrexate is a drug designed as an anti-folate to inhibit the metabolism of folic acid. The methotrexate enzyme-linked immunosorbent assay (ELISA) enables the monitoring of methotrexate levels during treatment of cancer and rheumatoid arthritis. The methotrexate assay is also appropriate for the detection of methotrexate contamination after its use as a selective agent for recombinant protein production in mammalian cell lines. The ultrasensitive assay allows for detection of as little as 1.4 ng/mL of methotrexate in human serum and plasma. It has also been validated for use in human urine, mouse plasma, mouse serum, rat plasma, and rat serum. The ELISA offers a broad dynamic range, reducing the need to dilute your samples. The kit allows for high throughput analysis and time-savings through the analysis of up to 38 samples in duplicate in just 90 minutes. The ELISA is thoroughly validated to ensure excellent reproducibility between experiments, and low cross-reactivity with structurally related molecules.
Enzo Life Sciences
For info: 800-942-0430
www.enzolifesciences.com

Multiphoton Laser Scanning Microscope
The FluoView FVMPE-RS series' high-speed scanner allows observation of ultrarapid biological responses, and the system can obtain vivid images from as deep as 8 mm below the tissue surface. Two new configurations now expand the FluoView FVMPE-RS series beyond the original upright frame version introduced in 2013 to offer even greater scope and flexibility for research. The new configurations also open up a wide range of observation possibilities suited to imaging a greater variety of biological specimens. The Gantry microscope frame features an ultrastable arch-like structure that allows considerable space beneath the objective to accommodate experiments of varied sizes. A volume of 640 mm wide, 355 mm high, and 520 mm deep is available if the stage is removed, providing sufficient space for the researcher's own experimental apparatus and providing flexibility to suit different observation purposes. The inverted microscope frame is ideal for observation of cells in three-dimensional cultures, where multiple layers of cells are cultured in a petri dish or similar vessel.
Olympus
For info: +49-(0)-40-23773-5913
www.olympus-lifescience.com

Hotplate Stirrers
Hotplate stirrers are designed to offer synthetic chemistry laboratories affordability, top-build quality, and high performance without compromising on safety. Manufactured in an ISO9001-2008 production facility, each hotplate stirrer incorporates two independent control circuits. The additional and independent safety circuit is for limiting the maximum heating plate temperature; this can be adjusted between 50ºC and 360ºC but cannot be changed accidentally. This ensures that the flashpoint of your reaction solvent is not exceeded, making it ideal for teaching laboratories. A hermetically sealed design protects the hotplate stirrer motor assembly from spillages ensuring long-term reliability and operator safety. For labs looking to regularly undertake unattended overnight reactions, Asynt hotplate stirrer packages are supplied with an additional third temperature controller, which improves reproducibility and accuracy to within 0.5ºC while maintaining operational safety. The hotplate stirrers also feature a very powerful magnetic drive with ramp start function, especially useful when stirring more viscous samples or for parallel synthesis of multiple tubes or flasks.
Asynt
For info: +44-(0)-1638-781709
www.asynt.com

No-Wash Potassium Ion Channel Assay Kit
The new homogeneous, no-wash assay is designed to measure ligand- and voltage-gated potassium channel activity. The FLIPR Potassium Assay Kit uses a novel thallium-sensitive indicator dye and a masking agent to significantly widen the conventional assay window, enabling studies of channels with low conductance or low expression levels. The kit's protocol eliminates the customary wash steps that introduce artificial variation and limit high throughput automation. Current thallium-based potassium ion channel assays require multiple buffer or media replacements, making them slow and cumbersome, and prone to well-to-well variation. Pervasive background noise also undermines accurate assessment of the small signals generated by many low-conductance channels or low-expressing cell lines. The FLIPR Potassium Assay Kit directly measures potassium channel function using a thallium-sensitive indicator dye that passively diffuses into cells as an acetoxymethyl ester. Cytoplasmic esterases cleave the dye into its fluorogenic form. A proprietary masking agent further reduces the background fluorescence and enhances the signal-to-noise ratio.
Molecular Devices
For info: 800-635-5577
www.moleculardevices.com/potassium

Mounting Media
The latest addition to the Vectashield Mounting Media product line is Vectashield HardSet with Phalloidin. This new formulation contains fluorescently labeled Phalloidin, that specifically binds actin filaments within a cell. The tetramethylrhodamine phalloidin in this product produces an orange-red fluorescent signal when excited at 544 nm and viewed at 572 nm. One or two drops are directly applied to the cell/tissue preparation similar to our other Vectashield products. Actin filament architecture can then be viewed along with a contrasting fluorescent marker for a specific target antigen. Vectashield Mounting Media are unsurpassed in preventing photobleaching of fluorescent proteins and fluorescent dyes (see website for compatibility).
Vector Laboratories
For: 650-697-3600
www.vectorlabs.com

Electronically submit your new product description or product literature information! Go to www.sciencemag.org/products/newproducts.dtl for more information.

Newly offered instrumentation, apparatus, and laboratory materials of interest to researchers in all disciplines in academic, industrial, and governmental organizations are featured in this space. Emphasis is given to purpose, chief characteristics, and availability of products and materials. Endorsement by *Science* or AAAS of any products or materials mentioned is not implied. Additional information may be obtained from the manufacturer or supplier.

POSITIONS OPEN

DIRECTOR OF THE WATER INSTITUTE

The Penn State Institutes of Energy and the Environment (PSIEE), in the Office of the Vice President for Research at The Pennsylvania State University, invites applications for Director of the Water Institute.

The Water Institute is the newest of the institutes under PSIEE. The inaugural Director will be charged with leading the unit in shaping the overall water related research portfolio; in coordination with over 120 exceptional faculty, distributed across eight colleges at University Park and several regional campuses. Current water research activity includes, three major centers supported by NSF and EPA, and over $40 million per year of external funding for water and closely allied research fields. The quality of Penn State's water scholarship is exceptional, with the fifth most citations and the highest citation per publication ratio of all major U.S. universities during the last 5 years. Additional information about Penn State's water programs and PSIEE are detailed in the Water Task Force Report and PSIEE Strategic Plan, both available at **website: http://psiee.psu.edu**.

The Director of the Water Institute must have a strong interest in facilitating interdisciplinary water scholarship, developing the Water Institute's grant portfolio, and increasing the exposure of Penn State as a national leader in water research. The Director will also participate in the recruitment of new faculty. Successful candidates must have a Ph.D., or equivalent credentials appropriate for a tenured or tenure-track professor; as well as an outstanding publication and external funding record in water research. The candidate's area of research may address any aspect of water science, policy, law, engineering, design, ethics, etc. The tenure home of the Director will be determined in consultation with the successful candidate and the relevant department. As an administrator, the position is subject to yearly goal setting and review, and regular 5-year performance reviews.

To apply, submit a cover letter, curriculum vita, and the names and contact information of at least three references. Applications will be reviewed beginning July 6, 2015 and will be accepted until the position is filled. Apply to **job 57767** at **website: http://apptrkr.com/201523736**.

CAMPUS SECURITY CRIME STATISTICS: For more about safety at Penn State, and to review the Annual Security Report which contains information about crime statistics and other safety and security matters, please go to **website: http://www.police.psu.edu/clery/**, *which will also provide you with detail on how to request a hard copy of the Annual Security Report.*

Penn State is an Equal Opportunity/Affirmative Action Employer, and is committed to providing employment opportunities to all qualified applicants without regard to race, color, religion, age, sex, sexual orientation, gender identity, national origin, disability, or protected veteran status.

FACULTY POSITIONS – MEDICAL SCHOOL

The new Center for Research on Environmental Disease, College of Medicine, University of Kentucky is seeking candidates for several faculty positions at the ASSISTANT/ASSOCIATE/PROFESSOR (tenure-track and tenured) levels with 12-month appointment. Applicants are sought in the broad area of environmental disease and those with NIH support will receive favorable considerations. Applicants should submit their curriculum vitae to **Dr. Xianglin Shi**, Professor and Director, Center for Research on Environmental Disease electronically to **e-mail: xshi5@email.uky.edu**. Review of applications will begin immediately and continue until the positions are filled.

Faculty Position in Epidemiology
Wayne State University School of Medicine

Wayne State University located in Detroit, Michigan is seeking to strengthen its Epidemiology Unit, which deals with the incidence, distribution, and possible control of diseases and other factors relating to health.

The Epidemiology Unit collaborates with Departments within the School of Medicine, and also with the Perinatology Research Branch of the Division of Intramural Research, NICHD, NIH, DHHS, which is housed at the Wayne State University campus.

As a key staff member in support of the PRB, this individual would help to accomplish the Branch's mission by (1) developing statistical analysis, programming strategies and methodologies in support of research projects, (2) evaluating and analyzing data using accepted statistical and biostatistical techniques, (3) working closely with the scientific team and collaborators to provide operational parameters to ongoing research, (4) training the next generation of researchers, (5) translating the results of the research through publications and technology transfer.

The individual chosen for this position will become part of a highly successful, fast-paced research group that focuses on clinical and basic research in perinatal medicine and related disciplines. The goal of this internationally recognized research is to develop novel diagnostic, therapeutic and preventative strategies to reduce adverse pregnancy outcome, infant mortality and handicap. The research agenda involves novel discovery technologies in functional genomics, proteomics, metabolomics and DNA analysis.

To be considered for this position, it is recommended that candidates demonstrate the following:

1. Thorough knowledge of biostatical methodologies, procedures and testing
2. Expertise in issues pertaining to the conduction and analysis of longitudinal studies
3. Competence in the area of mathematical modeling
4. Knowledge of data coordination, collection and statistical analysis methods and research coordination principles
5. Knowledge of medical and research protocols
6. Knowledge of computer software design and multiple programming languages
7. Demonstrated broad knowledge of the understanding of scientific principles, theories and technologies applicable to biological sciences, in general, and perinatology in particular
8. A sound understanding of academic research and related issues together with extensive experience in complex, multi-disciplinary programs (administrative and scientific)
9. Ability to foster intellectual productivity
10. Strong oral and written communication skills
11. Ability to work independently and collaboratively
12. Basic knowledge of perinatology is desirable

Academic and professional requirements:

1. Ph.D. in Epidemiology, Biostatistics, Statistics or related field
2. Minimum of five years of experience

Interested individuals should send:

a curriculum vitae,
a separate statement summarizing their experience and professional contributions,
and three references to:

Jennifer Turpin
Wayne State University School of Medicine
jturpin@med.wayne.edu

AAAS
ADVANCING SCIENCE, SERVING SOCIETY

Chief Operating Officer

AAAS is seeking an experienced and talented individual to serve as Chief Operating Officer (COO). Reporting to the Chief Executive Officer, the COO will partner with the CEO to provide overall strategic and operational oversight for a subset of grant-funded AAAS programs and will manage a group of Program Heads as their Chief Program Director. This newly created position will also provide leadership to AAAS operations; assist the CEO with the strategic planning process and will envision new programmatic initiatives in coordination with the CEO and the AAAS Program Heads. The COO will also oversee the AAAS innovation process to create a viable stream of new ideas, projects, and programs.

The COO will share management responsibility (with the CEO) for the AAAS Program Heads, Director of Development, Chief Technology Officer, Chief Human Resources Officer, and Director of Innovation, and will be responsible for ensuring the effective development and operation of a defined set of AAAS programs. The COO will work closely with the Director of Development to cultivate existing relationships with public and private funders, and work closely with the Chief Membership Officer to ensure that programmatic activities are aligned with and leveraged by the Membership enterprise. The COO will also work closely with the CFO/CLO as an executive colleague to ensure optimal internal operations, allowing the CEO to spend sufficient time on externally focused programs and activities.

This is an extraordinary opportunity for an individual with extensive program management experience to grow and further develop a proven set of programs that have already made significant impact, while also acting as the Chief of Operations for AAAS's core administrative functions. Position requires a minimum Master's degree (Ph.D. preferred) in a relevant field with at least 10 years of experience and a track record in senior program management in a scientific or technical organization with experience overseeing large administrative support units.

To see the full job description, please visit **http://www.aaas.org/page/employment-aaas**, where interested and qualified candidates may apply online. Please apply no later than **July 3, 2015**.

AAAS is an EO Employer. All qualified applicants will receive consideration for employment without regard to race, color, religion, sexual orientation, gender identity, national origin, age, disability, veteran status, or other protected category. AAAS uses E-Verify to confirm the employment eligibility of all newly hired employees.

COLUMBIA UNIVERSITY MEDICAL CENTER

Assistant Professor position in Urology and Systems Biology

In the era of precision medicine, the Department of Urology and the Department of Systems Biology seek to jointly recruit an Assistant Professor, to further our understanding of the regulatory mechanisms and pathways involved in bladder and prostate cancer initiation, progression, and in modulating sensitivity to targeted agents.

The ideal candidate would have deep expertise in computational systems biology, will have published seminal manuscripts in high impact journal to elucidate mechanisms related to prostate or bladder cancer related phenotypes using systems biology methodologies. The candidate need also to have significant training in experimental biology and should be able to either perform relevant biochemical assays in his/her lab or to guide the design of these experiments in collaboration with other labs.

Applications should include a CV, reprints of no more than three publications, a 3-4 page description of current research and research goals, and three or more letters of reference. Applications should be addressed to **Ms. Desi Tahiraj, Columbia University Department of Systems Biology, 1130 St. Nicholas Ave 8th Floor Room 801, New York, NY 10032**. Applications can also be sent via e-mail at **desi@c2b2.columbia.edu**.

Columbia University is an Equal Opportunity/ Affirmative Action Employer and encourages applications from women and underrepresented minorities.

M | PHARMACY
UNIVERSITY OF MICHIGAN

Research Assistant Professor/Research Associate Professor/Research Professor and Deputy Director of Pharmacokinetics (PK) Core

The College of Pharmacy in association with the Comprehensive Cancer Center at the University of Michigan (U-M) is recruiting a research assistant professor/research associate professor/research professor to serve as the deputy director in the Pharmacokinetics Core (PK Core). This well-funded core is part of a broader drug discovery effort at the U-M campus, and the Deputy Director will play a key role in supporting ongoing collaborations, expanding outreach, and further developing the core.

The PK Core (www.pkcore.org) has four objectives: (A) To support preclinical pharmacokinetics (PK) and metabolism for lead compound selection and dose regimen optimization; (B) To support clinical pharmacokinetics (PK) and optimize dose regimen in clinical studies; (C) To increase grants, publications, and patent applications; (D) To train students and postdoctoral fellows in DMPK studies in drug discovery and clinical trials.

The Deputy Director will work with the PK Core Director to oversee daily operations, including managing personnel and budget; communicating with collaborators; and writing reports, manuscripts, and patents. In addition, the successful candidate will serve as PI, Co-PI, and Co-I on independent grant applications; mentor graduate students and postdoctoral fellows involved in DMPK studies, and teach related courses.

The Deputy Director will hold a PhD degree in pharmaceutical sciences or related field with experience and skills in preclinical and clinical drug metabolism and pharmacokinetics (DMPK) to support drug discovery and clinical trials. Experiences in pharmacokinetic modeling, LC-MS, drug metabolism, drug discovery, pharmacokinetics in animal models, and pharmacokinetics in clinical trials are preferred.

Applicants should submit a letter and CV, including the names of at least 5 potential references, to **Patrina Hardy** (**thardy@med.umich.edu**).

By **Lui Lam**

From physics to revolution and back

As a boy, I was not interested in science; I was interested in girls. Upon graduating from high school in Hong Kong, I did not particularly want to work in science; I just wanted a job, because I rarely left the dinner table with my stomach full. For graduate school, I went to Columbia University with a scholarship. There, I was surrounded by Nobel laureates—Isidor Isaac Rabi, Polykarp Kusch, Tsung-Dao Lee—and laureates-in-waiting: James Rainwater, Jack Steinberger, Leon Lederman. The most important moment in my physics education was when I noticed Lee standing next to me in the men's room, peeing. Nobel laureates are ordinary people, I learned, just like you and me.

At Columbia, I was influenced by the student antiwar movement and the Cultural Revolution that was raging in China. I and several others (including Peter Kwong, now at Hunter College, and Jean Quan, who would become the mayor of Oakland, California) started the Chinatown Food Co-op; our aim was to "serve the people." I wasn't interested in solving small problems; I wanted to save the world, to return to China and join the revolution.

"I wanted to save the world, to return to China and join the revolution."

I finally made it in 1978, at the beginning of the country's "reform and opening up" movement. I was assigned to do physics at the Chinese Academy of Sciences' Institute of Physics. In China, the spring of 1978 is called "Science Spring" because for 10 years science had come to a virtual halt. Basic science was banned. My colleagues and I resumed the work with great enthusiasm; if China was in ruins, we figured, the best option was to fix it. I helped open the door to the West, discovering bowlics—a type of liquid crystal—and publishing the first paper by mainland-only authors ever to appear in *Physical Review Letters*.

We did not have journals—only copies of journals—and there was just one Chinese-made copying machine in the institute, which broke down every half hour or so. Everything was scarce, including tofu and writing paper, but we were not troubled by the minimal calories available to fuel us. We worked diligently, day and night, except on Sundays. Sundays were for washing clothes, by hand.

China started sending scientists to the West—many to the United States—as visiting scholars and to international conferences. Among China's billion people were dozens of notable physicists, but the number of excellent ones was smaller; I was the only government-approved doctoral mentor in liquid crystal physics. Physics research can't be learned properly by reading books or papers; it should be learned by working alongside masters. China did have a few masters—those who had been trained in the West before 1949—but they were all busy establishing institutes or working on the atomic bomb.

Today, China is making progress scientifically, but there is still some distance to go. The Cultural Revolution sacrificed a whole generation of scientists. Among all the problems this created, it led to a scarcity of experts who could act as academic judges. Qualitative assessment was replaced by counting papers—a poor substitute. The damage lingers.

Lately, and happily, China's priorities have shifted toward innovation. Innovation is not easy, though, in a culture that for 2000 years has prided itself on taking the middle course in everything, for the sake of harmony and stability. It's the opposite of the Socratic method that's at the heart of Western science. Great scientists like Galileo show that breakthroughs can be made even in environments that emphasize orthodoxy—but then no one was counting Galileo's papers. China has very good scientists, but the country needs to find its way of doing innovative science.

After 6 years, I left China and returned to the United States—not for scientific or political reasons, or due to material want, but for family. During a visit to the United States with our daughter, my wife announced that she intended to stay. Forced to choose between the motherland and a daughter, I chose my daughter. I left China on good terms.

Lui Lam, professor at San Jose State University in California, now works on humanities and complex systems. For more on life and careers, visit sciencecareers.org. Send your story to SciCareerEditor@aaas.org.

ILLUSTRATION: ROBERT NEUBECKER


Photos ©2014 AHA/Todd Buchanan

eppendorf & Science

PRIZE FOR NEURO BIOLOGY

2014 Winner
Eiman Azim, Ph.D.
Columbia University
For research on skilled limb movement

Call for Entries

Application Deadline June 15, 2015

Eppendorf & Science Prize for Neurobiology
The annual Eppendorf & Science Prize for Neurobiology is an international award which honors young scientists for their outstanding contributions to neurobiological research based on methods of molecular and cell biology. The winner and finalists are selected by a committee of independent scientists, chaired by Science's Senior Editor, Dr. Peter Stern. To be eligible, you must be 35 years of age or younger.

You could be next to win this prize and to receive
> Prize money of US$25,000
> Publication of your work in Science
> Full support to attend the Prize Ceremony held in conjunction with the Annual Meeting of the Society for Neuroscience in the USA
> An invitation to visit Eppendorf in Hamburg, Germany

It's easy to apply!

Learn more at: www.eppendorf.com/prize

eppendorf Science AAAS

Q&A

career perspectives

Dr. Liron Bar-Peled

Science & SciLifeLab Prize for Young Scientists, Grand Prize Winner,
Research Associate,
Lallage Feazel Wall Fellow of the Damon Runyon Cancer Research Foundation,
Scripps Research Institute,
La Jolla, California

The Science & SciLifeLab Prize is awarded annually to young scientists for outstanding life science research for which he/she was awarded a doctoral degree in the previous two years.

To apply for the 2015 *Science* & SciLifeLab Prize, please visit:
www.sciencemag.org/SciLifeLabPrize

Q: Will you please summarize your winning essay?

A: So, a fundamental question in cell biology is how cell size is regulated by the environment. And my essay describes exactly this, and how we began to map out a pathway that senses environmental nutrients, such as amino acids, and translates that into cell growth. And so interestingly, what we found was a very complicated signal transduction pathway that is, not surprisingly, deregulated in human diseases. And our hope is that by studying this pathway, not only can we discover the complex underpinnings of human diseases, but we can have a real impact on human health by using this pathway as a diagnostic tool to identify those diseases that can be readily treated with available therapeutics.

Q: How did you become interested in this particular field of research?

A: In college, I took this wonderful paper reading course, and one of the papers we covered dealt with how the signaling pathway mTORC1 senses oxygen levels. I became fascinated with how such a fundamental biological process' growth regulation could be controlled by different environmental stimuli. The more I read about this, it became clear to me that we didn't understand that much. The idea of mapping a completely unknown pathway really intrigued me, and I knew I wanted to delve into the unknown, and by working on this pathway I got to do just that. And because this pathway is heavily mutated in human diseases, I felt that I could also have an impact on human health by researching this area.

Q: Can you tell us about your experience in Stockholm and the prize ceremony?

A: I had such wonderful time, and it has really been so delightful to not only meet the different scientists in Stockholm, but also the other awardees and hear about their cutting-edge research. Being in the Hall of Mirrors—where the first Nobel Prize was awarded—was really awe-inspiring. It's a beautiful venue, and it really makes me feel incredibly honored to be able to participate in this process and the award.

Q: How do you see yourself and your research in the next 5 to 10 years?

A: In the next couple of years, I plan to start my own lab where I'll be focusing on how cells respond to oxidative stress using chemical methodologies and combining them with traditional cell biological approaches. Oxidative stress underlies a wide variety of human diseases, such as cancer and neurodegenerative disorders, and I hope that with our current approaches, not only will we be able to have a better biological understanding of the processes that are deregulated by oxidative stress, but we may also be able to develop therapeutic targets. In the next 5 to 10 years, I'd really like to do what I'm currently doing, which is using novel technologies to get a better mechanistic understanding of fundamental processes in biology.

Q: Do you have any advice for your peers who are interested in submitting an entry for next year's *Science* & SciLifeLab Prize?

A: Being able to communicate your research, in my mind, is almost as important as being able to plan experiments. Unfortunately, I think that scientific writing can often be filled with esoteric jargon, but if you can communicate your ideas in a clear and simple manner, not only will that help you deliver the message to your audience, but it will also help you to distill your ideas which will help your research as well. I also recommend that you really have fun with the process. It's rare as scientists that we can really just let our hair down and write a little more creatively than our typical manuscript.

NOTE:

Answers have been adapted from the original video format and edited for print.

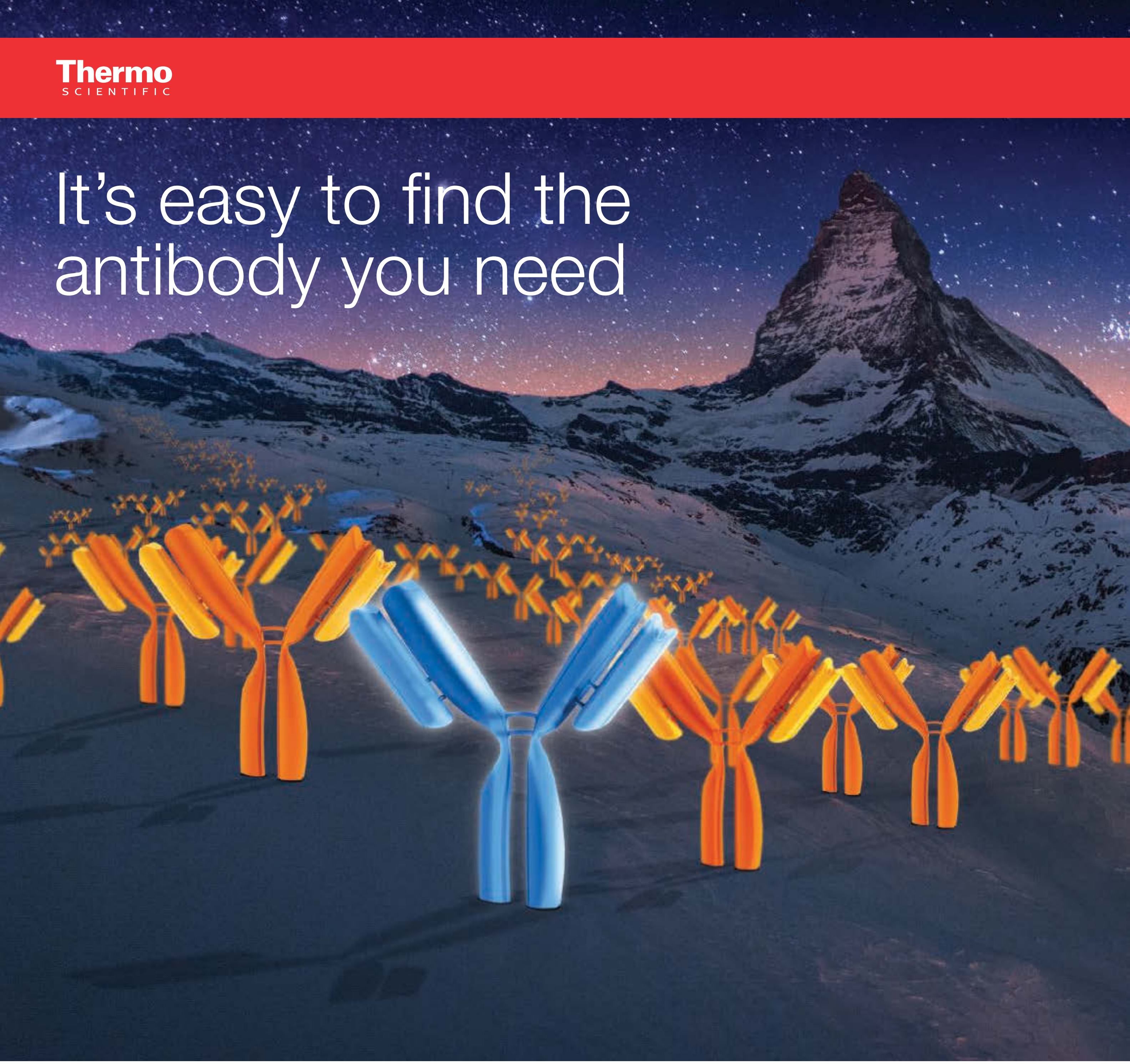
Thermo
SCIENTIFIC
It’s easy to find the antibody you need